Development of high-performance silicon carbide based temperature and humidity sensors using low cost, industry ready materials and fabrications techniques

by

Arjun Wadhwa

MANUSCRIPT-BASED THESIS PRESENTED TO ÉCOLE DE TECHNOLOGIE SUPÉRIEURE
IN PARTIAL FULFILLMENT FOR THE DEGREE OF
DOCTOR OF PHILOSOPHY
Ph.D.

MONTREAL, FEBRUARY 16, 2025

ÉCOLE DE TECHNOLOGIE SUPÉRIEURE
UNIVERSITÉ DU QUÉBEC

BOARD OF EXAMINERS

THIS THESIS HAS BEEN EVALUATED

BY THE FOLLOWING BOARD OF EXAMINERS

Dr. Sylvain G. Cloutier, thesis supervisor
Département de génie électrique à l'École de Technologie Supérieure

Dr. Martin Bolduc, co-supervisor
Département de génie mécanique à Université du Québec à Trois-Rivières

Dr. Éric David, president of the board of examiners
Département de génie mécanique à l'École de Technologie Supérieure

Dr. Ricardo Izquierdo, member of the jury
Département de génie électrique à l'École de Technologie Supérieure

Dr. Alexandre Robichaud, external examiner
Département des sciences appliquée à Université du Québec à Chicoutimi

THIS THESIS WAS PRESENTED AND DEFENDED

IN THE PRESENCE OF A BOARD OF EXAMINERS AND THE PUBLIC

ON JANUARY 14, 2025

AT ÉCOLE DE TECHNOLOGIE SUPÉRIEURE

ACKNOWLEDGEMENTS

I would like to take this opportunity to thank you my Family, my wife Pooja and my mother Vandana for their unconditional support and love through this endeavor. Pooja, thank you for patiently listening to me, allowing me to bounce ideas off of you and your constant motivation during the ups and downs of this PhD Journey. This journey would not be the same without you. Mom, thank you for your unwavering belief in me; this PhD is dedicated to you. Years ago you told me you wish you had done a PhD - this is your dream coming true.

I wish to thank my supervisor, Prof. Sylvain G. Cloutier. Thank you for giving me this opportunity to work with you and to learn from your vast knowledge. This PhD journey has been a mix of scientific research, industrial collaborations and immense exposure in terms of conferences and trade shows, none of which would have been possible without your support, patience and confidence in my abilities. I thank you for the critical decision making freedom you gave me which has allowed me to become a better researcher, professional and human being. I am grateful to you for making me a better person in all aspects of personal and professional life. Thank you for introducing me to the world of printed ceramics and semiconductors. Your insistence on deeply understanding semiconductor physics was instrumental in enhancing my knowledge on this subject.

I wish to express my eternal gratitude to my co-supervisor, Prof. Martin Bolduc. Without you I would have never undertaken this journey. Thank you for introducing me to ÉTS and Professor Cloutier. Over the years, your mentorship, guidance and friendship has been instrumental in shaping this thesis project and me as a human being. Thank you for believing in me and my ability to pursue a PhD during times of uncertainity and doubt.

I am extremely thankful to my colleagues; Alain, Debika, Jaime, Felipe, François-Xavier, Paul, Alexandre, Ahmed, Mohamad, Shayan, Abhiroop, Krunal, Julie, Aida and Fabrice. Thank you for your support, guidance and friendship throughout this journey. I cherish the scientific discussions, collaborations and personal interactions with each and everyone of you.

I would like to especially thank my co-authors in who's research projects I had the pleasure to participate. I would like to thank Laura Morelli for allowing me to develop printed structures for her project and our discussions over coffee. Thank you Mohamad Tahrenian for allowing me to contribute to two of your research article and thanks to Ahmed Mouley for your fantastic work on printed perovskites and allowing me to be a part of the project.

I cannot thank Mohammad Saadati, PhD enough for his support over the past 5 years. His patience, dedication and persevere towards the uncountable microscopy images, XRD and EBSD measurements acquired during this project is commendable. Your analytical thinking, grasp and comprehension of the subject matter often challenged me and improved the quality of this research project. I will fondly remember working along side you untill 2 am, your friendship and the numerous discussions we had both personal and professional. Thank you for being a very important part of this journey.

A special thank you to Mathieu Gratuze, PhD who was instrumental in several ways throughout this thesis project. Thank you for taking the time to teach me Matlab from scratch, debug my code and educate me on Overleaf. Thanks for spending countless hours in discussing and developing test plans and finding appropriate instruments to achieve the best results.

I am also grateful to support and research staff at ÉTS: Youssed Bekbouti, Normand Gravel, Mustapha Belhaj, Andre Zalzal and Christian Talbot for your support and participation in both academic and industrial research projects.

Lastly, I thank Josianne Lefebvre and Jean-Phillipe Masse at Polytechnique Montréal and Gwénaël Chamoulaud at UQAM for training me on several equipment and for performing countless measurements during the course of this project.

Développement de capteurs de température et d'humidité à base de carbure de silicium de température et d'humidité à base de carbure de silicium de l'industrie à faible coût et des techniques de fabrication.

Arjun Wadhwa

RÉSUMÉ

Les capteurs physiques imprimés ont été déployés avec succès dans l'industrie et la recherche universitaire au cours des deux dernières décennies. Bien que la plupart des capteurs imprimés soient suffisants pour des applications générales, la plupart des matériaux de détection et des matériaux supplémentaires utilisés sont sensibles aux facteurs environnementaux limitants. Pour que les capteurs imprimés puissent fonctionner dans des conditions environnementales élevées, telles que la température et l'humidité, on utilise souvent des matériaux céramiques. Le carbure de silicium (SiC) est traditionnellement très performant pour les applications de détection de température, d'humidité, de gaz et de photodétection, mais son utilisation dans les capteurs physiques imprimés a été fortement limitée. Le carbure de silicium offre des propriétés importantes telles que la tolérance aux températures élevées et aux produits chimiques corrosifs, tout en étant inerte et biocompatible. Les films imprimés en carbure de silicium à base de nanoparticules offrent une opportunité unique pour les applications de détection où des réseaux denses de nanopaticules SiC facilitent le mouvement des charges. Quelques tentatives ont été faites pour fabriquer des capteurs physiques entièrement imprimés basés sur des nanoparticules de SiC, la majorité des recherches étant encore en cours d'étude théorique et expérimentale, ce qui a conduit à une pénurie de capteurs imprimés SiC fabriqués commercialement. Cette thèse de doctorat vise à étudier et à faire progresser les capteurs de température et d'humidité SiC entièrement imprimés. En raison de leur tolérance élevée à la température, les dispositifs imprimés à base de SiC sont des candidats potentiels pour le déploiement dans des environnements difficiles tels que les températures ultra-élevées. Afin de faciliter l'utilisation de ces dispositifs, les interconnexions en argent imprimées doivent être robustes et durables dans ces conditions. Pour y parvenir, nous devons étudier le mécanisme de défaillance des encres d'argent commerciales à des températures élevées et mettre en œuvre des modifications pour améliorer la stabilité des encres dans ces conditions.

Après un examen approfondi de la littérature, nous commençons par établir les principales propriétés, les techniques de fabrication et les applications du carbure de silicium en tant que matériau de détection, ainsi que les capteurs imprimés conventionnels et les technologies d'interconnexion. Ensuite, nous formulons et fabriquons des capteurs de température et d'humidité à base de nanoparticules SiC à l'aide d'une technique additive peu coûteuse et prête à l'emploi, la sérigraphie. Cela nous permet de fabriquer des dispositifs fiables et reproductibles qui font l'objet d'études plus approfondies. L'architecture simple de l'impression du matériau de détection sur des électrodes interdigitées imprimées permet à ces capteurs d'être incorporés dans des applications de détection à grande échelle avec facilité et un coût supplémentaire insignifiant.

Après la fabrication du dispositif, les performances des capteurs de température et d'humidité sont évaluées. Nous signalons des capteurs d'humidité SiC très sensibles et flexibles, des temps d'adsorption et de désespoir bien supérieurs à ceux récemment rapportés dans la littérature. Nous démontrons également la mise en œuvre de ces dispositifs dans des outils de diagnostic médical et de prévention. Les capteurs de température imprimés en SiC sont très sensibles.

Mots-clés: Carbure de silicium, thermistance imprimée, capteur d'humidité imprimé, électronique imprimée, encre d'argent, électrodes interdigitées en argent, croissance du grain, épinglage zener, sérigraphie

Development of high-performance silicon carbide based temperature and humidity sensors using low cost, industry ready materials and fabrications techniques

Arjun Wadhwa

ABSTRACT

Printed physical sensors have been successfully deployed in industry and academic research over the past two decades. Although most printed sensors suffice for general purpose applications, most sensing and supplementary materials used are susceptible to limiting environmental factors. For printed sensors to perform at elevated environmental conditions such a temperature and humidity, often ceramic materials are employed. Silicon carbide (SiC) traditionally performs exceptionally well towards temperature, humidity, gas and photodetection applications, however its use in printed physical sensors has severely been limited. Silicon carbide offers significant properties such as high temperature and corrosive chemical tolerance along with being inert and bio-compatible. Nanoparticle based silicon carbide printed films pose a unique opportunity towards sensing applications where dense networks of SiC nanopaticles facilitate the movement of charge. Some attempts have been made towards fabricating fully printed physical sensors based on SiC nanoparticles with a majority of research still under theoretical and experimental investigation leading to a scarcity of commercial fabricated SiC printed sensors. This doctoral thesis aims to investigate and advance fully printed SiC temperature and humidity sensors. Owing to its high temperature tolerance, SiC based printed devices are potential candidates for deployment in harsh environments such as ultra high temperatures. In order to facilitate these devices the printed silver interconnects must be robust and sustainable under these conditions. To achieve this, we need to investigate the failure mechanism of commercial silver inks at high temperatures and implement modifications to enhance the inks stability at said conditions.

After an extensive literature review we first establish the key properties, fabrication techniques and applications of silicon carbide as a sensing material and conventional printed sensors and interconnect technologies. Next, we formulate and fabricate SiC nanoparticle based temperature and humidity sensors using industry ready, low cost additive technique; screen printing. This allows us to fabricate reliable and repeatable devices which are further investigated. The simple architecture of printing the sensing material atop printed interdigitated electrodes allows these sensors to be incorporated into large scale sensing applications with ease and insignificant cost addition.

Following the device fabrication, the performance of both the temperature and humidity sensors are evaluated. We report highly sensitive and flexible SiC humidity sensors adsorption and desperation times far superior to those recently reported in literature. We also demonstrate the implementation of these devices into medical diagnostic and prevention tools. The printed SiC temperature sensors are highly sensitive to changes in temperature with in a large range. We also investigate the impact of bending and humidity on these sensors with repeatable and adequate response. Lastly, we achieve significant operational temperature enhancement of commercial silver ink using silicon additives. The Zener pinning mechanism helps stabilize the

inks morphology and electrical conductivity at ultra high temperature making it an excellent low cost alternatives to precious metal inks. Overall, this doctoral thesis successfully delivers all printed, low cost SiC temperature and humidity sensors along with the understanding and means to modify commercial interconnect silver inks for high temperature applications.

Keywords: Silion carbide, printed thermistor, printed humidity sensor, printed electronics, silver ink, silver interdigitated electrodes, grain growth, zener pinning, screen printing

TABLE OF CONTENTS

Page

INTRODUCTION 1

CHAPTER 1 LITERATURE REVIEW 9
1.1 Ceramics in Printed Physical Sensors 9
1.1.1 Wide Band Gap Semiconductors 10
1.2 Silicon carbide - An overview 11
1.3 Bulk silicon carbide 13
1.3.1 Properties 13
1.3.1.1 Crystalline structure 13
1.3.1.2 Electronics properties 17
1.3.1.3 Thermal and mechanical properties 20
1.3.2 Fabrication techniques 23
1.3.2.1 Acheson method 23
1.3.2.2 Lely method 24
1.3.3 Applications 25
1.3.3.1 Power electronics 26
1.3.3.2 Medical devices 28
1.3.3.3 Sensing 29
1.4 Silicon carbide nanomaterials 33
1.4.1 Properties 33
1.4.1.1 Surface properties 34
1.4.1.2 Thermal properties 36
1.4.1.3 Electrical properties 37
1.4.1.4 Biocompatibility 38
1.4.2 Fabrication Techniques 39
1.4.2.1 Solid phase techniques 39
1.4.2.2 Liquid phase techniques 47
1.4.2.3 Vapor phase techniques 49
1.4.3 Sensing applications 51
1.5 Technological maturity of SiC nanomaterials based physical sensors 56

CHAPTER 2 STATE OF THE ART 57
2.1 Printed Electronics - An Overview 57
2.2 Printed materials 59
2.2.1 Overview of ink formulation 60
2.2.2 Conductive inks 62
2.2.3 Semiconducting ink 67
2.2.4 Dielectric inks 68
2.3 Printing techniques 69
2.3.1 Contact printing 70

2.3.2 Non-contact printing 71
2.3.2.1 Screen printing 75
2.4 Substrates 77
2.5 Post processing techniques 81
2.5.1 Sintering 82
2.5.2 Annealing 87
2.6 Characterization Techniques 88
2.6.1 EBSD - Electron Backscatter Diffraction 88
2.6.2 XPS - X-ray Photoelectron Spectroscopy 91
2.6.3 Raman Spectroscopy 95
2.6.4 Fourier Transform Infrared Spectroscopy (FTIR) 99
2.7 Device integration 102
2.7.1 Interdigitated electrodes (IDE's) 103
2.7.2 Limitations of printed IDE's 105
2.7.3 Grain growth 106
2.7.4 Zener Pinning 109
2.8 Printed Physical Sensors 113
2.8.1 Printed Humidity Sensors 113
2.8.2 Printed Temperature Sensors 117
2.9 Additive Manufacturing of silicon carbide 121

CHAPTER 3 FLEXIBLE SCREEN-PRINTED SIC-BASED HUMIDITY SENSORS 125
3.1 Introduction 126
3.2 Experimental Section 128
3.2.1 Materials 128
3.2.2 Ink Formulation and Device Fabrication 128
3.2.3 Characterization Methods 130
3.3 Results and Discussion 131
3.3.1 Material Characterization and Morphology 131
3.3.2 Humidity Sensing Mechanism 145
3.3.3 Device Integration 146
3.4 Conclusion 149

CHAPTER 4 ALL SCREEN PRINTED AND FLEXIBLE SILICON CARBIDE NTC THERMISTORS FOR TEMPERATURE SENSING APPLICATIONS 151
4.1 Introduction 152
4.2 Experimental Section 156
4.2.1 Materials 156
4.2.2 Ink Formulation 156
4.2.3 Device Design and Fabrication 156
4.2.4 Characterization Methods 157
4.3 Results and Discussion 159

4.3.1 Material Characterization 159
4.3.2 Morphology 160
4.3.3 Printed SiC Thermistor Characterization 161
4.3.4 Thermistor Performance 168
4.4 Conclusions 172

CHAPTER 5 GRAIN STRUCTURE ENGINEERING IN SCREEN-PRINTED SILVER FLAKE-BASED INKS FOR HIGH-TEMPERATURE PRINTED ELECTRONICS APPLICATIONS 175
5.1 Introduction 176
5.2 Materials and Methods 180
5.2.1 Materials 180
5.2.2 Ink Formulation 180
5.2.3 Sample Fabrication 181
5.2.4 Testing and Characterization 181
5.3 Results and Discussion 182
5.3.1 Material Characterization 182
5.3.2 Evolution of Electrical Conductivity 184
5.3.3 Evolution of Grain Size 187
5.3.4 Oxidation States 192
5.3.5 Grain Growth Kinetics 194
5.4 Conclusions 197

CONCLUSION AND RECOMMENDATIONS 201

APPENDIX I CHAPTER 3: FLEXIBLE SCREEN-PRINTED SIC-BASED HUMIDITY SENSORS 207

APPENDIX II CHAPTER 4: ALL SCREEN PRINTED AND FLEXIBLE SILICON CARBIDE NTC THERMISTORS FOR TEMPERATURE SENSING APPLICATIONS 215

APPENDIX III CHAPTER 5: GRAIN STRUCTURE ENGINEERING IN SCREEN-PRINTED SILVER FLAKE BASED INKS FOR HIGH-TEMPERATURE PRINTED ELECTRONICS APPLICATIONS 219

LIST OF REFERENCES 223

LIST OF TABLES

Page

Table 1.1 Ramsdell's, Zhdanov's, and Jagodzinski's notations of major SiC polytypes 14

Table 1.2 Lattice constants of SiC polytypes at room temperature 17

Table 1.3 Mechanical properties of SiC polytypes 23

Table 1.4 Harsh environmental conditions based on application areas 31

Table 1.5 0D - 3D nanostructures 34

Table 1.6 SiC nanoaprticle synthesis methods 39

Table 1.7 Reported materials and reaction conditions towards carbothermal reduction synthesis of SiC nanomaterails 46

Table 2.1 Ink properties requirements for different printing methods 61

Table 2.2 Conductive inks conductivity (S/m) comparison 62

Table 2.3 Comparing features, challenges, properties and outputs of various contact and non-contact printing techniques 74

Table 2.4 Comparing key properties of commonly used substrates 81

Table 2.5 Recent literature on additive manufacturing of SiC 124

Table 3.1 SiC humidity sensor ink formulations 129

Table 3.2 Humidity sensor response (% change in resistance R/R_0) over different SiC loadings and cure temperatures 140

Table 3.3 Comparison of sensing performance of recently reported humidity senors 144

Table 4.1 Electrical performance of various printed SiC thermistor inks 168

Table 4.2 State of the art of SiC based and printed thermistors 171

Table 5.1 Calculations of n, k, activation energies (Q) and R^2 values based on experimental results after 1 hour isothermal annealing at 400 °C, 500 °C, 600 °C and 700 °C 196

LIST OF FIGURES

Page

Figure 0.1 (a) Number of publications on devices fabricated with different printing technologies between 1993-2024 (b) % of publications per printing technology, Data assimilated from Scopus. 1

Figure 0.2 (a) Number of publications on printed physical sensors between 1993-2024. (b) % of publications per printing technology. Data assimilated from Scopus. 3

Figure 1.1 (a) Occupation sites (A,B and C) in a hexagonal closed-packed structure (b) Schematic of SiC polytypes. 15

Figure 1.2 (a) Ball and stick model of SiC polytypes (b) Primitive cell model of SiC polytypes 16

Figure 1.3 Electronic bandgap of SiC polytypes 18

Figure 1.4 Electronic bandgap temperature dependency of SiC polytypes 19

Figure 1.5 (a) Density of states and (b) intrinsic carrier density of SiC polytypes 21

Figure 1.6 Thermal conductivity of SiC polytypes 22

Figure 1.7 Acheson's process 24

Figure 1.8 Lely's method 25

Figure 1.9 Modified Lely's method 26

Figure 1.10 (a) Number of publications on various SiC based applications between 1993-2024 (b) Percentage of publications per SiC application type, Data assimilated from Scopus 27

Figure 1.11 GaN vs SiC vs. Si 27

Figure 1.12 SiC based (a) pressure sensor (b) strain sensor (c) temperature sensor (d) humidity sensor 30

Figure 1.13 Effect of various surface modifications on the properties of SiC/SiO_2 nanoparticles 35

Figure 1.14 Combustion synthesis of SiC nanoparticles 44

Figure 1.15 Sol-gel synthesis of SiC nanoparticles - process overview 47

Figure 1.16 (a) Schematic illustration of pulsed laser ablation in liquid for synthesizing SiC nanoparticles (b) TEM image of SiC nanoparticles produced using the pulsed laser ablation in liquid method (c) Image of a single β-SiC nanoparticle 48

Figure 1.17 Schematic illustration of CVD fabrication of SiC nanoparticles 49

Figure 1.18 SiC nano-material based applications..... 52

Figure 1.19 (a) SiC nano sheets based humidity sensor spin coated onto metallic electrodes (b) humidity sensor response (c) sensor response over multiple cycles..... 53

Figure 2.1 Key ingredients of printed inks used in flexible printed electronic devices 60

Figure 2.2 Comparing printing technologies..... 70

Figure 2.3 Comparing print speed versus achieved trace pitch for various printing techniques 71

Figure 2.4 (a) Screen (b) Flexographic (c) Gravure (d) Aerosol Jet (e) Inkjet printing process schematics.n..... 73

Figure 2.5 (a) Screen printing of silver ink (b) screen printing process parameters 75

Figure 2.6 (a) Thermal (b) photonic (c) laser (d) microwave (e) electrical sintering process schematics 83

Figure 2.7 (a) Experimental setup in FE-SEM for EBSD analysis, (b) Kikuchi pattern formation in EBSD..... 89

Figure 2.8 (a) XPS experimental setup (b) schematic representation of XPS mechanism 92

Figure 2.9 (a) Raman scattering mechanism (b) Raman spectrometer setup..... 97

Figure 2.10 FTIR spectrometer setup..... 101

Figure 2.11 (a) Geometrical specifications of interdigitated sensors (b) Flow of electric current between the electrodes (c) Electrical representation of interdigitated electrodes in printed physical sensors..... 103

Figure 2.12 Humidity sensor mechanism..... 113

Figure 2.13 (a) RTD (b) Thermistor (c) thermocouple 118

Figure 2.14 Number of publications on additive manufacturing of SiC between 1993-2024. Data assimilated from Scopus 121

Figure 3.1 (a) Device fabrication schematic (b) SiC humidity test setup. 129

Figure 3.2 (a) Characterization of the materials used to fabricate the SiC-based humidity-sensitive ink includes: (a) thermogravimetric analysis (TGA) of the SOL725 resin conducted from room temperature to 600 °C, (b) Raman spectroscopy confirming the cubic crystalline phase of the SiC nanoparticles, and (c) X-ray diffraction spectra verifying the cubic phase along with the presence of a hexagonal phase in the as-received SiC nanoparticles 132

Figure 3.3 Morphological characterization of the SiC nanoparticles and printed SiC humidity-sensitive films includes: (a) particle size distribution of SiC nanoparticles dispersed in various solvent systems, (b) particle size distribution determined through image processing analysis. Additionally, field emission scanning electron microscopy (FE-SEM) micrographs of the SiC humidity sensitive film cured at 300 °C are shown at magnifications of (c) 100x, (d) 10,000x, and (e) 100,000x 134

Figure 3.4 Energy dispersive X-ray (EDX) analysis micrographs display the distribution of (a) Si, (b) C, and (c) O species within the printed SiC film, confirming the material's composition and the presence of native surface oxidation on the SiC nanoparticles 135

Figure 3.5 Characterization of the printed SiC humidity-sensitive films includes: (a) X-ray photoelectron spectroscopy (XPS) spectra confirming the presence of Si, O, and C species in the printed films, (b) Fourier transform infrared (FTIR) spectra indicating the absence of hydrophilic $-OH$ functional groups, (c) viscosity versus shear rate curves for 20, 30, 40, and 50 wt.% SiC-loaded humidity-sensitive inks, and (d) viscosity as a function of SiC weight percentage 136

Figure 3.6 Energy dispersive X-ray (EDX) analysis micrographs display the distribution of (a) Si, (b) C, and (c) O species within the printed SiC film, confirming the material's composition and the presence of native surface oxidation on the SiC nanoparticles 138

Figure 3.7 Characteristics of the printed SiC humidity sensors include: (a) response of 20, 30, 40, and 50 wt.% SiC humidity sensors cured at 300 °C for 180 minutes. Performance of the 40 wt.% SiC sensors:

(b) adsorption/desorption plot showing a hysteresis of 6.5% at 60% RH, (c) response curve with polynomial fitting, (d) plot determining adsorption/desorption time constants via a drop test, (e) high-speed cycling of the SiC humidity sensor between 30-70% RH, (f) long-term cycling between 10-90% RH over a 3.5-hour period, (g) detection of minute variations in %RH using the 40 wt.% printed SiC humidity sensor, (h) long-term cycling between 10-90% RH in 10% RH increments, and (i) temperature coefficient of resistance measured at different temperatures 139

Figure 3.8 Representation of the humidity sensing mechanism: (a) schematic illustrating the adsorption of water molecules onto the SiC humidity sensor film, and (b) the reduction in charge carrier mobility with increasing %RH 145

Figure 3.9 Demonstration of the application of printed SiC humidity sensors for preventative healthcare: (a) sensor response during human breathing with SiC humidity sensors attached to the exterior of a KN95 mask, (b) determination of human respiration rate based on the sensor response, and (c) photograph of the breath monitoring setup used for the measurements 147

Figure 3.10 Demonstration of the application of printed SiC humidity sensors towards large area humidity detection: (a) sminiaturized implementation of a 6x3 array of SiC humidity sensors, (b) demonstration of the change in response of the printed SiC humidity sensor array with contact from human hand with and without a glove (barrier), (c) illustrating depicting the change in response 149

Figure 4.1 SiC thermistor schematic a) top view b) side view. 157

Figure 4.2 a)- c) SiC thermistor fabrication process d) High resolution optical microscopy image of printed SiC thersmitor. 158

Figure 4.3 SiC thermistor test setup. 159

Figure 4.4 Characterization of commercially sourced $3C-SiC$ particles a) XRD spectra, b) Raman spectra c) UV-VIS spectra with Tauc plot as inset to determine electronic band gap, d) SEM micrograph 161

Figure 4.5 EDX imaging of a) SiC particles representing b) Si c) C and d) O species 162

Figure 4.6 a), b) TEM micrographs and c) SAED pattern of SiC particles 162

Figure 4.7 a) Current-voltage characteristics and b) electrical conductivity of 30 wt.%, 35 wt.%, 40 wt.% SiC thermistor inks 163

Figure 4.8 SEM micrographs of a) and b) 30 wt.% c) and d) 35 wt.% e) and f) 40 wt.% SiC thermistor inks 164

Figure 4.9 a) Electrical resistance versus temperature of 30 wt.%, 35 wt.%, 40 wt.% SiC thermistors b) long term cycling c) thermal stability d) humidity stability e) change in baseline resistance after bend testing and f) electrical resistance versus temperature plot after bend testing of 30 wt.% SiC thermistor 166

Figure 4.10 Accuracy of printed 30 wt.% SiC thermistor calculated via the Steinhart's equation. 169

Figure 5.1 (a) Schematic of screen printing process to fabricate ink samples on alumina substrate (b) Thermal cycling ramp profile 181

Figure 5.2 (a) Raman spectra of pristine and modified ($Ag - Si$) ink (b) particle size distribution of Si nano particles as purchased 183

Figure 5.3 SEM micrographs of (a) pristine $Agink$ and (b) modified ($Ag - Si$) silver ink sintered at 250 °C. (c) EDX map of ($Ag - Si$) ink sintered at 250 °C with Si particles highlighted in red 184

Figure 5.4 Electrical conductivity of (a) pristine Ag and modified ($Ag - Si$) inks with (b) 3 wt.%, (c) 5 wt.%, (d) 7 wt.%, (e) 10 wt.% silver inks treated at incremental temperatures for 1 hour isothermal exposure, electrical conductivity of pristine Ag and modified ($Ag - 5wt.\%Si$) inks thermally treated at (f) 500 °C, (g) 500 °C, (h) 600 °C, (i) 700 °C, (j) 800 °C, (k) 900 °C over 10 mins, 1, 2, 3, 4 hours isothermal exposure 185

Figure 5.5 Accuracy of printed 30 wt.% SiC thermistor calculated via the Steinhart's equation. 188

Figure 5.6 SEM micrographs of pristine Ag ink thermally treated at (a) 400 °C, (b) 500 °C, (c) 600 °C, (d) 700 °C, (e) 800 °C and (f) 900 °C for 1 hour 189

Figure 5.7 EBSD micrographs of pristine Ag ink thermally treated at (a) 400 °C, (b) 500 °C, (c) 600 °C, (d) 700 °C, (e) 800 °C and (f) 900 °C for 1 hour 190

Figure 5.8 SEM micrographs of 5 wt.% modified ($Ag-5wt.\%Si$) ink thermally treated at (a) 400 °C, (b) 500 °C, (c) 600 °C, (d) 700 °C, (e) 800 °C and (f) 900 °C for 1 hour 191

Figure 5.9 EBSD micrographs of 5 wt.% modified ($Ag-5wt.\%Si$) ink thermally treated at (a) 400 °C, (b) 500 °C, (c) 600 °C, (d) 700 °C, (e) 800 °C and (f) 900 °C for 1 hour 192

Figure 5.10 SEM and EDX micrographs exhibiting the effect of (a) and (c) large Si particles and (b) and (d) smaller Si particles on the printed films morphology respectively 193

Figure 5.11 XPS analysis of the silver ink samples after annealing (a) % Oxygen concentration in silver oxide species for the pristine silver ink samples after a 3-hour isothermal annealing (b) % Oxygen concentration in silver oxide species for the pristine silver ink samples after a 4-hour isothermal annealing (c) % Oxygen in silicon oxide and total silicon oxide in the modified (Ag+Si) ink samples for 3 hour and 4 hour isothermal annealing 195

Figure 5.12 Arrhenius plot of the parameter k versus isothermal exposure temperatures 197

LIST OF ABREVIATIONS

0D	Zero dimensional
1D	One dimensional
2D	Two dimensional
3D	Three dimensional
APC	Ammonium polycarboxylate
AZO	Aluminum doped zinc oxide
BFO	Bismuth iron oxide
CCD	Charge-coupled device
CNT	Carbon nanotubes
CTE	Coefficient of thermal expansion
CVD	Chemical vapor deposition
DOD	Drop on demand
DSC	Differential scanning calorimetry
EBSD	Electron Backscatter Diffraction
EDX	Energy-dispersive X-ray spectroscopy
ETS	École de Technologie Supérieure
EV	Electric vehicle
FBCVD	Fluidized bed chemical vapor deposition
FE	Field emitter

FET	Field effect transistor
FTIR	Fourier Transform Infrared Spectroscopy
GaN	Gallium nitride
GO	Graphene oxide
GPa	Giga pascal
HMI	Human machine interface
HMTA	Hexamethylenetetramine
InP	Indium phosphide
IoT	Internet of Things
IPL	Intense pulsed light sintering
ITO	Indium tin oxide
JFET	Junction field effect transistor
LCD	Liquid crystal display
LCVD	Laser chemical vapor deposition
LTCC	Low Temperature Cofired Ceramic
MOD	Metal-organic decomposition
MOSFET	Metal-oxide-semiconductor field-effect transistor
MWCNT	Multi-walled carbon nanotubes
NTCR	Negative Temperature Coefficient of Resistance
OA	Phenolic resin with oxalic acid

OE-A	Organic and Printed Electronics Association
OLED	Organic light emitting diodes
OPV	Organic photovoltaic devices
OTFT's	Organic thin-film transistors
PCB	Printed circuit board
PC	Polycarbonate
PCVD	Plasma chemical vapor deposition
PEDOT	Poly(3,4-ethylenedioxythiophene) polystyrene sulfonate
PEN	Polyethylene naphthalate
PET	Polyethylene terephthalate
PI	Polyimide
PLAL	Pulsed laser ablation
PMMA	Polymethyl methacrylate
PS	Polystyrene
PVDF	Polyvinylidene fluoride
PVP	Polyvinyl alcohol
PZT	Lead zirconate titanate
R2R	Roll to roll
RF	Radio frequency
RFID	Radio frequency identification

rGO	Reduced graphene oxide
SEM	Scanning electron microscope
SiC	Silicon Carbide
SOI	Silicon on wafer
SWCNT	Single-walled carbon nanotubes
TCO's	Transparent conducting oxides
TFT	Thin film transistor
TGA	Thermogravimetric analysis
TEOS	Tetraethyl orthosilicate
TPU	Thermoplastic polyurethanes
USD	United States Dollar
WBG	Wide band gap
XPS	X-ray Photoelectron Spectroscopy
XRD	X-ray crystallography
%RH	Percentage relative humidity

LIST OF SYMBOLS AND UNITS OF MEASUREMENTS

A_{H_2O}	Water absorption
Ag	Silver
α	Coefficient of thermal expansion
β	Thermal index
bar	Pressure
cm	Centimeter
cm^{-1}	Wavenumber
cm^{-1}	Cubic centimeter
cm^2/Vs	Square centimeter per Volt second
cps	Centipoise (Viscosity)
E	Elongation
E_{g0}	Electronic bandgap
eV	Electron volt
eV K^{-1}	Electron volt per Kelvin
GHz	Giga Hertz
Gpa	Gigapascal
g/cm^{-3}	Grains per cubic centimeter (Density)
h	Hours
h	Plank's constant

Hz	Hertz
I-V	Current voltage characteristic
J/gK	Joules per gram Kelvin (Specific heat)
K	Kelvin
kHz	Kilo Hertz
kJ/mol	Kilo joule per mole
kΩ/sq	Kilo ohm per square
kV	Kilo volt
MΩ	Megaohm
M_c	Conduction band minima
m^*_{de}	Mass of electron
m^*_{dh}	Mass of hole
m/min	Meters per minute
mbar	Pressure
mN/m	Milli Newton per meter (Surface tension)
mV/°C	Millivolts per degree Celsius
Mpa	Megapascal
n_c	Density of states of the conduction band
n_v	Density of states of the valence band
N	Layer count

N_c	Density of states effective mass of the conduction band
N_v	Density of states effective mass of the valence band
nm	Nanometer
Ω	Ohm
Ωcm	Ohm centimeter
Ω/sq	Ohms per square
ppm	Parts per million
R	Roughness
R_s	Sheet resistance
S/m	Siemens per meter
s	Seconds
T	Temperature
T_g	Glass transition temperature
T_m	Melting point
T_{max}	Maximum operational temperature
θ	Angle of incidence
λ	Wavelength
V	Volt
W/cm.K	Watts per centimeter Kelvin
wt.%	Weight percent

μm	Micrometer
ρ	Density
ρ_v	Volumetric resistance
Å	Angstrom
°C	Degree Celsius

INTRODUCTION

Historical context of printed physical Sensors

In recent years, the development of all printed physical sensors represents a significant advancement in the field of sensor technology. To develop these sensors for modern applications, there is a growing need for mass-scale, cost-effective approaches with smart material combinations (Jiang, Islam, He, Huang, Cao, Advincula, Dahotre, Dong, Wu & Choi, 2023). Printing technologies for sensor development are an emerging field that dynamically meets these demands. Printed electronics refer to electronic devices manufactured through an additive printing process, involving the direct deposition of materials onto a substrate in a patterned manner (Suganuma, 2014).

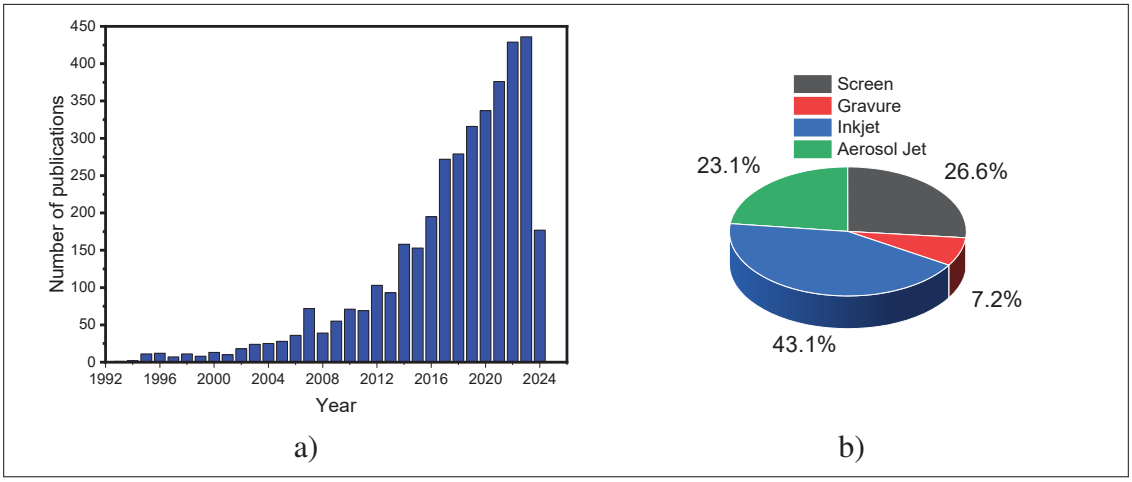

Figure 0.1 a) Number of publications on devices fabricated with different printing technologies between 1993-2024 (b) % of publications per printing technology Data assimilated from Scopus

Functional printing technologies have become increasingly popular towards fabricating physical sensors in the past two decades (Figure 0.1 a)) (Zikulnig, Chang, Bito, Rauter, Roshanghias, Carrara & Kosel, 2023). Independent market research (GreyViews, 2021) suggests that the printed electronics market value is set to increase from 10.02 Billion USD in 2021 to an estimated

39.54 Billion USD untill 2029. Researchers fabricate physical sensors using printing techniques such as inkjet printing (Kant, Shrivas, Kumar, Dewangan et al., 2023), screen printing (Beniwal, Ganguly, Aliyana, Khandelwal & Dahiya, 2023), and aerosol jet printing (Wadhwa, 2015), which offer numerous advantages over traditional sensor fabrication methods. Figure 0.1 b) compares the number of publications based on each printing technology towards fabricating physical sensors. Screen printing by far surpasses the other major printing techniques due to its unique advantages and low cost high volume proposition. According to GreyViews (2021), currently, 64% of printed devices are fabricated via screen printing.

The use of printing technologies allows for the creation of flexible, lightweight, and cost-effective sensors that can be easily integrated into a wide range of applications ranging from environmental monitoring, on and in body measurements, consumer electronics, agriculture, supply chain etc (Barmpakos & Kaltsas, 2021). As compared to conventional IC chip manufacturing process, printed devices offer a less complex alternative with minimal material losses and little to no hazardous chemical waste (Cui, 2016). Moreover, by using printed technologies the overall production and capital costs can potentially be reduced to 1/10 or lower as compared to conventional fabrications processes with the additional advantages of multi-material and substrate flexibility all encompassed in one printing process (Suganuma, 2014).

A printed electronics development road map published by the Organic and Printed Electronics Association (OE-A) (Donald Lupo,Klaus Hecker & Ranfeld, 2017) indicates the main sectors expected to exponentially grow over the coming years:

- **IoT**: smart packaging and labels, environmental and goods monitoring, energy management, sensor networks for structural heath monitoring.
- **Medical Devices**: smart dressing and packaging, smart disposable patches for patient vital monitoring, smart wound treatment,

- **Automotive**: flexible and customisable heaters, OLED lighting and displayed, HMI (human machine interface) touch displays and sensors.

- **Consumer electronics**: Flexible displays, conformal touch surfaces, flexible batteries, wearable sensors, RFID tags and passive antennas.

These key sectors employ printed sensors for various applications. Among several possibilities; temperature (Wadhwa, Guerrero, Gratuze, Bolduc & Cloutier, 2024), relative humidity (Farahani, Wagiran & Hamidon, 2014a), pressure (Narakathu, Eshkeiti, Reddy, Rebros, Rebrosova, Joyce, Bazuin & Atashbar, 2012), gas (Dai, Ogbeide, Macadam, Sun, Yu, Li, Su, Hasan, Huang & Huang, 2020) and strain (Amjadi, Kyung, Park & Sitti, 2016) sensors are most widely employed in industry. Figure 0.2 a) depicts a substantial increase in number of articles published on various printed physical sensors in the last two decades and Figure 0.2 b) illustrates the % publications per sensor type. It is clear that development and optimization of novel printed temperature and humidity sensors are dominant across the academic landscape.

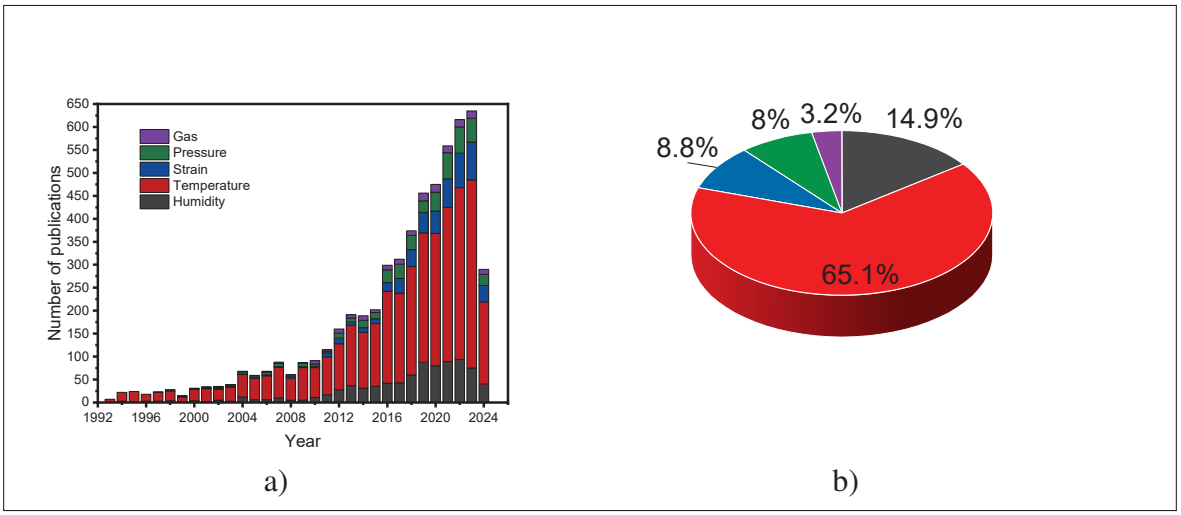

Figure 0.2 (a) Number of publications on printed physical sensors between 1993-2024
(b) % of publications per printing technology
Data assimilated from Scopus

Objectives and Motivations

The purpose of this doctoral thesis is to explore and better understand the fundamental relationship between device fabrication parameters and physical properties of printed physical sensors made with silicon carbide (SiC) nanoparticles. Based on this fundamental understanding we are able to tailor the printed sensors physical response based on the ink formulation and vice versa. Ultimately, we will be able to develop precise, reproducible and repeatable devices based on the knowledge assimilated. Further, this thesis will emphasis on the development of novel devices fabricated via commercially available materials and with the potential of ultra low cost, high volume manufacturability, enabling large scale deployment across various industries. In recent years, conventional SiC devices have gained a lot of mainstream traction in critical applications such as electric vehicle batteries (Saha, Kumar & Panda, 2022), harsh environment sensing (Li, Liu, Sheng, Li, Zhang & Jiang, 2024), power electronics (Wan, 2024) etc. However, the use of SiC as an active sensing material in low cost and flexible printed sensors has sparsely been explored thus far. Motivated by its many advantages and the zeal to contribute to practical science, we identify SiC as a promising candidate due to the following reasons:

- SiC, also known as carborundum is a hard compound sparingly found in nature as an extremely rare mineral moissanite (Taka, 2016). However, the two building blocks of SiC, silicon and carbon are extremely abundant in nature. Owing to its abundant use and simple yet stable chemical structure, mass manufacturing of SiC in various forms is possible (Abderrazak & Hmida, 2011).

- Due to ever increasing demand of SiC in various forms for several applications, several fabrications approaches have been developed by industry and the scientific communication towards mass productions ranging from powdered form (abrasives) to SiC wafers (micro-electronics). Market research (Precedence, 2023) predicts that the over all SiC market is estimated to grow by 200% by 2033 with a market evaluation of 11.29 Billion US$. This

ensures a steady supply of SiC which is essential and is often underestimated by academic researchers.

- SiC is traditionally mass manufactured by the Acheson process (Guichelaar, 1997) in rectangular cross-section electrical resistance furnaces. Higher purity SiC is manufactured using the Lely process (Heydemann, Schulze, Barrett & Pensl, 1996). Thus, the SiC supply chain is inelastic owing to these large scale mass manufacturing processes. It is estimated that the price per metric ton of SiC ranges between US$822 - US$1,070 in 2019 depending on the geographic region studied (Intratec, 2019). These prices are set to decline over time as the demand of SiC for various applications increases and production techniques are optimized for higher yields.

- Owing to its excellent chemical inertness, oxidation resistance, ultra-high melting point, and bio-compatibility; SiC particles have been utilized for various applications ranging from composites (Bagheri, Shamsipur, Abdollahzadeh & Mirsalehi, 2023), field emittors (FE's) (Li, Lou, Li, Wang, Gao, Shao, Chen & Yang, 2021), Field effect transistors (FETs) (Mousa & Teker, 2021), sensors (Wu, Zhou, Yue, Wei & Pan, 2015), elecro-chemical devices (Puttananjegowda, Takshi & Thomas, 2022), supercapacitiors (Nguyen, Aberoumand & Dao, 2021c) and microwave absorbers (Singh, Bhaskar, Narayanan, Kumar & Debnath, 2024).

Since the early 2000's, digitization of manufacturing technologies also known as Industry 4.0 has revolutionized several industries by integrating smart technology, data, and automation (Lasi, Fettke, Kemper, Feld & Hoffmann, 2014). Combining physical processes with computational systems involving embedded computers monitoring and controlling physical processes (often with feedback loops) allows for real time corrections and optimization of processes leading to unprecedented improvements in efficiency and yield (Majid, Habib, Javed, Rizwan, Srivastava, Gadekallu & Lin, 2022). The inclusion of physical sensing networks plays a vital role in assimilating data across greenhouses (Maraveas & Bartzanas, 2021), data centers (Medina-

Santiago, Azucena, Gómez-Zea, Jesús-Magaña, de la Luz Valdez-Ramos, Sosa-Silva & Falcon-Perez, 2019), food monitoring (Karim, Hassan, Akanda & Mallik, 2018) etc. In these applications, printed temperature, humidity, pressure, strain etc. sensor can play a vital role.

A wide variety of functional metarials have been studied and employed in both academic and industrial establishments towards developing low cost printed physical sensors. Materials ranging from metals, polymers to ceramics and their composites have been developed. These developments will be discussed in detail in the following sections. However, very little work has been done towards the use of SiC nanoparticles towards developing printed physical sensors. During the course of this doctoral thesis, I focus on developing and characterizing all printed, flexible SiC based temperature and humidity sensors using low-cost, commercially avaiable materials and low cost manufacturing techniques. Additionally, we study the effect of ceramic inclusion on commercially available silver screen printable inks to enhance their maximum operational temperature for high temperature applications.

The following are the key motivations central to success of this doctoral thesis:

- The proposed methodologies must use straightforward and industry-ready deposition methods. By doing so, an easier technological integration from lab scale to the industry can be achieved.
- The proposed devices should use less material quantity compared to the literature to be economically attractive.
- The proposed devices should provide innovative solutions to the problems that limit large-scale deployment of the technologies previously mentioned.

The successful development of all printed, low-cost sensors for harsh environments paves the path towards reduced complexity in structural health monitoring and preventative maintenance.

Contributions and Innovations

SiC based devices have been employed across a wide range of applications and industries. However, cumbersome and high cost intensive methods such as chemical vapor deposition (CVD) (Li, Cai, Hu, Liu, Dai, Xu, Zhang, Zhang, Liu, Kosinova et al., 2023a), sputtering (Kim & Chung, 2011) and supttering (Puttananjegowda *et al.*, 2022) have often been involved in developing such devices. As a result, SiC based devices find use in niche applications such as hazardous sensing environments, sub-orbital space flight, power electronics etc. Following the complex deposition method used to fabricate SiC based devices, we decided to choose simpler deposition methods which are more suitable toward industry and large-scale applications.

The main contributions of this doctoral thesis are as follows:

- Novel SiC nanoparticles have been successfully used to fabricate low-cost, flexible and printed sensing devices. This materials has been only sparingly used in the field of printed electronics and printed physical sensors thus far.
- All devices are fabricated via screen printing which is a low cost and high throughput production technologies.
- We developed high sensitivity and low hysteresis flexible screen printed SiC thermistors for wide temperature range applications.
- We also developed high sensitivity and reproducible SiC humidity sensors using SiC and studied their applications for medical interventions via a KN 95 mask
- We extensively studied the effect of silicon inclusions on the morphology, electrical and thermal properties of low cost silver screen printed inks thereby allowing us to increase their operations by over 300 °C.

Thesis Overview

This thesis is divided into six chapters. In Chapter 1, we present an extensive literature review on the fundamental properties, fabrication techniques, applications and technological maturity of SiC in the realm of additive manufacturing. Chapter 2 introduces concepts including an overview of key printed electronics technologies such as printing technique, materials used and sintering technologies. In this chapter, we also highlight some of the kep characterization techniques that have been utilized to better understand some of the key chemical and physical properties of the materials used and the sensors produced.

Chapters 3-5 are original research articles submitted or published in peer reviewed journals. And finally, Chapter 6 highlights the statement of original contributions, perspectives and future works that can improve upon the research carried out during this doctoral thesis.

CHAPTER 1

LITERATURE REVIEW

1.1 Ceramics in Printed Physical Sensors

Ceramics, being inorganic and nonmetallic, play a vital role in our everyday lives. They are utilized in various fields such as construction (including tiles, glass, and bricks) and transportation (like shuttles, airplanes, and automobiles). Among all materials, ceramics are the most extensively manufactured and utilized by humans (Bhalla, Guo & Roy, 2000). Ceramic materials are renowned for their exceptional properties, including high temperature resistance, chemical inertness, mechanical strength, and electrical insulation, making them ideal candidates for fabricating printed physical sensors. These sensors are increasingly vital in various application. The following are some of the salient ceramic materials used towards sensing applications fabricated via printed technologies:

- **Piezoelectric Ceramics**: Ceramics such as lead zirconate titanate (PZT) (Ouyang, Cormier, Williams & Borkholder, 2016), barium titanate ($\mathrm{BaTiO_3}$) (Li & Lim, 2022), and zinc oxide (ZnO) (Beduk, Bihar, Surya, Castillo, Inal & Salama, 2020) and bismuith iron oxide ($\mathrm{BiFeO_3}$) (Fourmont, Bai, Fortier & Cloutier, 2022b) are widely used in printed sensors due to their ability to generate an electric charge in response to mechanical stress. This property is particularly useful in temperature, pressure, force, and vibration sensors.

- **Conductive Ceramics**: Conductive ceramics, such as indium tin oxide (ITO) (Gilshtein, Bolat, Sevilla, Cabas-Vidani, Clemens, Graule, Tiwari & Romanyuk, 2020) and aluminum-doped zinc oxide (AZO) (Matei, Constantinescu, Mitu, Filipescu, Ion, Ionita, Brajnicov, Alloncle, Delaporte, Emandi et al., 2015), are essential for creating transparent conductive paths and electrodes in printed sensors. These materials offer excellent electrical conductivity and transparency, making them suitable for applications in touch screens, flexible displays, and transparent electrodes. ITO is extensively used in resistive and capacitive touch sensors, where its transparency and conductivity are critical (Granqvist, 2007).

- **Dielectric Ceramics**: Dielectric ceramics like barium titanate ($BaTiO_3$) (Craton, He, Roch, Chahal & Papapolymerou, 2019), strontium titanate ($SrTiO_3$) (Kohler, Nikfalazar, Friederich, Wiens, Sazegar, Jakoby & Binder, 2015), and alumina (Al_2O_3) (Chen & Brandon, 2016) are crucial for their insulating properties and high dielectric constants. These materials are used in capacitive sensors, where they serve as the dielectric layer between the conductive plates. $BaTiO_3$ is particularly favored for its high dielectric constant, which enhances the sensitivity and miniaturization of capacitive sensors (Yamamoto, Lanagan, Bhalla, Newnham & Cross, 1989). Alumina, with its excellent thermal and chemical stability, is used in harsh environments for temperature and pressure sensors (Buchanan, 2018).

- **Gas Sensing Ceramics**: Ceramic such as tin dioxide (SnO_2) (Rieu, Camara, Tournier, Viricelle, Pijolat, de Rooij & Briand, 2016), tungsten trioxide (WO_3) (Guo, Tian, Liang, Yang, Tang, Li, Liu, Zheng, Chen & Wu, 2023), and zinc oxide (ZnO) (Manjunath, Pujari, Patil & Mandal, 2020) are widely used in gas sensors. These materials change their electrical resistance when exposed to certain gases, making them ideal for detecting pollutants and hazardous gases. SnO_2 is commonly used in carbon monoxide sensors due to its high sensitivity and fast response time (Zuo, Tavakoli, Mathavakrishnan, Ma, Lim, Rotondo, Pauzauskie, Pavinatto & MacKenzie, 2020). WO_3 and ZnO are used in sensors for detecting nitrogen oxides (Lee, Han, Huh & Lee, 1999) and hydrogen sulfide (Engel, Benito-Altamirano, Tarantik, Pannek, Dold, Prades & Wöllenstein, 2021) respectively.

1.1.1 Wide Band Gap Semiconductors

Wide band gap semiconductors (WBG) have garnered significant interest in various applications due to their superior electrical, thermal, and mechanical properties compared to conventional silicon based devices. In the realm of printed physical sensors, WBG materials such as silicon carbide (SiC), gallium nitride (GaN), and zinc oxide (ZnO) offer numerous advantages that make them particularly suitable for demanding environments and high-performance sensing applications. WBG semiconductors have a larger band gap, typically greater than 2.0 eV, which translates to high breakdown voltages, excellent thermal conductivity, and inherent robustness

to high-temperature environments (Neudeck, Okojie & Chen, 2002). These properties are crucial for physical sensors, which often need to operate reliably under extreme conditions. For instance, SiC and GaN can function effectively at temperatures exceeding 600 °C, far surpassing the thermal limits of silicon-based devices (Roccaforte, Fiorenza, Greco, Nigro, Giannazzo, Iucolano & Saggio, 2018). The maximum operational temperature of silicon (Si)-based devices is typically around 150 °C - 200 °C for standard applications, beyond which performance degrades due to increased leakage currents and carrier mobility changes. Advanced high-temperature Si devices with specialized doping and insulation can operate up to 300 °C. Beyond this, Si undergoes excessive intrinsic carrier generation, making it unsuitable for stable operation. The high breakdown voltage of WBG semiconductors also enables the creation of sensors that can operate at higher voltages and power levels, making them ideal for applications in power electronics and harsh industrial environments (Baliga, 2018). Additionally, their strong resistance to radiation and chemical degradation further enhances their suitability for aerospace, automotive, and energy sectors (Harris, 1995).

Ink formulations for WBG materials have been developed to facilitate their use in various printing techniques, such as inkjet printing, screen printing, and aerosol jet printing (Gupta, Arunachalam, Cloutier & Izquierdo, 2018; Wu, Gong, Kuehne, Kanibolotsky, Chen, Perepichka, Mackintosh, Gu, Skabara, Pethrick et al., 2009). For example, SiC nanoparticle inks can be used to create temperature sensors that exploit the material's stability at high temperatures (Wadhwa *et al.*, 2024). Similarly, ZnO inks are employed in the fabrication of strain gauges and piezoelectric sensors due to their excellent piezoelectric properties and high sensitivity (Wang, et al., 2012).

1.2 Silicon carbide - An overview

Silicon carbide (SiC) is a versatile material with applications across various industries. Its two most well-known uses are as an abrasive material and, more recently, as a wide bandgap semiconductor for high-power, high-temperature electronic devices. The use of SiC in semiconductor devices has only become feasible in the past twenty years, following the commercial

availability of SiC single crystals. While thin films and nanoparticles of SiC are still uncommon, monolithic SiC and SiC-containing composites have been available for much longer. A challenge in working with SiC is its ability to crystallize into various polymorphs, with the most common being $3C - SiC$ ($\beta - SiC$) and the hexagonal $2H$, $4H$, and $6H$ phases. Its high melting point makes it difficult to achieve reasonable bulk densities in polycrystalline materials. Additionally, SiC forms Schottky barriers with most metals, and the formation of its native oxide, SiO_2, can create issues in oxidizing atmospheres. Despite these challenges, the scientific community has ingeniously turned some of these drawbacks into advantages for various applications.

SiC is rare in nature, with the first synthesis reported by Swedish chemist Jöns Jakob Berzelius in 1824 (Berzelius, 2022). In 1892, Acheson developed a process for synthesizing SiC from silica, carbon, and additives like salt (Acenson, 1893). This method, known as the Acheson process, enabled the mass production of SiC powders for industrial applications such as cutting, grinding, and polishing. As a by-product of this process, ingots containing small single crystalline SiC platelets, primarily $6H - SiC$, were produced. Although not pure, these platelets were used for fundamental studies on SiC's physical and chemical properties. A significant milestone in this research was Round's discovery of electroluminescence (yellow light emission) from SiC in 1907 (Round, 1991). Around the same time, Moissan discovered natural SiC and studied it as a mineral, leading to its mineralogical name, "Moissanite" (Moissan, 1905).

In 1955, Lely successfully grew relatively pure SiC crystals using a sublimation technique known as the Lely method (Lely, 1955). These crystals were predominantly $6H - SiC$, though they often included foreign polytypes. The high crystal quality of Lely platelets sparked the first wave of research into SiC as a semiconductor in the 1960s. During this period, the primary focus was on developing high-temperature devices and blue light-emitting diodes (Marshall, Faust & Ryan, 1974; O'Connor & Smiltens, 1960). Shockley highlighted the potential of SiC for high-temperature electronics (Marshall *et al.*, 1974). Significant academic research on $SiC's$ optical properties was conducted by (Choyke, 1969). However, due to the small size of Lely platelets and an inconsistent material supply, research and development of SiC semiconductors slowed in the late 1970s, leaving the technology underdeveloped. Meanwhile, polycrystalline

SiC technology advanced, leading to the commercialization of SiC-based ceramics, heating elements, passive components, and thermistors.

SiC is a IV-IV ceramic with unique chemical and physical properties. The strong chemical bonding between silicon (Si) and carbon (C) atoms gives SiC high hardness, chemical inertness, and high thermal conductivity (Harris, 1995). As a semiconductor, SiC has a wide bandgap, high critical electric field strength, and high saturation drift velocity. Both n-type and p-type doping are relatively easy in SiC, making it exceptional among wide bandgap semiconductors. The ability of SiC to form silicon dioxide (SiO_2) as a native oxide is a significant advantage for device fabrication. Due to these properties, SiC is a promising material for high-power and high-temperature electronics (Davis, Kelner, Shur, Palmour & Edmond, 1991),(Ivanov & Chelnokov, 1992),(Morkoc, Strite, Gao, Lin, Sverdlov & Burns, 1994).
Both bulk and nanomaterial forms of SiC pose unique characteristics with applications in various fields. Hence it is essential to detail the properties, fabrication techniques and applications of both forms of SiC individually as seen in the next sections of this chapter. Although we exclusively utilize SiC nanopowders for the development of our sensors in this PhD project, the knowledge of bulk SiC materials helps us understand device operating principles and performance which are essential to the success of our devices. Additionally, by understanding physical sensors made with both forms us SiC helps us realize the trade offs between device processing techniques, fabrication costs and device performance.

1.3 Bulk silicon carbide

1.3.1 Properties

1.3.1.1 Crystalline structure

SiC is a compound semiconductor that strictly adheres to a stoichiometry of 50% silicon (Si) and 50% carbon (C). The electronic structures of neutral Si and C atoms in their ground states are:

$$Si, 14e^- : 1s^2 2s^2 2p^6 3s^2 3p^2 \tag{1.1}$$

$$C, 6e^- : 1s^2 2s^2 2p^2 \tag{1.2}$$

Both silicon (Si) and carbon (C) atoms are tetravalent, each having four valence electrons in their outermost shells. In a SiC crystal, Si and C atoms form tetrahedral structures by sharing electron pairs in sp^3-hybrid orbitals, resulting in strong covalent bonds. Each Si atom is bonded to four C atoms, and each C atom is bonded to four Si atoms. The high bond energy of the $\mathrm{Si}-\mathrm{C}$ bond (4.6 eV) gives SiC a range of remarkable properties. Crystallographically, SiC is a prime example of polytypism, a phenomenon where a material can have different crystal structures that vary in stacking sequence without changing its chemical composition. In a hexagonal close-packed system, variations in the occupied sites along the c-axis create different crystal structures, known as polytypes as seen in Figure 1.1a). There are three possible sites, labeled A, B, and C. Consecutive layers cannot occupy the same site, so a layer on top of an "A" site must occupy either a "B" or "C" site, and similarly, an "A" or "C" site over a "B" site. While most materials typically stabilize into one stacking structure, such as zincblende or wurtzite, SiC can crystallize into over 200 different polytypes.

Table 1.1 Ramsdell's, Zhdanov's, and Jagodzinski's notations of major SiC polytypes
Adapted from Kimoto & Cooper (2014)

Ramsdell's notation	**Zhdanov's notation**	**Jagodzinski's notation**
2H	11	h
3C	∞	k
4H	22	hk
6H	33	hkk
15R	$(32)_3$	hkkhk

In Ramsdell's notation, polytypes are represented by the number of $\mathrm{Si}-\mathrm{C}$ bilayers in the unit cell and the crystal system (C for cubic, H for hexagonal, and R for rhombohedral). 3C-SiC is commonly referred to as $\beta-\mathrm{SiC}$, while other polytypes are called α-SiC. The

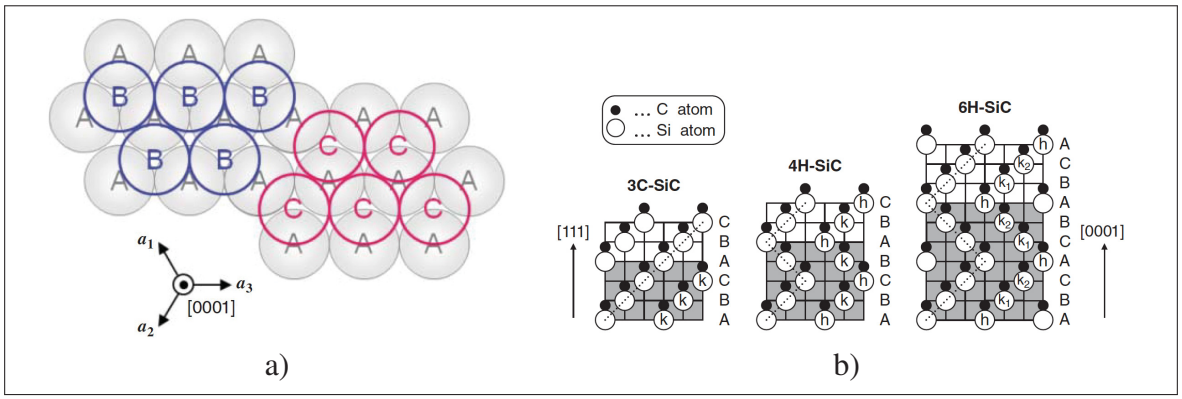

Figure 1.1 (a) Occupation sites (A,B and C) in a hexagonal closed-packed structure (b) Schematic of SiC polytypes
Taken from (Kimoto & Cooper, 2014)

structures of common SiC polytypes, including $3\mathrm{C}-\mathrm{SiC}$, $4\mathrm{H}-\mathrm{SiC}$, and $6\mathrm{H}-\mathrm{SiC}$, are illustrated schematically in Figure 1.1b), where open and closed circles represent Si and C atoms, respectively. The potential sites in a hexagonal close-packed structure are labeled A, B, and C. The stacking sequence for $3\mathrm{C}-\mathrm{SiC}$ can be described as ABCABC, or simply ABC. Similarly, $4\mathrm{H}-\mathrm{SiC}$ can be described by the sequence ABCB (or ABAC), and $6\mathrm{H}-\mathrm{SiC}$ by ABCACB. These structures are depicted in a ball-stick model in Figure 1.1a). Because multiple notations exist for defining stacking structures, the major SiC polytypes are described using Ramsdell's, Zhdanov's, and Jagodzinski's notations in Table 1.1. Figure 1.1b) shows the primitive cells and fundamental translation vectors of (a) cubic $(3\mathrm{C})\mathrm{SiC}$ and (b) hexagonal SiC. The "$3\mathrm{C}$" structure corresponds to the zincblende structure, common in $\mathrm{III}-\mathrm{V}$ semiconductors like GaAs and InP. The wurtzite structure, seen in GaN and ZnS, is denoted by "2H". The reason for the existence of so many SiC polytypes remains unclear. Generally, crystals with strong covalent bonding tend to crystallize in the zincblende structure, while those with high ionicity favor the wurtzite structure. $\mathrm{SiC}'\mathrm{s}$ intermediate ionicity (11% according to Pauling's rule) might explain its polytypism. The space groups are T_d^2 for $3\mathrm{C}-\mathrm{SiC}$, C_{6v}^4 for hexagonal polytypes, and C_{3v}^4 for rhombohedral polytypes. Hexagonal and rhombohedral polytypes are uniaxial, exhibiting unique polarized optical properties.

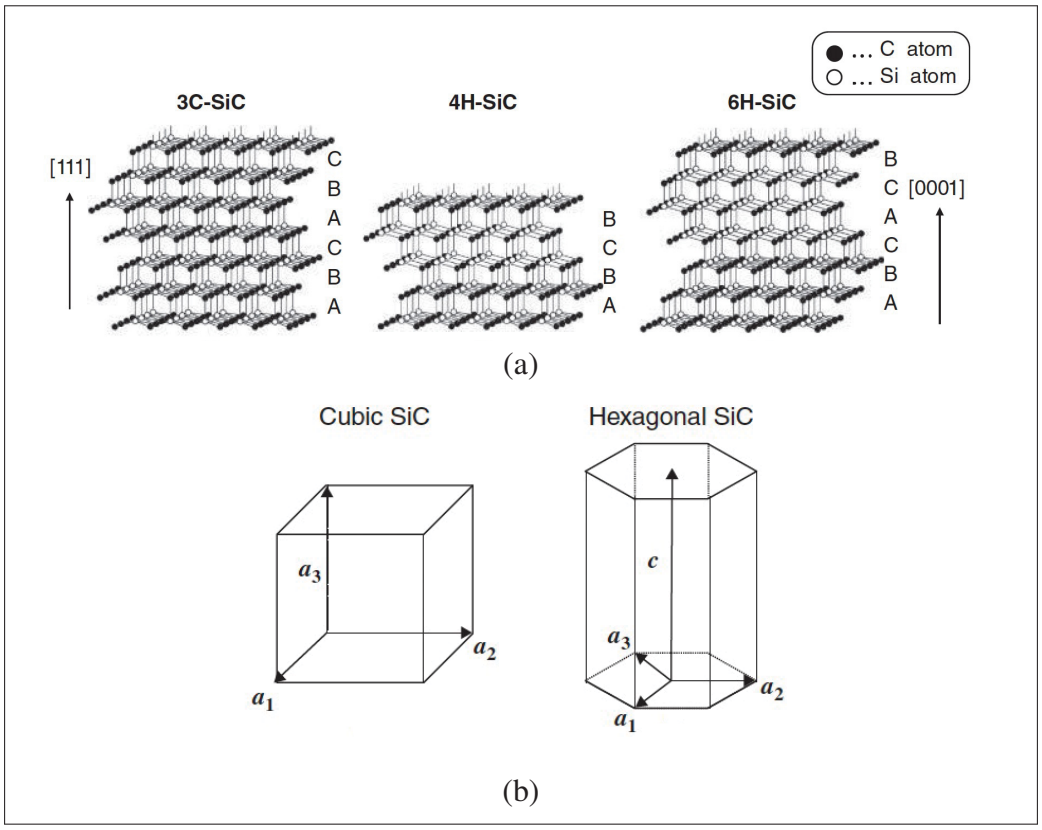

Figure 1.2 (a) Ball and stick model of SiC polytypes (b) Primitive cell model of SiC polytypes
Taken from Kimoto & Cooper (2014)

Due to the various ways to stack $\mathrm{Si}-\mathrm{C}$ bi-layers, SiC has several lattice sites with different structures of immediate neighbors. Lattice sites with hexagonal-structured surroundings are called "hexagonal sites", while those with cubic-structured surroundings are called "cubic sites." In Figure 2.2, these are labeled as "h" for hexagonal and "k" for cubic. $4\mathrm{H}-\mathrm{SiC}$ has one hexagonal and one cubic site, $6\mathrm{H}-\mathrm{SiC}$ has one hexagonal and two different cubic sites, and $3\mathrm{C}-\mathrm{SiC}$ has only cubic sites. The difference in the location of the second-nearest neighbors at hexagonal and cubic sites creates different crystal fields. This causes the energy levels of dopants, impurities, and point defects (like vacancies) to vary depending on the lattice site, a phenomenon known as the "site effect" (Choyke & Patrick, 1962; Ikeda, Matsunami & Tanaka, 1980; Suttrop, Pensl, Choyke, Stein & Leibenzeder, 1992).

Table 1.2 Lattice constants of SiC polytypes at room temperature
Taken from (Kimoto & Cooper, 2014)

Polytype	a(Å)	c(Å)
3C	4.3596	-
4H	3.0798	10.0820
6H	3.0805	15.1151

The stability and nucleation probability of SiC polytypes are highly temperature-dependent. For instance, $3C-SiC$ is unstable and transforms into hexagonal polytypes like $6H-SiC$ at very high temperatures, above 1900 °C - 2000 °C. This instability makes it challenging to grow large $3C-SiC$ ingots at a reasonable rate. Similarly, $2H-SiC$ is unstable at high temperatures, and large crystals of $2H-SiC$ have not been successfully produced. As a result, $4H-SiC$ and $6H-SiC$ polytypes are very popular and have been extensively studied. Despite its instability, $3C-SiC$ remains a popular polytype because it can be grown heteroepitaxially on silicon substrates. In addition to these main polytypes, $15R-SiC$ is occasionally obtained and has been studied to some extent.

Table 1.2 lists the lattice constants of major SiC polytypes at room temperature. While the lattice constants appear different due to the varying crystal structures, all SiC polytypes have nearly the same $Si-C$ bond length of 1.89 . The height of the $Si-C$ bilayer along the c-axis (unit height) is 2.52 , with $3C-SiC$ and $2H-SiC$ having a slightly smaller height of 2.50 .

1.3.1.2 Electronics properties

Band structure

Figure 1.3 shows the electronic band structures of $3C-SiC$, $4H-SiC$, $36H-SiC$ polytypes (Lambrecht, Limpijumnong, Rashkeev & Segall, 1997; Persson & Lindefelt, 1997). All SiC polytypes exhibit an indirect band structure.

The electronic band gap of $2H-SiC$ is 2.36 eV, $4H-SiC$ is 3.26 eV, $6H-SiC$ is 3.02 eV. The ratio of the number of hexagonal sites to the number of $Si-C$ bi-layers in a unit cell is defined

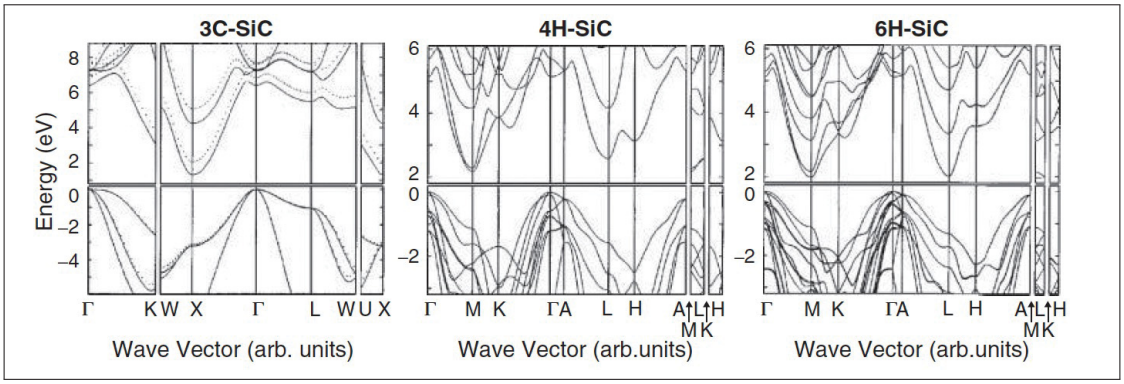

Figure 1.3 Electronic bandgap of SiC polytypes
Taken from (Kimoto & Cooper, 2014; Persson & Lindefelt, 1997)

as the "hexagonality" of SiC (Choyke & Devaty, 2004; Van Haeringen, Bobbert & Backes, 1997). The hexagonality is 1 for $2\mathrm{H}-\mathrm{SiC}$, 0 for $3\mathrm{C}-\mathrm{SiC}$, 1/2 for $4\mathrm{H}-\mathrm{SiC}$ and 1/3 for $6\mathrm{H}-\mathrm{SiC}$. Interestingly, the electronic bandgap of the SiC polytypes increases with increase in hexagonality. Additionally, the change in bandgap of SiC in inversely dependable on temperature. As temperature is increase the electronic bandgap decreases and is governed by the Equation 1.3 and as seen in Figure 1.4 (Adachi, 2009; Choyke, 1969).

$$E_g(T) = E_{g0} - \frac{\alpha T^2}{T+\beta} \tag{1.3}$$

Here, E_{g0} is the electronic bangdap at 0 K, T is the absolute temperature and α and β and the fitting parameters where α = 8.2 x 10^{-4} eV K^{-1} and β = 1.8 x 10^3 K.

The effective mass of electrons for the $3\mathrm{C}$, $4\mathrm{H}$, amd $6\mathrm{H}-\mathrm{SiC}$ are dependent on the polytype, whereas the effective mass of holes has a weak dependancy on the polytype (Chen, Son, Janzen, Hofmann & Meyer, 1997; Son, Persson, Lindefelt, Chen, Meyer, Hofmann & Janzén, 2004; Volm, Meyer, Hofmann, Chen, Son, Persson, Lindefelt, Kordina, Sörman, Konstantinov et al., 1996). This is because the $\mathrm{Si}-\mathrm{C}$ covalent bond structure is the same for all SiC polytypes indicating that the minima of the valance bands are the the same energy level.The difference s

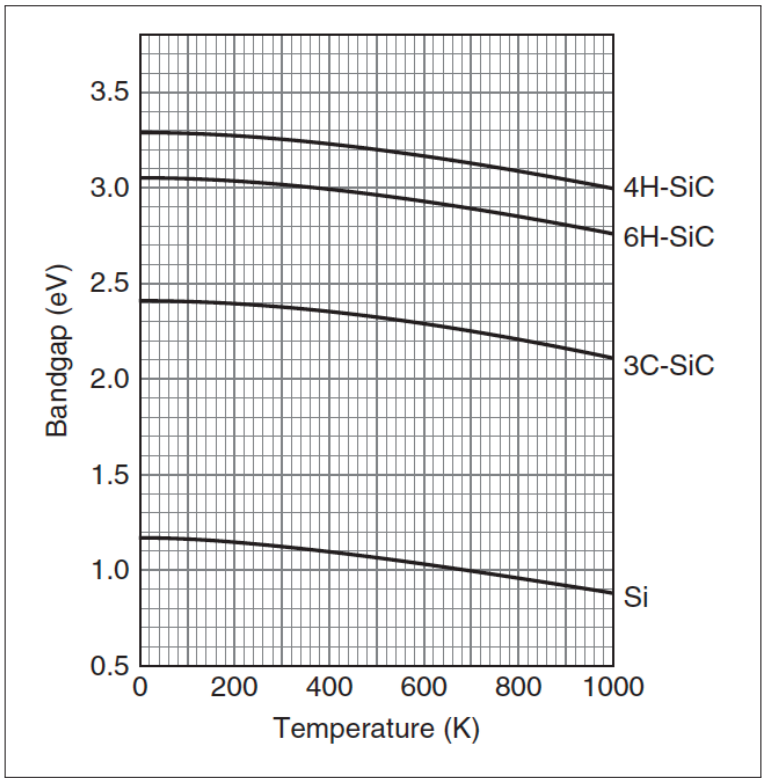

Figure 1.4 Electronic bandgap temperature dependency of SiC polytypes
Taken from (Kimoto & Cooper, 2014)

electron mass of different polytypes significantly impacts the electron mobility which will be discussed in the next section.

Carrier density and mobility

Given the known band structure, the effective densities of states in the conduction band (N_C) and valence band (N_V), as well as the intrinsic carrier density (n_i), can be calculated using Equations 1.4, 1.5 and 1.6 (Sze & Ng, 2007).

$$N_c = 2M_c\left(\frac{2\pi m_{de} * kT}{h^2}\right)^{3/2} \tag{1.4}$$

$$N_v = 2\left(\frac{2\pi m_{dh} * kT}{h^2}\right)^{3/2} \tag{1.5}$$

$$n_i = \sqrt{N_c N_v} exp(\frac{-E_g}{2kT}) \tag{1.6}$$

Here, M_c represents the number of conduction band minima, m^*_{de} and m^*_{dh} represent the effective masses of electrons and holes respectively and h is the Planck's constant. N_c and N_v are the density-of-state effective mass of electrons and holes. Figure 1.5 illustrates the temperature dependence of the effective densities of states in the bands and the intrinsic carrier density for major SiC polytypes, alongside that of Si. The temperature dependence of bandgaps is considered. At room temperature, the intrinsic carrier density in SiC is extremely low due to its wide bandgap; 0.13 cm^{-3} for 3C-SiC, 5×10^{-9} cm^{-3} for 4H-SiC, and 1×10^{-6} cm^{-3} for 6H-SiC. This low intrinsic carrier density is the primary reason why SiC electronic devices can operate at high temperatures. Silicon carbide has a much wider bandgap compared to silicon (Si, 1.12 eV). A wider bandgap results in a significantly lower intrinsic carrier concentration because the probability of thermally generated electron-hole pairs decreases exponentially with increasing bandgap energy. This means that even at high temperatures >300°C 300 °C, SiC maintains a low leakage current and stable electrical properties, whereas Si devices suffer from excessive intrinsic carrier generation, leading to performance degradation. Thus, the low intrinsic carrier density is a key factor enabling SiC devices to function efficiently at elevated temperatures.

Electron mobility (μ_n) in dependent on the unit cell of different SiC polytypes and is perpendicular to the c-axis (Schadt, Pensl, Devaty, Choyke, Stein & Stephani, 1994; Schaffer, Negley, Irvine & Palmour, 1994). Hexagonal SiC polytypes exhibit a strong anisotrophy in their electron mobility due to the different lengths of the c-axis while $3C-SiC$ has an isotropic mobility. The room temperature electron mobility of $3C-SiC$ is 800 cm^2/Vs, 900 cm^2/Vs $\parallel$ c-axis and 800 cm^2/Vs $\perp$ c-axis $4H-SiC$ and 60 cm^2/Vs $\parallel$ c-axis and 400 cm^2/Vs $\perp$ c-axis $6H-SiC$ (Ayalew, 2004).

1.3.1.3 Thermal and mechanical properties

Thermal conductivity is a material property that measures the ability of a material to conduct heat. It quantifies the rate at which heat energy passes through a material due to a temperature

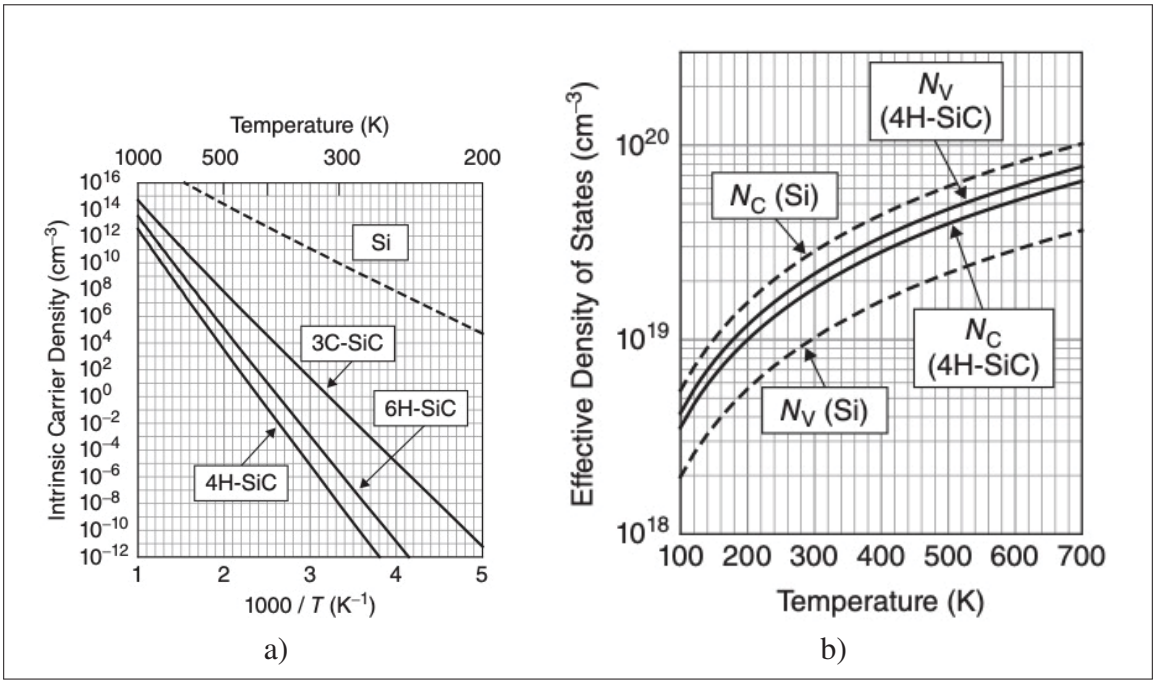

Figure 1.5 (a) Density of states and (b) intrinsic carrier density of SiC polytypes Taken from (Kimoto & Cooper, 2014)

gradient. Mathematically, it is defined as the amount of heat transferred per unit time through a unit area of the material, divided by the temperature gradient across the material expressed in W/cm·K. SiC is known for its high thermal conductivity, which is one of the reasons it is used in high-temperature and high-power electronic applications. The thermal conductivity of silicon carbide varies depending on the specific polytype and the purity of the material. For the most common polytypes (Morelli, Heremans, Beetz, Woo, Harris & Taylor, 1994; Slack, 1964):

- $4H - SiC$: 3.7 to 4.9 W/cm·K.
- $6H - SiC$: 3.5 to 4.9 W/cm·K.
- $3C - SiC$: 2.0 to 3.3 W/cm·K.

Figure 1.6 (Harris, 1995) illustrates the thermal conductivity of the above mentioned SiC polytypes versus temperature. These values are significantly higher than those of Si, which has

a thermal conductivity of about 1.5 W/cm·K at room temperature, making SiC an excellent material for applications requiring efficient heat dissipation.

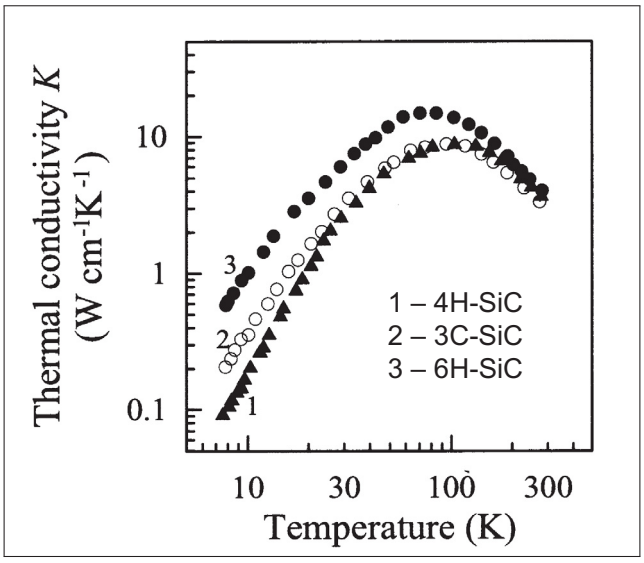

Figure 1.6 Thermal conductivity of SiC polytypes
Taken from (Harris, 1995)

SiC is one of the hardest materials known. Table 1.3 presents the primary mechanical properties of SiC and Si (Adachi, 2009; Harris, 1995), indicating that the polytype dependence is minimal. SiC′s hardness and Young's modulus between 380 to 700 GPa (Zorman & Parro, 2008) are significantly higher than those of Si. SiC′s Poisson's ratio of 0.21 is quite similar to that of other semiconductors. Also, SiC maintains its high hardness and elasticity even at very high temperatures. At room temperature, SiC has a yield strength of up to 21 GPa and is estimated to be 0.3 GPa at 1000 °C, whereas the yield strength of Si drops to 0.05 GPa at 500 °C (Suzuki, Yonenaga & Kirchner, 1995).

Table 1.3 Mechanical properties of SiC polytypes
Taken from (Adachi, 2009; Harris, 1995)

Properties	**SiC**	**Si**
Density (g cm^{-3})	3.21	2.33
Young's modulus (GPa)	390-690	160
Fracture strength (GPa)	21	7
Poisson's ratio	0.21	0.22
Elastic constant (GPa)		
c_{11}	501	166
c_{12}	111	64
c_{13}	52	-
c_{33}	553	-
c_{44}	163	80
Specific heat ($Jg^{-1}K^{-1}$)	0.69	0.7
Thermal conductivity (W/ cm.K)	2.0 - 4.9	1.4- 1.5

1.3.2 Fabrication techniques

1.3.2.1 Acheson method

The initial commercial method employed for SiC growth was the "Acheson process," which involved synthesizing SiC crystals in an electrical resistance furnace using a mixture of silica (SiO_2), coke (carbon), sawdust, and salt ($NaCl$) (Acheson, 1893). This process, depicted in Figure 1.7, utilized a central core of graphite and coke as a resistive heating element. The reactant mixture surrounded this core and was heated to approximately 2700 °C for a specific duration before gradually cooling. Sawdust was included to create porosity, allowing carbon monoxide and other gases to escape, while $NaCl$ acted as a purifier to react with and remove impurities as chloride vapors.

Temperature variations within the furnace resulted in different zones: the outermost region remained cooler, keeping the reactants unreacted; the intermediate region formed amorphous SiC; and the core region reached the highest temperatures, facilitating SiC formation. However, at very high temperatures, SiC decomposed into graphite and silicon vapors, with graphite remaining in the core and reacting with silicon vapors from cooler regions to form crystalline SiC.

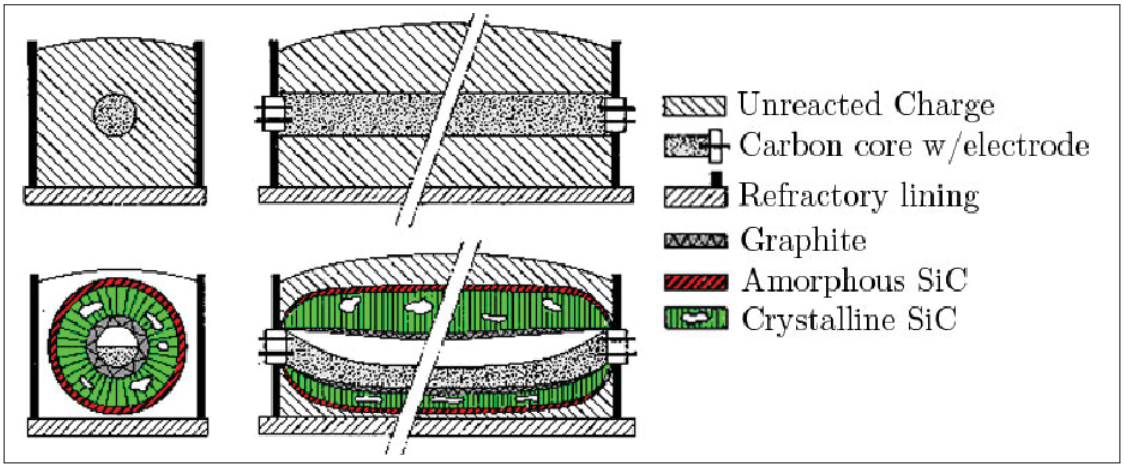

Figure 1.7 Acheson's process
Taken from (Davidsen, 2011)

Platelets, up to 2-3 cm in size, formed in cavities where carbon monoxide escaped, though crystal sizes decreased with distance from the core. While the Acheson process lacked consistency in crystal size and quality, the crystals produced could serve as seeds for further growth methods like physical vapor deposition (Byrappa & Ohachi, 2003; Knippenberg, 1963).

1.3.2.2 Lely method

In 1955, Jan Anthony Lely introduced the "Lely method," a sublimation process for SiC crystal production (Anthony, 1855). Illustrated in Figure 1.8, this method used a cylindrical graphite crucible filled with SiC lumps, closed with a SiC or graphite lid, heated to around 2500 °C in an argon atmosphere. SiC powder near the crucible walls sublimed due to the higher temperature, and SiC crystals nucleated on the cooler inner surface of the crucible. This process continued until all SiC lumps were graphitized, yielding high-quality, pure crystals. However, the Lely method had a slow growth rate unsuitable for industrial scale, though the produced SiC platelets could be used as seed crystals or epitaxial growth substrates (Byrappa & Ohachi, 2003; Knippenberg, 1963).

Tairov & Tsvetkov (1978) introduced a refined version, the "seeded sublimation growth" or "modified Lely method" . This technique minimized spontaneous nucleation by using a seed

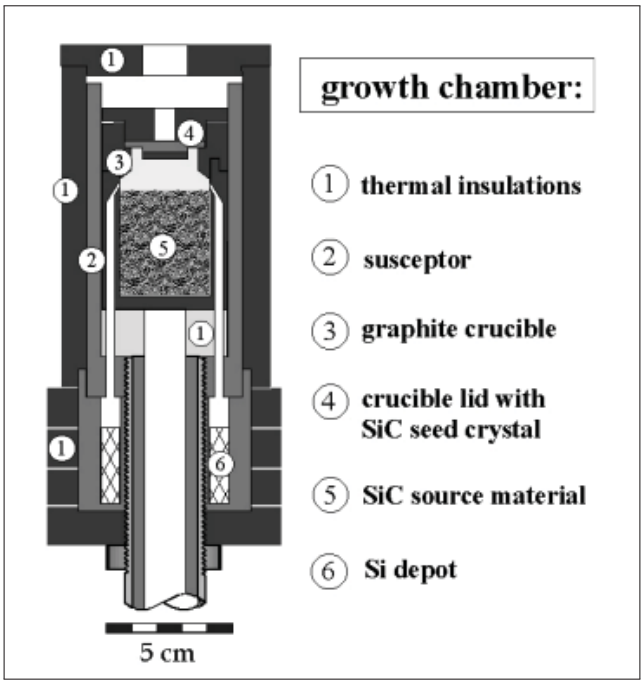

Figure 1.8 Lely's method
Taken from (Anthony, 1855)

crystal for controlled growth. Operating within a quasi-closed graphite crucible heated to 1800 °C - 2600 °C, SiC sublimed from a source (powder) at the crucible's bottom to a seed crystal at its top, facilitated by a thermal gradient (Figure 1.9). This method enabled the growth of larger, high-quality SiC crystals at a higher rate. The resulting SiC boules could be sliced into wafers, marking a significant advancement in SiC crystal production for commercial applications, including as substrates for electronics via physical vapor transport, a technique still used with modifications today.

1.3.3 Applications

Silicon carbide has emerged as a pivotal material in the electronics industry, renowned for its exceptional properties that significantly enhance the performance and efficiency of electronic devices. SiC′s wide bandgap, high thermal conductivity, and robust mechanical strength make it an ideal candidate for high-power and high-frequency applications. For over two decades now,

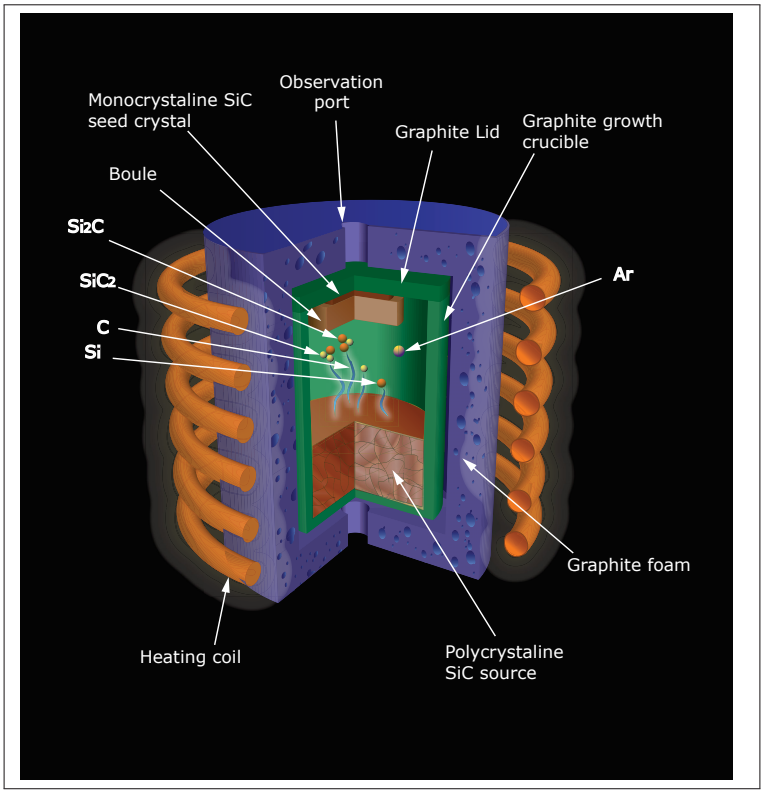

Figure 1.9 Modified Lely's method
Taken from (Semmelroth *et al.*, 2004)

academic researchers have shown increasing interest in using SiC towards pioneering research. Figure 1.10 a) shows an exponential increase in SiC applications based scientific literature. This section highlights some of the key application areas of bulk SiC materials.

1.3.3.1 Power electronics

As seen from Figure 1.10 b), one of the primary applications of SiC is in power electronics, where it is used to manufacture devices such as Schottky diodes (Chvála, Marek, Drobnỳ, Stuchlíková, Messina, Vinciguerra & Donoval, 2022), MOSFET's (Wang & Jiang, 2020), and power inverters (Wang, Song, Zhang, Li, Ahmad & Gong, 2020a). These SiC-based components are instrumental in improving the efficiency and compactness of power conversion systems, reducing energy losses, and enabling higher operating temperatures compared to traditional silicon-based devices.

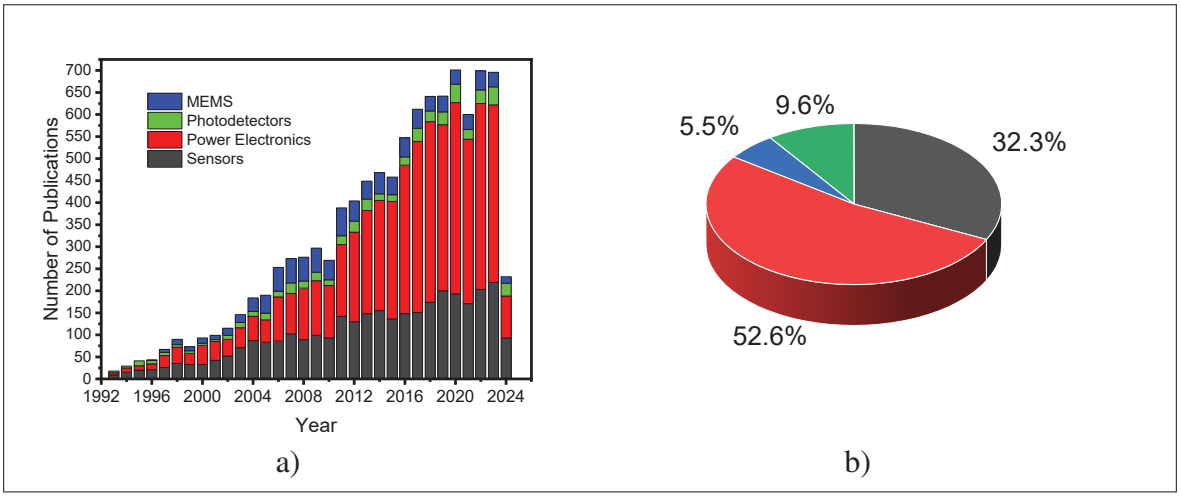

Figure 1.10 (a) Number of publications on various SiC based applications between 1993-2024 (b) Percentage of publications per SiC application type
Data assimilated from Scopus

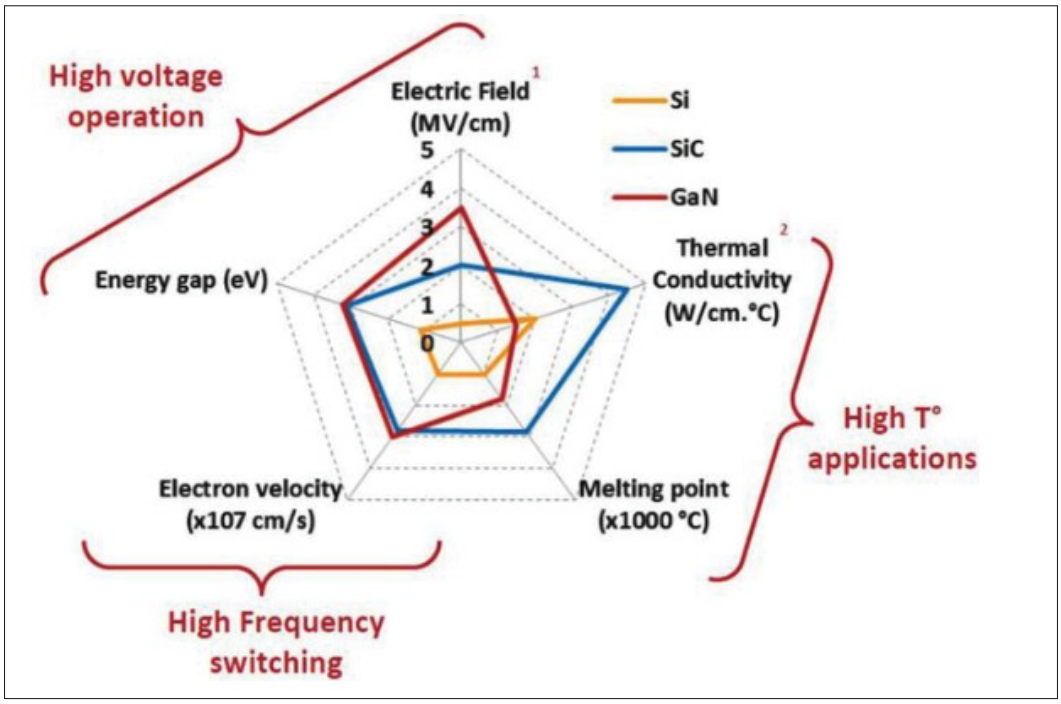

Figure 1.11 GaN vs SiC vs. Si
Taken from (Bigorra *et al.*, 2000)

Silicon is widely used in power electronics for its established fabrication processes and cost-effectiveness but has limitations in high temperature and high power applications. Where as gallium nitride offers higher efficiency, faster switching speeds, and can handle higher voltages, making it suitable for high-frequency applications. SiC excels in high voltage, high temperature, and high efficiency environments, providing better thermal conductivity and lower energy losses as compared to both Si and GaN (Bieniek, Janczyk, Sitnik & Messina, 2019) (Figure 1.11). In the automotive sector, SiC is revolutionizing electric vehicle (EV) technology by enhancing the performance of powertrain and charging systems. SiC devices allow for faster switching speeds and higher energy efficiency, leading to extended driving ranges and reduced charging times for EV's (Saha *et al.*, 2022). Additionally, $SiC's$ durability and thermal stability make it suitable for harsh environments, such as those found in aerospace and industrial applications, where reliability and longevity are critical (Middelburg, van Driel & Zhang, 2020). Moreover, SiC is gaining traction in renewable energy systems, including solar inverters and wind turbines (Appadurai & Raj, 2022; Park, Kieferndorf, Burkart & Agostini, 2020c), where it contributes to more efficient energy conversion and management. As the demand for high-performance and energy-efficient electronic devices continues to grow, SiC is poised to play a crucial role in advancing the capabilities of modern electronics.

1.3.3.2 Medical devices

Silicon carbide's biocompatibility, mechanical strength, and chemical stability make it an ideal material for a variety of medical applications, ranging from implants to biosensors (Saddow, 2022). One of the primary applications of SiC in the medical field is in implantable devices. $SiC's$ high mechanical strength and wear resistance are advantageous for load-bearing implants such as hip and knee replacements (Rade, Martinčič, Novak & Kobe, 2013). Additionally, its biocompatibility minimizes adverse reactions in the body, promoting better integration with biological tissues. SiC is also utilized in biosensors, particularly those used for monitoring physiological conditions in real time. These sensors can be used for detecting glucose levels, pH, and various biomarkers, providing critical data for managing chronic diseases

like diabetes (Oliveros, Guiseppi-Elie & Saddow, 2013). SiC coatings are used to enhance the durability and functionality of medical instruments and devices, such as catheters and stents. These coatings prevent corrosion and biofouling, thereby extending the lifespan and reliability of the devices (Afonso Camargo, Mohiuddeen, Fares, Partain, Carey IV, Ren, Hsu, Clark & Esquivel-Upshaw, 2020; Gryshkov, Klyui, Temchenko, Kyselov, Chatterjee, Belyaev, Lauterboeck, Iarmolenko & Glasmacher, 2016). Another promising application of SiC is in the development of neural interfaces (Frewin, Locke, Mariusso, Weeber & Saddow, 2013). Due to its biocompatibility and electrical properties, SiC can be used to fabricate electrodes that interface with neural tissues. These electrodes can be employed in brain-machine interfaces (BMIs) for prosthetic control and neurological research, providing a stable and long-lasting connection with neural tissues without causing significant immune responses.

1.3.3.3 Sensing

Silicon technology falls short in harsh environments characterized by high temperatures, corrosive species, vibrations, or radiation. Silicon's electronic behavior degrades at temperatures above 200 °C due to its intrinsic carrier density, which becomes much higher than that of wide bandgap materials like GaN or SiC. This increase leads to device failure as the intrinsic carrier density surpasses the dopant concentration. Therefore, silicon's electronic properties are unsuitable for high-temperature requirements. Additionally, silicon undergoes plastic deformation at temperatures above 500 °C, limiting its mechanical feasibility. To enhance compatibility with harsh environments, Silicon On Insulator (SOI) wafers and extensive packaging are used, increasing cost and complexity. Fiber optics are often employed to interface sensors in such conditions, as analog electronics fail at elevated temperatures. Table 1.4 highlights the high conditions of temperature and pressure sustained in various demanding fields.

Harsh environments include the presence of corrosive species (gases, liquids), vibrations, radiation, and/or high pressure. Examples of such environments are the geographical poles, arid deserts, volcanoes, deep ocean trenches, the upper atmosphere, Mt. Everest, outer space, and the conditions on every planet in the Solar System except Earth. In practical applications,

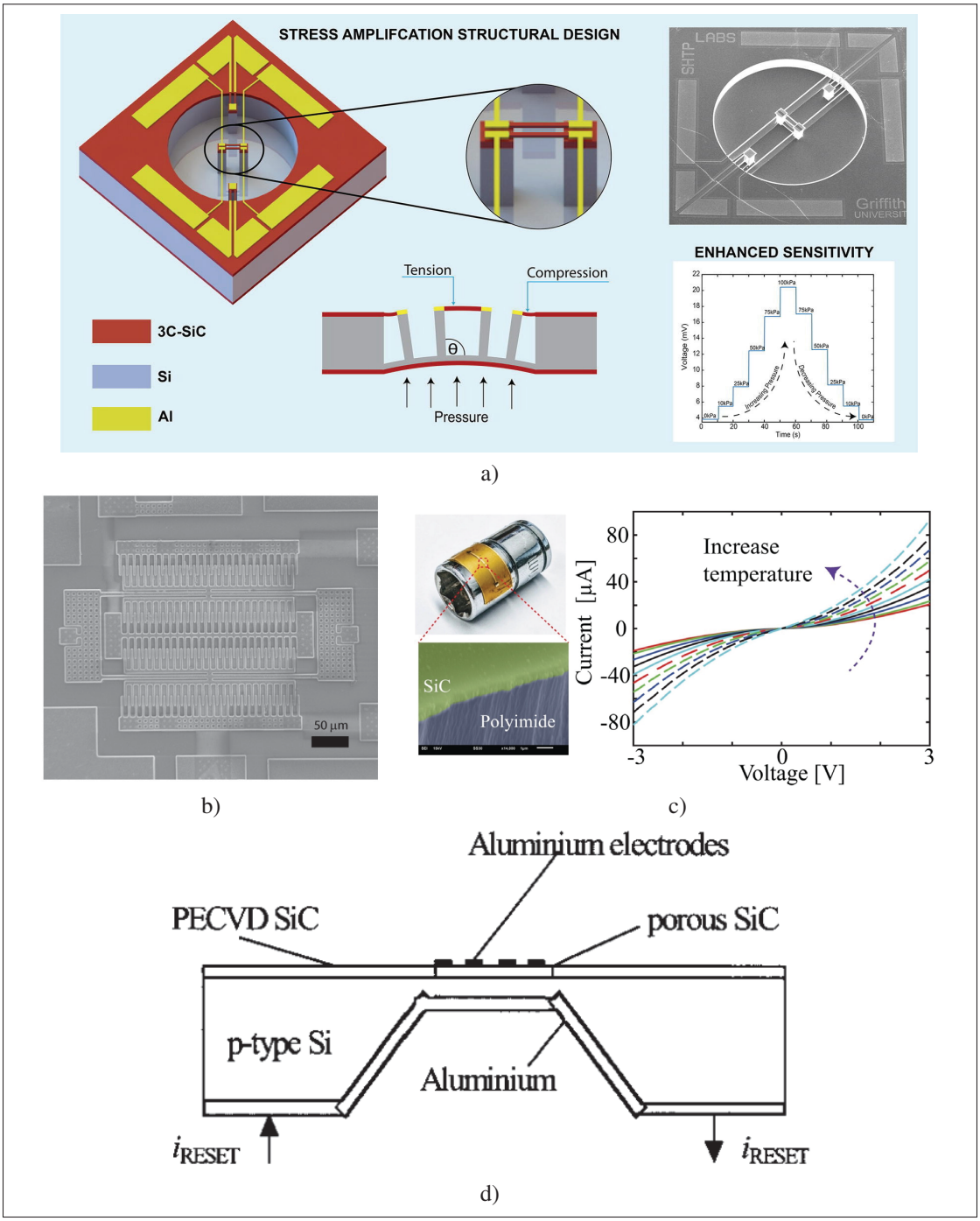

Figure 1.12 SiC based (a) pressure sensor (b) strain sensor (c) temperature sensor (d) humidity sensor
Taken from (Connolly *et al.*, 2004a; Eickhoff *et al.*, 1999; Jamshidi *et al.*, 2007; Phan *et al.*, 2020) respectively

Table 1.4 Harsh environmental conditions based on application areas
Adapted from (Middelburg *et al.*, 2020)

Application	Pressure	Temperature
Medical	69 mbar	50 °C
Oil refining	344 bar	-
Combustion engines	0-100 bar	574 °C
Geothermal wells	14 bar	350 °C
Oil and gas	-	275 °C
Aerospace / turbine engines	1-50 bar	50 °C - 650 °C
Industrial gas turbines	345 bar	450 °C - 600 °C

harsh environments can be found in boreholes, under the hood of automobiles (motor area), and in power applications like energy grids (Middelburg *et al.*, 2020). SiC sensors are renowned for their ability to operate in extreme environments, such as high temperatures, harsh chemical conditions, and high radiation levels. This makes them ideal for applications in industries such as automotive, aerospace, and energy. This section details recently reported physical sensors fabricated via bulk, grown or wafer based forms of SiC. Figure 1.12 illustrates some of the common SiC based sensors recently reported in literature.

Temperature sensors: Temperature measurements under harsh conditions is imperative for applications such as aerospace where such sensors help monitoring jet engine components, improving fuel efficiency and safety. Temperature sensors can also be paired with mechanical sensors for temperature compensation. Due to the prevalence of affordable thermocouples with junctions and ceramic packaging, there has been limited research on SiC temperature sensors. Thin film SiC elements have been used as thermistors to measure temperature changes via resistance (Nagai & Itoh, 1990) and SiC JFET's have been characterized for use in temperature monitoring circuits (Casady, Dillard, Johnson & Rao, 1996). Rao, Pangallo, Pezzimenti & Della Corte (2015) presented a high sensitivity $4\mathrm{H}-\mathrm{SiC}$ shottky diode based temperature sensors sabaivle of measuring temperatures upto 300 °C with a sensitivity of 5.11 mV/°C. The same research team also proposed a $4\mathrm{H}-\mathrm{SiC}$ p-i-n diode based architecture with a sensitivity of 2.66 mV/°C at 300 °C with high repeatibility and a very small error or 0.5%. Zhang, Lin, Senesky & Pisano (2014b) developed a $4\mathrm{H}-\mathrm{SiC}$ pn junction based tempeature

sensor capable of performing upto 600 °C with a sensitivity of 3.5 mV/°C. The common denominator between all the above listed SiC based temperature sensors is the need need for complex, high volume and expensive fabrications techniques such as PECVD etc.

Humidity sensors: Similar to temperature sensing, SiC based devices are adept for sensing variations in relative humidity (%RH) under harsh monitoring environments where conventional metal oxide or polymer based humidity sensors would fail Connolly *et al.* (2004a). Researchers have developed novel SiC based humidity sensors via various approaches. Connolly *et al.* (2004a) developed a 0.5μm PECVD deposited SiC film based humidity sensor on aluminum electrodes capable of detecting changes between 10-90 %RH while being exposed to harsh environments, automotive exhaust and ammonia. Connolly, French, Pham & Sarro (2002) deposited $p - SiC$ onto silicon wafer via PECVD process followed by chemical etching via hydoflouric acid. The resultant device exhibited a sensitivity of 55% at 85%RH with an absorption time of 1.5-2 minutes and a desorption time of 2-3 minutes. Further, SiC based nano-composites and nano-sctructures have also been utilized to fabricate humidity sensors owing to their increased surface to volume ratio. These sensors will be discussed in later sections of this thesis.

Pressure sensors: Doped SiC exhibits stable piezoresistive behavior up to 800 °C (Shor, Goldstein & Kurtz, 1993), making it a prime candidate for high-temperature pressure sensors. Research has shown the selective growth of $3C - SiC$ on SOI wafers, allowing operation up to 200 °C (Eickhoff *et al.*, 1999) (Figure 1.12 d)). To extend this range, SiC diaphragms have been used, addressing coefficient of thermal expansion (CTE) mismatch issues and enabling functionality under significant temperature variations. A design utilizing photoelectrochemically etched $6H - SiC$ diaphragms with epitaxially grown n-type $6H - SiC$ elements has achieved pressure detection up to 6.9 MPa at 600 °C with minimal junction leakage and no plastic deformation (Ned, Okojie & Kurtz, 1998; Ned, Kurtz, Masheeb & Beheim, 2001). For moderate-temperature operations in harsh environments, SiC coatings provide anti-erosion protection and resistance to KOH etching for Si pressure sensors.

Strain sensors: Various physical conditions such as temperature swings, fluctuating pressures, and large external forces can cause internal stresses in aerospace components, leading to fatigue, delamination, and failure (Senesky, Jamshidi, Cheng & Pisano, 2009). Strain sensors measure these internal forces, but must be attached to the active structure, exposing them to harsh conditions that can affect their accuracy. Current commercial strain sensors do not meet the growing demand for precise monitoring in aerospace applications. $\mathrm{SiC}'\mathrm{s}$ superior mechanical and chemical properties make it ideal for harsh environment sensors. A SiC resonant strain sensor provides a strain resolution of 0.11, operates in a 10-20 kHz bandwidth, withstands 10 kgs shocks, and functions at temperatures up to 300 °C, in corrosive environments (Azevedo, Jones, Jog, Jamshidi, Myers, Chen, Fu, Mehregany, Wijesundara & Pisano, 2007). Capacitive strain sensors, which are relatively temperature insensitive, have also been developed using SiC. A high-resolution SiC-coated capacitive strain gauge demonstrated a strain resolution of 0.88 in a 120 Hz bandwidth and operated at temperatures up to 370 °C. This design uses SOI substrates, making it a low-cost, manufacturable option for critical aerospace components and applications (Jamshidi *et al.*, 2007).

1.4 Silicon carbide nanomaterials

1.4.1 Properties

SiC nanomaterials have been widely developed and studied by researchers and have been utilized in several applications. Amongst the various polytypes, cubic $3\mathrm{C}-\mathrm{SiC}$ nano-structures have been most widely synthesized and studied (Wu *et al.*, 2015). Nano-structures range form 0D (zero dimensional) to 3D (three dimensional) depending on the number of dimensions in the nanometer scale of the structure. Table 1.5 highlights the types of structures pertaining to each dimension. Researchers have developed SiC nano-structures across all dimensions which have a great potential for applications that can affect our daily lives. In this PhD project we focus on employing 0D $3\mathrm{C}-\mathrm{SiC}$ nanoparticles. These are low cost and abundantly available commercially making then the ideal candidate to fabricate SiC devices and sensors. Moreover,

SiC nanoparticles exhibit unique and novel properties distinct from those of bulk SiC due to their size effect.

Table 1.5 0D - 3D nanostructures

Dimension	Structures
0D	Nanoparticles, Nanospheres, Quantum dots (QD's)
1D	Nanowires, Nnaotubes, Nanobelts
2D	Nanoflakes, Nanoplatelets and Superlattices
3D	Conjugation of other nanostructures

1.4.1.1 Surface properties

Compared to bulk materials, nanoparticles have exceptionally high specific surface areas, making their surface properties such as chemical stability, dispersibility, and overall application potential very crucial (Bantz, Koshkina, Lang, Galla, Kirkpatrick, Stauber & Maskos, 2014; Verma & Stellacci, 2010). The surface properties of SiC nanoparticles are pivotal for preparing stable colloidal solutions such a printable inks. Methods like chemical etching and pulsed laser ablation (PLAL) can enhance hydrophilicity but are often unsuitable for large-scale production. Surface modification methods have been proposed to address this (Mahović Poljaček, Tomašegović, Strižić Jakovljević & Donevski, 2023). For instance, Iijima & Kamiya (2008) utilized 2,2-azobisisobutyronitrile (AIBN), 2,2-azobis(2-methylpropionamidine)dihydrochloride (AMPA), and 2,2-azobis[N-(2-carboxyethyl)-2-methylpropionamidine]n-hydrate (ACMPA) to introduce carboxyl and amino groups onto SiC nanoparticle surfaces, improving their dispersibility in water and stabilizing colloidal solutions. In addition to chemical modification, adsorption techniques have been explored to enhance particle dispersion in solutions. Loganathan & Sankaran (2017) investigated polyethylene glycol and chitosan for stabilizing SiC colloidal dispersions, showing that surface oxygen facilitated hydrogen bonding with polyethylene glycol, while chitosan increased stability via ionization, enhancing electrostatic repulsion between particles.

SiC nanoparticles are also crucial for synthesizing polymer-based nanocomposites (Kueseng & Jacob, 2006), although challenges like Van Der Waals interactions and poor compatibility with

polymers often hinder uniform dispersion and performance (Saini, Sharma, Rozra, Dhiman, Aggarwal & Sharma, 2015). Surface modifications, whether organic or inorganic, have been effective in overcoming these challenges. Organic modifications involve grafting organic materials onto SiC surfaces to prevent agglomeration and enhance interface bonding with resins (Rong, Zhang, Shi, Ji, Wetzel & Friedrich, 2003). Inorganic modifications, such as using concentrated HNO_3 (Saini, Sharma, Dhiman, Chandak, Aggarwal & Sharma, 2017), introduce functional groups like $C^{\smile}O$ and $^{\smile}C^{\smile}C-$ on SiC surfaces, facilitating uniform dispersion in matrices like polyvinyl alcohol (PVA).

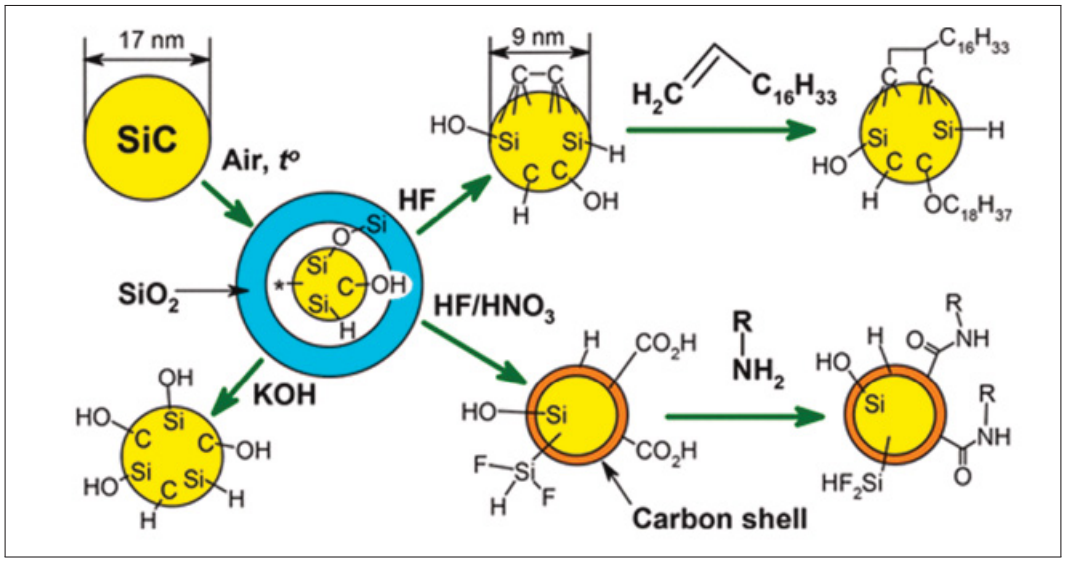

Figure 1.13 Effect of various surface modifications on the properties of SiC/SiO_2 nanoparticles
Taken from (Alekseev *et al.*, 2017)

High-temperature synthesis methods like combustion, carbothermic reduction, and sol-gel processes can lead to SiO_2 layer formation on SiC particle surfaces, influencing their properties (Gao, Wang, Zhao, Huang, Gao & Liu, 2020). Mekuria, Zhang & Fouad (2019) demonstrated that introducing nanoparticles into polyimide (PI) significantly enhanced tensile strength and glass transition temperatures compared to pure SiC nanoparticles, due to better compatibility between SiO_2 and PI. As seen in Figure 1.13, Surface treatment of SiC/SiO_2 nanoparticles by using KOH, HF, and HF/HNO_3 mixtures produced hydroxyl and carboxyl groups on their

surfaces, enhancing hydrophilicity and stability in aqueous colloidal dispersions (Alekseev *et al.*, 2017).

1.4.1.2 Thermal properties

SiC, with its extremely high melting point (2700 °C) and excellent chemical stability, is ideal for high-temperature device applications (Casady & Johnson, 1996). Nanoparticles, due to their large surface area from the size effect, exhibit distinct thermal properties. The concept of "nanothermodynamics" is a relatively new interdisciplinary theory that explores the difference between the properties of microscopic and nanoscopic systems (Chamberlin, 2003). Nanothermodynamics of sevearal metallic materials have been rigorously studied (Yang & Mai, 2014); however, the same for SiC nanomaterials is still largely unknown.

Huseynov & Naghiyev (2021) used thermogravimetric analysis (TGA) to study the thermal properties of $\beta - SiC$ nanoparticles. They observed that due to the high specific surface area, SiC nanoparticles adsorb water and other compounds. As the temperature increased, these impurities were removed, initially decreasing the sample mass. At temperatures above 800 °C, the mass increased due to SiC oxidation. They also found that neutron irradiation transformed ^{31}Si to ^{31}P, enhancing $SiC's$ oxidation resistance without significant changes in differential scanning calorimetry (DSC) and TGA curves, indicating good radiation-resistant properties. Nanofluids containing SiC nanoparticles have attracted attention for their heat transfer properties. Angayarkanni & Philip (2015) found that the thermal conductivity of nanofluids increased linearly with the volume fraction of SiC nanoparticles, achieving a 15.8% increase at a 4.2% volume fraction. Timofeeva, Smith, Yu, France, Singh & Routbort (2010) studied the effects of interfacial and particle size on heat transfer, discovering that while surface charge had no impact, larger particle sizes increased thermal conductivity due to a reduced solid-liquid interface area.

With excellent thermal stability below 800 °C and radiation resistance, SiC nanoparticles are promising for aerospace and nuclear energy applications. They also significantly enhance the thermal conductivity of nanofluids, offering great potential for heat transfer applications.

1.4.1.3 Electrical properties

As a third-generation semiconductor, SiC possesses excellent electrical properties, making it ideal for high-frequency semiconductor devices. The size effect can influence these properties, and certain SiC nanomaterials exhibit unique electrical characteristics (Huseynov & Naghiyev, 2021; Sellin & Vaitkus, 2006; Zhou, Liu & Zhang, 2006). This section discusses current research on the electrical properties of SiC nanoparticles, focusing on dielectric constant and conductivity. See, Hassan, Hashim, Wahab, Halim, Abdullah & Azis (2016) studied how temperature and frequency affect the dielectric properties of $\beta - SiC$ nanoparticles. They found that the dielectric constant decreases with increasing frequency, showing a relaxation peak at 10 kHz. Additionally, the dielectric constant fluctuates with temperature changes, likely due to simple electron hopping in the bandgap theory. Element doping significantly impacts the electrical conductivity of SiC nanoparticles. Researchers have developed SiC nanoparticles doped with various elements, such as Co, Fe, Cu, Ni, and N_2, to enhance their dielectric constant. When these elements replace Si atoms in the lattice, vacancies are formed due to differences in atomic valence, increasing the dielectric constant. For example, Fe doping creates p-type material with $Fe - Si$ defects, improving the electrical conductivity.

Huseynov & Garibov (2017); Huseynov (2017,1) found that neutron irradiation introduces new doping elements, further increasing the dielectric constant. The authors also investigated the effects of temperature, frequency, and neutron irradiation on the conductivity of SiC nanoparticles. They observed that conductivity remains unchanged below 1 kHz but increases proportionally above this frequency. Conductivity also rises with temperature, from 2 x 10^{-6} S/m at 100 K to 8 x 10^{-5} S/m at 400 K, indicating that higher temperatures and frequencies generate more carriers. Neutron irradiation induces a nuclear phase transition of Si atoms, producing ^{31}P, which increases n-type donor concentration and thus conductivity.

1.4.1.4 Biocompatibility

Studies have confirmed that bulk SiC has good biocompatibility and minimal effect on the human body (Oliveros *et al.*, 2013; Saddow, 2011). However, SiC nanomaterials differ from bulk SiC, with researchers finding that SiC whiskers can be toxic to cells, similar to asbestos (Svensson, Artursson, Leanderson, Berglind & Lindgren, 1997; Vaughan, Jordan & Karr, 1991). Therefore, it is necessary to investigate the biocompatibility of SiC nanoparticles.

The toxicity of SiC nanomaterials may depend on their morphology. Chen, Li, Zhao, Li, Hableel, Lemaster, Bai, Sen & Jokerst (2018a) found that SiC nanowires significantly reduced the proliferation of human mesenchymal stem cells (hMSCs), while SiC nanoparticles had little effect. Moreover, SiC nanowires prevented hMSCs from differentiating into osteocytes or adipocytes. Lozano, Laloy, Alpan, Mejia, Rolin, Toussaint, Dogné, Lucas & Masereel (2012) evaluated the toxicity of SiC nanoparticles in rats, finding no damage to major organs or abnormalities in urine, suggesting no poisoning. While these studies indicate good biocompatibility of SiC nanoparticles, some research suggests potential toxicity. Pourchez, Forest, Boumahdi, Boudard, Tomatis, Fubini, Herlin-Boime, Leconte, Guilhot, Cottier et al. (2012) found no cytotoxic effects but observed cellular responses related to oxidative stress and inflammation, indicating possible toxicity. Barillet, Jugan, Laye, Leconte, Herlin-Boime, Reynaud & Carrière (2010a); Barillet, Simon-Deckers, Herlin-Boime, Mayne-L'Hermite, Reynaud, Cassio, Gouget & Carrière (2010b) reported that SiC nanoparticles caused redox disturbances and DNA damage in hepatocytes, pulmonary cells, and kidney cells, although they did not cause cell death. The differing conclusions on the biocompatibility of SiC nanoparticles may be due to their selective cytotoxicity. Mognetti, Barberis, Marino, Di Carlo, Lysenko, Marty & Géloën (2010) found that SiC nanoparticles significantly inhibited the proliferation of oral squamous carcinoma cells while having a smaller effect on immortalized cell lines, suggesting cell-type-dependent toxicity.

Overall, the biocompatibility of SiC nanoparticles varies with cell type, challenging the assumption that SiC is biologically inert. Further research on their cytotoxicity is needed to advance the development of SiC nanoparticles in medical and biological fields.

1.4.2 Fabrication Techniques

Zero-dimensional SiC nanomaterials have garnered significant interest due to their potential applications in optoelectronics (Kamat, 2008; Nozik, Beard, Luther, Law, Ellingson & Johnson, 2010). Numerous methods have been developed to fabricate 0D nanostructures with precise size control. This section emphasizes the advancements in the synthesis of 0D SiC nanoparticles. Here we identify three distinct categories of fabrication processes namely solid phase, liquid phase and vapor phase as summarized in Table 1.6.

Table 1.6 SiC nanoaprticle synthesis methods
Adapted from (Wang *et al.*, 2022)

Category	Method
Solid phase	physical milling mechanical alloying carbothermal reduction combustion synthesis chemical etching
Liquid phase	sol-gel liquid phase laser ablation
Vapor phase	chemical vapor deposition

1.4.2.1 Solid phase techniques

Physical milling

Physical milling is a common top-down synthesis technique used to break solid materials into smaller particles in material preparation. This method primarily utilizes the extremely high local impact created by the high-speed rotation of high-energy ball milling to disrupt lattice bonds and crush large particles into nanoparticles. For synthesizing SiC nanoparticles, the starting material can be either micro-sized particles (Manikandan & Jancirani, 2014; Rao, Catherin, Murthy, Rao & Raju, 2011) or bulk SiC (Muzha, Fuchs, Tarakina, Simin, Trupke, Soltamov, Mokhov, Baranov, Dyakonov, Krueger et al., 2014). Rao *et al.* (2011) used high-energy ball milling to break down micro-sized SiC particles into nanoparticles and thoroughly

investigated the impact of milling time on the resulting product. The crystal structure and chemical composition of the products were analyzed using X-Ray Diffraction which showed that increased milling time lead to the decrease in the intensity of the (111) SiC peak, while peak broadening increased, indicating a reduction in its crystallinity. Calculations using the Pseudo-Voigt function (Sánchez-Bajo & Cumbrera, 1997) revealed that the crystallinity of SiC decreased from 74% to 49% after 50 hours of milling. Additionally, Scherer's equation indicated that the average crystallite size dropped from 108.36 nm to 26.34 nm. Similar findings were reported by Manikandan & Jancirani (2014) who also observed that high-energy ball milling reduced the crystallite size of SiC and increased its amorphous nature. However, some impurities from the milling balls used as media were found in the product. During high-energy ball milling, particles are progressively refined through the impact and compression of high-energy balls, leading to the combination of newly exposed surfaces. This process also induces high-density crystal defects (Gomari & Sharafi, 2010) which is driven by free energy, atoms on the crystal surfaces and grain boundaries diffuse to form new phases (Yang & Shaw, 1996). This research indicates that the technology for synthesizing SiC nanoparticles via physical milling is relatively advanced, allowing for easy scale-up and large-scale production. Nonetheless, the amorphous transformation and impurities introduced during milling negatively affect the final product.

Mechanical alloying

This process employs silicon and carbon particles are rat materials. The composition and structure of SiC particles through the mechanical alloying method are closely linked to reaction parameters such as milling time, charge ratio, and milling speed. Sherif El-Eskandarany, Sumiyama & Suzuki (1995) synthesized SiC nanoparticles using a high-energy vibrating ball mill noted that prolonged milling times resulted in more spherical particles, improved reaction yield, and reduced particle size from 1 µm after 100 hours to 0.5 µm after 300 hours. They identified three main stages in the synthesis process: initial fragmentation of silicon and carbon particles by high local impact, subsequent diffusion reaction between them to form SiC, and further milling to produce SiC particles with nano grain size of 7 nm. Yang & Shaw (1996)

examined the effects of milling speed, charge ratio, and milling time and reported that that higher milling speeds promoted the formation of crystalline $\beta - \mathrm{SiC}$, while increased charge ratio and milling time reduced crystallinity due to higher defect content. Using high-resolution electron microscopy, they proposed two mechanisms for SiC synthesis during alloying: diffusion of carbon atoms in amorphous silicon to form $\mathrm{Si(C)}$ solid solution, and diffusion of carbon atoms in cubic silicon to form $\beta - \mathrm{SiC}$. Research by Gaffet & Harmelin (1990) and Shen, Koch, McCormick, Nemanich, Huang & Huang (1995) suggested that milling could only induce up to 10% amorphization in silicon, indicating that SiC synthesis primarily occurred through the second mechanism, resulting in $\beta - \mathrm{SiC}$ nanoparticles. Overall, while the mechanical alloying process is straightforward and capable of large-scale production, it leads to a broad particle size distribution, formation of amorphous SiC and introduction of impurities due to degradation of milling balls. Thus, mechanical alloying is not ideal for synthesizing high-purity, high-crystallinity SiC nanoparticles.

Chemical etching

Due to its stable chemical properties, SiC requires a special etching solution for nanoparticle synthesis. Zhu, Liu, Wu, Xu, Zhang & Chu (2007) used a mixture of concentrated nitric acid and hydrofluoric acid as the etching solution. Their synthesis process involved two main steps: first, bulk $\beta - \mathrm{SiC}$ was etched at 100 °C for 1 hour to produce porous SiC, where $\mathrm{HNO_3}$ oxidized part of the SiC to $\mathrm{SiO_2}$ and HF removed the oxidized $\mathrm{SiO_2}$. Second, the porous SiC was ultrasonically treated in ethanol for 30 minutes, resulting in $\beta - \mathrm{SiC}$ nanoparticles less than 6.5 nm in diameter. Károlyházy, Beke, Zalka, Lenk, Krafcsik, Kamarás & Gali (2020) used $\mathrm{6H\check{}SiC}$ as the starting material and an etching solution of $\mathrm{Na_2S_2O_6}$ and HF. Their etching process, conducted at 150 °C for 2 hours, produced nanoparticles as small as 1 nm. These studies demonstrate that chemical etching can synthesize extremely small nanoparticles with various crystal structures by selecting different raw materials. Besides chemical etching of bulk SiC with special solutions, electrochemical etching is another approach. Similar to chemical etching, this method also requires ultrasonic treatment to produce SiC nanoparticles from porous SiC. Wu,

Fan, Qiu, Yang, Siu & Chu (2005) studied the effect of etching current densities on the product, finding that the particle size slightly increased with higher etching current densities, with a maximum size of less than 10 nm. Compared to high-energy ball milling methods, chemical etching can produce single-crystal SiC nanoparticles with smaller sizes. However, this method requires toxic etching solutions which increase the process risk. Additionally, the high cost and low yield limit its scalability, making it suitable only for laboratory-scale production.

Combustion synthesis

Combustion synthesis is widely considered as a well established process with high reaction speeds and conversion rates. Here, silicon or silica and carbon sources are used to synthesize SiC in a relatively simple and low cost way. Combustion synthesis utilizes several heating sources some of which have been detailed below:

- **Furnace**: Larpkiattaworn, Ngernchuklin, Khongwong, Pankurddee & Wada (2006) synthesized $\beta - \mathrm{SiC}$ nanoparticles using a furnace and found that higher reaction temperatures, faster heating rates, and longer reaction times increased the reaction conversion rate. Wang, Hou, Xu & Tian (2015b) discovered a relationship between reaction temperature and the crystal structure where at 1800 °C the product was mainly $\beta - \mathrm{SiC}$, while at 1950 °C $\alpha - \mathrm{SiC}$ was formed whose concentration increased with increase in temperature. This suggests that higher temperatures facilitate the conversion of $\beta - \mathrm{SiC}$ to $\alpha - \mathrm{SiC}$. Although the combustion reaction between carbon and silicon efficiently produces SiC nanoparticles, it requires high-quality carbon sources with fine particle sizes, raising production costs. Consequently, alternative carbon precursors like fullerenes (KAWAMURA, YAMANE, YAMADA, YIN & SATO, 2007) and sucrose (Jiang, Gao, Kong, Jin, Wei, Li & Xing, 2019a) have been explored for SiC nanoparticle synthesis.

- **Plasma heating**: This process involves using a hypersonic pulsed $\mathrm{Si^{\smile}C}$ jet of sputter-ion plasma directed at a barrier, generated by a pulse high-current coaxial magnetoplasma accelerator. (Sivkov, Nikitin, Pak & Rakhmatullin, 2013) used copper as the barrier and synthesized SiC nanoparticles in an Ar atmosphere, resulting in mainly β-SiC nanoparticles

with diameters around 100 nm, demonstrating the method's feasibility. They further investigated the effect of input energy on SiC nanoparticle synthesis, finding that particle size increased with input energy (Sivkov, Nikitin, Pak & Rakhmatullin, 2015) who also compared carbon fibers and graphite for arc plasma discharge ignition, concluding that graphite provided more stable ignition and produced SiC with up to 99 wt% purity.(Nikitin, Sivkov, Rahmatullin & Ivashutenko, 2017) found that reaction yield increased with plasma input energy, peaking at 95% yield at 21.0 kJ, but decreased with further energy increase.

Combustion synthesis techniques generally use non-spontaneous energy sources where the reaction between silicon and carbon courses is low exothermic (73 kJ/mol at 1200 °C) (Mukasyan, Lin, Rogachev & Moskovskikh, 2013) leading to incomplete conversation reducing reaction yields. This form of combustion reaction is also known as self-propagating high-temperature synthesis (SHS). Measures such as preheating (Gadzira, Gnesin, Mykhaylyk & Andreyev, 1998; Yamada, Miyamoto & Koizumi, 1986), mechanical activation (Yang, Li, Qi, Zhang, Zhang & Yan, 2011; Yang, Lin & Li, 2009b) and catalysts (Agathopoulos, 2012) have been employed to maximum conversion of both raw materials into SiC to maximize process yield. Modifying the combustion system also results in improved SiC nanoaprtile yield. Yermekova, Mansurov & Mukasyan (2010) fabricated $\beta - \mathrm{SiC}$ nanoparticles using a magnesiothermic reduction process where they used $\mathrm{SiO_2}$˘Mg˘C as the reactants in an argon atmosphere and the exothermic oxidation of Mg sustains the reaction temperature. Nersisyan, Lee, Lee & Jeong (2020) used $\mathrm{Na_2CO_3}$ and Si particles which is an exothermic reaction that maintains their reaction temperature to also form $\beta - \mathrm{SiC}$ nanoparticles as seen in Figure 1.14. Langenderfer, Fahrenholtz, Chertopalov, Zhou, Mochalin & Johnson (2020) employed 1,3,5-Trinitro-1,3,5-triazinane (RDX), and 2,4,6-trinitrotoluene (TNT) whose detonation also resulted in $\beta - \mathrm{SiC}$ nanoparticles. Combustion synthesis techniques are a high yield, low energy consuption and environmentally friendly method of producing large scale quantities of SiC nanoparticles, however the lack of control on the reaction kinetics often leads to a large particle size destruction and agglomeration. Table 1.7 summaries the fabrication of SiC nanomaterails processes fabricated via various combustion synthesis processes.

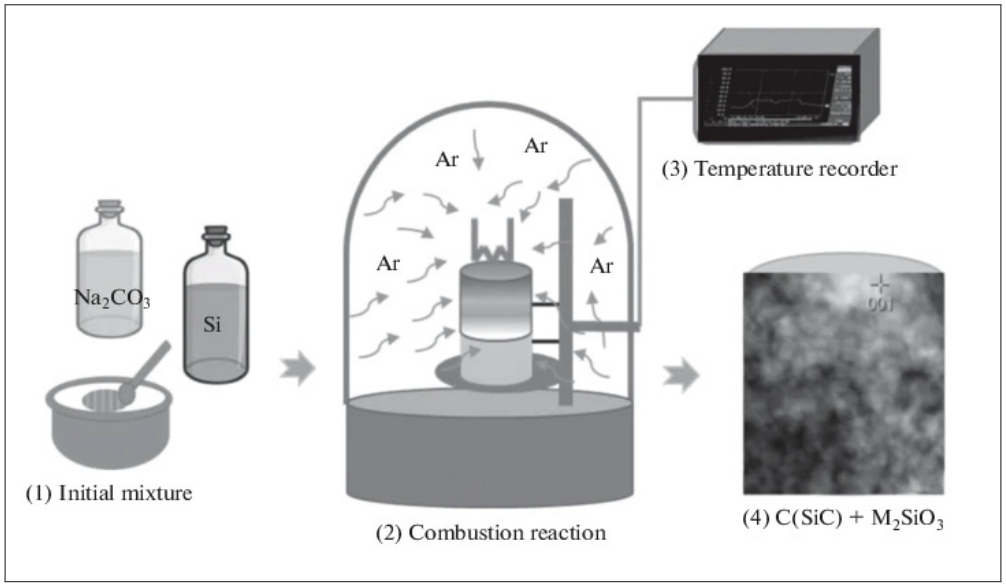

Figure 1.14 Combustion synthesis of SiC nanoparticles
Taken from (Nersisyan *et al.*, 2020)

Carbothermal reduction

Carbothermal reduction is a high-temperature reduction reaction using carbon as the reducing agent. It offers several advantages, including low cost, simplicity, strong process designability, and high conversion rates. The Achenson process first developed in 1893 producted SiC at 2700 °C and is considered as a predecessor of modern carbothermal synthesis techniques. Equations 1.7-1.10 illustrate that production of gaseous SiO is reaction temperature dependent and can be combined with carbon to form SiC nanoparticles (Matovic, Saponjic, Devecerski & Miljkovic, 2007; Ohsaki, Cho, Sano, Uchiyama & Kobayashi, 1998). Formation of SiO is dependent on the initial solid state reaction between the silica and carbon raw materials. In order to reduce reaction temperature, processes such as mechanical milling (Zhong, Shaw, Manjarres & Zawrah, 2010), catalysts (Zhang, Li, Wang, Long, Wang & Kan, 2010) and microwave heating (Kappe, 2004). Additionally, carbothermal reduction processes requires high temperatures close to the melting point of silica leading to agglomeration problems. Researchers have proposed a core shell methods to mitigate this issue (Koc, Glatzmaier & Sibold, 2001). Naturally occurring sources of carbon such as rice husk (Kavitha, Balasubramanian & Vashistha, 2011) and macadamia shells

(Rajarao & Sahajwalla, 2016) have also been been combined with silica via the carbothermal process to fabricate high quality SiC nanparictles. Table 1.7 summarizes recent publications towards on synthesis of SiC nanomaterails using carbothermal reduction.

$$SiO_2(s) + C(s) \rightarrow SiO(g) + CO(g) \tag{1.7}$$

$$2C(s) + SiO(g) \rightarrow SiC(s) + CO(g) \tag{1.8}$$

$$SiO_2(s) + CO(g) \rightarrow SiO(g) + CO_2(g) \tag{1.9}$$

$$C(s) + CO_2(g) \rightarrow 2CO(g)) \tag{1.10}$$

Table 1.7 Reported materials and reaction conditions towards carbothermal reduction synthesis of SiC nanomaterials Adapted from (Sun *et al.*, 2022)

Si source	**C source**	**Temperature**	**Pressure (kPa)**	**Time (h)**	**Catalyst**	**Product**	**Reference**
Silica fume	Phenolic resin powde	1450 °C	101	4	NaCl +NaF	SiC nanowires	Zhang, Li, Jia, Lin, Huang & Zhang (2015)
Mesoporous silica	Carbon nanotube	1100 °C	101	20	-	SiC nanotubes	Seo, Sankarasubramanian & Lee (2018)
Microfine silica	Graphite flakes	1600 °C-1700 °C	101	4	-	SiC nanoparticles	Raju, Sen, Sarkar & Jacob (2021)
SiO_2 nanoparticle	Glucose	1400 °C	101	2	-	SiC	An, Wang, Zhu, Cao & Xue (2019a)
Molecular sieves	Carbonized sucrose	1400 °C	101	9	-	SiC nanoparticles	Shcherban, Filonenko, Yaremov, Sergiienko, Ilyin & Murzin (2017)
Glass fiber (from e-waste)	Char (from e-waste)	1350 °C	-	-	-	SiC nanoparticles	Rajagopal, Rajarao & Sahajwalla (2017)
Rice husk +Coconut shell	-	1400 °C	101	3	-	SiC wiskers	Lodhe, Selvam, Udayakumar & Balasubramanian (2016)
SiO	Corn cob	1350 °C	vacuum	2	-	SiC nanoparticles	An, Xue, Cao, Zhu & Wang (2019b)
OMHS	Carbon nanofiber	1400 °C	101	1	-	SiC nanofibers	Chesnokov, Luchihina & Prosvirin (2015)
Si powder	Carbon nanotubes	1200 °C	5×10^{-7}	100	-	SiC nanotubes	Taguchi, Yamamoto, Kodama & Asaoka (2015)
Si powder	Multiwalled carbon nanotube	1100 °C-1300 °C	5×10^{-6}	5-100	-	Double thick walled SiC nanotubes	Taguchi, Yamamoto & Ohba (2021)
Si wafer (111)	Graphene	1200 °C	101	2	-	SiC nanowires	Zhang, Sheng, Fang, An, Yu, Liu & Zhao (2017)
Si powder	Carbon nanotubes	1350 °C-1550 °C	101	3-5	-	SiC nanotubes	Hart, Owuor, Hamel, Bhowmik, Asif, Gentles, Ozden, Tsafack, Keyshar, Mital et al. (2020)
Si powder	Graphite	1300 °C	101	3	-	SiC wiskers	Wang, Li, Jin & Sang (2015a)
Si substrate	Carbon film	1000 °C	1×10^{-6}	3	Al	SiC nanowires	Yu, Zhu, Yang, Dai, Baraban, Cuniberti & Han (2015)

1.4.2.2 Liquid phase techniques

Sol-gel synthesis

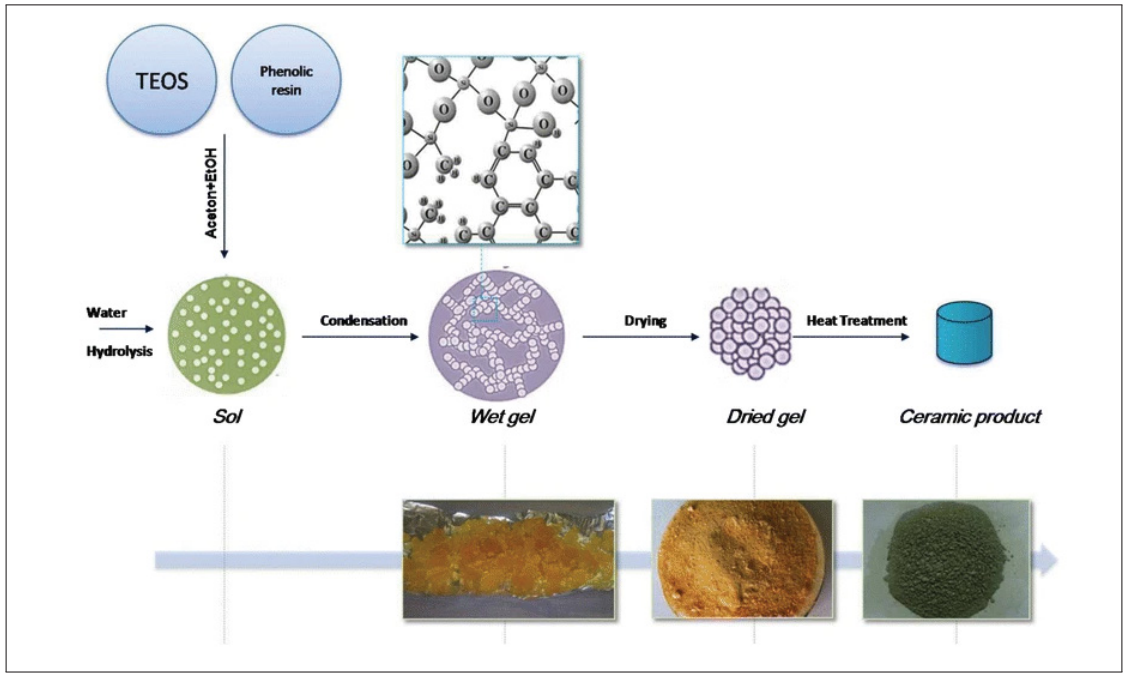

Figure 1.15 Sol-gel synthesis of SiC nanoparticles - process overview
Taken from Najafi *et al.* (2011)

The sol-gel method for preparing SiC nanoparticles typically uses liquid Si-containing materials such as colloidal SiO_2, tetraethyl orthosilicate, and methyl trimethoxysilane as the silicon source, and phenolic resin, sucrose, or starch as the carbon source. Some organic silicon polymers containing both silicon and carbon can also be used. The synthesis involves two main steps: first, the reaction precursor is prepared through hydrolysis, gelation, and drying; then, the precursor is heat-treated at high temperatures to form SiC particles as seen in Figure 1.15. This method is based on carbothermal reduction but avoids the non-uniform mixing of silicon and carbon particles. Hydrolysis and gelation in the sol-gel method can take several days, so catalysts are added to speed up the process. Li, Tian & Dong (2000) used tetraethyl orthosilicate (TEOS) and phenolic resin with oxalic acid (OA) and hexamethylenetetramine (HMTA) as catalysts. OA controlled the pH, affecting the hydrolysis rate of TEOS, while HMTA promoted coagulation

and gelation. Adjusting dispersants and reaction times can influence the size and morphology of SiC nanoparticles. Najafi *et al.* (2011) used TEOS and resol to synthesize $\beta - \mathrm{SiC}$ by adding ammonium polycarboxylate (APC) as a dispersant to control particle size. They found that a pH below 4 stabilized the solution and produced $\beta - \mathrm{SiC}$ nanoparticles under 10 nm, while a pH of 4–7 decreased stability and increased particle size. While the sol-gel method ensures even mixing of reactants, it complicates the process and can lead to the transformation of nanoparticles into whiskers and nanowires during heating. Preventing this transformation is a challenge for the sol-gel method.

Liquid phase laser ablation

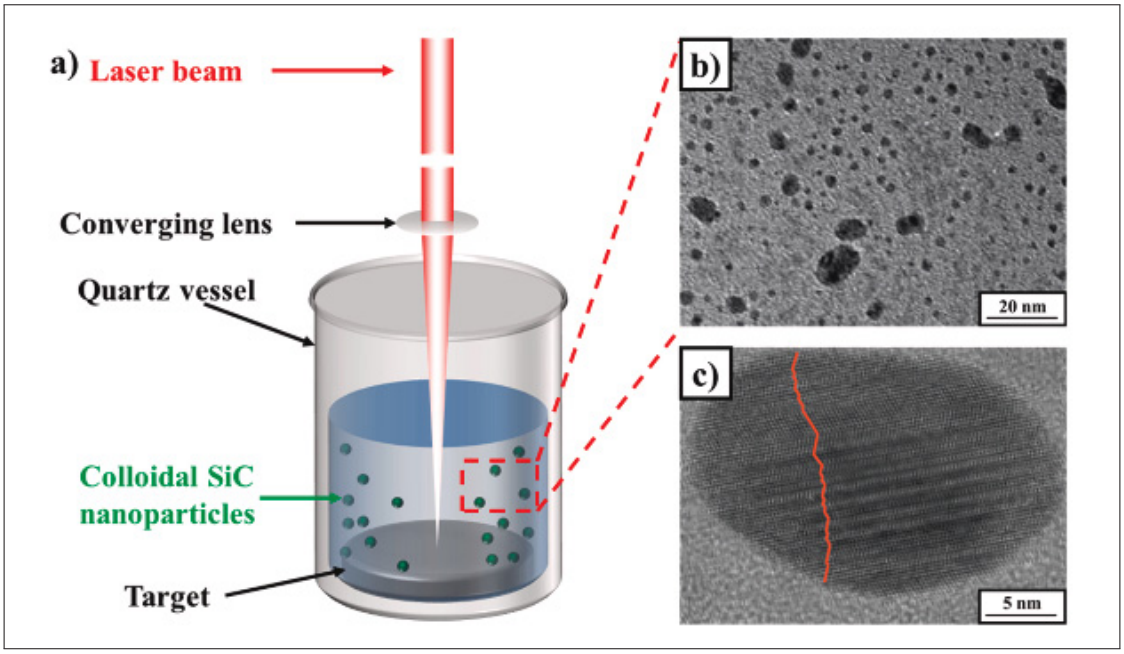

Figure 1.16 (a) Schematic illustration of pulsed laser ablation in liquid for synthesizing SiC nanoparticles (b) TEM image of SiC nanoparticles produced using the pulsed laser ablation in liquid method (c) Image of a single β-SiC nanoparticle
Taken from Zakharko *et al.* (2011)

Pulsed laser ablation in liquid (PLAL) is the process in which a laser beam with sufficient energy irradiates the target, it generates high pressure and temperature at the liquid-solid interface. This condition ablates the target into nanoparticles, which can be collected by evaporating the

solution (Figure 1.16). This method offers several advantages, including a simple process, environmental friendliness, low cost, and high purity of the resulting nanoparticles. Here, SiC crystalline targets or wafers are submerged in liquids such as water Castelletto, Almutairi, Thalassinos, Lohrmann, Buividas, Lau, Reineck, Juodkazis, Ohshima, Gibson et al. (2017); Zakharko *et al.* (2011), acetone (Yamada, Araki, Ishihara & Miyajima, 2019), ethanol (Yang, Cai, Zeng & Xu, 2009a) and hezane (Yu, Terakawa, Hayashi, Asaka, Itoigawa, Ono & Takayanagi, 2017). The PLAL method shows significant potential for synthesizing SiC nanoparticles. The resulting homogeneous colloidal solution facilitates further applications of SiC nanoparticles. Additionally, nanoparticles produced by ablating the SiC target in water retain their original crystal structure, enabling the synthesis of $\alpha - \mathrm{SiC}$ nanoparticles. However, this method is not suitable for large-scale production and poses challenges for commercial applications.

1.4.2.3 Vapor phase techniques

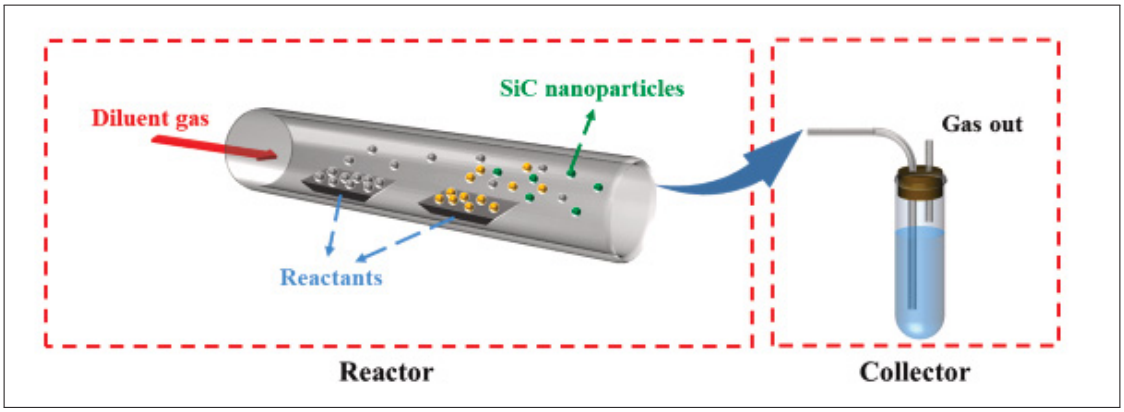

Figure 1.17 Schematic illustration of CVD fabrication of SiC nanoparticles
Taken from Gupta *et al.* (2007)

Synthesizing nanomaterials via gas phase reactions is mainly achieved through physical vapor deposition (PVD) and chemical vapor deposition (CVD). Due to the high boiling point of SiC, PVD is less suitable (Wellmann, Müller, Queren, Sakwe & Pons, 2006). CVD involves heating gaseous reactants to high temperatures to induce chemical reactions, originally used for coating surfaces but now adapted for nanomaterial synthesis, also known as chemical vapor synthesis.

Figure 1.17 highlights the operaitng principle of the CVD process. CVD has gained popularity due to its short processing time, narrow particle size distribution, small average diameter, and high purity of particles (Creighton & Ho, 2001). For instance, using dimethyldichlorosilane (DMS) in CVD can synthesize ultrafine, high-purity SiC nanoparticles, where factors like reaction temperature and gas concentration significantly influence the product's size and purity (Huang, Liang, Jiang & Tan, 1996). Hexamethyldisilane (HMDS) was used as a reactant to synthesize SiC nanoparticles with hydrogen and argon as dilution gases Gupta *et al.* (2007). The deposition rate of SiC nanoparticles varied with different hydrogen and argon ratios, peaking at a 1:1 ratio, which was found to be the most effective. Excessive hydrogen formed silicon, while too little hydrogen led to amorphous carbon, inhibiting crystalline SiC production. Thus, a 1:1 ratio of hydrogen and argon was optimal for HMDS pyrolysis to synthesize SiC nanoparticles.

Various CVD technologies have emerged, which are more environmentally friendly as they use plasma or laser energy instead of furnace heating. These methods allow for more precise control over the reaction process:

- **Plasma CVD (PCVD)**: Ko, Koo, Cho, Hwnag & Kim (2012b) synthesized SiC nanoparticles using TEOS, hexamethyldisilazane, and vinyltrimethoxysilane via PCVD, resulting in a product primarily composed of SiC with minor amounts of amorphous carbon and $\mathrm{SiO_2}$, which can be purified by heating and HF pickling. Lin, Gerbec, Sushchikh & McFarland (2008) used tetramethylsilane, finding that hydrogen from the reactants was released as hydrocarbons, with $\mathrm{C_2H_6}$ being the main gas in argon plasma and $\mathrm{C_2H_2}$ in hydrogen plasma. This indicates plasma gas composition is crucial for controlling the silicon and carbon ratio in the product.

- **Laser CVD (LCVD)**: Since the 1980's (Haggerty & Cannon, 1981), lasers have been used to synthesize sinterable nanoparticles, offering greater reaction controllability in a small area compared to other heating methods. Borsella, Caneve, Fantoni, Piccirillo, Basili & Enzo (1989) experimented with $\mathrm{C_2H_2}$, $\mathrm{C_2H_4}$, and $\mathrm{C_3H_6}$ reacting with $\mathrm{SiH_4}$, finding that the $\mathrm{SiH_4 - C_2H_2}$ mixture generated significant heat and efficiently produced SiC nanoparticles. In contrast, $\mathrm{SiH_4 - C_2H_4}$ and $\mathrm{SiH_4 - C_3H_6}$ mixtures were less effective due to insufficient

heat. El-Diasty (2004) introduced theoretical concepts for CO_2 laser-induced pyrolysis, explaining the main mechanism of laser heating and improving the control of laser pyrolysis reactions.

- **Fluidized bed chemical vapor deposition (FBCVD)**: FBCVD allows for continuous mass production of SiC nanoparticles, with reaction conditions like temperature and atmosphere affecting particle size and purity (Liu, Liu & Chang, 2017) synthesized SiC nanoparticles using HMDS via FBCVD, finding that reaction temperature and atmosphere significantly influenced the nanoparticle size. Higher temperatures reduced particle size, while low temperatures with high hydrogen concentration produced silicon impurities, and high temperatures with low hydrogen concentration led to carbon formation.

CVD methods produce high-purity SiC nanoparticles with fine particle sizes, offering flexibility in preparation processes. However, the high cost and toxicity of reactants, along with the need to improve conversion rates and manage exhaust gases, present significant challenges.

1.4.3 Sensing applications

Similar to bulk or wafer based SiC, SiC nanomaterials find applications fabricating sensors, catalysts, structural reinforcement, energy storage, anti-reflective and anti-microbial coatings etc (Sun *et al.*, 2022; Xu *et al.*, 2021) (Figure 1.18). Development of SiC based physical sensors is centric to the theme of this PhD project, hence, in this section, we focus on studying SiC nanomaterials based sensing devices.

Humidity sensors:

Wang, Wang, Hu & Li (2012a) developed capacitive SiC nanowire sensors and examined their humidity sensing properties at room temperature. Their findings indicated a capacitance increase of over 960% as relative humidity varied from 11% to 95% at a frequency of 100 Hz, demonstrating strong sensitivity. The sensors had response and recovery times of approximately

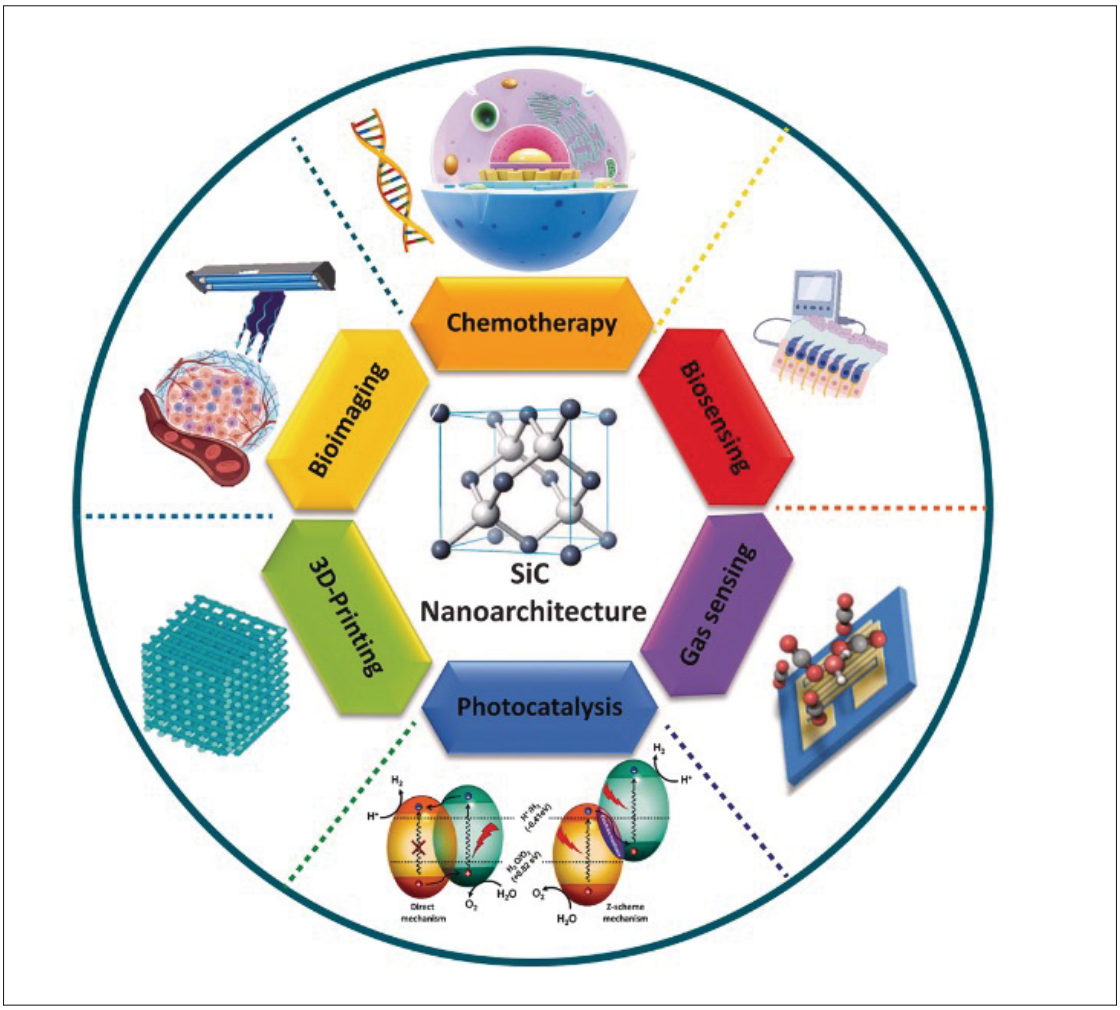

Figure 1.18 SiC nano-material based applications
Taken from (Xu *et al.*, 2021)

105 and 85 seconds, respectively, which were significantly shorter than those of porous SiC-based humidity sensors.

Sun *et al.* (2018b) spin coated $3C-SiC$ nanowires grown via carbothermal reduction onto interdigitated electrodes fabricated with silver and palladium. The resultant device (Figure 1.19) exhibits a high sensitivity of 16991.1 at 95%RH with a absorption and desorption time of 3 seconds each. Gong-yi, Jun, Gang, Wei, Zeng-yong, Yi-he, Tian-jiao & Xiao-dong (2014). Sun *et al.* (2018b) also developed novel nanocomposites from $PVA-TiO_2$ nanocomposites doped with SiC nanoparticles for use as humidity sensors that are highly sensitive, flexible,

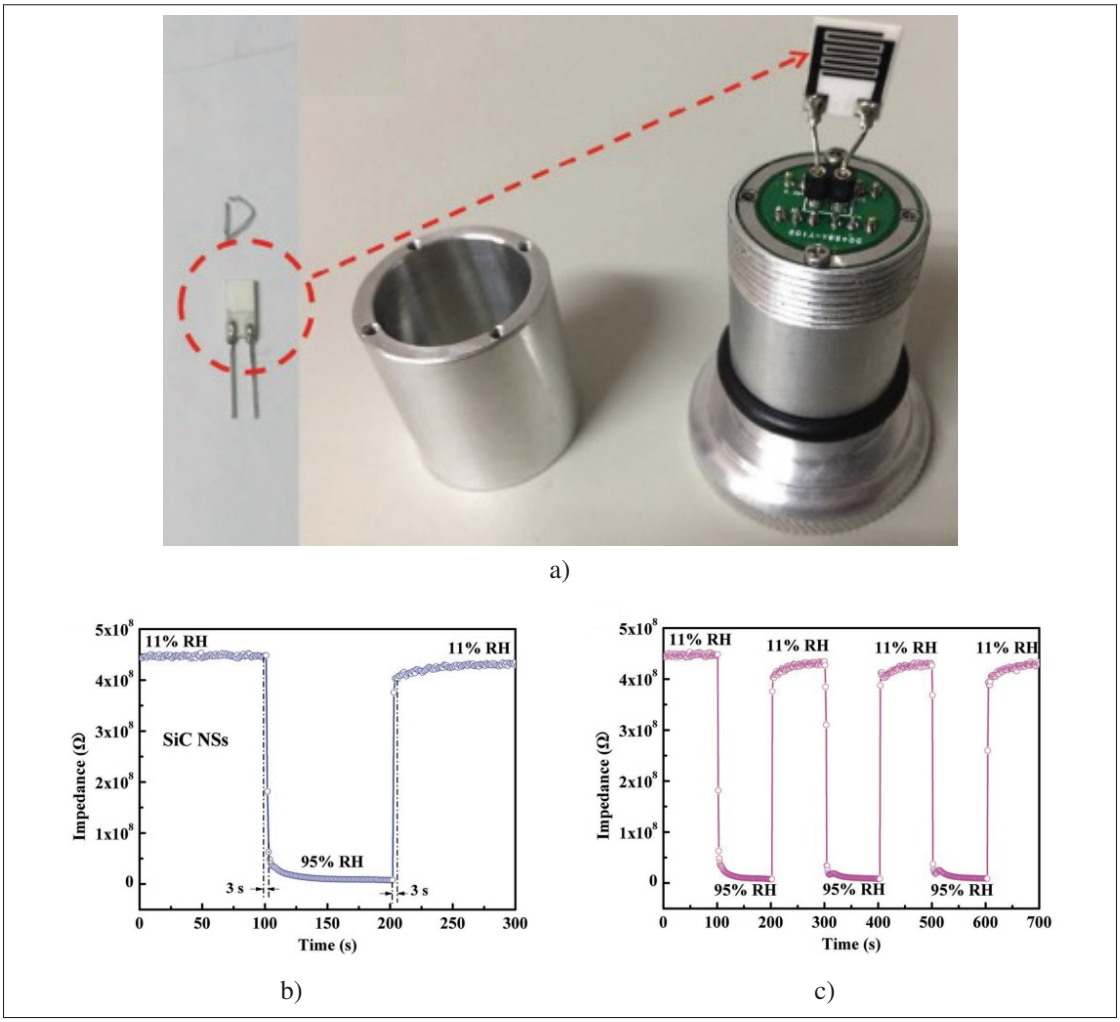

Figure 1.19 (a) SiC nano sheets based humidity sensor spin coated onto metallic electrodes (b) humidity sensor response (c) sensor response over multiple cycles Taken from Sun *et al.* (2018b)

corrosion-resistant, and low-cost. Both experimental and theoretical investigations into the structural and optical properties of the $\mathrm{PVA}-\mathrm{TiO_2}-\mathrm{SiC}$ nanocomposites were conducted using optical microscopy and FTIR were performed. Results indicated that the optical absorbance of the $\mathrm{PVA}-\mathrm{TiO_2}$ nanocomposites increased with higher concentrations of SiC nanoparticles. Additionally, the energy band gap of the $\mathrm{PVA}-\mathrm{TiO_2}$ nanocomposites decreased, while the optical constants increased as the SiC nanoparticle concentration rose. The $\mathrm{PVA}-\mathrm{TiO_2}-\mathrm{SiC}$ nanocomposites were tested as humidity sensors within a relative humidity range of 40-80%

RH. Experimental findings showed that the electrical resistance of the $PVA - TiO_2 - SiC$ nanocomposites decreased with increasing relative humidity, demonstrating high sensitivity to relative humidity.

Gas sensors: SiC is a key material for specialized gas sensing applications due to its wide bandgap, high resistance to oxidation and corrosion, and high electron mobility. It can detect hazardous or colorless, odorless gas leaks in extreme conditions. Highly porous SiC nanomaterials, in particular, provide high sensitivity and a broad dynamic range for gas sensing, with their porous structure ensuring quick and efficient sensor performance. While a high surface area is crucial for enhancing the performance of SiC nanomaterial-based sensors, the low reactivity of SiC limits their gas sensing capabilities (Wang, Wang, Lei, Xie, Wu, Gou, Han, Shi & Fang, 2016). To address this, chemical modification of the SiC surface with various metal oxides and noble elements has been employed to improve sensor performance. Resistive metal oxides like ZnO and SnO_2 were deposited on SiC to form heterojunctions, enhancing selectivity and reproducibility (Sun, Wang & Wang, 2020). F-doped SiC nanocages (Wu, Zhang, Sun, Liu, Yu & Lv, 2017), synthesized by treating SiC powder with HNO_3 and HF solutions, exhibited high selectivity towards H_2S gas, with a linear relationship between H_2S concentration and cataluminescence intensity, achieving a response time of 0.6 seconds and a recovery time of 1.0 second (Miller, Akbar & Morris, 2014). SiC nanotubes, whose electrical properties are independent of diameter and chirality, showed significantly enhanced sensitivity when doped with boron and nitrogen (Wang *et al.*, 2016).

Doping SiC with noble metals like Pd and Pt also enhances sensor sensitivity due to their catalytic activity. A H_2 gas sensor fabricated with $Pd - SiC$ nanocauliflower thin films achieved response and recovery times of 10 and 18 seconds, respectively, at 380 °C for 100 ppm H_2, showing high sensitivity and selectivity (Kumar, Kumar & Chandra, 2018). Replacing Pd with Pt; Pt nanoclusters@SiC nanosheets were synthesized, showing a near-linear response to hydrogen at low concentrations (600 ppm) at 300 °C. An RF-magnetron sputtering method was used to prepare a $Pd\breve{}Pt - SiC - PSi$ sensor, which detected 100 ppm H_2 at 350 °C with high stability and reproducibility (Sun, Wang & Wang, 2019).

Pressure sensors: Silicon-based pressure sensors are limited to operating below 250 °C. Among mainstream semiconductor materials, SiC is considered the most viable candidate to replace silicon in these demanding conditions. SiC-based piezoelectric pressure sensors, for example, have been shown to function up to 600 °C. SiC nanomaterial combines the advantages of low-dimensional structures with superior physical properties, offering high stability and great sensitivity across a wide operating temperature range. However, its low gauge factor may still limit its applications.

Wu, Fang, Guo, Zhao, Tian & Jiang (2020) used COMSOL and ANSYS software to optimize the structural design of SiC piezoresistive pressure sensors, focusing on diaphragm structure, material configuration, piezoresistor arrangement, and sensing material dimensions. Preliminary experiments confirmed the theoretical results, with the highest output sensitivity achieved by arranging four piezoresistors in a radial direction. SiC nanowires were deposited on a silicon substrate with a thickness of approximately 300 nm to form a pressure sensor (Phan, Dowling, Nguyen, Dinh, Senesky, Namazu, Dao & Nguyen, 2018). Although both bulk SiC and SiC nanowires demonstrated similar linear relationships between applied pressure and resistance change, SiC nanowires exhibited higher sensitivity. Additionally, a high-sensitivity piezoresistive sensor was fabricated using p-type cubic SiC nanowires through a top-down process (Phan, Dinh, Kozeki, Nguyen, Qamar, Namazu, Nguyen & Dao, 2016a). This cubic SiC nanowire sensor showed 5.4 times higher sensitivity than regular SiC sensors. The SiC sensors also demonstrated impressive electromechanical sensing capabilities, with a gauge factor of up to 87 and stable wide-range compression-resistance response, outperforming carbon-based composite sensors.

Bio sensors: Due to their excellent biocompatibility, non-toxic SiC nanomaterials are well-suited for use in biomaterials and biosensing substrates (Oliveros *et al.*, 2013). Nanosized SiC-based biosensors have been developed for controlled, on-demand drug release (Ponraj, Dhanabalan, Attolini & Salviati, 2016). Additionally, molecular-sized colloidal SiC nanoparticles have been identified as promising candidates for in vivo bioimaging applications. Water-dispensable, molecular-sized SiC nanoparticles, with a size range of 1–4 nm, have been successfully produced, demonstrating strong and broad surface-related luminescence. In contrast, larger SiC

nanoparticles exhibited luminescence associated with structural defects and lacked the quantum confinement effect (Beke, Jánosi, Somogyi, Major, Szekrényes, Erostyák, Kamarás & Gali, 2016).

1.5 Technological maturity of SiC nanomaterials based physical sensors

As mentioned earlier, this PhD project focuses exclusively on the development of fully screen printed, flexible physical sensors based on SiC nanomaterials. We observe wide spread research done on developing physical sensors based on SiC nanomaterails in recent years. However, these reported devices often utilize complex 1,2 and 3D structures such as SiC nanowires, composites with other nanomaterials and dopants to enhance device performance. Such materials often require extensive and cost intensive manufacturing processes which limit their reliability and scalability. Additionally, the use of small batch processing techniques such as spin coating and vapor deposition further limit cost efficiency and scalability.

One approach to minimize material complexity and fabrication costs is to employ relatively simple printing technologies to fabricate SiC nanomaterial based based physical sensors. The field of printed electronics has steadily become vital towards the fabrication of low cost and high volume devices over the past two decades. Well established printing technologies such as screen printing are being used towards building functional devices for large scale deployment in industries such as IoT and medical diagnostics and preventative care. The next chapter will highlight key components employed towards building a successful printed functional device.

CHAPTER 2

STATE OF THE ART

2.1 Printed Electronics - An Overview

Printed electronics encompasses a range of printing technologies used to create electrical devices on substrates such as flexible or stretchable materials. With growing interest in both printing technology and electronics, innovations have emerged to produce novel electronics through low-cost, large-area printing processes. Often associated with organic or plastic electronics, printed electronics involves using inks composed of cmetals (silver, copper, gold), polymers both conductive and insulating, which can be deposited using solution-based, vacuum-based, or other processes. This field specifies the process and can utilize any printable materials like organic and inorganic semiconductors, metallic conductors, and nanomaterials, depending on the requirements of the selected printing method.

Key components of printed electronics include:

- A rigid or flexible substrate
- A printable ink (condutive, insulating or sensing)
- A suitable continuous or batch printing process

The term "printed electronics" dates back to the early 20th century, initially aimed at fabricating flexible conductors to simplify electronic circuit interconnections. By the 1950s, the development of printed circuit boards (PCB's) using copper sheet lamination occurred. In the early 1990s, the contemporary concept of printed electronics, including conductors, semiconductors, and insulators using inks, was introduced, focusing on depositing conductive wires with conductive ink. Techniques like spray-coating, stamping, and inkjet printing have since enabled roll-to-roll processing, and transfer printing has allowed traditional silicon-based devices to be transferred onto flexible substrates. Applications span healthcare, displays, memory, and sensors, with

potential for future technology integration in clothes, clocks, and human skin (Coombs, 2001; Rim, Bae, Chen, De Marco & Yang, 2016; Tong, 2022).

The development of flexible electronics began in the 1960s, driven by the need to capture solar energy for space applications and the energy crisis. Flexible solar panels offered advantages like larger active areas, lighter weight, and greater resistance to thermal and vibration shocks. This led to further use in flexible ribbons and wires in computers. Unlike rigid silicon electronics, flexible devices can be demonstrated on plastics, paper, fibers, and biological tissues, necessitating low-temperature processing. This has spurred the development of organic conductors and semiconductors and advanced solution-based techniques, promoting alternative manufacturing technologies like 3D and roll-to-roll printing. As Industry 4.0 increases the integration between systems, human and data towards a more robust and connected manufacturing environment; printed devices play an instrumental part in applications such as environmental monitoring, energy generation and storage, biomedical sensors, robotics, prosthetics, implantable electrodes, and wearable systems (Tong, 2022). For instance, large deformation experienced at complex surfaces like the knees and elbows of a humanoid robot requires stretchable devices (Morelli, Gagnon & Zednik, 2023). The development of flexible and stretchable devices has paved the way for applications such as wearable electronics, consumer electronics, and conformable electronics (Dang, Vinciguerra, Lorenzelli & Dahiya, 2017).

The success of printed flexible systems largely stems from materials engineering innovations, leading to novel inks and printable materials composed of nanomaterials, polymers, and composites. Modern printed devices include soft, stretchable, and anatomically compliant devices that integrate efficiently with the body and withstand mechanical stress (Ko, Kapadia, Takei, Takahashi, Zhang & Javey, 2012a). This progress has resulted in diverse physical and chemical sensors and contributed to the trillion sensors movement aimed at meeting sensor demand across various applications, such as IoT and healthcare. While printing technologies are well-established, developing new printable inks for flexible electronics is crucial. These inks must maintain conductivity under mechanical deformation and endure various ambient

conditions. Innovations in materials science, particularly in ink formulations, are essential for achieving high-performance flexible and wearable devices (Eckstein, 2016).

2.2 Printed materials

Printed electronics have transformed into an interdisciplinary field encompassing microelectronics, chemistry, and printing/process engineering. This field involves the formulation of functional inks, managing thermodynamic effects during and after printing, and understanding drying mechanisms. Conductive materials are crucial alongside organic semiconducting compounds for components like wiring, electrodes, and contacts. Presently, a wide range of printable metals are available in the form of metal-organic decomposition (MOD) inks, nanoparticle dispersions, or nanowire dispersions. These include precious metals such as gold, silver, and platinum, as well as the more affordable copper. Additionally, carbon-based materials like graphene and carbon nanotubes (CNT's) are used in transparent electrode systems, demonstrating excellent performance. Significant advancements have been made in reducing the sintering conditions of silver inks from 200 °C - 300 °C to nearly room temperature. Furthermore, highly conductive and transparent polymer electrodes have been extensively researched, representing the only solution-processable, uniformly conductive, and transparent electrode material. Extensive development of conductive, semiconducting, and resistive inks has continued to drive the creation of fully printed electronic devices on economical and flexible substrates such as PET or paper. New sintering techniques, including photonic sintering, low-pressure argon plasma, microwave, or DC current sintering, have expanded the possibilities for solution-processable metal inks (e.g., Au, Cu, Pt) on low-temperature substrates. However, a seemingly minor step in the printing process has proven to be much more complex than initially thought. Almost every printing technique and source material requires a customized formulation, considering factors such as boiling point, viscoelastic properties, and thermodynamic effects during printing and drying, often requiring adjustments (Eckstein, 2016).

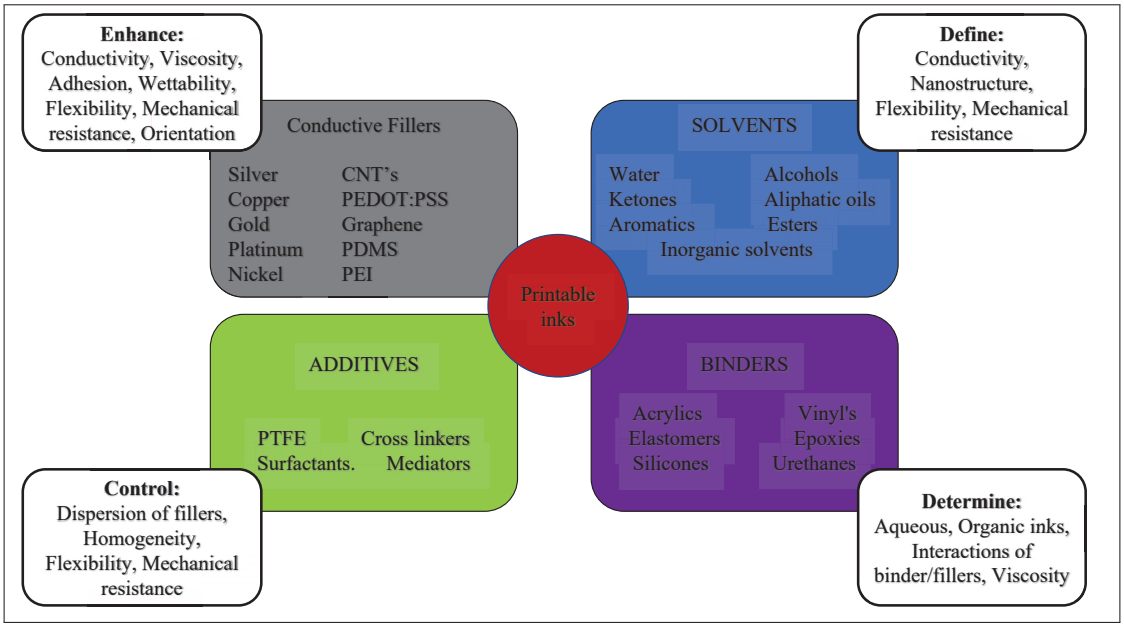

Figure 2.1 Key ingredients of printed inks used in flexible printed electronic devices Adapted from (Bocchetta *et al.*, 2020)

2.2.1 Overview of ink formulation

Figure 2.1 highlights the key ingredients used in fabricating a successful printed ink along with the contribution of each component towards its success. The selection of components for inks ultimately depends on the type of printing methodology to be used.

- Fillers, the active component of the ink, give it the characteristics needed for specific applications. These fillers can be metallic, ceramic, organic, or a combination, depending on the application. Advances in nanoscience and printing technology have led to the creation of inks with custom-made nanomaterials, such as nanosheets, nanowires, nanoparticles, or their composites.

- Another crucial component of ink is the binder, a polymeric material that ensures the even dispersion of fillers within the ink. Upon printing, binders hold the ink components together as the solvent evaporates and help the printed trace adhere to the substrate. Various binders with acrylic, silicone, styrene, fluoroelastomers, or urethane backbones have been developed

for printing flexible, stretchable, and self-healing devices. The choice of binder depends on the properties of the fillers and the application of the printed devices. For example, water-soluble binders should be avoided for devices exposed to aqueous media. UV and heat curing binders have been developed to meet diverse application needs.

- The solvent, which allows the ink to flow, is another essential component. It should provide good solubility to the polymeric binder and impart favorable viscosity, surface tension, and homogeneity. Ideal solvents for a particular set of binders and fillers can be selected based on Hillenbrand and Hansen solubility parameters, which estimate the cohesive energy between a solvent molecule and other ink components. This selection is crucial for obtaining homogeneous ink formulations and optimal printability, especially when printing multilayer devices. In such cases, using different sets of solvent and binder for each layer can minimize the risk of the solvent dissolving and damaging the underlying printed film.

- Beside's fillers, binders, and solvents, additives are included to impart desired rheological, wetting, healing, or stretching properties to the inks. Additives such as surfactants, adhesion improvers, humectants, penetration promoters, and stabilizers are used to tailor the ink properties for specific applications.

Table 2.1 Ink properties requirements for different printing methods
Adapted from (Suganuma, 2014)

Parameter	**Screen Printing**	**Inkjet printing**	**Flexography / Gravure**	**Dispense**
Viscosity (cP)	500 - 5000 or more	10 - 20	50 - 1000	more than 300,000
Trace width (μm)	50 - 500	10 - 50	10 - 100	1 - 100
Trace thickness (μm)	5 - 250	1 - 10	less than 1	1 - 100
Printing speed (m/min)	70	1	1000	less than 1

Different printing methods require specific ink properties for precise resolution and performance. As seen in Table 2.1, screen printing can reproducibly print high-aspect-ratio structures due to the high viscosity of the inks, which typically range from 1000 to 10,000 cps for thin films but can go as high as 50,000 cps for thicker prints. In contrast, gravure and flexography, which are template-based printing techniques, use less viscous inks for fabricating thin films. These

techniques use patterned rolls or plates to apply ink to substrates at high speeds, requiring suitable solvents and contact times for rapid solvent evaporation.

Non-template direct write printing methods rely on dispensing technology (pneumatic, piezo-electric, aerosol, electrohydrodynamic, and thermal). These systems require low-viscosity inks (10–20 cps) for easy and reproducible ink registration onto the substrate. However, this restricts the range of compatible fillers and limits the concentration of fillers in the ink. Nozzles used in these systems can clog if the solid ink components are larger than the nozzle opening. Despite these challenges, highly flexible, stretchable, and self-healing printed devices have been developed. Such properties are essential for creating "skin-like" devices that can withstand mechanical stress and conform to the human skin for various on-body applications involving extreme tensile stress.

2.2.2 Conductive inks

Table 2.2 Conductive inks conductivity (S/m) comparison
Adapted from (Suganuma, 2014)

Ink materials		**Electrical Conductivity (S/m)**
Metals	Ag	6.2×10^5
	Cu	5.9×10^5
	Au	4.4×10^5
	Pt	1.0×10^5
	Ni	61.4×10^5
Orgainc	PEDOT:PSS	5×10^3
Ceramic	ITO	3×10^4
Carbon	CNT's	10^2 - 10^4
	Graphene	10^6 - 10^8

Conductivity (S/m) represents the effectiveness of a conductor following the printing and sintering processes. Beyond the conductivity of the active material in the ink, the uniformity of the printed layer significantly influences the performance of the printed pattern. Various materials and their composites have been developed for various printing techniques to create conductive features. Table 2.2 compares electrical conductivity of the most widely used conductive inks. These

conductive materials can be broadly classified into metal-based, carbon-based, organic-based, and other types of conductive materials:

Metallic nanoparticle based inks: Ink formulations utilizing metal particles with high conductivity, such as silver (Ag) and copper (Cu), offer a distinct advantage over other conductive materials like organic polymers. The size and morphology of the metal particles impact the final conductivity of the printed pattern through the uniformity of the layer and the quality of particle contact. During printing, inks are in a fluid state, and particle dispersion within the ink must remain stable against aggregation and precipitation to ensure optimal performance during the process and in the final product. After deposition on the substrate, the ink should wet the surface appropriately, then dry and adhere to the substrate. Metallic particles are brought into contact on the substrate to achieve conductivity through various sintering methods. Sintering involves welding particles together at temperatures below their melting point. Due to these requirements, ink formulation is a complex process that demands significant R&D efforts. Factors such as ink dispersion stability, solid content, surface wetting, and the sintering process all affect the uniformity of the printed pattern. The sintering process must decompose the organic polymers used in the inks and bring the metallic particles into contact. Impurities from the ink formulation, such as organic stabilizers and binders, can reduce the conductivity of the printed pattern (Kamyshny, Steinke & Magdassi, 2011).

- **Copper inks:** Although silver has the advantage of higher conductivity compared to copper, its high cost significantly limits its use and scalability. Copper, on the other hand, is preferred due to its good conductivity and cost-effectiveness (Bhore, 2013). The creation of copper-based conductive electrodes typically involves the use of conductive inks made from copper nanoparticles dispersed in a suitable solvent (Deng, Jin, Cheng, Qi & Xiao, 2013; Eun, Chon, Yoo, Song & Choa, 2015). However, despite copper's economic viability, it is more susceptible to oxidation. The formation of copper oxide reduces the ink's conductivity and increases the sintering temperature, which can cause deformation of the substrate. This limitation hampers the wide spread or industrial use of copper-based inks.

- **Silver inks:** Silver nanoparticles demonstrate excellent conductivity (6.3 x 10^7 S/m at 20 °C) and offer several advantages for ink-based applications. They are more resistant to oxidation than copper, less expensive than gold nanoparticles, corrosion-resistant, possess significant antibacterial properties, and are thermally conductive (Karthik, Singh et al., 2015). These attributes make silver nanoparticles a highly suitable choice for synthesizing conductive metal inks (Shen, Zhang, Huang, Xu & Song, 2014). However, it's important to note that they are more costly than copper nanoparticles, which can impede their scalability for industrial use (Yang & Wang, 2016). In recent literature, silver is the most common material used to print conductive electrodes for physical sensors. We will discuss this in further detail in the coming sections of this chapter.

Carbon derivatives based inks: Carbon-based materials, such as carbon black, graphene, carbon nanotubes (CNT's), and carbon nanofibers, are significant conductive materials. They are often incorporated into polymeric materials to create conductive inks due to their excellent conductive and sensing properties. For example, carbon black particle inks have been utilized to produce flexible strain sensors and piezoresistive sensors through material extrusion, allowing for the embedding of functional sensors and electronics in a single, cost-effective process (Chang, He, Mao, Zhou, Lei, Li, Li, Chua & Zhao, 2018).

Two-dimensional graphene flakes, 0.34 nm thick like graphite's interlayer spacing, boast a high Fermi velocity (10^6 m/s) and intrinsic in-plane conductivity. The sheet resistance (R_s) of graphene varies inversely with layer count (N), approximately Rs ≈ 62.4/N [Ω/square]. Synthesis methods include mechanical exfoliation from graphite, chemical vapor deposition (CVD), and thermal decomposition of SiC. Graphene oxide (GO), derived from graphite oxidation in strong acids, is favored for conductive inks due to water dispersibility and enhanced conductivity post-reduction (chemical or thermal). Pristine graphene dispersions, made by ultrasonication in water or solvents like terpineol and ethanol, often require stabilizers (e.g., SDS, PVP). GO's functional groups (hydroxyl, epoxy, carbonyl, carboxylic) allow dispersal in water and polar solvents like DMF and THF without stabilizers, unlike pristine graphene. To achieve low resistivity in graphene ink films (0.002–0.1 wt% loading), multiple printing passes are needed.

Post-deposition annealing (3300 °C - 400 °C in air or higher in inert atmospheres) reduces resistivity by removing organic stabilizers. Thermal or chemical reduction of GO to graphene affects only surface layers; reactive inkjet printing combines GO with reducing agents (e.g., ascorbic acid with $FeCl_2$) at 60 °C to form conductive films ($\geq$100 kΩ/square).

Carbon nanotubes (CNT's) are cylindrical nanostructures made of one-atom-thick carbon sheets, known as graphene, arranged in either semiconducting or metallic configurations depending on their chirality. They can exist as single-walled (SWCNT's) or multi-walled (MWCNT's) varieties, with lengths ranging from less than a micron to tens of microns. SWCNTs typically have diameters of 0.4–4 nm, while MWCNT's range from a few to tens of nanometers in outer diameter. CNT's exhibit low intrinsic electrical resistivity, such as 10^{-6} Ω cm for SWCNTs and 3×10^{-5} Ω cm for MWCNTs, though higher resistivities are common due to synthesis-related defects. Introducing acceptor dopants can enhance conductivity, beneficial for applications like flexible electronics. CNT's are synthesized primarily via methods like electric arc discharge, laser ablation, and chemical vapor deposition (CVD). Each method offers unique advantages for producing high-purity nanotubes suitable for various applications. Challenges in formulating CNT inks include achieving stable dispersions in liquids with low viscosity, often addressed through chemical modification or surfactant use. These inks are crucial for applications like conductive printing, enabling fabrication methods such as inkjet and aerosol jet printing. CNT films, fabricated through techniques like rod-coating or inkjet printing, offer high electrical conductivity and transparency, crucial for flexible electronics and functional textiles due to their mechanical robustness and flexibility.

Conductive polymers based inks: Conducting polymers, discovered in the late 1970s, have gained significant attention due to their light weight and high flexibility. They offer the potential to replace traditional metal-based devices, leading to fully plastic electronic devices. However, a major challenge is the low conductivity of some solution-processible organic compounds, which can hinder device performance (Vacca, Mascia, Rizzardini, Corgiolu, Palmas, Demelas, Bonfiglio & Ricci, 2015). Polymers like PEDOT, polypyrrole, and polyaniline are used in inkjet and aerosol jet printing. These materials have a conjugated pi-electron system, giving them

conductive properties. They are employed in sensing applications, electrochromic displays, batteries, fuel cells, and anti-static layers. Despite their benefits, these polymers generally have lower conductivities than metallic inks and may require inert atmospheres due to their sensitivity to humidity and oxygen. Their non-Newtonian behavior complicates printing, as droplets can form long tails that eventually detach, creating satellite droplets. This behavior is due to elastic stresses from extensional flow in the nozzle. Additionally, substrate roughness affects their conductivity. For example, inkjet-printed photovoltaic devices perform better than spin-coated ones due to finer phase separation from rapid drying (Cummins & Desmulliez, 2012).

Among these polymers, PEDOT stands out for its high conductivity, environmental stability, and transparency, making it ideal for organic photovoltaic devices (OPV's) and organic light-emitting diodes (OLED's). PEDOT, combined with poly(styrene sulfonic acid) (PSS), enhances water dispersibility. The conductivity of PEDOT:PSS films, however, is typically low (1 S/cm), which may be due to coil structures with low particle interconnections. Adding surfactants, graphene oxide, or polar solvents like ethylene glycol (EG) can significantly improve conductivity, reaching up to 467 S/cm (Vacca *et al.*, 2015; Xia, Zhang & Ouyang, 2010). Combining PEDOT:PSS with other conductive polymers, like polyaniline (PANI), creates hybrid systems with tunable properties. PANI, with high conductivity and a porous structure, is synthesized through chemical or electrochemical oxidative polymerization. Its characteristics depend on redox equilibria influenced by pH. PANI, active at acidic pH, can form multilayer complexes with anionic polymers, enhancing redox activity at higher pH. These composites present novel properties and unique structures (Shi, Liu, Xu, Song, Lu, Jiang, Zhou, Zhang & Jiang, 2013).

Transient oxide based conductive inks: Transparent conducting oxide's (TCO's) are materials that exhibit both transparency and electrical conductivity, making their films valuable in various applications such as flat panel displays, electroluminescent devices, transparent electrodes, touch screens, portable electronics, flexible electronics, optics, biochemical and environmental sensors, transparent heaters, multi-functional windows, and solar cells. Typically, TCO's are metal oxIDE's characterized by high optical transmittance and high electrical conductivity. They are also known as wide-bandgap oxide semiconductors with a bandgap greater than 3.2 eV. These

materials allow high optical transmission at visible wavelengths (400–700 nm) while achieving electrical conductivity comparable to metals, often enhanced by doping with other elements. Additionally, TCO's reflect near-infrared and infrared wavelengths. Since their bandgaps are in the ultraviolet region, they minimally absorb visible light, rendering them transparent to the human eye. These distinctive properties make TCO's essential in modern electronics that require optical access behind electrical circuitry. For a film to qualify as a TCO substrate, it must have low electrical resistivity (10-3 to 10-4 Ω cm) and high optical transparency in the visible light range (>80% transmittance), due to their wide bandgap (Coutts, Young, Gessert, Ginley & Hosono, 2011; Gordon, Dorfman, Kirk & Adams, 2012).

2.2.3 Semiconducting ink

Semiconductive materials, which lie between conductors and insulators, exhibit electrical conductivity in the range of 10^{-10} to 10^{2} S/cm. This conductivity can be altered through doping, which involves introducing impurities into the material's lattice structure. These modifications enable their use in various applications, including variable resistance, current flow control, sensitivity to light or heat, signal amplification, energy conversion, Thin Film Transistor (TFT's), organic photovoltaics (OPV's), and organic light-emitting diodes OLED's (Smith, 2013). Inorganic semiconductors like silicon, gallium arsenide (GaAs), indium phosphide (InP), and gallium nitride (GaN), along with emerging organic nanomaterials such as carbon nanotubes or metallic oxide's, have been successfully incorporated into semiconductive inks in different structural forms, ranging from nanowires to free-standing nanomembranes (Bhattacharya, Fornari & Kamimura, 2011; Garlapati, Divya, Breitung, Kruk, Hahn & Dasgupta, 2018; Kim & Hone, 2017).

Organic semiconductors combine the properties of polymers—such as solubility, mechanical strength, and physicochemical properties—with the electrical conductivities of inorganic materials. These are classified into polymers and small-molecule materials. Soluble polymers can be processed from solutions, while small-molecule materials are divided into pigments (insoluble) and dyes (soluble), which usually require thermal evaporation (Martins, Pereira,

Lima, Garcia, Mendes-Filipe, Policia, Correia & Lanceros-Mendez, 2023). Advancements in organic semiconductors have introduced features like flexibility, lightweight, and large-area applicability, leading to the development of devices for printed electronics, including OPV's (Eric & Ramsden, 2016) and organic thin-film transistors (OTFT's) (Fukuda, Hikichi, Sekine, Takeda, Minamiki, Kumaki & Tokito, 2013), as well as biosensors and microfluidics (Dorfman, Adrahtas, Thomas & Frisbie, 2020).

Inorganic semiconducting micro/nanoscale particles, wires, ribbons, sheets, and bars (e.g. ZnO, $\mathrm{TiO_2}$, CuO, $\mathrm{SnO_2}$, $\mathrm{In_2O_3}$, or $\mathrm{MoS_2}$) are promising as active components in semiconductive inks. These materials provide organized paths for carrier flow, can be produced in extremely small sizes suitable for inkjet printing, and their electrical properties can be optimized based on filler content. Single-walled carbon nanotubes (SWNT's) can offer superior electrical properties compared to their inorganic counterparts. For high-performance devices, arrays of SWNT's are preferred to avoid percolation transport pathways and tube/tube junction resistances inherent in random networks of SWNT's, though random networks are easier to produce (Bhattacharya *et al.*, 2011).

2.2.4 Dielectric inks

Dielectric inks are materials that act as electrical insulators. While they may seem non-functional, they are crucial in various aspects printed electronics, such as circuit protection, insulation in multilayer circuits, and the fabrication of capacitors and transistors (Kaija, Pekkanen, Mäntysalo, Koskinen, Niittynen, Halonen & Mansikkamäki, 2010; Serway, Jewett & Peroomian, 2000; Tan, Choong, Kuo, Low & Chua, 2022; Varghese & Sebastian, 2017; Zhou, Han & Roy, 2014). They are insulators that do not allow electric current to pass through them. When a potential is applied, they undergo polarization. Key parameters for assessing the performance of dielectric layers include insulation resistance, breakdown voltage, dielectric constant, and the presence of pinholes/pores. Dielectric inks can be composed of either inorganic nanocomposite suspensions or organic polymers. Common organic polymers used for these inks include polymethyl methacrylate (PMMA), polyimide (PI), polystyrene (PS), polyvinylidene fluoride

(PVDF), polyvinylpyrrolidone (PVP), and polyvinyl alcohol (PVA) (Khan, Thielens, Muin, Ting, Baumbauer & Arias, 2020). Ensuring compatibility of the dielectric inks with both substrates and other functional inks is essential. Additionally, desirable properties include low-temperature processing, smooth surface finishes, high optical transparency, and low cost (Cui, 2016; Khan *et al.*, 2020).

In multilayer circuits, dielectric inks play an insulating role between layers of conductive traces, allowing conductive inks to be deposited without short-circuiting. Commercially available dielectric layers typically have an insulation resistance greater than 10X, which can be affected by pores/pinholes. These pinholes, formed during the drying process, can let conductive pastes pass through, causing interlayer shorting. Bias and humidity can drive conductive paste to form cations, which migrate through these pores, leading to shorting. The dielectric layers must be thick enough to prevent electrical leakage, but high voltages can compromise their insulating abilities. Smooth, defect-free dielectric layers are crucial for optimal printability and insulation (Kaija *et al.*, 2010). Dielectric pastes often consist of ceramic material, a devitrifying agent, binder, and an organic solvent for screen printing.

2.3 Printing techniques

Printing technologies employed towards fabricating printed circuits and devices can be broadly classified into two categories (Figure 2.2) namely, contact and non-contact printing. Both technology classes offer immense advantages towards research and mass fabrication of devices. Selecting the optimal printing method is essential towards the success and cost effectiveness of the device. Often selecting the appropriate printing technology for a particular application is driven by the trade off between the desired printed feature size and over all print speed as compared in Figure 2.3. In this section we highlight the differences and advantages of these printing methods.

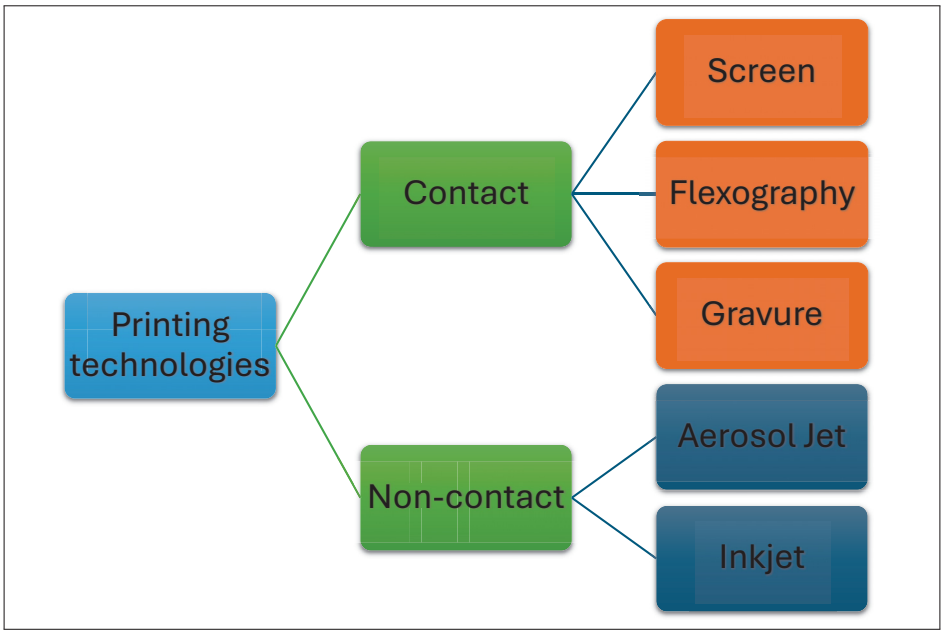

Figure 2.2 Comparing printing technologies

2.3.1 Contact printing

Modern contact printing technologies, though predominant, face challenges such as high material wastage and limitations in resolution and material compatibility (substrates, inks, solvents).

- **Screen printing:** is a mature technique, performed either in a batch or in a roll-to-roll (R2R) process. The batch system involves a mesh in direct contact with the substrate, using a blade to distribute ink, while the R2R process uses a roller instead of a squeegee, allowing continuous, high-speed production but at higher costs and cleaning difficulty. Screen printing often used suffers from significant material waste and low resolution.

- **Flexography:** is a R2R direct printing technology utilizing a ceramic anilox roller with micro-cavities to collect and transfer ink to a printing plate. The process ensures continuous high-speed printing but can produce a "Halo effect" due to compression between the plate and substrate, limiting image stability and resolution. It is used for on-label battery testers, drug delivery patches, printed batteries, and e-label applications.

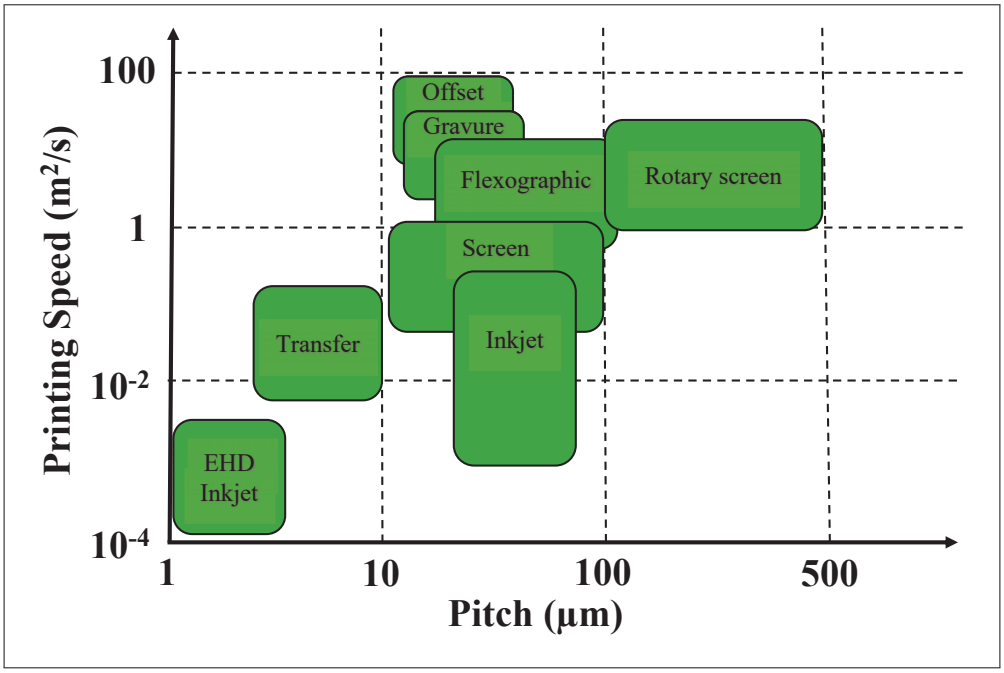

Figure 2.3 Comparing print speed versus achieved trace pitch for various printing techniques
Adapted from (Lupo *et al.*, 2013)

- **Gravure printing:** is the reverse of flexography, involves transferring ink through capillary action from an engraved plate, capable of high-quality patterns at high speeds and suitable for low-viscosity inks. Key factors for quality include ink properties, cell spacing, feature dimensions on the cylinder, and shear force. Widely used in magazine production, medical ECG pads, RFID devices, thin-film transistors, solar cells, and sensors, gravure printing's main limitations include jagged lines for high-resolution needs and frequent cylinder replacements, adding maintenance costs.

2.3.2 Non-contact printing

Non-contact printing technologies offer several including reduced risk of contamination and substrate damage, as well as improved pattern alignment, which is essential for multilayered devices. These technologies, which do not require physical masks and only need digital images, simplify the switching process without additional costs. However, they can face challenges when

printing multilayered devices on substrates such as wood, glass, metals, rubbers, and polymers, which may deform under high temperatures.

- **Aerosol jet printing:** Aerosol jet printing, also known as Maskless Mesoscale Materials Deposition (M3D), is a versatile non-contact material deposition technology developed by Optomec. It aerosolizes various inks, including metal nanoparticle suspensions, and directs them onto substrates using a focused jet stream of nitrogen. This low-temperature process supports a wide range of substrates and complex designs, making it ideal for applications like displays, thin film transistors, and solar cells. Additionally, it is scalable for high-volume production and capable of printing on non-planar surfaces.

- **Inkjet printing:** is another emerging non-contact drop on demand (DOD) method that directly deposits droplets from digital content without masks, making it suitable for a wide range of materials and applications, from transducers and transistors to 3D electric circuits and biomedical materials. Despite its adaptability and low environmental impact, inkjet printing faces challenges such as nozzle clogging, low process velocity and rigid ink rheology, making it more suited for laboratory research and innovative fabrication rather than industrial production.

Figure 2.4 illustrates the operating principle of the above discussed printing techniques. Table 2.3 compares the principles, features, drawbacks, ink requirements and printed feature outcomes for all the above mentioned printing techniques.

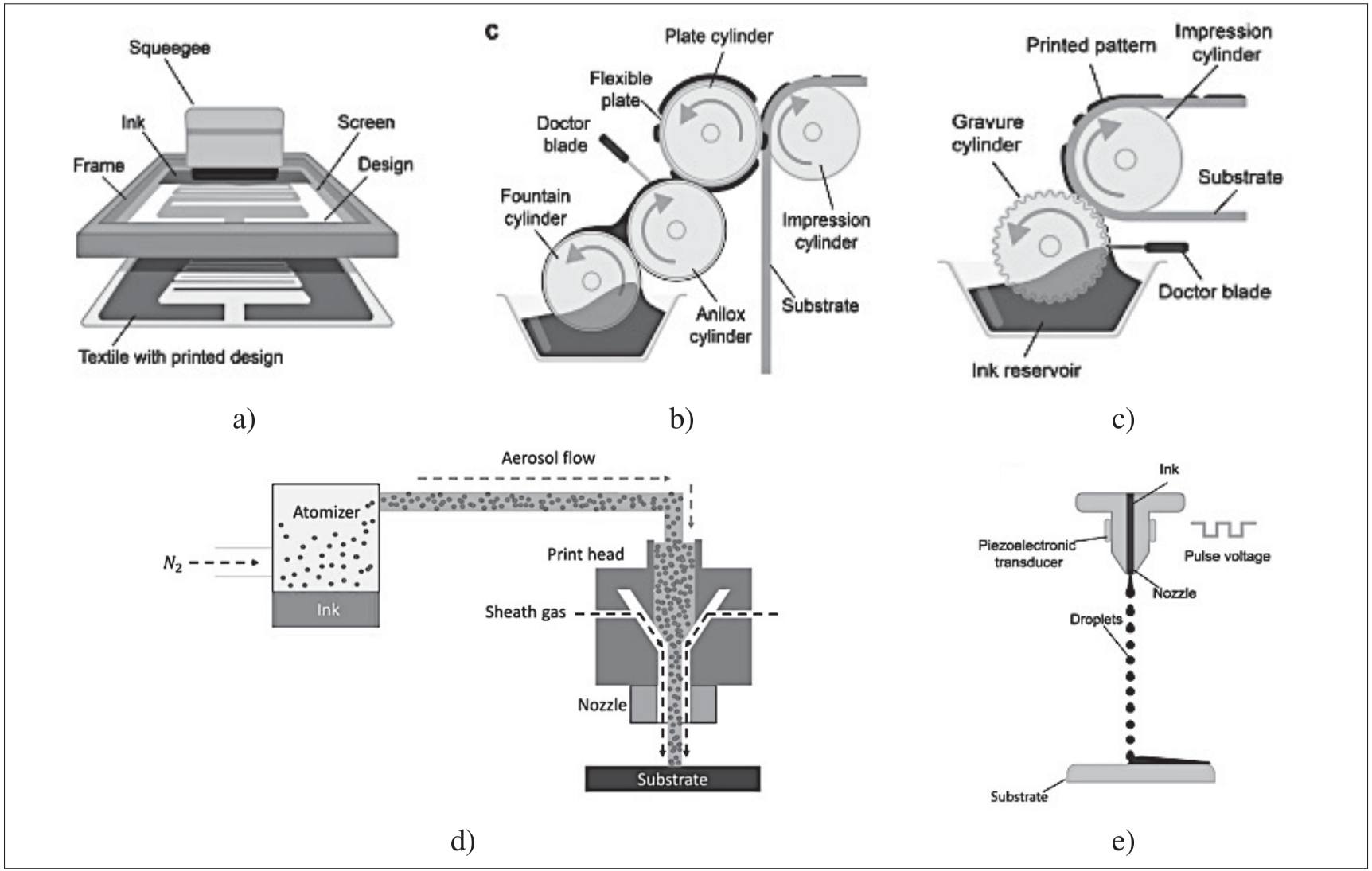

Figure 2.4 (a) Screen (b) Flexographic (c) Gravure (d) Aerosol Jet (e) Inkjet printing process schematics
Taken from (Hung *et al.*, 2020; Islam *et al.*, 2024)

Table 2.3 Comparing features, challenges, properties and outputs of various contact and non-contact printing techniques Adapted from (Cruz *et al.*, 2018b; Martins *et al.*, 2023)

Technique	**Features**	**Challenges**	**Viscosity (Pa.s)**	**Print thickness (μm)**	**Print resolution (μm)**	**Surface tension (mN/m)**	**Printing speed**
Contact printing							
Screen	Mature printing technique for continuous and batch printing. High speed and versatile.	Cleaning is difficult with high material wastage, aggressive solvent degrade masks, low reslotion, only high viscosity inks.	0.1-10	0.002-100	30-100	38-47	High
Flexography	High speed and low cost process, high flexibility and low pressure printing, better printing resolution than gravure.	halo effect caused by printing plate compression, complex alignment process and marbling effect.	0.01-0.1	0.17-8	30-80	13.9-23	High
Gravure	high quality and speed with low cost. Can print lower viscosity inks.	Costly printing cylinder with low shelf life, parameter optimization process is complex.	0.01-1.1	0.02-12	50-200	41-44	High
Non-contact printing							
Aerosol Jet	Can print complex and multi axis designs, low ink wastage, droplet jetting via pneumatic and ultrassnic atomization, large catelogue of materails avaiable, effective for printing high cost materials.	prone to nozzle clogging, successful jetting highly driven by ink rheology and operator skill, slow printing process.	0.001-1	0.01-0.5	15-100	15-35	Medium
Inkjet	can use low viscosity inks, low material consumption and wastage, effective for printing high cost materials.	prone to nozzle clogging, low printing speeds.	0.002-0.1	0.01-0.5	15-100	15-35	Medium / slow

2.3.2.1 Screen printing

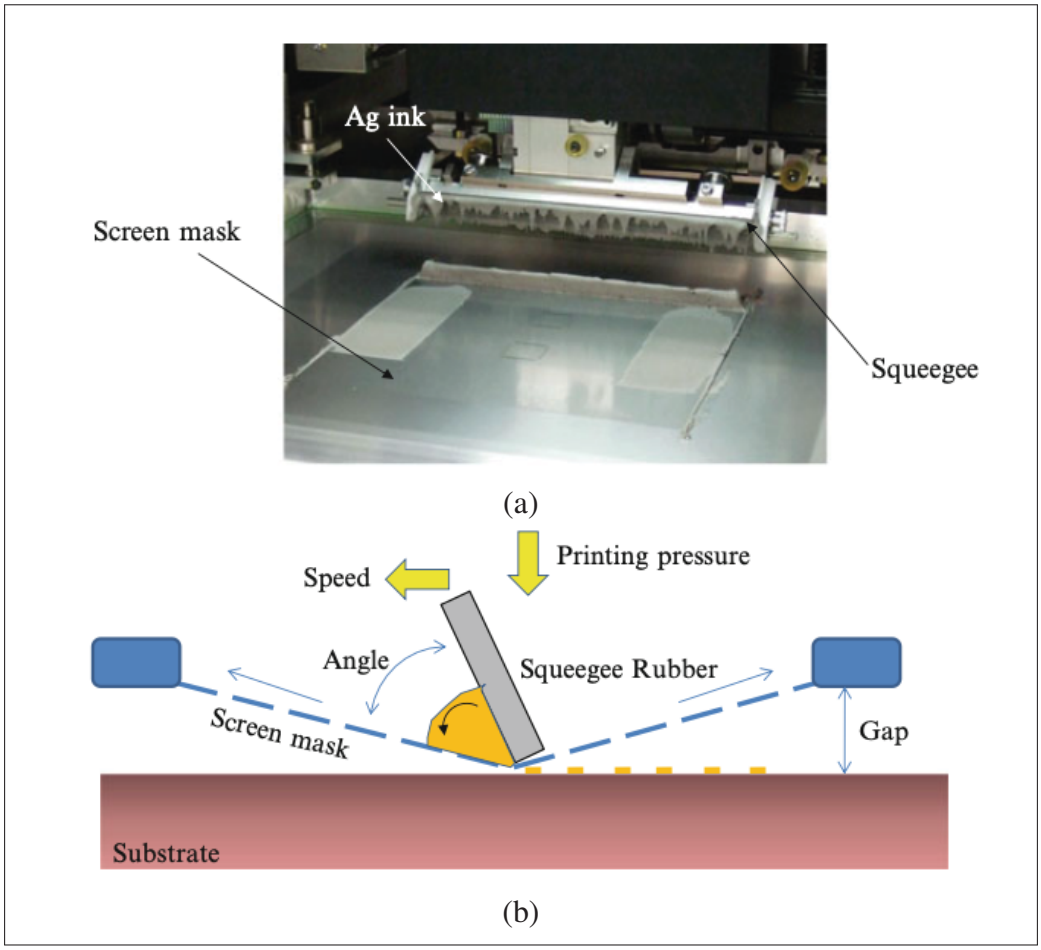

Figure 2.5 (a) Screen printing of silver ink (b) screen printing process parameters Taken from (Suganuma, 2014)

In this PhD project, we focus our efforts on utilizing screen printing as the primary technique towards our printed sensors and their corresponding electrodes. Hence, in this section we delve deeper into this subject. Screen printing is a pivotal technique in the realm of printed electronics, offering a versatile and cost-effective method for the mass production of various electronic components. The process involves the use of a patterned screen or stencil through which conductive, semi-conductive, or insulating inks are transferred onto substrates to form electronic circuits. This technique is highly valued for its ability to print on a wide array of substrates, including flexible materials like polymers, which are crucial for developing wearable

and flexible electronics (Zavanelli & Yeo, 2021). One of the primary advantages of screen printing is its scalability, allowing for the high-throughput manufacturing of electronic devices at relatively low costs. This is particularly beneficial for applications in consumer electronics, where large quantities of devices are required (Krebs, Jørgensen, Norrman, Hagemann, Alstrup, Nielsen, Fyenbo, Larsen & Kristensen, 2009). Moreover, screen printing enables the precise deposition of materials with thickness control, which is essential for the functionality of printed electronic components such as transistors, sensors, and photovoltaic cells (Suganuma, 2014).

Printing process: As illustrated in Figure 2.5, the process begins with the preparation of the screen, typically made of a fine mesh stretched over a frame. The desired pattern is created on the screen using a photolithographic process, where UV light is used to harden a photoresist, leaving the desired pattern open for ink transfer. During printing, a squeegee forces the ink through the open areas of the mesh onto the substrate below, accurately replicating the pattern on the screen (Perelaer, Schubert & Jena, 2010).

Mesh selection: Materials like nylon, stainless steel, polyester, silk, and chrome-plated wire are commonly used for making mesh. A mesh is composed of both porous and non-porous areas, with the porous areas forming the desired pattern. When subjected to mechanical pressure from squeezing or rollers, ink flows through these porous regions and is transferred onto the substrate. In the case of screen printing with thermosetting inks, temperature affects the ink's crosslinking behavior, which in turn influences its viscosity. If the viscosity of the ink increases quickly when poured onto the screen, the likelihood of clogging the mesh also rises. To address this issue, using heated ink is more effective, and the screen mesh must be able to withstand higher temperatures. Therefore, metals with melting points higher than the inks are often chosen for screen meshes (Iijima, 1991; Khaled, Hassan, Girgis & Metelka, 2008).

Materials: The choice of ink is crucial, as it must possess suitable rheological properties to ensure smooth transfer through the screen and adherence to the substrate. Conductive inks, often composed of silver, copper, or carbon nanotubes, are commonly used due to their excellent electrical properties (Suganuma, 2014).

The printed patterns are then subjected to post-printing processes such as drying or curing to solidify the ink and enhance its electrical conductivity. Advances in screen printing technology have also led to the development of multi-layer printing, enabling the creation of complex circuits and devices by sequentially printing multiple layers of different materials (Magdassi, Azoubel, Layani, Grouchko & Kamyshny, 2012). This is particularly important for the fabrication of advanced components like organic light-emitting diodes (OLED's) and thin-film transistors (TFT's), where precise layer alignment and material compatibility are critical (Lee, Choi, Chae, Chung & Cho, 2009). Despite its advantages, screen printing in printed electronics also faces challenges. The resolution of printed features is generally lower compared to other printing techniques like inkjet printing, which can limit its application in devices requiring fine features (Singh, Haverinen, Dhagat & Jabbour, 2010). However, ongoing research and development are continuously improving the resolution and performance of screen-printed electronics. Additionally, the development of new conductive and semi-conductive inks, as well as advancements in screen materials and printing techniques, are expanding the capabilities and applications of screen printing in printed electronics (Dimitriou & Michailidis, 2021).

2.4 Substrates

The substrate serves as the physical support for other components, also functioning as an electrical insulator to separate various conductive elements. Characteristics like ease of fabrication and lower cost make printed electrodes more favorable compared to solid electrodes. In this section we classify substrates into two main categories; rigid and flexible which are detailed as follows:

Rigid substrates:

Often times ceramic materials are employed as rigid substrates owing to their high thermal and mechnical properties which are critical in harsh environments such as chemical processing, high temperature and pressure applications, space and sub-orbital aerospace applications etc. Ceramics are solid materials composed of both metals and non-metals, with varying crystalline structures. Depending on their arrangement, they can range from highly ordered to non-crystalline

amorphous ceramics, such as glass. These materials are bonded by ionic or covalent forces, giving them properties like poor electrical conductivity, high thermal stability, significant hardness and brittleness, high melting points, and low ductility (Mitchell, Lagerlöf & Heuer, 1985). Low-temperature co-fired ceramic (LTCC) substrates are particularly suitable for applications in actuators, transducers, and sensors due to their relatively low Young's modulus of 90–110 GPa. The substrate's ability to support the use of more cost-effective conductive materials and its faster firing process provide's additional benefits. However, there remains a potential issue where the glass in LTCC could interact with deposited films, possibly altering their properties.

Flexible substrates:

In flexible printed electronics, substrates generally dictate the mechanical properties of the integrated system. A flexible substrate must be highly deformable, mechanically robust, and exhibit high tolerance for repeated bending to meet the demands of flexible technologies and integrated components. Device applications may require different substrate characteristics, such as flexibility or stiffness, transparency or opacity, smoothness or roughness, and thermal expansion or heat resistance. Different printing methods also have specific substrate requirements, including mechanical properties, thickness ranges, and flexibility. Inks used in printed electronics often require post-treatment processes like high temperatures, chemical functionalization, or UV radiation, which can damage some substrates. Considering these factors is crucial for achieving successful integration of substrate, printing technique, and printed material.

Substrate selection criteria (Tong, 2022; Yang, 2016):

- **Thermal properties:** Heat resistance is crucial for flexible substrates, requiring a glass transition temperature (T_g) or melting temperature high enough to withstand processing temperatures. A low coefficient of thermal expansion (CTE) is also necessary to prevent cracking or delamination of deposited layers. Thermal stability is important primarily for fabrication, though operating temperatures remain fairly constant. Some applications,

especially outdoors, require a wide range of operating temperatures. Effective heat dissipation through the substrate is ideal, demanding high thermal conductivity.

- **Chemical properties:** The substrate should not release contaminants, be inert against process chemicals, and exhibit strong barrier properties against air and moisture. For several applications, specific low water and oxygen permeation rates are required. Resistance to solvents and chemicals used in processing is also desirable, though temporary protective layers can be used.

- **Dimensional stability:** The substrate must resist deformation caused by moisture, solvents, chemicals, and thermal cycling. This requires low moisture absorbency, chemical resistance, and a low CTE.

- **Electrical and RF properties:** Electrically insulating substrates minimize coupling capacitances, while RF properties determine the performance of planar antennas.

- **Mechanical properties:** The substrate needs a high elastic modulus for rigidity and a hard surface to support device layers under impact. Flexibility is essential, allowing the substrate to bend/stretch without cracking or degrading. Advances in polymers may lead to fully bendable and stretchable electronics.

- **Optical properties:** High transparency and low birefringence are required for display applications, especially LCD's. The substrate should not exhibit birefringence to avoid image distortion.

- **Surface flatness and roughness:** Poor flatness can cause image distortion, while rough surfaces can affect electrical functions. Smooth substrates that adhere strongly to deposited layers are necessary to endure bending stress.

- **Cost:** Although not a material property, cost is a significant factor. Flexible electronics offer potential for reduced production costs alongside their diverse applications.

Substrate materials can be broadly classified into three categories: polymers, metals, and glasses (Harris, Elias & Chung, 2016; Monne, Lan & Chen, 2018). Glasses are rigid, while metal foils,

despite being flexible and capable of withstanding high temperatures, are limited in stretchability and design flexibility, making both unsuitable for flexible electronics. In contrast, the development of lightweight, flexible (stretchable and bendable), and recyclable / biodegradable polymer-based substrates has advanced the field of printed electronics. Additionally, biodegradable and non-toxic natural materials with insulating properties are suitable for flexible substrates, reducing the ecological impact.

Many polymers, ranging from amorphous to semi-crystalline, have been tested as flexible substrates, including polyethylene naphthalate (PEN), polyethylene terephthalate (PET), polycarbonate (PC), polyimide (PI), and polyvinylidene fluoride (PVDF) (Tong, 2022). Stretchable and flexible substrates include polydimethylsiloxane (PDMS), polyurethane (PU), and thermoplastic polyurethanes (TPU). Paper, a natural polymer, has also gained attention in printed electronics due to its low cost, flexibility, sustainability, and biodegradability. Table 2.4 compares the salient properties of commonly used flexible polymeric substrates in printed electronics. Below we highlight the three most commonly used polymeric substrates in printed physical sensors applications:

- **Polyimide (PI):** Polyimide is synthesized by polymerizing an aromatic dianhydride and an aromatic diamine. It is known for its excellent heat resistance (Glass transition temperature (T_g) between 360 and 410 °C), chemical resistance (no known organic solvents for the film), rigidity, flexibility, and electrical properties. However, polyimide absorbs water, with a high moisture absorption rate of 4% after 24 hours at 23 °C, leading to poor dimensional stability. It is not optically transparent, appearing yellow, which limits its use in display applications but makes it competitive for products like RFIDs. With a CTE of 20 ppm, polyimide is similar to other polymers.

- **Polyethylene naphthalate (PEN):** PEN is chemically similar to PET and is produced by the polycondensation of ethylene glycol and naphthalene-2,6-dicarboxylic acid. It offers greater heat resistance (Tg = 120 °C), chemical resistance, and dimensional stability compared to PET.

- **Polyethylene terephthalate (PET):** PET is a plastic resin and the most common type of polyester, made through the polycondensation of ethylene glycol and terephthalic acid. Due to its lack of heat resistance (Tg = 80 °C), it is often used in printed circuit boards for large circuits that do not require soldering.

Table 2.4 Comparing key properties of commonly used substrates
Adapted from (Martins *et al.*, 2023)

Property	**Unit**	**PI**	**PET**	**PEN**	**Glass**	**Al foil**
Glass transition temperature (T_g)	C	360 - 410	70-110	120-155	540	500
Melting temperature (T_m)	C	250-452	115-258	269	1000-1800	660
Denisty (ρ)	g cm^{-3}	1.36-1.43	1.39	1.36	2.5	2.7
Volume resistance (ρ_v)	Ωm	2 x 10^{19}	10^{21}	10^{16}	10^{9}-10^{13}	10^{-8}
Young's modulus	MPa	2.5 x 10^{3}	2-4.1 x 10^{2}	1-5 x 10^{2}	6.5 x 10^{4}	7 x 10^{4}
Elongation (E)	%	3	12	7	3	12-25
Maximum operational temperature (T_{max})	C	400	150	100	500	350
Coefficient of thermal expansion (α)	ppm/C	8-20	15-33	20	3	25.5
Water absorption (A_{H_2O})	%	1.3-3	0.4-0.6	0.3-0.4	-	-
Minimum sheet thickness	μm	0.5	1.4	1.2	25	6
Transparency (T)	%	-	90	69	100	-
Roughness (R)	-	Exellent	Poor	Poor	Exellent	Poor
Dimensional stability	-	Exellent	Exellent	Exellent	Exellent	Exellent
Solvent resistance	-	Exellent	Exellent	Exellent	Exellent	Exellent

2.5 Post processing techniques

Sintering and annealing are terms used to describe various post-treatment steps that are used after a conductive ink is printed. By definition, and in terms of their use in printed electronics, these two terms do not have the same meaning.

2.5.1 Sintering

This section focuses on key sintering techologies that have been employed in printed electronics. Figure 2.6 illustrates the same. Sintering generally refers to a heat treatment process involving two main stages. First, heat causes the removal of stabilizing molecules such as polymeric or surfactant agents, as well as other nonvolatile components like wetting and rheological agents, which remain in the printed pattern after drying. This temperature is known as the curing temperature (Perelaer, Abbel, Wünscher, Jani, van Lammeren & Schubert, 2012). After the organic layer is lost, nanoparticles come into physical contact, begin to weld together, interdiffuse, and transform small contact areas into thicker necks, forming a two-dimensional structure (Alexey Kamyshny; Beedasy & Smith, 2020). Despite this, the final result is often not fully dense due to residual porosity caused by surface imperfections or contaminants (Beedasy & Smith, 2020). Sintering treatments post-printing are used for metallic nanoparticle-based inks (such as gold, silver, copper, aluminum, and others) (He, Chen, Zhang, Williams, Fang & Shen, 2020; Karthik *et al.*, 2015; Lee, Lee & Lee, 2018; Saidina, Eawwiboonthanakit, Mariatti, Fontana & Hérold, 2019; Yamashita, Sakai & Murata, 2019) to enhance electrical conductivity. Developing nanoparticle-based inks for conductive tracks involves removing non-metallic components to enable electron movement through the printed material. This can be achieved through strategies like evaporation, desorption, or decomposition of the non-metallic components, facilitating close contact between the metallic particles in the dried printed trace (Cano-Raya, Denchev, Cruz & Viana, 2019a). The required temperature range for sintering varies depending on factors like the ink's solvent boiling points, metallic particle size and aspect ratio, the number of printed layers, the degree of conductive network formation, and the dissociation temperatures of the metal precursor salts.

- **Thermal sintering:** is the most commonly used technique for sintering metallic nanoparticle-based inks to produce conductive patterns, as it is often the most reliable method and can be performed with low-cost, user-friendly equipment (Saroia, Wang, Wei, Lei, Li, Guo & Zhang, 2020). In thermal sintering, the deposited ink and substrate are exposed to high temperatures, typically between 100 °C-400 °C (Cano-Raya *et al.*, 2019a), inside an oven, tube furnace,

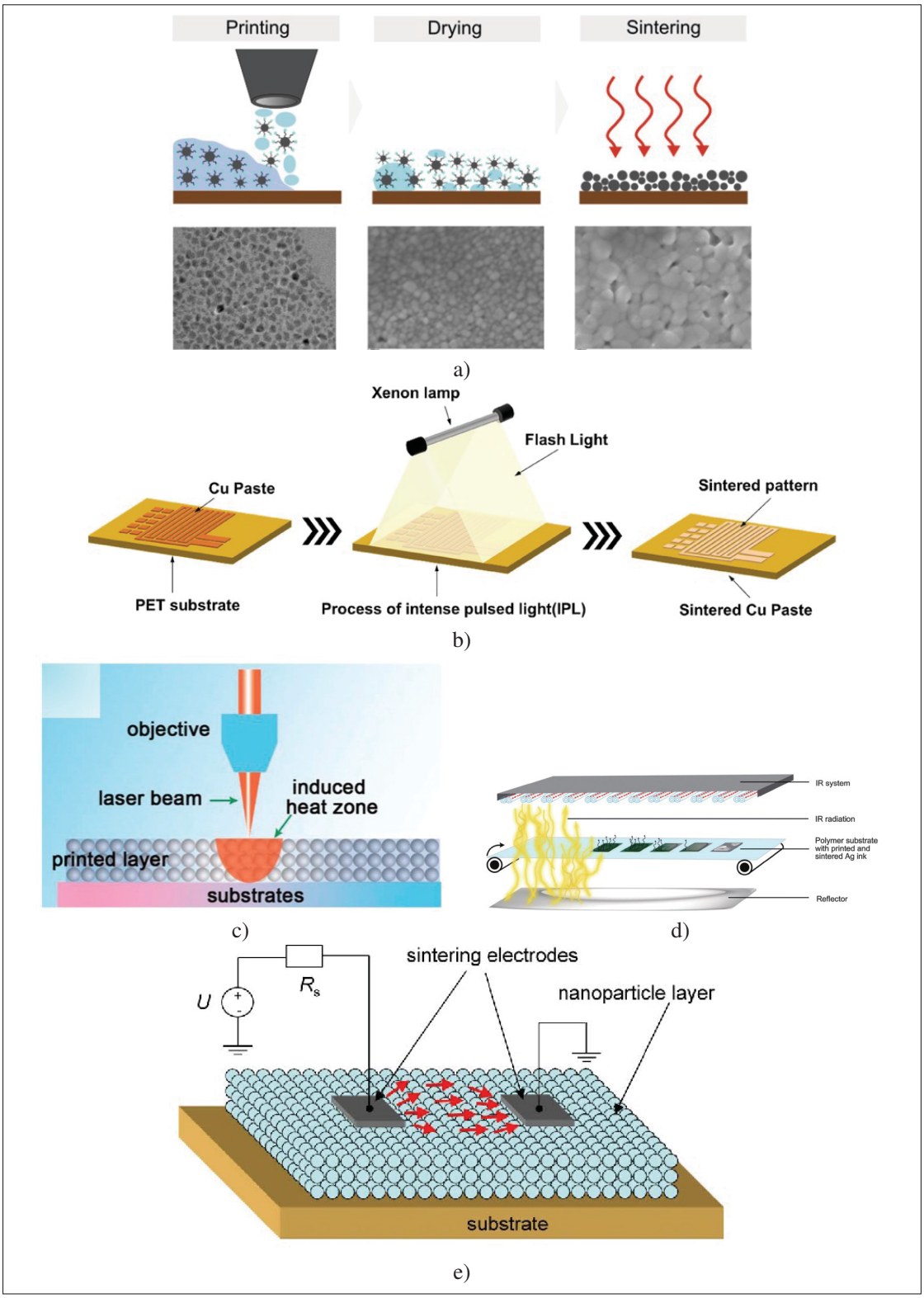

Figure 2.6 (a) Thermal (b) photonic (c) laser (d) microwave (e) electrical sintering process schematics
Taken from (Allen *et al.*, 2011; Lu *et al.*, 2023; Mo *et al.*, 2019a; Shin *et al.*, 2018)

or on a hot plate, depending on the required temperature. This process usually takes more than 30 minutes and often requires protective sintering conditions like vacuum, inert atmospheres (such as N_2 or Ar), or reducing atmospheres (formic acid and H_2) to prevent oxidation of nanoparticles such as copper and platinum (Kim & Kim, 2010; Li, Li, Wang, Liu & Chen, 2016; Wünscher, Abbel, Perelaer & Schubert, 2014). Despite its wide usage, thermal sintering is limited by the high temperatures and long processing times, which hinder cost-effective scalable production and prevent the use of some flexible substrates popular in printed electronics, such as PET, polyethylene, and cellulose, due to their relatively low glass transition temperatures and limited thermal stability. More specific and expensive polymer substrates like PI or polyacrylate can be used as alternatives.

- **Electrical sintering:** involves applying an electric current across the printed region, leading to local heating within the ink by resistive energy dissipation (Joule effect) (Allen *et al.*, 2011; Allen, Aronniemi, Mattila, Alastalo, Ojanperä, Suhonen & Seppä, 2008). This method takes short sintering times (on the scale of milliseconds, depending on the printed area's geometry) and allows for instantaneous control/monitoring of the sintering procedure via current measurements. For effective sintering, the printed pattern must be slightly conductive to generate ohmic heating, involving some preprocessing steps like thermal curing to create initial conductance before applying electrical current (Roberson, Wicker & MacDonald, 2012). One way to perform electrical sintering is through direct contact with a DC current, providing direct feedback on the sintering progress and enabling optimization of the final conductivity by limiting the maximum current applied (Werner, Godlinski, Zöllmer & Busse, 2013). However, the need for direct contact throughout the process hinders industrial fabrication and is unsuitable for sintering large areas (Wünscher *et al.*, 2014).

- **Plasma sintering:** uses an ionized gas to decompose stabilizers and sinter printed patterns (Tendero, Tixier, Tristant, Desmaison & Leprince, 2006). Plasma can vary in characteristics by using different gases, such as inert gases (Ar, N_2), reducing gases (H_2), or oxidizing gases (O_2). However, only inert gases are typically used for flexible substrates, as oxidative and reductive gases can deform polymeric substrates. Plasma sintering manifests a skin effect,

making it difficult to sinter the bottom layers of printed materials quickly and effectively, usually requiring at least 30 minutes.

- **Photonic sintering:** is a promising alternative, using lasers, flashlights, and other photon sources to provide energy to the material (Niittynen, Abbel, Mäntysalo, Perelaer, Schubert & Lupo, 2014). This process can be cataloged by radiation wavelengths: infrared (IR), visible (intense photonic flash), and ultraviolet (UV). Intense pulsed light (IPL) uses a xenon lamp to emit radiation selectively absorbed by printed arrays, sintering metallic nanoparticles to create conductive paths without significantly impacting plastic substrates due to its short processing time (Gerlein, Benavides-Guerrero & Cloutier, 2024; Lim, Kim, Jang & Lim, 2017). Photonic technologies are typically effective in material sintering when selected based on the following criteria: using a specific wavelength to which the target nanostructured material selectively responds, successfully manipulating and controlling the irradiation parameters, and employing specific photo-responsive chemical agents. Intense pulsed light (IPL), also known as flash lamp annealing (FLA), utilizes a xenon lamp that emits radiation in the 200 to 1200 nm range. The energy emitted as photons is selectively absorbed by printed arrays, sintering metallic nanoparticles to form conductive paths. Usually, IPL has minimal impact on plastic substrates due to its short processing time (Dexter, Gao, Bansal, Chang & Malhotra, 2018).

- **Laser sintering:** utilizes a focused laser beam and can be implemented using either pulsed lasers or continuous wave (CW) lasers. Lasers can rapidly induce temperatures up to 500 °C, making this technique suitable for thermally stable substrates such as PI, silicon, or glass (Shou, Mahajan, Ludwig, Yu, Staggs, Huang & Pan, 2017). However, (Park, Jeong, Lee, Lee, Seok, Yang, Choi & Kang, 2016) demonstrated the effectiveness of NIR-laser sintering for Cu nanoparticles produced by spin-coating on various polymeric substrates, including PEN, PET, and PI. Infrared (IR) technology, through irradiation in the NIR to MIR range (700 – 15,000 nm), facilitates contactless and selective sintering and drying of printed metallic patterns. The primary advantage of IR sintering is its short sintering time, typically 2-15 seconds, which enables the sintering of metallic nanoparticles printed on thermally sensitive paper.

The main benefits of photonic sintering include fast processing, scalability, and operation under ambient conditions, making it an attractive manufacturing solution for nanoparticle sintering in applications like RFID tags, flexible electronics, sensors, and solar cells (Mo *et al.*, 2019a).

- **Microwave sintering:** achieves efficient sintering of metal nanoparticles printed on paper and plastic substrates through rapid heating of printed conductive tracks. Theoretically, this sintering process is explained by the Maxwell-Wagner effect (Vu, Teyssedre, Le Roy & Laurent, 2017), where the interaction between conductive particles and microwave radiation leads to charge accumulation at the material's interface, electric conduction, and the formation of eddy currents (Beedasy & Smith, 2020). Unlike traditional sintering, microwave sintering relies on a distinct heating process influenced by several parameters, including the material's physicochemical properties, environmental conditions, and boundary conditions (Awotunde, Adegbenjo, Obadele, Okoro, Shongwe & Olubambi, 2019). The effectiveness of microwave sintering for metals is largely determined by the thickness of the conductive track, as metals have a limited penetration depth for microwave radiation (1-2 μm at 2.54 GHz) (Cummins & Desmulliez, 2012). This technique is particularly beneficial for polymeric substrates, which are mostly transparent to microwave radiation, thereby minimizing substrate damage (Sun, Wang & Yue, 2016). Additional advantages of microwave heating include selective material heating, short processing times, non-contact heating, the ability to treat waste in situ, and lightweight equipment and processes (Grundas, 2011).

- **Chemical sintering:** methods involve the removal of the protective shell from nanoparticles using chemical substances, making it an effective sintering process. Some methods rely on the decomposition and oxidation of the protective agent, but most follow a colloid chemistry approach: desorption of the protective layer followed by the coalescence of metallic nanoparticles. This method can be performed at room temperature. Key advantages of this post-treatment process include its simplicity, suitability for light- and heat-sensitive substrates, and the elimination of expensive equipment, enabling the production of conductive printed patterns at room temperature. Chemical sintering can also involve adding chemicals

to previously printed ink to convert non-conductive behavior into a conductive response. Different types of inks, such as nanoparticles-based, metal-organic dielectrics, and salt inks, require various sintering methodologies, leading to multiple technological approaches (Kamyshny & Magdassi, 2019; Vaseem, Lee, Kim & Hahn, 2016).

2.5.2 Annealing

Similar to sintering methods, annealing processes are post-printing techniques crucial for achieving the final electrical conductivity of printed paths. Annealing is widely used to enhance the optical and structural properties of thin films in the semiconductor industry, particularly in the fabrication of solar cells, transistors, and other technological devices (Park, Kang & Kim, 2020a). Unlike sintering, which fuses isolated particles together, annealing often relieves internal stresses in materials and is applied to metallic oxide films to activate their semiconducting properties. Annealing temperatures above 350 °C are necessary to remove any organic residues (Park *et al.*, 2020a). In this process, the material is heated, held at a suitable temperature for a specified duration, and then cooled, typically to room temperature. Thermal annealing is conducted on a hot plate or inside a furnace, where the material can be exposed to a controlled gas environment such as N_2, H_2, or Ar in a vacuum to manage the oxidation process (Yuan, Liu, Li, Li, Cao, Su, Cheng, Yuan, Zhang & Li, 2017). Successful annealing post-treatments require controlling three main variables: the applied temperature, the duration of exposure to this temperature, and the gas environment during the process. These parameters significantly influence the electronic performance of printed metal oxide films by affecting chemical conversion, metal-oxide-metal bond formation, densification, and crystallization, which are generally associated with higher dielectric constants and the film's refractive index.

Thermal annealing is also employed for semiconducting carbon-based nanoparticles like graphene and carbon nanotubes to remove solvents, binders, or surfactant components, which reduces the film's thickness and sheet resistance (Calabrese, Pimpolari, Conti, Mavier, Majee, Worsley, Wang, Pieri, Basso, Pennelli et al., 2020; Horike, Fukushima, Saito, Koshiba, Morimoto, Misaki & Ishida, 2018; Xu, Zhao, Pecunia, Xu, Zhou, Dou, Gu, Lin, Mo, Zhao et al., 2017). In

some instances, annealing is used to convert graphene oxide (GO) into reduced graphene oxide (rGO). For example, Huang, Tang, Guo, Feng, Zhang, Li, Qian & Xie (2020) demonstrated that ink-jetted GO layers annealed at 600 °C in a N_2 atmosphere yielded conductive rGO patterns with an electrical conductivity of 2.58×10^2 S/m. High-temperature annealing is essential for oxide films to transition from a sol to a gel state, which limits its use with flexible substrates due to the risk of cracking from thermal expansion incompatibilities. Consequently, there has been considerable effort to lower annealing temperatures by modifying the precursors and solvents in the fabrication process. Additionally, alternative annealing methods such as microwave, UV-assisted, and Laser Spike Annealing (LSA) have been developed.

2.6 Characterization Techniques

In order to fabricate an efficient and reliable sensor, we must first fundamentally understand the materials properties, its interaction with applied stimuli and analyze the physical phenomena that drive the changes observed. These can be achieved by various analytical tools and techniques. During the course of this PhD research project, we have employed several important techniques ranging form optical and electron beam based microscopy, light based spectroscopy and elmental chemical analysis. In this section we detail the operating principles, advantages and limitations of four of the most important techniques used namely Electron Backscatter Diffraction (EBSD), X-ray Photoelectron Spectroscopy (XPS), Raman Spectroscopy and Fourier Transform Infrared Spectroscopy (FTIR).

2.6.1 EBSD - Electron Backscatter Diffraction

Electron Backscatter Diffraction (EBSD) is a microstructural-crystallographic technique utilized in scanning electron microscopy (SEM) to examine the crystallographic orientation of materials. This technique is pivotal for understanding the texture and grain structure of crystalline materials, providing essential insights into material properties and behavior.

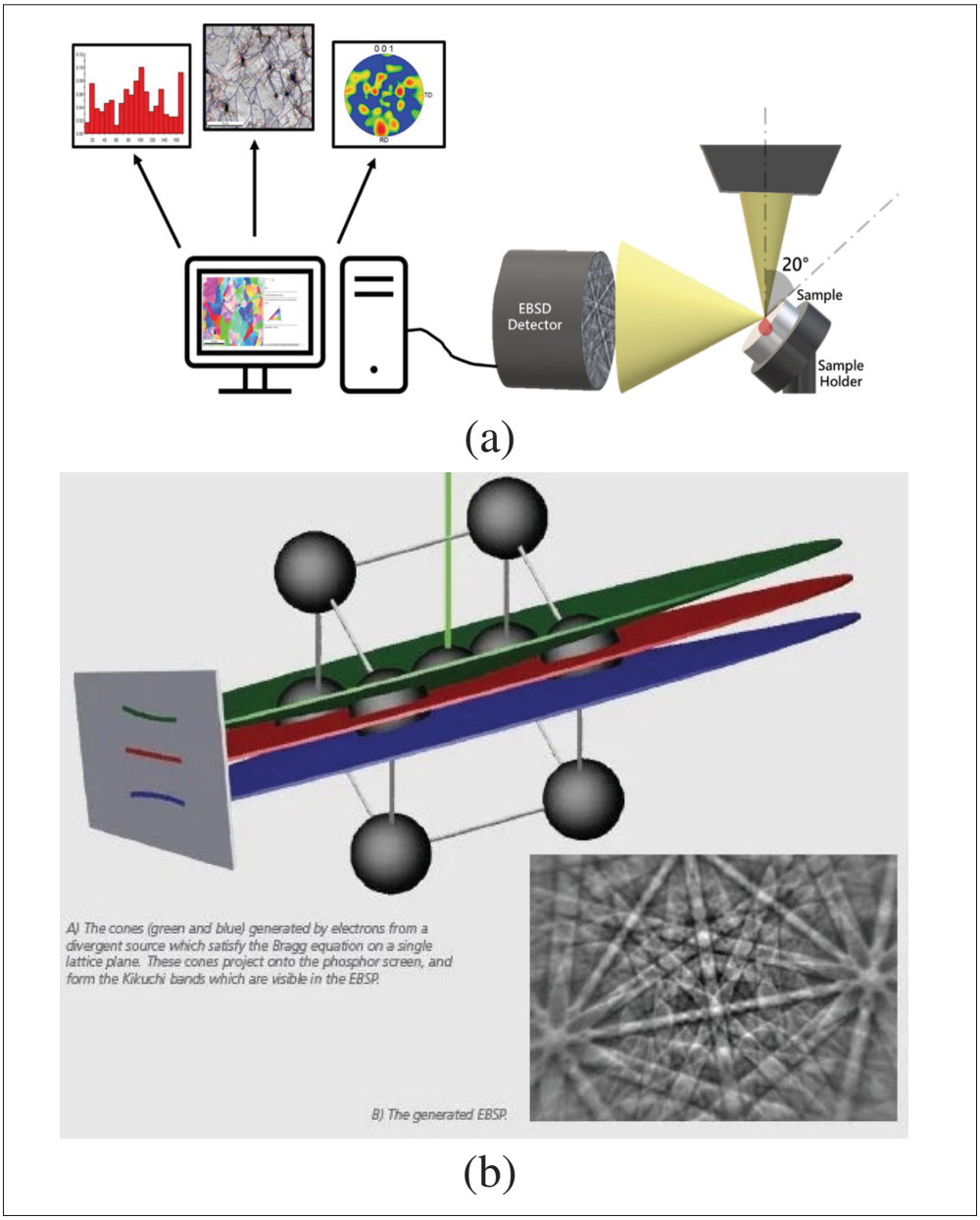

Figure 2.7 (a) Experimental setup in FE-SEM for EBSD analysis, (b) Kikuchi pattern formation in EBSD
Taken from (ebs, 2015; Carneiro & Simões, 2020)

Figure 2.7 illustrates the data acquisition setup and data interpretation involved in EBSD analysis. The SEM operates at an accelerating voltage typically between 10-30 kV. The electron beam interacts with the sample surface, producing a cloud of backscattered electrons (Figure 2.7 a)). These electrons are diffracted by the crystal planes and form a diffraction pattern (kikuchi

patterns) on the phosphor screen (Figure 2.7 b)). The pattern is then captured by the CCD camera and analyzed to determine the crystallographic information. Electrons are scattered elastically and in-elastically. The elastically scattered electrons undergo diffraction according to Bragg's law, which describes the condition for constructive interference of scattered waves (Equation 2.1):

$$n\lambda = 2d \sin\theta \tag{2.1}$$

Here, n is the order of reflection, λ is the wavelength of the electrons, d is the interplanar spacing of the crystal, and θ is the angle of incidence. The diffraction of backscattered electrons produces a pattern of Kikuchi lines, which are characteristic of the crystal structure and orientation. These patterns are captured by a phosphor screen and a CCD camera positioned within the SEM. The diffraction pattern is analyzed using software to identify the crystallographic planes and orientations. This involves comparing the experimental patterns with theoretical patterns generated from known crystal structures. The indexed patterns are then used to construct orientation maps, where each pixel corresponds to a specific crystallographic orientation. These maps provide detailed information about the texture and grain structure of the material. Advanced software algorithms play a crucial role in pattern indexing and orientation mapping. These algorithms utilize databases of crystal structures and apply mathematical techniques such as Hough transforms to accurately identify and index the diffraction patterns.

Applications:

- **Grain Boundary Characterization:** Identifying the nature and distribution of grain boundaries, including special boundaries like twin boundaries.
- **Phase Identification:** Differentiating between different crystallographic phases in multiphase materials.
- **Strain and Deformation Analysis:** Investigating strain distribution and deformation mechanisms in materials subjected to mechanical stress.

Advantages:

- **High Spatial Resolution:** EBSD can achieve spatial resolutions down to nanometer scales, enabling detailed examination of microstructures.
- **Quantitative Analysis:** Provides quantitative information on crystallographic orientations and grain boundary characteristics.
- **Non-Destructive:** EBSD is a non-destructive technique, preserving the sample for further analysis.stress.

Limitations:

- **Surface Preparation:** Requires meticulous surface preparation to obtain high-quality diffraction patterns. Surface roughness and contamination can degrade the patterns.
- **Sample Constraints:** Works best with crystalline materials and may not be applicable to amorphous materials.
- **Time-Consuming:** Data acquisition and analysis can be time-consuming, especially for large areas or high-resolution mapping.

2.6.2 XPS - X-ray Photoelectron Spectroscopy

X-ray Photoelectron Spectroscopy (XPS), also known as Electron Spectroscopy for Chemical Analysis (ESCA), is a powerful analytical technique for investigating the surface chemistry of materials. XPS provides quantitative and qualitative information about the elemental composition, chemical state, and electronic state of the elements within a material. Since its development by Kai Siegbahn in the 1960's, XPS has become an essential tool in material science, chemistry, and surface engineering. Figure 2.8 a) depicts the process schematic of the XPS system. The core principle of XPS is based on the photoelectric effect, first described by Albert Einstein in 1905. In XPS, when a material is irradiated with monochromatic X-rays, photoelectrons are ejected from the surface atoms of the material (Figure 2.8 b)). The kinetic

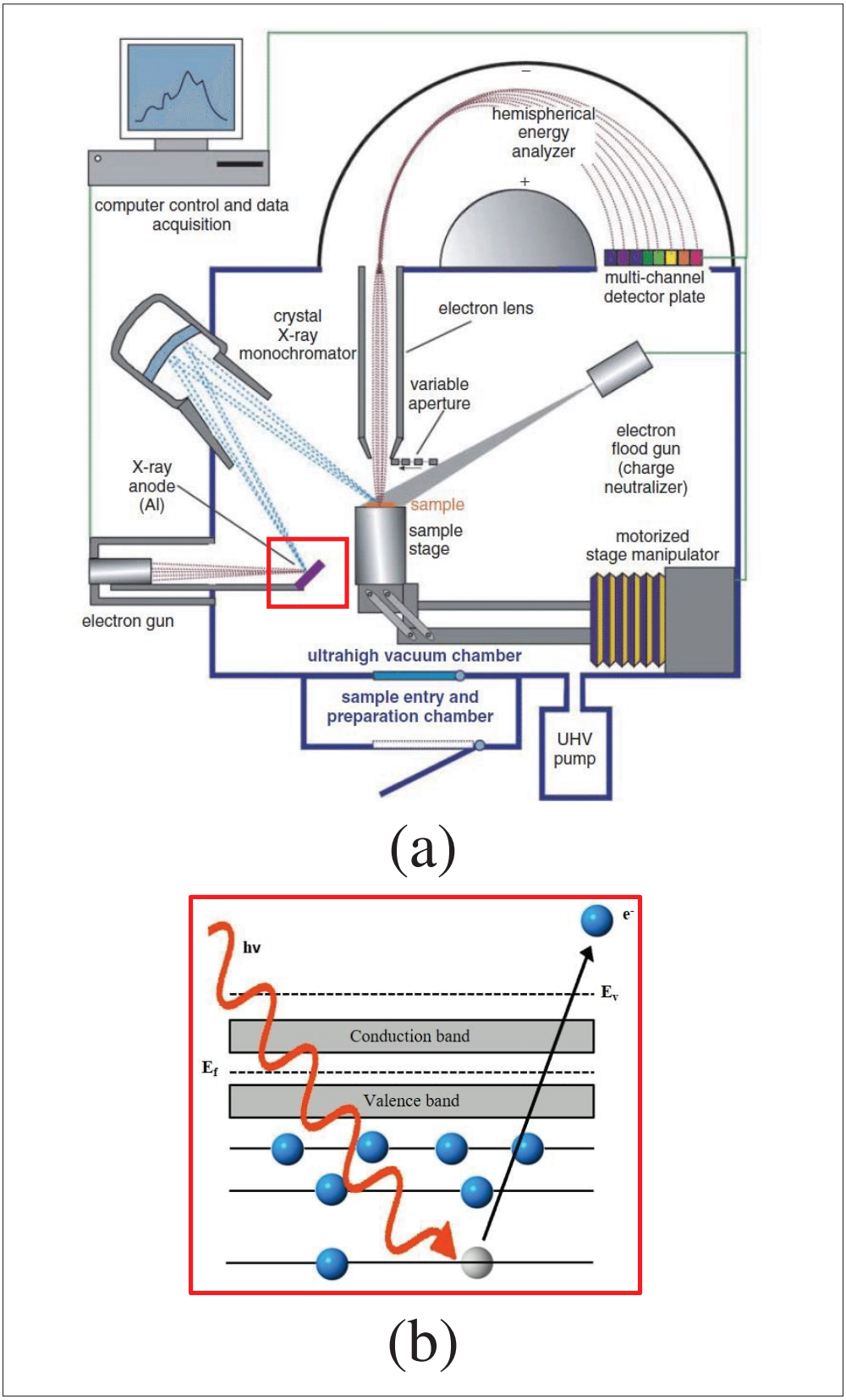

Figure 2.8 (a) XPS experimental setup (b) schematic representation of XPS mechanism Taken from (ebs, 2015; Carneiro & Simões, 2020)

energy of these emitted photoelectrons is measured, providing information about the binding energies of the electrons within the atoms of the sample. The interaction of X-ray photons with atoms leads to the ejection of core electrons if the photon energy ($h\nu$) exceeds the binding energy (E_b) of the electrons. This process can be expressed as (Equation 2.2):

$$h\nu = E_k + E_b + \phi \tag{2.2}$$

where:

- $h\nu$ is the energy of the incident X-ray photon,
- E_k is the kinetic energy of the emitted photoelectron,
- E_b is the binding energy of the electron,
- ϕ is the work function of the spectrometer (the energy required to bring the electron to the vacuum level).

By measuring the kinetic energy E_k of the photoelectrons, the binding energy E_b can be determined. Each element has unique binding energies for its core electrons, allowing for precise elemental identification.

A typical XPS system comprises several key components:

- **X-ray Source:** Commonly, Al $\kappa\alpha$ (1486.6 eV) or Mg $\kappa\alpha$ (1253.6 eV) X-ray sources are used. These provide monochromatic X-rays necessary for the ejection of core electrons.
- **Ultra-High Vacuum (UHV) Chamber:** The sample is placed in a UHV environment to prevent the emitted photoelectrons from colliding with gas molecules, which could scatter the electrons and reduce the resolution and accuracy of the measurements.
- **Electron Energy Analyzer:** This component measures the kinetic energy of the photoelectrons. The hemispherical electron energy analyzer is commonly used for its high resolution and efficiency in energy discrimination.

- **Detector:** The detector counts the number of electrons at each kinetic energy, producing a spectrum of intensity versus kinetic energy. Modern detectors often use multichannel arrays to increase data acquisition speed and sensitivity.

The XPS spectrum consists of peaks corresponding to the binding energies of core electrons from different elements in the sample. Moreover, XPS is highly surface-sensitive due to the short mean free path of the emitted photoelectrons (typically 1-10 nm). This makes it ideal for studying surface compositions and thin films. For depth profiling, an ion sputtering process is used to sequentially remove layers of the material, allowing analysis at various depths. Analyzing these peaks provIDE's critical information:

- **Elemental Identification:** Each element has a set of characteristic binding energies, allowing for precise identification of the elements present on the surface.
- **Chemical State Analysis:** The binding energy of core electrons is influenced by the chemical environment of the atoms. Chemical shifts in binding energy can reveal different oxidation states and types of chemical bonding.
- **Quantitative Analysis:** The intensity of the peaks (area under the peaks) is proportional to the number of atoms contributing to that peak. By comparing the peak areas, the relative atomic concentration of elements can be determined.

Applications:

- **Material Science:** Characterizing surface composition and chemistry of materials, thin films, and coatings.
- **Catalysis:** Understanding the chemical states and compositions of catalyst surfaces, crucial for catalytic activity studies.
- **Semiconductors:** Analyzing chemical composition of semiconductor surfaces and interfaces, important for device fabrication and performance.

- **Corrosion Studies:** Investigating corrosion products, oxide layers, and protective coatings on metals.
- **Polymers and Organic Materials:** Studying surface chemistry of polymers and organic films, essential for applications in electronics, coatings, and biomedical devices.

Advantages:

- **Surface Sensitivity:** Provides detailed information about the top few nanometers of the material's surface.
- **Chemical State Information:** Ability to differentiate between different oxidation states and chemical environments.
- **Quantitative Analysis:** Allows for the quantitative determination of elemental composition.
- **Non-Destructive:** Generally, the analysis is non-destructive, preserving the sample for further studies.

Limitations:

- **Surface Sensitivity:** While beneficial for surface studies, it limits the analysis to the very surface, which may not represent the bulk material.
- **Vacuum Requirement:** The necessity for ultra-high vacuum conditions can be a constraint for certain samples, particularly those that are volatile or sensitive to vacuum
- **Complex Data Interpretation:** Interpreting XPS spectra can be complex, requiring careful deconvolution of overlapping peaks and consideration of background signals.

2.6.3 Raman Spectroscopy

Raman spectroscopy is a powerful analytical technique used to study vibrational, rotational, and other low-frequency modes in a system. Named after Indian physicist C.V. Raman, who discovered the Raman effect in 1928, this technique relies on inelastic scattering of

monochromatic light, usually from a laser in the visible, near-infrared, or near-ultraviolet range. The process provides a molecular fingerprint of the material, making it invaluable in various fields such as chemistry, materials science, and biology. The fundamental principle behind Raman spectroscopy is the interaction between light and matter, particularly the inelastic scattering of photons by molecules. When a photon encounters a molecule, it can be absorbed, transmitted, or scattered. In most cases, scattering occurs elastically, known as Rayleigh scattering, where the scattered photons have the same energy (and thus wavelength) as the incident photons. However, a small fraction of the light (about 1 in 10 million photons) is scattered inelastically, where the scattered photons have a different energy due to the exchange of energy with vibrational modes in the molecule. This inelastic scattering is termed the Raman effect.

The Raman effect can be described using quantum mechanics. When incident photons from the laser interact with the molecules, they can excite the molecules from their ground vibrational state to a virtual energy state, which is a non-real, short-lived state. The molecule can then relax back to a different vibrational state, emitting a photon in the process. The energy difference between the incident photon and the scattered photon corresponds to the energy difference between the initial and final vibrational states of the molecule. The energy shifts observed in Raman scattering provide information about the vibrational modes of the molecules, which can be used to identify and characterize materials. There are two types of inelastic scattering in Raman spectroscopy as represented in Figure 2.9 a):

- **Stokes Scattering:** Here, the molecule gains energy from the incident photon, resulting in scattered photons with lower energy (longer wavelength) than the incident photons. This is more commonly observed because most molecules are initially in their ground vibrational state.

- **Anti-Stokes Scattering:** In this case, the molecule loses energy to the incident photon, resulting in scattered photons with higher energy (shorter wavelength). This is less common as it requires the molecules to be in an excited vibrational state initially.

A typical Raman spectrometer consists of several key components as seen in Figure 2.9 b):

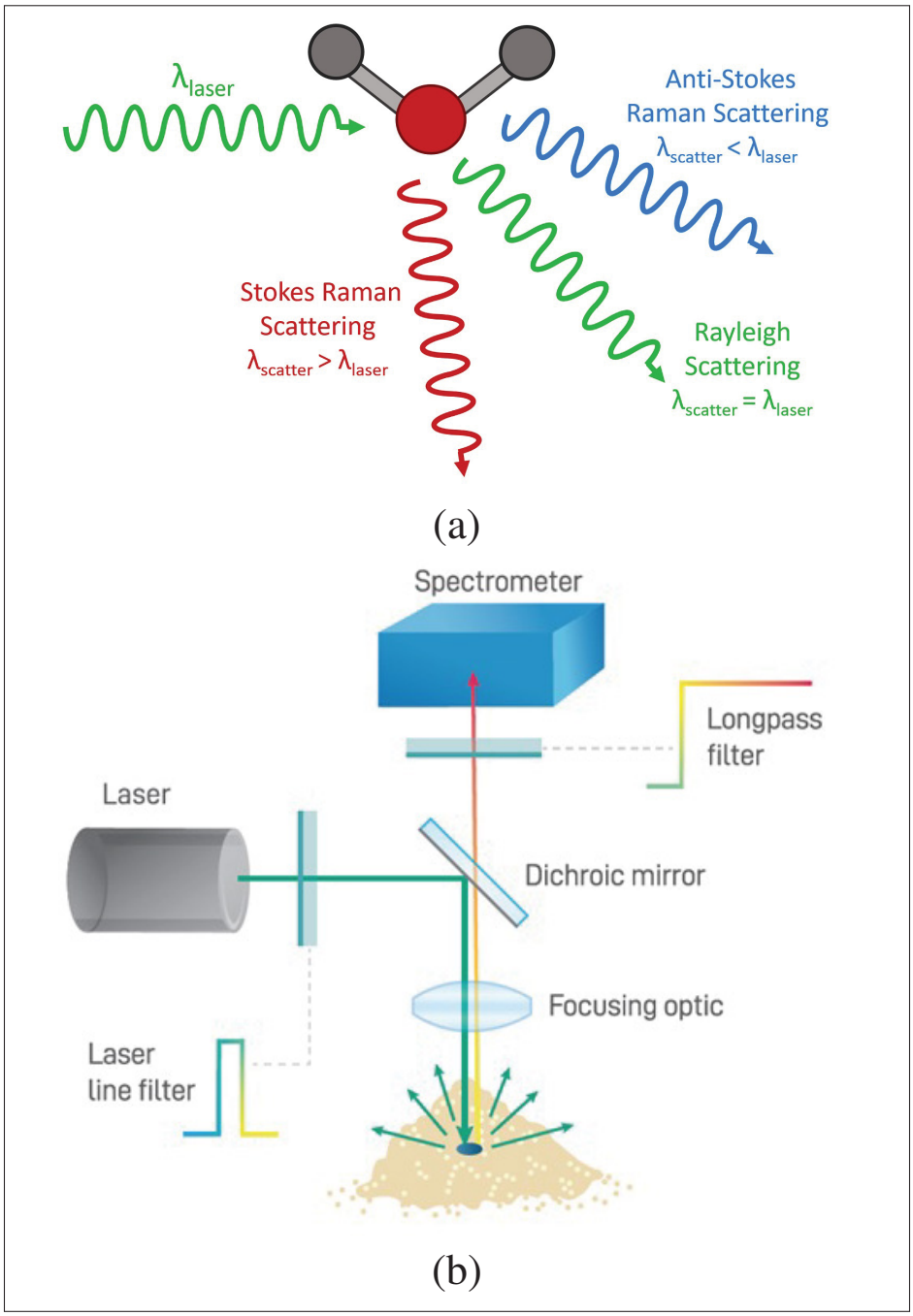

Figure 2.9 (a) Raman scattering mechanism (b) Raman spectrometer setup
Taken from (Instruments; Photonics)

- **Laser Source:** The laser provides monochromatic light, usually in the visible, near-infrared, or near-ultraviolet range. Common laser sources include Argon ion lasers, Krypton ion lasers,

and diode lasers. The choice of laser wavelength depends on the sample and the desired resolution and sensitivity.

- **Sample Illumination System:** The laser light is focused onto the sample using lenses or mirrors. The sample can be in various forms, such as solid, liquid, or gas.

- **Collection Optics:** Scattered light from the sample is collected and directed to a spectrometer. This is typically done using lenses or fiber optics.

- **Spectrometer:** The spectrometer disperses the scattered light into its constituent wavelengths. This can be done using a diffraction grating, prism, or other dispersive elements.

- **Detector:** The dispersed light is detected and measured. Common detectors include charge-coupled devices (CCDs) and photomultiplier tubes (PMTs).

The result of a Raman spectroscopic measurement is a Raman spectrum, which is a plot of intensity versus Raman shift. The Raman shift is usually expressed in wavenumbers (cm^{-1}) and is given by the difference between the incident and scattered photon energies. Each peak in the Raman spectrum corresponds to a specific vibrational mode of the molecule, providing a molecular fingerprint that can be used for identification and characterization.

Applications:

- **Chemical Identification:** Raman spectroscopy can be used to identify unknown substances by comparing their spectra to reference spectra.

- **Material Science:** It is used to study the composition, structure, and properties of materials, including polymers, nanomaterials, and semiconductors.

- **Biology and Medicine:** Raman spectroscopy is employed in the study of biological molecules, cells, and tissues. It is also used in medical diagnostics, such as identifying cancerous tissues.

- **Pharmaceuticals:** The technique is used for quality control and characterization of pharmaceutical products, including the identification of polymorphs.

- **Environmental Science:** Raman spectroscopy can detect and quantify pollutants and study environmental samples.

Raman spectroscopy offers several advantages:

- **Non-destructive:** It does not require extensive sample preparation and preserves the sample.
- **High Specificity:** Provides detailed information about molecular vibrations, making it highly specific for molecular identification.
- **Minimal Interference from Water:** Raman scattering from water is weak, making it suitable for studying aqueous solutions.

However, it also has some limitations:

- **Weak Signal:** The Raman effect is inherently weak, requiring sensitive detectors and powerful laser sources.
- **Fluorescence Interference:** Fluorescence from the sample or impurities can overwhelm the Raman signal.
- **Laser Damage:** High-intensity laser light can damage sensitive samples.

2.6.4 Fourier Transform Infrared Spectroscopy (FTIR)

FTIR is a powerful analytical technique used to obtain the infrared spectrum of absorption or emission of a solid, liquid, or gas. FTIR spectroscopy is widely utilized in various fields including chemistry, biology, and materials science due to its ability to provide detailed information about molecular composition and structure. The fundamental principle of FTIR is based on the absorption of infrared radiation by molecules. When a molecule absorbs infrared radiation, it undergoes transitions between vibrational energy levels. Different bonds and functional groups within a molecule absorb characteristic frequencies of IR radiation, leading to a unique spectrum that acts as a molecular fingerprint.

Components of an FTIR Spectrometer (Figure 2.10):

- **Infrared Source:** A stable, broad-spectrum IR source, such as a Globar (silicon carbide) or Nernst glower, emits continuous infrared radiation.
- **Interferometer:** The core component of an FTIR spectrometer is the interferometer, typically a Michelson interferometer. It splits the IR beam into two paths using a beam splitter. One path reflects off a stationary mirror, and the other reflects off a movable mirror. The two beams recombine, causing interference, which results in an interferogram—a signal that contains information across all IR frequencies.
- **Sample Compartment:** The combined beam passes through or reflects off the sample. The sample absorbs specific wavelengths of the IR radiation, creating a unique absorption pattern.
- **Detector:** The remaining IR radiation reaches the detector. Common detectors include deuterated triglycine sulfate (DTGS) for general purposes or mercury cadmium telluride (MCT) for high sensitivity. The detector measures the intensity of the IR radiation as a function of its wavelength.
- **Fourier Transform Algorithm:** The computer processes the interferogram using a mathematical Fourier transform to convert it into an IR spectrum, representing intensity versus wavenumber (cm^{-1}).

In the interferometer, the IR beam is split by a beam splitter into two beams that travel different paths. The movable mirror alters the path length of one beam, causing a phase shift relative to the other beam. When the beams recombine, they interfere constructively or destructively depending on the difference in path length. This interference pattern is recorded as an interferogram, which contains information about all wavelengths in the IR spectrum simultaneously. The Fourier transform is a mathematical operation that decomposes the interferogram into its constituent sine and cosine waves. The resulting spectrum reveals the intensity of IR radiation as a function of frequency. The process involves several steps:

- **Data Acquisition:** The interferogram is digitized and recorded.

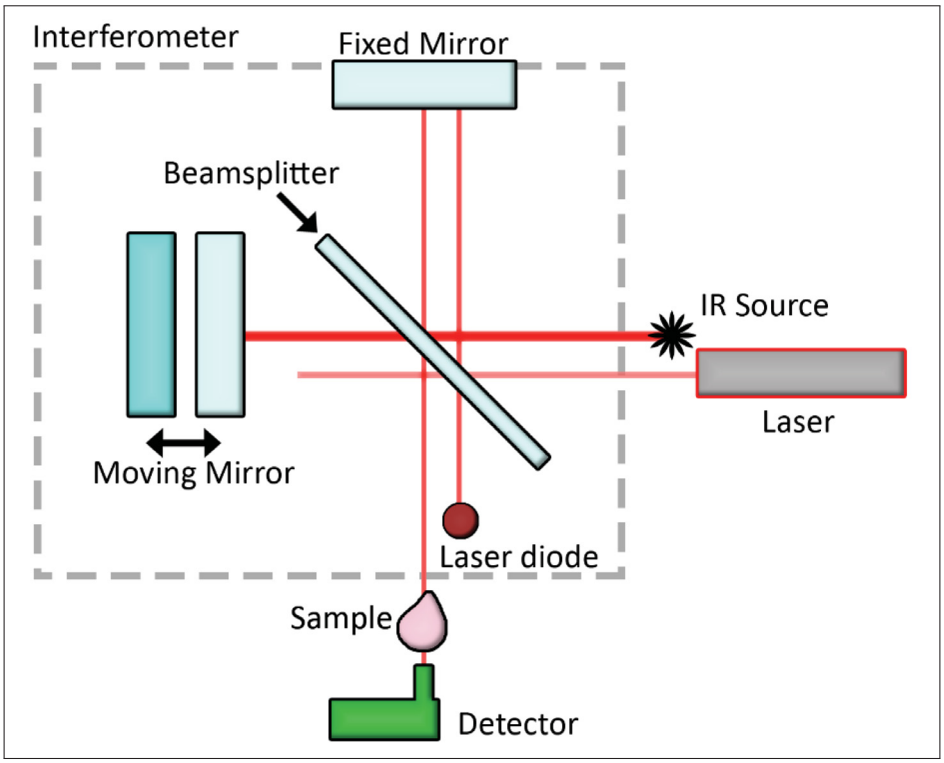

Figure 2.10 FTIR spectrometer setup
Taken from (Delfino *et al.*, 2021)

- **Fourier Transformation:** The computer applies the Fourier transform algorithm to convert the time-domain interferogram into a frequency-domain spectrum.
- **Phase Correction:** Phase errors are corrected to ensure an accurate spectrum.
- **Baseline Correction and Apodization:** These processes remove background noise and smooth the spectrum.

Applications:

FTIR spectroscopy is employed in numerous applications:

- **Chemical Analysis:** Identifying chemical compounds and functional groups in organic and inorganic substances.
- **Pharmaceuticals:** Quality control and identification of active pharmaceutical ingredients.

- **Environmental Monitoring:** Detecting pollutants and analyzing air, water, and soil samples.
- **Materials Science:** Characterizing polymers, coatings, and nanomaterials.
- **Biology and Medicine:** Studying biological tissues, cells, and macromolecules.

Advantages:

- **Speed:** FTIR can collect spectral data rapidly because it measures all wavelengths simultaneously (Fellgett's advantage).
- **Sensitivity:** It provides higher signal-to-noise ratios due to the multiplex advantage, where all the detector's energy is used to measure the spectrum.
- **Precision:** The use of a laser as an internal reference ensures precise wavelength calibration.
- **Versatility:** FTIR can analyze a wide variety of sample types and states (solid, liquid, gas).

2.7 Device integration

Electrodes play a crucial role in printed sensing devices, as they form the interface between the sensor and external circuits, enabling signal transmission. In resistive sensing devices, the electrode material and design directly influence the sensor's sensitivity, response time, and overall performance (Al-Qahtani, Ali, Khan & Bermak, 2023). For instance, the choice of electrode material impacts the electrical conductivity and chemical stability of the sensor. Materials like silver, gold, and carbon-based inks are commonly used for printed electrodes due to their high conductivity, flexibility, and ease of integration into various substrates through additive manufacturing processes such as screen printing etc (Claudel, Ngo, Kourtiche & Nadi, 2020).

The geometry of the electrodes, including their shape, spacing, and surface area, significantly affects the sensing mechanism. Proper electrode design also helps in minimizing parasitic resistances and ensuring uniform electric field distribution across the sensing layer (Ali, Khan & Bermak, 2019). Additionally, the stability of the electrodes under operational conditions,

such as mechanical stress and environmental factors, is paramount for the long-term durability of the sensing device. Electrode degradation or delamination can lead to sensor failure, thus making material choice and fabrication quality critical for the device's reliability.

2.7.1 Interdigitated electrodes (IDE's)

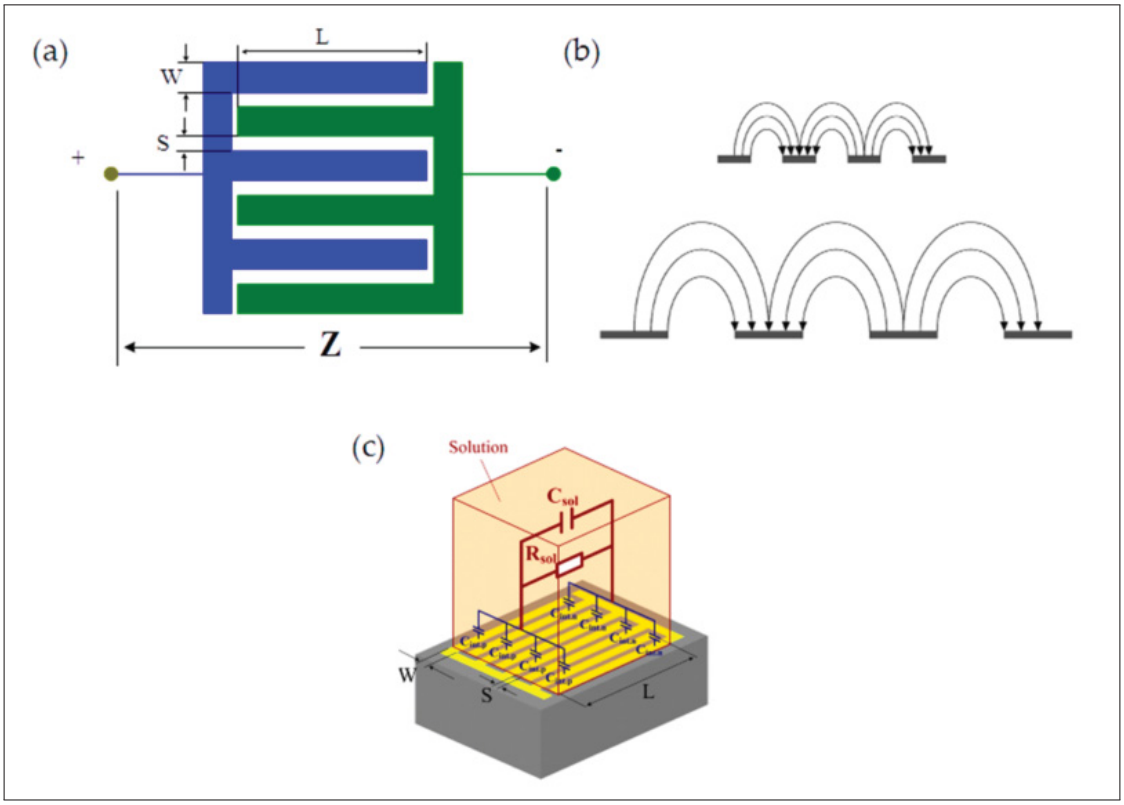

Figure 2.11 (a) Geometrical specifications of interdigitated sensors (b) Flow of electric current between the electrodes (c) Electrical representation of interdigitated electrodes in printed physical sensors
Taken from (Claudel *et al.*, 2020)

Interdigitated electrodes (IDE's) are widely used in printed sensing devices due to their ability to provide high sensitivity, ease of fabrication, and versatility across various sensing applications. IDE's consist of two sets of comb-like electrodes arranged in an interlocking pattern on a substrate (Abbas, 2020). This configuration increases the surface area for interaction between the electrodes and the sensing material, enhancing the sensitivity of the device. In printed

sensing devices, IDE's are typically fabricated using conductive inks or pastes through printing techniques such as inkjet printing, screen printing, or aerosol jet printing, which makes them attractive for low-cost, flexible, and scalable sensor fabrication.

- **IDE design considerations:** Figure 2.11 a) illustrates the typical design of IDE electrodes where key design parameters such as electrode length (L) width (W), gap spacing (S), and the number of electrode fingers directly affect the sensor's performance Alexander Jr, Price & Bhansali (2010). Reducing the gap spacing between the electrodes minimizes the distance over which the sensing material bridges the electrodes, leading to greater sensitivity. Smaller gaps result in a higher likelihood of resistance changes in the material when exposed to the analyte, as the electric field between electrodes is intensified, promoting faster and more pronounced responses . Similarly, reducing the electrode width can increase sensitivity by concentrating the electric field, making the sensor more responsive to small changes in the material's resistivity due to interaction with the analyte (Ali *et al.*, 2019). The number of electrode fingers also affects sensitivity by increasing the effective sensing area. A higher number of fingers leads to more interaction points between the analyte and the sensing material, enhancing the signal generated by resistance changes . However, excessive fingers may lead to higher parasitic resistances, potentially diminishing the sensor's signal-to-noise ratio and overall performance.

- **Sensing mechanism:** As seen in Figure 2.11 b) and c) IDE's are used to measure changes in the electrical resistance of a sensing material placed between or on top of the electrodes. When exposed to an external stimulus such as gas, humidity, or temperature, the properties of the sensing material—typically a semiconducting or polymer material—change, which in turn alters the resistance across the IDE's (Park, Lee, Hwang & Cho, 2020b). The IDE pattern ensures a large effective sensing area and short diffusion path for the stimulus, improving the sensor's response time and sensitivity. Additionally, the IDE's allow for the detection of minute changes in resistance by maximizing the interaction between the electrodes and the sensing medium.

- **IDE applications:** In gas sensors, for example, metal oxide semiconductors such as SnO_2 or ZnO are often used as the sensing material, with the IDE's acting as electrodes to measure the changes in conductivity upon exposure to gases like CO, NO_2, or O_2 (Vinoth & Gopalakrishnan, 2020). The interdigitated geometry provides a large surface area for gas adsorption, which improves the detection limit and response time of the sensor. In humidity sensing, polymers such as polyimide or polyaniline are commonly used. These materials undergo changes in resistance when they absorb or release water molecules, which is easily detected by the IDE's. IDE-based humidity sensors are advantageous because they can be printed on flexible substrates, allowing for integration into wearable devices and environmental monitoring systems. Biosensors also benefit from the use of IDE's. In these devices, the electrodes are often functionalized with biomolecules such as enzymes, antibodies, or DNA probes, which interact with specific target molecules. Upon interaction, the electrical resistance between the IDE's changes, providing a direct measure of the presence and concentration of the target analyte. This approach is particularly useful for point-of-care diagnostics, where rapid, sensitive detection of biological markers is required.

The ease of fabricating IDE's with various printing technologies is one of their significant advantages in the development of low-cost, flexible, and scalable sensing devices. Printing techniques like screen printing, inkjet printing, and aerosol jet printing enable the deposition of conductive materials, such as silver or carbon-based inks, in the form of interdigitated patterns. As discussed earlier in this thesis, these methods allow for the precise control of electrode geometry, which is critical for optimizing sensor performance. Additionally, the ability to print on flexible substrates such as polyethylene terephthalate (PET) or polyimide makes IDE-based sensors suitable for applications in wearable electronics, flexible electronics, and large-area sensing networks.

2.7.2 Limitations of printed IDE's

IDE's are widely used in sensor applications due to their flexibility, low cost, and ease of integration with flexible substrates. A large majority of applications using printed physical

sensors tend to be used at room temperature or slightly elevated temperatures with are well with in the operational limits of the printed active sensing materials, substrate and printed IDE's. However, all three factions of printed sensors begin to fail under high temperature operations conditions typically beyond 200 °C to 300 °C. Assuming the substrate and printed active materials are rated to withstand high operational temperatures, the IDE's generally printed via conductive metals such as silver tend to fail due to factors such as grain growth and increased structural defects. Understanding these limitations is essential for optimizing the performance of IDE's in high-temperature applications. In the next sections we discuss the fundamental factors that lead to grain growth and its control via the Zener pinning mechanism which are critical to enhancing low temperature and cost silver inks for high temperature applications.

2.7.3 Grain growth

Grain growth in particle-based films is a critical phenomenon influencing the microstructure and, consequently, the properties of the materials. Understanding the mechanism of grain growth is essential for optimizing the performance of materials used in various applications, such as electronic devices, coatings, and structural components. Grain growth is a thermally activated process that occurs to reduce the overall energy of the system. It involves the movement of grain boundaries, which are regions of high energy due to the misalignment of crystallographic orientations between neighboring grains (Higgins, 1974). The primary driving force for grain growth is the reduction of total grain boundary energy, which decreases as the average grain size increases (Burke & Turnbull, 1952).

The kinetics of grain growth can be described by the following equation (Equation 2.3):

$$D^n - D_0^n = kt \tag{2.3}$$

where D is the grain diameter at time t, D_0 is the initial grain diameter, n is the grain growth exponent (typically ranging from 2 to 4), and k is a rate constant that depends on temperature and material properties .

Grain growth mechanism:

- **Normal grain growth:** Normal grain growth, also known as self-similar growth, occurs when the growth rate of grains is proportional to their size. This process is driven by the reduction in grain boundary energy and is typically observed in the absence of impurities, second-phase particles, or other inhibiting factors. The growth rate can be influenced by factors such as temperature and the presence of vacancies and dislocations (Louat, 1974).

- **Abnormal grain growth:** Abnormal grain growth, or secondary recrystallization, occurs when certain grains grow much larger than their neighbors. This can happen due to the presence of anisotropic grain boundary energies or because of specific orientations that have lower energy barriers for growth. Abnormal grain growth can lead to a bimodal grain size distribution and is often undesirable in applications requiring uniform microstructures (Najafkhani, Kheiri, Pourbahari & Mirzadeh, 2021).

- **Ostwald ripening:** Ostwald ripening is a process where larger grains grow at the expense of smaller grains. This occurs because larger grains have lower surface energy compared to smaller grains. The driving force for this mechanism is the reduction in the total surface energy of the system. Ostwald ripening is significant in systems where there is a considerable difference in grain sizes and can lead to coarsening of the microstructure over time (Voorhees, 1985).

Factors influencing grain growth:

- **Temperature:** Temperature is a crucial factor influencing the rate of grain growth. Higher temperatures increase the mobility of atoms and grain boundaries, accelerating grain growth. The relationship between temperature and grain growth rate is often described by an Arrhenius-type Equation 2.4:

$$k = k_0 \exp\left(-\frac{Q}{RT}\right) \tag{2.4}$$

  where k_0 is a pre-exponential factor, Q is the activation energy for grain boundary migration, R is the gas constant, and T is the absolute temperature (Chen, Chen, Su, He, Tan, Xu, Huang, Dai & Lu, 2022).

- **Time:** Grain growth is a time-dependent process. The longer the material is held at an elevated temperature, the more significant the grain growth. The grain growth exponent n provides insights into the dominant mechanism of grain growth and the influence of time on the process.

- **Impurities and secondary-phase particles:** The presence of impurities and second-phase particles can hinder grain growth by pinning grain boundaries. This phenomenon, known as Zener pinning, is described by the Zener Equation 2.5:

$$R = \frac{\gamma}{fP} \tag{2.5}$$

  where R is the grain radius, γ is the grain boundary energy, f is the volume fraction of the second-phase particles, and P is the pinning pressure exerted by the particles. Zener pinning is critical in controlling grain size in many industrial materials (Najafkhani *et al.*, 2021).

- **Initial grain size and distribution:** The initial grain size and distribution play a significant role in the grain growth process. Materials with a wide grain size distribution tend to exhibit faster grain growth due to the presence of smaller grains that are more susceptible to Ostwald ripening.

Grain growth in particle based films:

In metal films, such as those made from silver or gold, grain growth is influenced by factors like deposition method, substrate interaction, and thermal annealing. For instance, in silver films, grain growth can be accelerated by thermal treatments, leading to enhanced electrical conductivity and mechanical properties. Ceramic films, such as those made from zirconia or alumina, exhibit grain growth behaviors that are significantly influenced by sintering temperatures and the presence of dopants. Dopants can either enhance or inhibit grain growth depending on their nature and concentration. In polycrystalline thin films used in solar cells and other electronic devices, grain growth is critical for improving carrier mobility and overall device efficiency. Techniques such as post-deposition annealing and controlled cooling rates are employed to optimize grain size and orientation (Thompson & Carel, 1996a).

2.7.4 Zener Pinning

The Zener pinning mechanism, named after physicist Clarence Zener, is a crucial phenomenon in materials science that plays a significant role in the stabilization of microstructures during thermal treatments. This mechanism involves the interaction between dispersed second-phase particles and the grain boundaries in polycrystalline materials. By hindering the movement of these boundaries, Zener pinning contributes to the refinement and stabilization of grain structures, which is essential for improving mechanical properties in various engineering applications (Shahandeh & Militzer, 2013).

Fundamentals of Zener Pinning:

Grain growth in polycrystalline materials occurs because of the reduction in total grain boundary energy, which drives the system towards a lower-energy state. This results in a coarser microstructure, which can adversely affect the material's mechanical properties, such as strength and toughness. Zener pinning occurs when inert second-phase particles are introduced into the matrix. These particles, which do not dissolve into the matrix, interact with the grain boundaries, exerting a pinning force that opposes the boundary movement. The effectiveness of Zener

pinning depends on several factors, including the size, distribution, and volume fraction of the particles.

Mathematical Description of Zener Pinning:

The classic Zener pinning model provides a quantitative description of the pinning force exerted by the particles. The pinning pressure P_z exerted by a uniform distribution of spherical particles can be expressed as (Equation 2.6):

$$P_z = \frac{3\gamma f}{2r} \tag{2.6}$$

where: - γ is the grain boundary energy, - f is the volume fraction of the second-phase particles, - r is the radius of the particles.

This equation indicates that the pinning pressure is directly proportional to the volume fraction of particles and inversely proportional to their size. Therefore, a higher volume fraction and smaller particle size enhance the pinning effect (Hazzledine & Oldershaw, 1990).

Influence of Particle Characteristics:

The size, distribution, and shape of the particles significantly influence the effectiveness of Zener pinning. Smaller particles are more effective in pinning grain boundaries because they provide a larger total surface area for interaction. However, extremely small particles might dissolve or coarsen during high-temperature treatments, reducing their pinning efficiency. The spatial distribution of particles also plays a crucial role. A uniform distribution ensures a consistent pinning force across the grain boundaries. In contrast, clustering of particles can create regions with insufficient pinning, allowing localized grain growth. Additionally, non-spherical particles can offer more complex interactions with the grain boundaries, potentially enhancing the pinning effect depending on their orientation and morphology.

Applications of Zener Pinning:

Zener pinning is widely utilized in various metallurgical processes to control the grain structure of metals and alloys. Some notable applications include:

- **Aluminum Alloys:** In aluminum alloys, dispersoids such as Al_2Cu, Al_3Zr, and Al_3Sc are added to control grain growth during heat treatment processes. These dispersoids enhance the mechanical properties of the alloys by refining the grain structure.

- **Steel:** In steels, carbides, nitrides, and oxides are used to pin grain boundaries during thermomechanical treatments. For example, titanium nitride (TiN) and vanadium carbide (VC) particles are effective in controlling grain growth in high-strength low-alloy (HSLA) steels.

- **Superalloys:** Nickel-based superalloys used in high-temperature applications, such as turbine blades, benefit from the addition of refractory elements like tantalum and hafnium, which form stable carbibes and oxides that inhibit grain growth.

- **Ceramics:** In ceramic materials, Zener pinning is employed to stabilize the grain structure during sintering processes. For instance, in alumina ceramics, the addition of zirconia particles can effectively inhibit grain growth, enhancing the material's mechanical strength and toughness.

Limitations and Challenges:

While Zener pinning is an effective mechanism for grain boundary stabilization, it has certain limitations and challenges:

- **Particle Coarsening:** During high-temperature treatments, second-phase particles can coarsen, reducing their effectiveness in pinning grain boundaries. This coarsening can occur through mechanisms such as Ostwald ripening and particle coalescence.

- **Dissolution:** Some second-phase particles may dissolve into the matrix at elevated temperatures, particularly if the matrix has a high solubility for the particle-forming elements. This dissolution reduces the volume fraction of particles and, consequently, the pinning pressure.

- **Thermal Stability:** The thermal stability of the second-phase particles is crucial for maintaining effective Zener pinning at high temperatures. Particles that undergo phase transformations or react with the matrix can lose their pinning capability.

- **Optimizing Particle Distribution:** Achieving a uniform distribution of particles throughout the matrix can be challenging, particularly in large-scale manufacturing processes. Inhomogeneities in particle distribution can lead to uneven grain growth and microstructural inconsistencies.

Zener pinning in particle based films:

In printed films, particularly those fabricated via techniques such as inkjet or aerosol jet printing, Zener pinning is critical because it influences the microstructural properties of the films, such as grain size, uniformity, and electrical properties. Smaller grain sizes typically result in higher resistance due to increased grain boundary scattering, which can be detrimental for applications requiring high conductivity. However, controlled grain size reduction through Zener pinning may enhance the performance of films in applications where grain boundaries act as active sites, such as in sensors. The selection of the particle size, concentration, and distribution is key to optimizing Zener pinning. By carefully controlling the dispersion of pinning particles in printed films, it is possible to tailor the microstructure to achieve desired electrical, thermal, or mechanical properties. This control is particularly valuable in printed physical sensors, where the interplay between mechanical flexibility and electronic performance is essential. Thus, understanding and manipulating Zener pinning in printed films can significantly impact their functionality, performance and reliability of printed sensors.

2.8 Printed Physical Sensors

The goal of this PhD project is to develop low cost, reliable and repeatable temperature and humidity sensors based on silicon carbide nanomaterials fabricated via screen printing. Thus, it is imperative we establish a strong understanding of the operating principles of said sensors. In this section, we dive into the different mechanisms by which printed humidity and temperature sensors respond to external stimuli, their advantages and prospective applications.

2.8.1 Printed Humidity Sensors

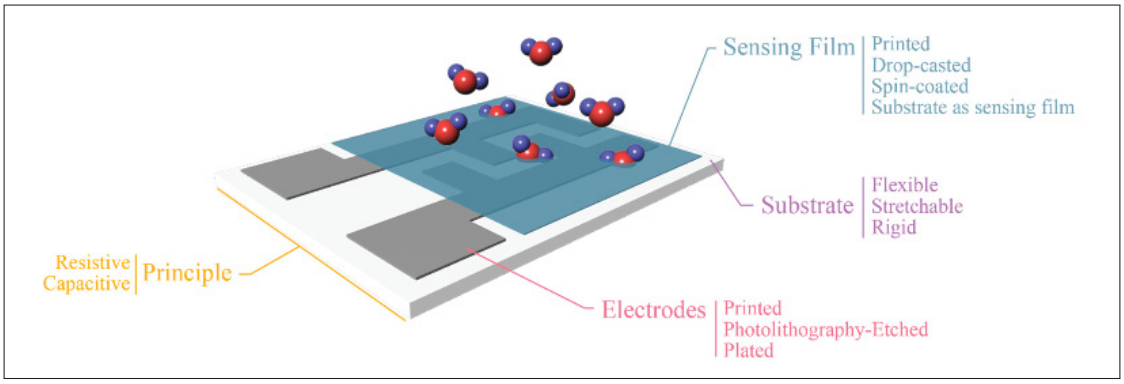

Figure 2.12 Humidity sensor mechanism
Taken from (Barmpakos & Kaltsas, 2021)

Printed humidity sensors represent a significant advancement in the field of sensor technology, leveraging the advantages of printed electronics to create flexible, low-cost, and easily manufacturable devices. Printing techniques such as screen (Beniwal *et al.*, 2023), inkjet (Virtanen, Ukkonen, Bjorninen, Elsherbeni & Sydänheimo, 2011), or roll-to-roll printing (Jeong, Noh & Lee, 2019a) have been largely utilized to fabricate such humidity sensors. As seen in Figure 2.12, when water molecules are absorbed by the sensing film, they diffuse into the porous structure of the deposited active film there by changing their electrical properties based on two primary mechanisms:

- **Resistance:** These sensors measure changes in electrical resistance due to the absorption of water molecules by the hygroscopic material. As humidity increases, the material absorbs

more water, leading to changes in ion conductivity or swelling of the polymer matrix, which in turn affects the resistance (Zhang, Maddipatla, Bose, Hajian, Narakathu, Williams, Mitchell & Atashbar, 2020a).

- **Capacitance:** These sensors measure changes in capacitance caused by the dielectric properties of the hygroscopic material. Water molecules increase the dielectric constant of the material, resulting in a measurable change in capacitance (Reddy, Narakathu, Atashbar, Rebros, Rebrosova, Bazuin, Joyce, Fleming & Pekarovicova, 2011b).

Among these two, resistive type humidity sensors provide a straightforward interface with readout electronics as compared to their capacitive counterparts (Barmpakos & Kaltsas, 2021). Active films are printed atop conductive interdigitated electrodes (IDE's) generally printed with silver inks (Rivadeneyra, Fernández-Salmerón, Banqueri, López-Villanueva, Capitan-Vallvey & Palma, 2014). The sensor operates by applying a voltage across the electrodes and measuring the resulting current, which is inversely proportional to the resistance of the sensing material. The resistance value is then correlated to the relative humidity using a pre-established calibration curve. Calibration is essential to ensure accurate and reliable measurements and involves exposing the sensor to known humidity levels and recording the corresponding resistance values. In this study we aim to develop resistance based humidity sensors using SiC nanopartiles (as further discussed in Chapter 3). Resistance based humidity sensors operate based on two distinct operating principles based on how the incoming water molecules interact with the active sensing film:

Negative resistance change: Negative resistance change humidity sensors operate based on the principle that their electrical resistance decreases as the relative humidity increases. This phenomenon is deeply rooted in the interaction between the sensor material and water molecules present in the environment.

- **Ion Conduction:** In many hygroscopic materials, water absorption leads to the dissociation of water molecules into hydroxyl ions (OH-) and protons (H+) (Roveti, 2001). The presence

of ions enhances the overall mobility of charge carriers in the material, thereby reducing its resistance.

- **The Grotthuss mechanism:** also known as the proton hopping mechanism, describes how protons (H+) "hop" through a network of hydrogen-bonded water molecules, contributing to ionic conductivity and there by significantly decreasing electrical resistance (Farahani *et al.*, 2014a).

- **Electron-hole recombination:** In semiconducting polymers, water absorption can influence the electron-hole conduction mechanism. Water molecules can act as dopants, modifying the charge carrier density and mobility within the polymer matrix (Nowak, Mistewicz, Nowrot, Szperlich, Jesionek & Starczewska, 2014). This alteration in charge transport properties directly affects the material's electrical resistance.

Positive resistance change:

When the ambient humidity increases, water vapor in the air is absorbed by the hygroscopic material. This absorption process leads to a change in the electrical properties of the material, typically resulting in an increase in resistance. Various materials can be employed in positive resistance change humidity sensors, including polymers, ceramics, and composites. Polymers like polyimides (Yoo, Lim, Min, Lee, Lee & Park, 2010a), polyaniline (Zeng, Liu, Diamond & Lau, 2010), and polyvinyl alcohol (Karunarathne, Wijesinghe, Rathuwadu, Karalasingam, Manoharan, Sameera, Sandaruwan, Amaratunga & De Silva, 2020) are commonly used due to their significant hygroscopic nature and sensitivity to moisture. Ceramic materials like alumina (Al_2O_3) (Juhász & Mizsei, 2009) and silica (SiO_2) (Su & Tsai, 2004) are also popular because of their stable and reproducible resistance changes upon exposure to humidity.

- **Water Absorption:** This absorption can occur through various mechanisms, such as adsorption on the surface, capillary condensation in pores, or direct absorption into the bulk of the material. Adsorption refers to the adherence of water molecules onto the surface of the sensing material, while absorption involves the penetration of water molecules into the bulk of the material. Both processes are influenced by the material's porosity, surface area, and

chemical composition. In porous materials, capillary condensation can occur, where water vapor condenses into liquid form within the pores at humidity levels lower than the saturation point (Zhang, Zhang, Cao, Guo, Han, Hu, Wu, She & He, 2021). This phenomenon is governed by the Kelvin equation, which relates the vapor pressure of a liquid in a capillary to the radius of curvature of the meniscus and the surface tension of the liquid (Shimizu, Arai & Seiyama, 1985). All these mechanisms contribute to the inhibition of conductive pathways between adjacent particles with in the active sensing film, there by increasing overall electrical resistance.

- **Swelling Effect:** In polymer-based sensors, the absorption of water can cause the material to swell. This swelling can change the microstructure and morphology of the polymer, affecting its conductive pathways and, consequently, increasing its electrical resistance (Zeng *et al.*, 2010).

Factors such as active material, substrate and readout method selection plays a vital role in the operational capabilities and performance of a printed humidity sensor. In Chapter 3 of this thesis, we present a detailed comparison of recently reported printed resistive humidity sensors and traditional silicon cardide based humidity sensors against the all printed silicon carbide humidity sensors fabricated by us.

Advantages of Printed Humidity Sensors:

- **Flexibility and Conformability:** Printed sensors can be fabricated on flexible substrates, allowing them to be integrated into various applications, including wearable devices and smart packaging.

- **Low Cost:** The printing processes used to manufacture these sensors are cost-effective, making it possible to produce large quantities at a relatively low cost.

- **Scalability:** Techniques like roll-to-roll printing enable the mass production of sensors, making them suitable for large-scale deployment.

- **Customization:** The printing process allows for easy customization of sensor design and size, enabling the development of application-specific sensors.

Applications:

- **Environmental Monitoring:** These sensors are used for monitoring humidity levels in the environment, helping in weather forecasting and climate studies.
- **Industrial Processes:** They are employed in industries where precise humidity control is essential, such as in food processing, pharmaceuticals, and electronics manufacturing.
- **Healthcare:** Printed humidity sensors are integrated into wearable devices for monitoring skin hydration and detecting respiratory conditions.
- **Smart Packaging:** These sensors are used in packaging to monitor and maintain optimal humidity levels, ensuring the quality and freshness of products.

2.8.2 Printed Temperature Sensors

Printed temperature sensors are an integral part of modern sensor technology due to their flexibility, low cost, and ease of integration into various devices (Kuzubasoglu & Bahadir, 2020). As seen in Figure 2.13, several types of printed temperature sensors have been developed, each employing different sensing mechanisms and materials to measure temperature accurately.

- **Resistive Temperature Detectors (RTDs):** Printed RTDs operate on the principle that the electrical resistance of certain materials changes predictably with temperature. Conductive inks, often composed of metals like nickel (Turkani, Maddipatla, Narakathu, Altay, Fleming, Bazuin & Atashbar, 2019), silver (Hai, Su, Zhu, Pan & Luo, 2024) or platinum (Shen, Kim, Bailey, Ma & Dardona, 2018), are printed on flexible substrates. These inks provide a linear resistance-temperature relationship, making them suitable for precise temperature measurements.

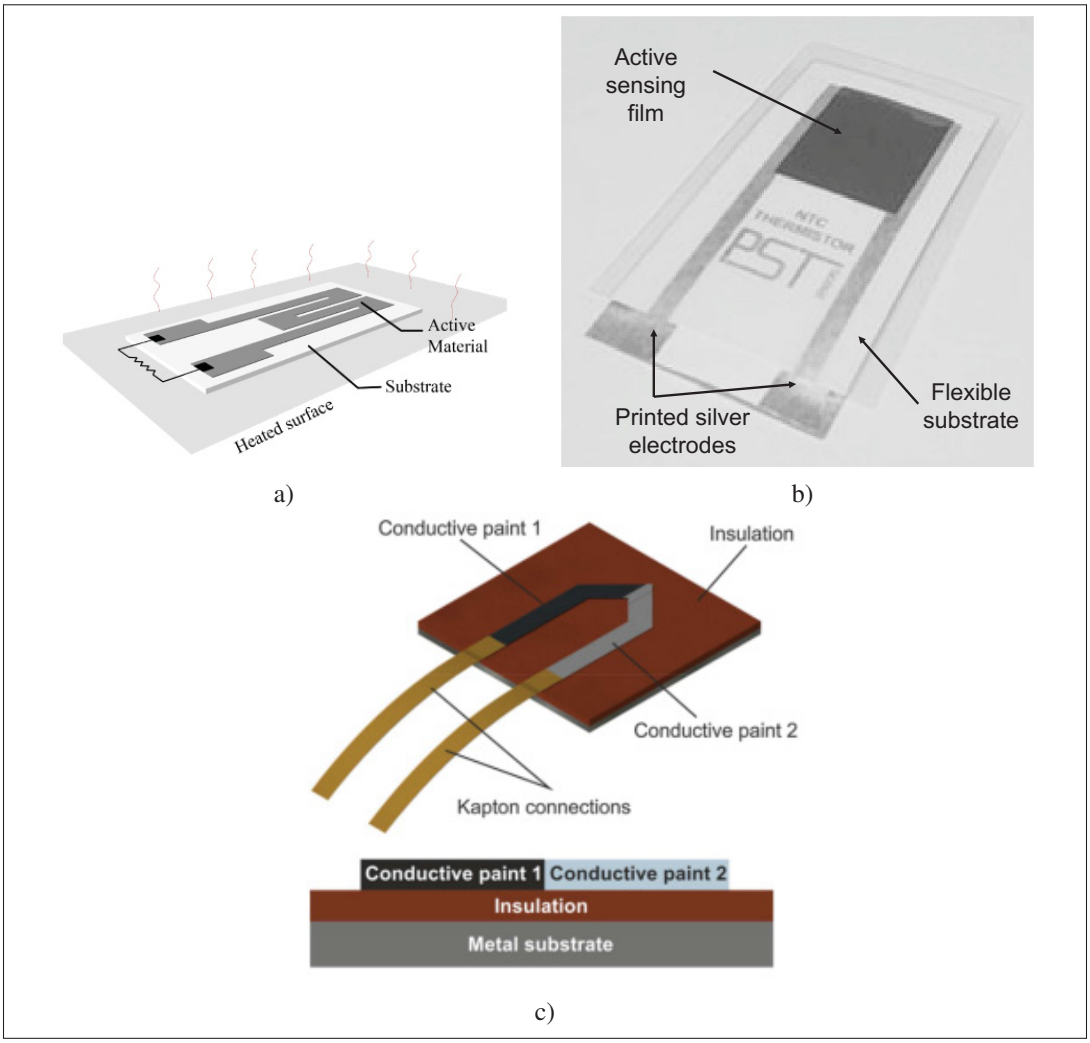

Figure 2.13 (a) RTD (b) Thermistor (c) thermocouple
Taken from (Kimoto & Cooper, 2014; Knoll *et al.*, 2018a; Männl *et al.*, 2014) respectively

- **Thermistors:** Thermistors are another class of resistive sensors, typically made from ceramic materials with a high temperature coefficient of resistance (Wadhwa *et al.*, 2024). Negative Temperature Coefficient (NTC) thermistors, which decrease in resistance as temperature rises, are commonly used in printed formats. The inks used contain metal oxide nanoparticles (Fourmont *et al.*, 2022b; Katerinopoulou, Zalar, Sweelssen, Kiriakidis, Rentrop, Groen, Gelinck, van den Brand & Smits, 2019b), which are deposited onto flexible substrates via printing methods. Thermistors are advantageous for applications requiring high sensitivity and a compact form factor.

- **Thermocouples:** Thermocouples operate based on the Seebeck effect, which occurs when two dissimilar metals are joined at one end, creating a junction. When there is a temperature difference between the junction and the other reference junction, a voltage (thermoelectric EMF) is generated proportional to the temperature difference. This voltage can be measured and converted into temperature readings. Printing thermocouples involves depositing layers of conductive inks made from different metals such as silver-nickel (Cruz, Azevedo, Cano-Raya, Manninen & Viana, 2021), condutive organic polymers such as (PEDOT:PSS) and polyaniline (PANI) (Seeberg, Røyset, Jahren & Strisland, 2011), metal oxIDE's such as $\mathrm{In_2O_3/ITO}$ (Liu, Ren, Shi, Liu, Zhang, Liu, Ye, Jing, Tian & Jiang, 2018b).

Other less common printed temperature sensing devices are based on capacitive and piezoelectric mechanisms. These sensors also exhibit changes in their respective responses with increase in temperature. However, complexity of readout electronics, circuit design and additional processing steps such as poleraization make these less viable and hence less studied. In this Phd project, we focus our efforts on developing silicon carbide based screen printed thermistors as detailed in Chapter 4. Thermistors offer several advantages over RTD's and thermocouples, such as larger change in resistance per degree of temperature change, faster response times, simplicity of design, small form factor and low cost. Thermistors are broadly classified into two types based on their temperature coefficient:

- **Negative Temperature Coefficient (NTC) Thermistors:** These thermistors decrease in resistance as temperature increases. They are typically used in temperature sensing and compensation applications. NTC thermistors are typically made from ceramic materials composed of oxIDE's of transition metals such as manganese, nickel, cobalt, and copper. The resistance R of an NTC thermistor decreases exponentially with an increase in temperature. This relationship is described by the Steinhart-Hart equation:

$$\frac{1}{T} = A + B\ln(R) + C\ln^3(R) \tag{2.7}$$

where A, B, and C are material-specific constants, T is the absolute temperature, and R is the resistance of the thermistor. The conductivity of NTC thermistors increases with temperature due to an increase in the intrinsic carrier concentration. As temperature rises, more charge carriers are excited across the bandgap, enhancing the material's conductivity and thus reducing its resistance. The temperature dependence of resistance in NTC thermistors can also be expressed as:

$$R(T) = R_0 \exp\left(\frac{E_a}{kT}\right) \tag{2.8}$$

where R_0 is the resistance at a reference temperature, and E_a is the activation energy for conduction.

- **Positive Temperature Coefficient (PTC) Thermistors:** These thermistors increase in resistance as temperature increases. They are often used as current limiters and overcurrent protection devices. PTC thermistors are typically made from polycrystalline ceramic materials based on doped barium titanate ($\mathrm{BaTiO_3}$). These materials exhibit a sharp increase in resistance at a certain threshold temperature, known as the Curie temperature. The operating principle of PTC thermistors is associated with a phase transition from a ferroelectric to a paraelectric state. Below the Curie temperature, the material is in a ferroelectric state with low resistance. Above this temperature, it transitions to a paraelectric state with high resistance. The resistance increase in PTC thermistors is due to the formation of potential barriers at the grain boundaries. As temperature rises, these barriers become more pronounced, impeding the flow of charge carriers and increasing resistance. The resistivity ρ of PTC thermistors as a function of temperature can be described by:

$$\rho(T) = \rho_0 \exp\left(\frac{E_b}{kT}\right) \tag{2.9}$$

where ρ_0 is the resistivity at a reference temperature, and E_b is the energy barrier at the grain boundaries .

Printed thermistors find applications in several industries such as wearables, smart textiles, consumer electronics, automobile, medical devices etc. Several active materials have been used to fabricate printed thermistors over a wide sensing range. Metal oxides such as bismuth iron oxide (BFO) (Fourmont *et al.*, 2022b) and nickel oxide (Huang, Kao & Liao, 2013), carbon based derivatives such as nano-tubes (Turkani, Maddipatla, Narakathu, Bazuin & Atashbar, 2018a) and conductive polymers such as PEDOT:PSS (Maskey, Shrestha, Sun, Park, Park, Parajuli, Shrestha, Jung, Ramasundaram, Koirala et al., 2020) have been widely investigated in recent literature. Chapter 4 enlists a detailed comparison between reported and our printed SiC thermistors.

2.9 Additive Manufacturing of silicon carbide

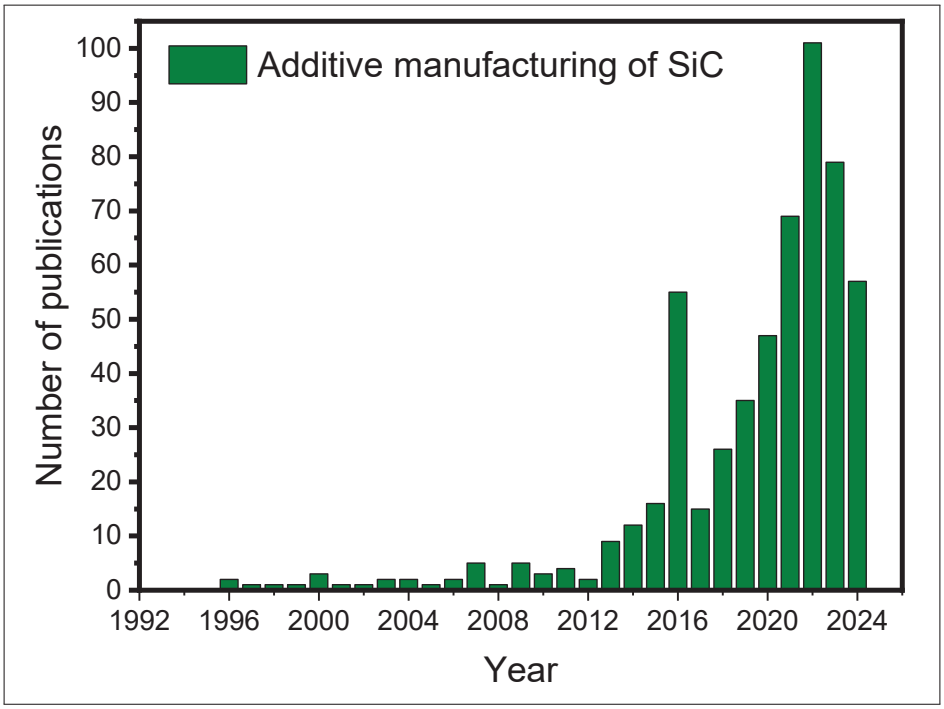

Figure 2.14 Number of publications on additive manufacturing of SiC between 1993-2024
Data assimilated from Scopus

Silicon carbide has steadily gained importance in the field of additive manufacturing in recent years. We observed a sharp increase in the number of publications around this subject in the last decade as seen in Figure 2.14. Although a vast majority of reports are based on more

conventional additive manufacturing (AM) processes such as stereolithography, binder jet printing, selective laser sintering etc as reported in Table 2.5. Additive manufacturing of SiC typically involves creating a printed green body followed by a densification step. In some cases, single-step, layer-by-layer consolidation methods have been successfully demonstrated. The preforming stage employs techniques commonly used for AM of metal and ceramic components, while the densification of the green body is achieved through conventional processes for bulk SiC (Koyanagi, Terrani, Harrison, Liu & Katoh, 2021).

To the best of our knowledge, extremely limited work has been done to use fully printed and flexible, silicon carbide based devices towards physical sensing applications. Due to the ultra high melting point of silicon carbide nanoparticles (2730 °C) (Elements), sintering printed films will require extreme temperatures much greater than the temperature tolerance of robust polymeric substrates such as polyimide and conductive electrode inks such a silver and gold. Some attempts have been made to fabricate all printed flexible SiC temperature sensors where SiC nanoparticles based inks were drop casted onto polyimide substrate and then sintered using a 3000 mW laser (Aljasar, Xu & Qasaimeh, 2022). Mott & Evans (2001) developed a inkjettable ink with SiC nanoparticles and polycarbosilane (polymeric precursor to SiC) dispersed in octane which were then pyrolized to create dense films. Phan, Zhong, Nguyen, Park, Dinh, Song, Vadivelu, Masud, Li, Shiddiky et al. (2019b) developed a flexible SiC based implantable membrane to continuously detect cellular electrical activity. Here, think films of SiC were grown on silicon wafer, delaminated via a complex process using phosphate-buffered saline and then transferred onto polyimide substrate. Chuasontia, Sirisom, Nakpathomkun, Toommee, Pechyen, Tangnorawich & Parcharoen (2023) developed a $CNT - SiC - Ag$ based ink dispersed in chitosan solution that was used for non-enzymatic paraoxon residuals detection. Here, the SiC composite ink was applied to printed carbon condutive electrodes via drop casting and dried at 70 °C to form a conductive network for sensing.

Complex fabrication and sintering processes have thus far been utilized towards printed flexible SiC based physical sensors. The aim of this research project is to develop simple and low cost techniques to fabricate optimal SiC based temperature and humidity sensors that take advantage

of non-sintered, densly packed SiC nanoparticle networks which are achieved at much lower temperatures than their melting point a discussed earlier.

Table 2.5 Recent literature on additive manufacturing of SiC
Adapted from (Koyanagi *et al.*, 2021)

AM process	**Sintering method**	**Processing temperature**	**Reference**
Pre-ceramic polymer			
Stereolithography	polymer pyrolysis	600 °C	Park *et al.* (2009)
Stereolithography	pyrolysis + sintering	1300 °C - 1400 °C	Chen *et al.* (2018b); de Hazan & Penner (2017)
Powder based			
Stereolithography	Polymer impregnation and pyrolysis	1200 °C	He *et al.* (2019)
Direct ink writing	Liquid-phase sintering	1550 °C - 1700 °C	Gómez-Gómez *et al.* (2019)
Gel casting using 3D printed scphaold	Liquid-phase sintering	1900 °C	Tu & Jiang (2018)
Selective laser sintering	Reactive sintering of Si and C	1550 °C	Liu *et al.* (2018a)
Binder jet printing	Polymer impregnation and pyrolysis	1000 °C	Polozov *et al.* (2020)
Binder jet printing	Reaction bonding by molten silicon infiltration	1400 °C	Zocca *et al.* (2019)
Direct ink writing	Chemical vapor infiltration	1000 °C	Terrani *et al.* (2020); Zhu *et al.* (2020)
Laminated objective manufacturing	Reactive bonding wih molten silicon inclusions	1500 °C - 1600 °C	Klosterman *et al.* (1999); Weisensel *et al.* (2004)
Reactive chemical based			
Reactive Chemical based	Laser chemical vapor deposition	930 °C	Zhang *et al.* (2012)

CHAPTER 3

FLEXIBLE SCREEN-PRINTED SIC-BASED HUMIDITY SENSORS

Wadhwa Arjun[1], Perrotton Alexandre[1], Teherian Hassan Mohamad[2], Zirakjou Abbas[1], Benavides-Guerrero Jaime[1], Gratuze Mathieu[1], Vaussenat Fabrice [1], Bolduc Martin [2], Cloutier G. Sylvain [1]

[1] Département de Génie Électrique, École de Technologie Supérieure, 1100 Rue Notre-Dame Ouest, Montréal, Québec, H3C 1K3, Canada
[2] Département de génie mécanique, Université du Québec à Trois-Rivières, Trois-Rivi‘eres, QC G8Z 4M3, Canada

Article submitted to
Nature Communications Engineering
April 15, 2024.
https://www.nature.com/commseng/

Abstract

Humidity sensors are essential components in modern technology, spanning applications from residential appliances to the Internet of Things (IoT). However, conventional commercial sensors are typically rigid, constrained by narrow relative humidity (%RH) operating ranges, and require complex fabrication processes. In this study, we present a highly sensitive cubic silicon carbide ($3C - SiC$) nanoparticle-based relative humidity sensor, fabricated via serigraphic printing on to 5 mil thick flexible polyimide (Kapton®) substrate. Devices are tested across a broad humidity range of 10–90 %RH at ambient temperature and their performance is evaluated in a controlled humidity chamber. The sensor exhibits a robust response of 45.2% R/R_0, with a sensitivity of 5.34 Ω/%RH, an adsorption time of 18 seconds, and a desorption time of 46 seconds. Additionally, the device demonstrates low hysteresis of 6.5% at 60%RH, with excellent repeatability and stability over 3.5 hours of continuous cycling. To showcase their potential for real-world applications, the printed sensors are integrated into a commercial KN95 mask for monitoring respiration parameters, such as respiration rate. This integration highlights the

potential for future exploration in human health monitoring, utilizing fully printed, low-cost sensing devices.

Keywords

Silicon Carbide, Humidity Sensor, Printed Electronics, Printed Silver IDE's, wide band-gap semiconductor

3.1 Introduction

In recent years, functional printing techniques have gained significant traction in the fabrication of cost-effective, flexible electronic devices and sensors. These approaches have enabled the development of straightforward, additively-manufactured sensor architectures, typically comprising an active sensing region coupled with metallic interdigitated electrodes (IDEs) for the measurement of parameters such as humidity (Tachibana, Wang, Sekine, Takeda, Hong, Yoshida, Abe, Miura, Watanabe, Kumaki & Tokito, 2022), temperature (Fourmont *et al.*, 2022b), and strain (Wang, Sekine, Takeda, Yokosawa, Matsui, Kumaki, Shiba, Nishikawa & Tokito, 2020b). Among these applications, the detection of relative humidity (%RH) has garnered considerable attention due to its relevance in a wide range of industries. Sectors with humidity-sensitive environments, such as precision agriculture (Imam, Choudhary & Sachan, 2015), healthcare (Barmpakos, Segkos, Tsamis & Kaltsas, 2017), and the transportation of high-value goods (Wen, Zhang, Jiang, Wu, Li, Sun & Guo, 2020), are ideal candidates for the deployment of low-cost, single-use humidity sensors.

The fundamental operation of humidity sensors is predicated on the interaction between water molecules and the active sensing region, leading to changes in electrical properties that correlate with variations in %RH. Humidity sensors typically adopt resistive (Zhang, Turkani, Hajian, Bose, Maddipatla, Hanson, Narakathu & Atashbar, 2019) or capacitive (Komazaki & Uemura, 2019) sensing architectures, with less common designs incorporating calorimetric (Soga, Jimbo, Suzuki & Citterio, 2013) or acoustic (Caliendo, Verona, D'Amico, Furlani, Iucci & Russo,

1993) principles. Resistive humidity sensors are particularly popular due to their simplicity, cost-effectiveness, and ease of integration with detection circuitry (Lu, Xu, Yang, Tang, Yang, Fujita, Honda, Arie, Akita & Chueh, 2021). These sensors operate by detecting changes in the electrical resistance of a hygroscopic material, which occurs as a result of water molecule absorption, allowing for the quantification of %RH (Farahani, Wagiran & Hamidon, 2014b).

Over the years, various materials have been employed in resistive humidity sensors, including carbon-based nanomaterials, polymers, organic semiconductors, metal oxides, and ceramics (Dubey & Kumar, 2018; Jeong, Noh & Lee, 2019b; Komazaki & Uemura, 2019; Tachibana *et al.*, 2022; Wang *et al.*, 2020b; Zhang *et al.*, 2019). While these materials offer good reproducibility and longevity, they are often constrained by narrow humidity operating ranges, slow response times, and susceptibility to harsh environmental conditions.

Wide bandgap semiconductors, such as ZnO (II-VI), GaN (III-V), and SiC (IV-IV), have emerged as promising candidates in the field of printed and flexible electronics (Arrabito, Aleeva, Pezzilli, Ferrara, Medaglia, Pignataro & Prestopino, 2020; Dong, Liu, Li, Chen & Wang, 2023; Lerner, Eisenbrandt, Bonafede, Meitl, Fecioru, Trindade, Reiner, Waltreit & Bower, 2016; Syed, Zavabeti, Ou, Mohiuddin, Pillai, Carey, Zhang, Datta, Jannat, Haque, Messalea, Xu, Russo, McConville, Daeneke & Kalantar-Zadeh, 2018). In particular, SiC stands out due to its exceptional mechanical strength, chemical inertness, biocompatibility, thermal stability, and high electron mobility (Sun, Han, Wu, Wang & Wang, 2018a; Sun, Wang & Wang, 2018c). These properties render SiC suitable for long-term operation in corrosive, high-temperature, and oxidizing environments (Müller, Krötz & Niemann, 1994; Phan, Dinh, Kozeki, Qamar, Namazu, Dimitrijev, Nguyen & Dao, 2016b). SiC has been explored for resistive humidity sensing applications in various forms, including crystalline wafers, nanowires, and nanocomposites (Ahmed, Abduljalil & Hashim, 2019b; Li, Ma, Peng, Chen, Chu, Li, Hu & Li, 2014; Wang, Wang, Hu & Li, 2012b). Moreover, sophisticated fabrication techniques, such as direct growth and top-down/bottom-up approaches, have been utilized in conjunction with transfer and conventional printing methods to produce complex and expensive devices (Nguyen, Nguyen, Nguyen, Yadav, Dinh, Masud, Singha, Do, Barton, Ta, Kashaninejad, Ooi, Nguyen & Phan, 2021a).

To the best of our knowledge, SiC nanoparticles have not yet been employed in the fabrication of fully-printed humidity sensors, despite the successful production of SiC devices via other deposition and etching methods (Chen, Wang, Xue, Huang, Zhou & Zhang, 2018c; Gómez-Gómez, Moyano, Román-Manso, Belmonte, Miranzo & Osendi, 2019; Mott & Evans, 2004; Terrani, Lach, Wang, Coq, Linton, Petrie, Koyanagi & Byun, 2021; Zhou, Zhang, Wang, Zhang, Zhang, Chen, Huang, He & Fang, 2023). In this study, we develop a novel humidity sensor by formulating a low-cost active ink from commercial SiC nanoparticles. The material properties of this ink are comprehensively characterized using multiple techniques. We then fabricate a SiC-based humidity sensor by screen-printing the ink onto IDEs printed with commercial silver ink. Various SiC loadings and curing times are systematically investigated across a wide %RH range (10–90%) to optimize sensor performance, minimize hysteresis, and achieve rapid adsorption/desorption times. The sensing mechanism is thoroughly examined, and the fabricated devices are integrated into a commercial KN95 facemask to demonstrate their potential for respiratory monitoring applications.

3.2 Experimental Section

3.2.1 Materials

Cubic Silicon Carbide ($3C-SiC$, beta phase, 99+%, 80 nm, cubic) nanoparticles were sourced from US Research Nanomaterials, Inc. (US2022). Flexible printed circuit (FPC) Kapton®, with a thickness of 0.005 inches, was obtained from American Durafilm. Loctite® EDAG 725A silver screen printing paste and Resin SOL725 were procured from Henkel. All materials were used as received without further modification.

3.2.2 Ink Formulation and Device Fabrication

Precise quantities of $3C-SiC$ nanoparticles were mixed with the ink vehicle (SOL725) to achieve solid loading fractions of 20, 30, 40, and 50 wt%. The powder and ink vehicle were carefully weighed and combined, followed by thorough dispersion using a planetary mixer

(Thinky Mixer Model AR-310). The mixing process involved 3 minutes of mixing and 3 minutes of degassing, for a total of 6 minutes, ensuring homogeneity and producing a stable dispersion with a shelf life exceeding 6 months. A total of 10 grams of ink was prepared for each formulation, as detailed in Table 3.1.

Table 3.1 SiC humidity sensor ink formulations.

Ink name	SiC nanoparticles (gms)	SOL725 (gms)
20-SiC	2	8
30-SiC	3	7
40-SiC	4	6
50-SiC	5	5

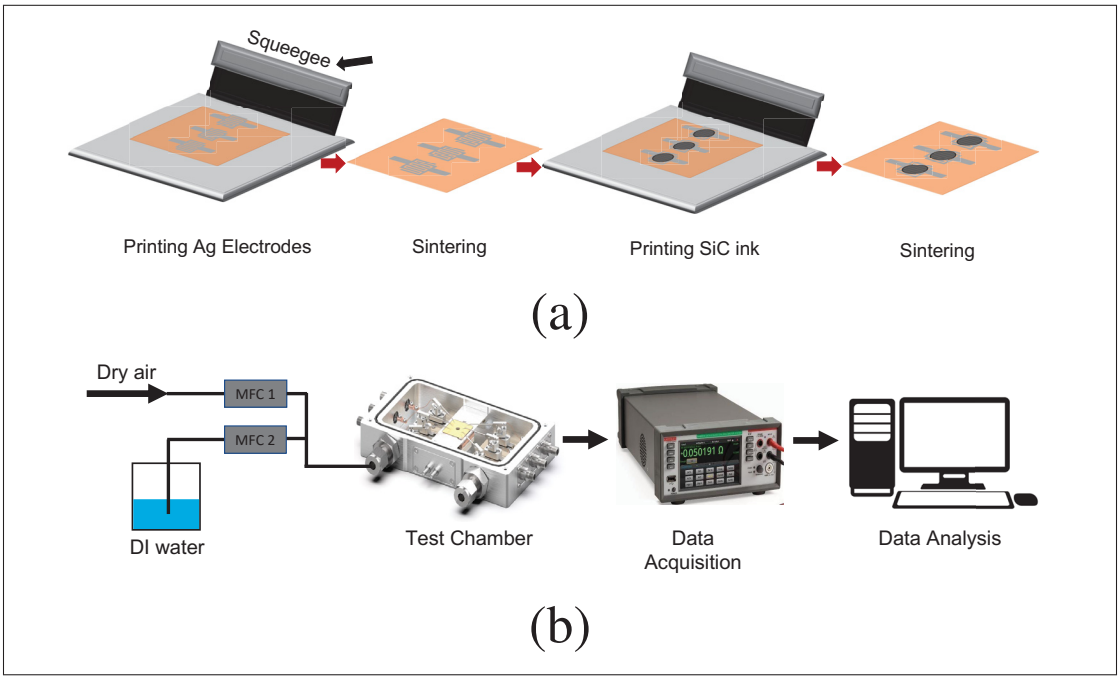

Figure 3.1 (a) Device fabrication schematic (b) SiC humidity test setup

Commercial polyimide (Kapton®) substrates were prepared by cleaning with 99.9% pure acetone (Millipore Sigma 270725). Both the silver and SiC humidity sensing inks were printed using a 325-mesh stainless steel screen, yielding a wet film thickness of approximately 25.4 microns. The silver paste was printed onto the Kapton® substrate using a KEKO P250 automatic screen printer, following an interdigitated finger pattern with a trace width of 0.5 mm, trace spacing of 0.5 mm, and overall dimensions of 15 mm × 15 mm, as illustrated in Figure I-1 in the supporting

information. The printed silver electrodes were cured in air at 300 °C for 60 minutes using a Manncorp (MC301N) reflow oven.

Subsequently, the active SiC-based ink was printed on top of the cured silver electrodes in a circular format with a diameter of 7.5 mm. The final sensor architecture was then cured in the reflow oven at 300 °C in air for 60, 120, and 180 minutes to investigate the effect of curing time on device performance. A schematic representation of the printing process is provided in Figure 3.1a).

3.2.3 Characterization Methods

Field emission scanning electron microscopy (FE-SEM) was conducted using a Hitachi SU8230 system equipped with a Bruker FlatQUAD EDS detector for elemental analysis. X-ray diffraction (XRD) patterns of the SiC nanopowder were acquired using an Anton Paar - XRDynamics 500 system with a Copper source. XRD spectra was analysed using the HighScore Plus software version: 4.6a and PDF-5+ ICDD database. Raman spectra was acquired using a WITec alpha300A Raman microspectroscopy system equipped with a 532 nm green laser. Ultraviolet-visible (UV-Vis) absorption spectra of the SiC powder were recorded using a Perkin-Elmer Lambda 750 spectrometer. Particle size of the SiC nanoparticles was measured using a Zetasizer Ultra Particle Size Analyzer (Malvern Panalytical) and via image processing using software Image J (version: 1.54g). Viscosity of the SiC inks was measured using a Anton Parr Physica MCR 501 viscomenter with the 25 mm diameter spindle system. X-ray photoelectron spectroscopy (XPS) was performed to analyze chemical bonding and oxidation states using an Escalab 250Xi (Thermo Fisher Scientific) system with a monochromated Al K_α source operating at 218.8 W. Thermogravimetric analysis (TGA) was performed to determine the curing temperature of the SiC ink using a Pyris Diamond TG/DTA system. Conductivity measurements of the printed SiC films were carried out using an Ossila T2001A3 four-point probe. The humidity sensors were tested in a controlled humidity and temperature environment using a 6-channel micro-probe station (Nextron® MPS-PT6C). The two-wire resistance measurements were recorded via a 40-channel digital multimeter (Keithley 2790-L), as depicted in Figure 3.1b).

Current-voltage (I-V) characteristics of the thermistors were obtained using a Keithley DAQ6510 digital multimeter and a Keithley 2400 source-measure unit (SMU). Custom MATLAB scripts were developed to process the raw data extracted from both the humidity test chamber and the digital multimeter. Breath monitoring experiments were conducted by the second author of this study, with protocols approved by the ethics review committee at ÉTS (No. H20231007). All experiments involving human subjects were performed in accordance with relevant guidelines and regulations.

3.3 Results and Discussion

3.3.1 Material Characterization and Morphology

To optimize device performance, it is essential to ensure the complete removal of the polymeric resin (SOL725) from the printed films. Thermogravimetric analysis (TGA) of a 30 wt.% SiC and 70 wt.% SOL725 ink (Figure 3.2a)) was conducted between room temperature (23 °C) and 600 °C in air at a heating rate of 10 °C/min. The analysis shows a 17.5% reduction in sample weight between 30 °C and 200 °C, corresponding to the volatilization of high-volatility components in the ink vehicle. A further 33.6% weight reduction between 200 °C and 228 °C is attributed to the burning off of low-volatility components in the resin. An additional 9.5% reduction in weight is observed between 228 °C and 300 °C, which can be attributed to the removal of polymeric components, including surfactants and dispersants. The precise chemical composition of SOL725 was not disclosed by Henkel during this study. Beyond 300 °C, further weight reduction may result from the combustion of residual polymeric materials, potentially leading to carbonaceous deposits on the sensing film, which could negatively impact device performance. Consequently, 300 °C was identified as the optimal sintering temperature.

Raman spectra of the SiC powder (Figure 3.2)b) confirm its cubic crystal structure. Notable peaks were observed at 785, 897, 1346, 1588, 2684, and 2916 cm^{-1}. Peaks at 785 and 897 cm^{-1} correspond to the transverse and longitudinal optical modes of $3\mathrm{C}-\mathrm{SiC}$, respectively (Lebedev, Oganesyan, Kozlovski, Eliseyev & Bulat, 2019a). The peak at 1346 cm^{-1} corresponds to the

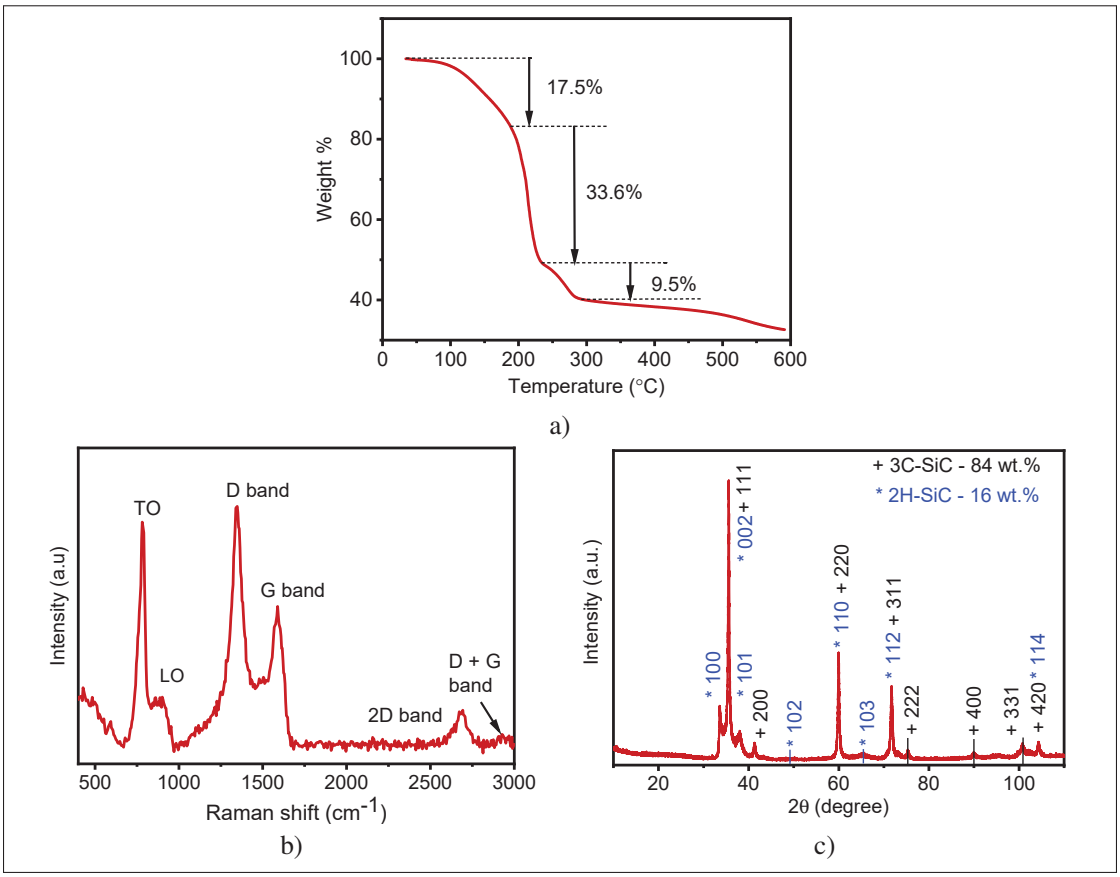

Figure 3.2 (a) Characterization of the materials used to fabricate the SiC-based humidity-sensitive ink includes: (a) thermogravimetric analysis (TGA) of the SOL725 resin conducted from room temperature to 600 °C, (b) Raman spectroscopy confirming the cubic crystalline phase of the SiC nanoparticles, and (c) X-ray diffraction spectra verifying the cubic phase along with the presence of a hexagonal phase in the as-received SiC nanoparticles

D band of carbon, while the 1588 cm^{-1} peak represents the G band associated with the A_{1g} vibrational mode of carbon (Hsu, Cloutier, Palefsky & Xu, 2010). The peaks at 2684 cm^{-1} and 2916 cm^{-1} correspond to the second-order D band (2D band) and the D+G band, respectively (Dragomir, Valant, Fanetti & Mozharivskyj, 2016b; Zhu, Guo, Lin, Hao, Shang, Jia, Chen, Jin, Wang & Chen, 2012b).

XRD patterns of the SiC particles (Figure 3.2) further validate its cubic crystalline structure, with distinct diffraction peaks observed. Peaks at 2θ = 35.6°, 41.4°, 59.9°, 71.7°, 75.4°, 89.9° and 104.4° correspond to the 111, 200, 220, 311, 222, 400, 331 and 420 crystal planes of the $3C-SiC$ structure, in line with ICDD card 04-008-2393. The presence of $2H-SiC$ peaks at 2θ = 33.6°(100), 35.5°(002), 38.1°(101), 49.7°(102), 60.1°(110), 65.5°(103), 71.8°(112) and 104.289°(114) (ICDD card 01-070-2550) suggests a blending of two phases during nanoparticle fabrication. To further investigate, default Rietveld refinement was performed in HighScore Plus software, the Rietveld refinement spectra along with the relevant parameters are highlighted in Figure I-5 and Table I-1 in the supporting information. The analysis revealed that the SiC nanopowder comprises approximately 84 ± 1 wt.% of the 3C-SiC phase and 16 ± 4 wt.% of the 2H-SiC phase. It is important to note that accurate phase quantification was challenging due to peak overlap between the two phases.

A thorough investigation was conducted to determine the particle size distribution of the as-received SiC nanopowder. Following the methodology outlined by Nikkam et al. (Nikkam, Saleemi, Haghighi, Ghanbarpour, Khodabandeh, Muhammed, Palm & Toprak, 2014), we analyzed the particle size distribution of the SiC nanoparticles using dynamic light scattering (DLS) with various solvents, including acetone, deionized water (DI water), ethylene glycol (EG), a 1:1 blended ratio of DI water and EG, ethanol, isopropanol (IPA), and N-Methylpyrrolidone (NMP) (Figure 3.3a)). The DLS analysis revealed significant variability in the measured mean particle sizes, ranging from 1.41 μm in NMP to 0.3 μm in ethanol. This variation is likely due to different degrees of agglomeration or aggregation of the SiC nanoparticles within the various solvent systems. In addition to DLS, particle size distribution was further analyzed using the ImageJ software, where individual SiC particle diameters were measured from field emission scanning electron (FE-SEM) microscopy micrographs (Figure 3.3b)). The results indicate a wide distribution, with particle sizes ranging from 0.02 μm to 0.15 μm, yielding a mean particle size of 0.047 μm. This finding aligns with the manufacturer's reported specifications of 0.05–0.13 μm (noa, b).

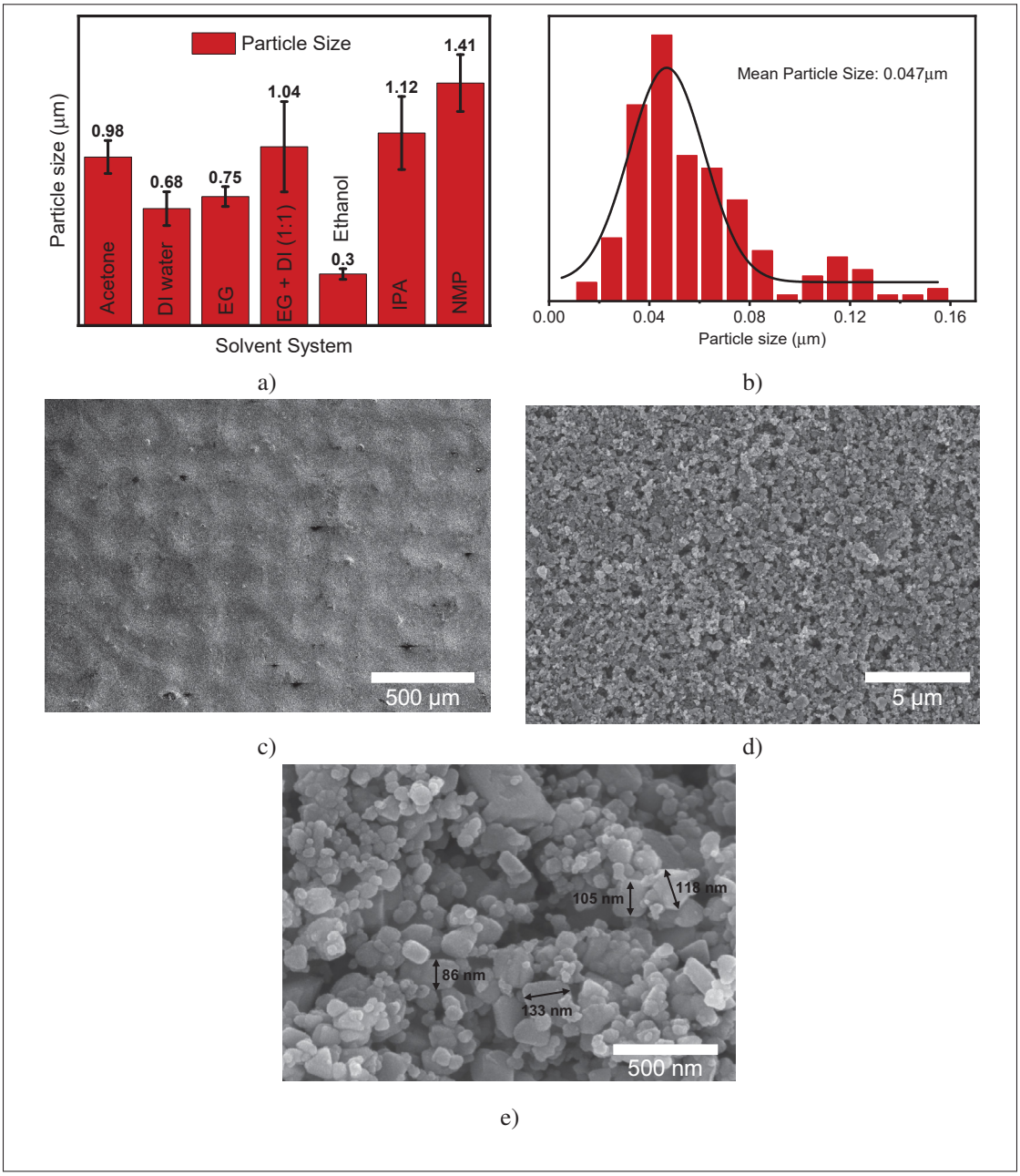

Figure 3.3 Morphological characterization of the SiC nanoparticles and printed SiC humidity-sensitive films includes: (a) particle size distribution of SiC nanoparticles dispersed in various solvent systems, (b) particle size distribution determined through image processing analysis. Additionally, field emission scanning electron microscopy (FE-SEM) micrographs of the SiC humidity sensitive film cured at 300 °C are shown at magnifications of (c) 100x, (d) 10,000x, and (e) 100,000x

SiC-based humidity sensing films with 20, 30, 40, and 50 wt.% loadings were printed directly onto the prepared Kapton® substrates. The morphology and structure of the 40 wt.% SiC sensing film were analyzed via FE-SEM and energy dispersive X-ray analysis (EDX). As shown in Figure 3.3c), the printed film is homogeneous, porous, and free of cracks. ASTM F2252 / F2252M-13e1 tests (noa, a) confirmed excellent adhesion of the printed film to the Kapton® substrate. Further magnifications (Figures 3.3d) and 3.3e)) reveal a densely packed network of SiC nanoparticles with intermittent pores. These pores facilitate the adsorption/desorption process, significantly improving the sensor's response times (Tachibana *et al.*, 2022).

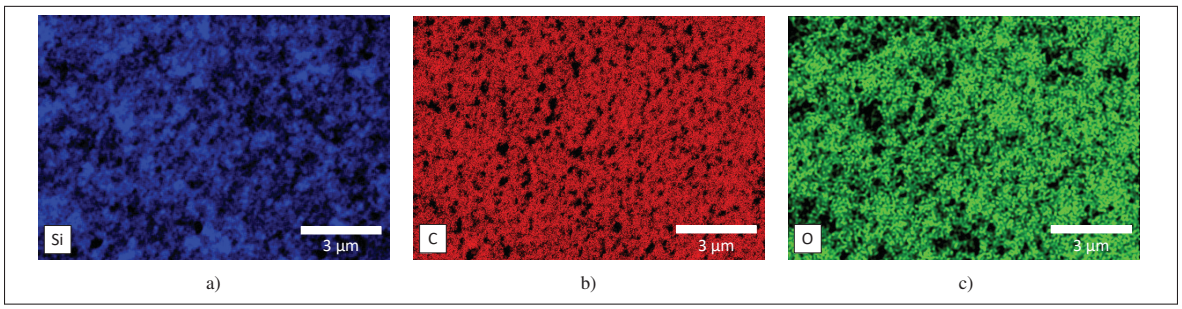

Figure 3.4 Energy dispersive X-ray (EDX) analysis micrographs display the distribution of (a) Si, (b) C, and (c) O species within the printed SiC film, confirming the material's composition and the presence of native surface oxidation on the SiC nanoparticles

Elemental mapping (Figures 3.4 a), b), c)) confirms a homogeneous distribution of Si and C elements, along with the presence of oxygen, indicating the formation of a native oxide layer on the SiC nanoparticles (Sun *et al.*, 2018c). High resolution optical microscopy images (Figure I-2a), b)) provided in the supplementary material, further validate the printed IDE and sensing film thickness. The silver ink achieved an average layer height of 12 µm, while the printed sensing film atop the IDEs reached 23 µm (Figures I-2c), d)).

The presence of functional groups on the surface of SiC nanoparticles, crucial to humidity sensing, was characterized by XPS analysis. The full XPS spectra (Figure 3.5a)) indicate the presence of silicon (Si_{2p}), carbon (C1s), and oxygen (O1s). Table I-2 (Supplementary Infor-

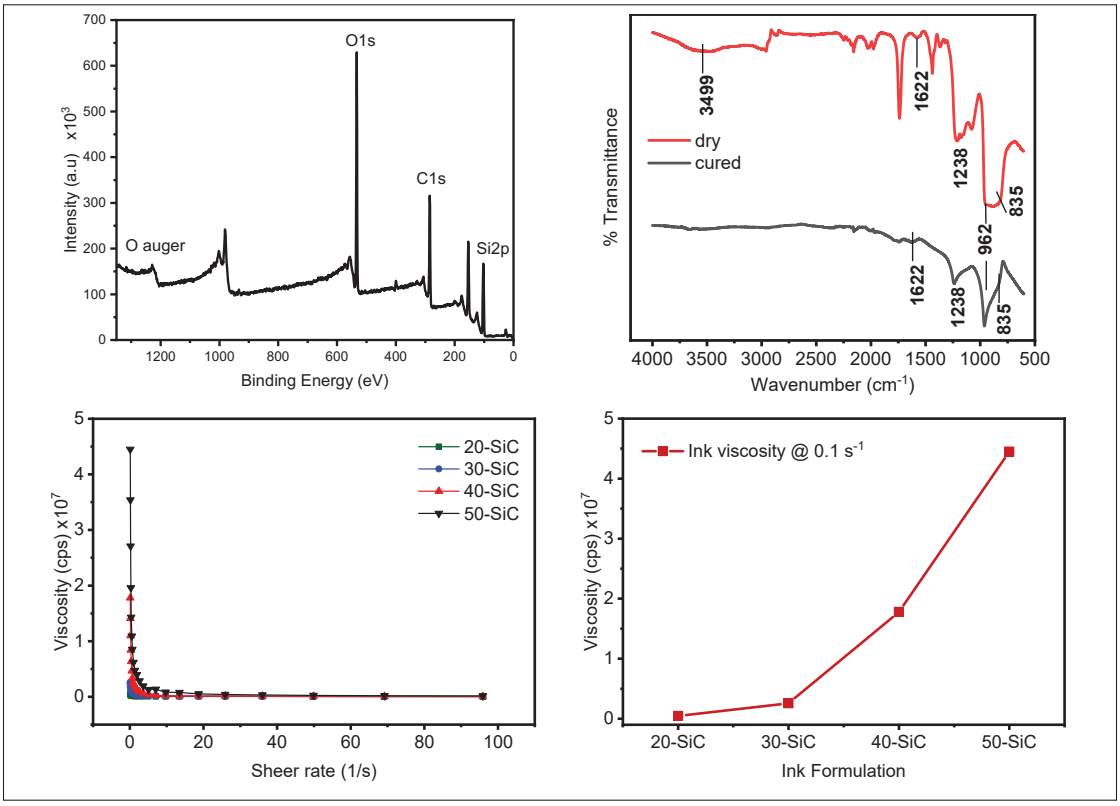

Figure 3.5 Characterization of the printed SiC humidity-sensitive films includes: (a) X-ray photoelectron spectroscopy (XPS) spectra confirming the presence of Si, O, and C species in the printed films, (b) Fourier transform infrared (FTIR) spectra indicating the absence of hydrophilic $-$OH functional groups, (c) viscosity versus shear rate curves for 20, 30, 40, and 50 wt.% SiC-loaded humidity-sensitive inks, and (d) viscosity as a function of SiC weight percentage

mation) shows that oxygen accounts for 30.8% of the atomic weight, likely due to oxygen-rich functional groups and silicon oxide formation. XPS spectra of individual species have been analyzed and presented in Figure I-4 in the Supplementary Information section. Deconvolution of the O1s peak (Figure I-4a)) revealed the presence of Si-O and C-O species at 533.5 eV. Similarly, deconvolution of the Si_2p peak (Figure I-4b)) identified peaks corresponding to $Si-C$, $Si-CO$, and $Si-O_2$, indicating an oxide layer formation during curing (Sun *et al.*, 2018c). Analysis of the C1s peak (Figure I-4c)) revealed $C-C$, $C-O$, and $O-C=O$ functional groups at 285, 287.2, and 289.8 eV, respectively (Duan, Jiang, Zhao, Huang, Wang, Zhang, Wu, Liu, Zhen & Tai, 2021b). Further calculations revealed that 29.2% of the oxygen species bond

with silicon, while only 1.6% bond with carbon. The absence of $C-OH$ bonding suggests a negligible amount of hydrophilic functional groups on the nanoparticle surface.

Fourier transform infrared (FTIR) spectroscopy was used to analyze the chemical structure of the SiC ink. Figure 3.5b) compares the spectra of ink cured at 300 °C for 180 minutes with ink dried at 80 °C for 60 minutes. Both samples exhibited peaks at 835 cm^{-1} and 962 cm^{-1}, corresponding to $Si-C$ and $Si-O-Si$ stretching vibrational modes, respectively (Jiang, Gao, Kong, Jin, Wei, Li & Xing, 2019b). Peaks at 3499 cm^{-1} and 1622 cm^{-1} correspond to $-OH$ stretching and bending modes, respectively, due to the physical adsorption of water vapor (Luo, Zhang, Hu, Zhang, Sun, Shen & Zhang, 2020; Sun *et al.*, 2018c). The absence of the 3499 cm^{-1} peak in the cured sample suggests the complete removal of hydroxyl groups from the SiC surface, whereas the 1622 cm^{-1} peak in the cured sample indicates minimal water vapor adsorption after fabrication. The lack of hydrophilic hydroxyl groups on the SiC surface likely impedes the adsorption and ionization of water molecules, limiting the flow of charge carriers across a broad %RH range. We hypothesize that the device's performance is driven by a swelling mechanism, resulting in a positive resistance change with increasing relative humidity (Montes-García & Samorì).

Viscosity is a key parameter in optimizing the flow characteristics of screen-printable inks, typically ranging between 1x10^3 to 2x10^7 centipoise (cps) according to IPC standards (ipc). Figure 3.5c) illustrates the viscosity behavior of 20, 30, 40, and 50 wt.% SiC-loaded inks over a shear rate range of 0.1–100 $(1/s)$ at room temperature. As the SiC loading increases, a significant rise in viscosity is observed, particularly between the 30 wt.% and 50 wt.% inks at a shear rate of 0.1 $(1/s)$ (Figure 3.5d)). The viscosity of the 40 wt.% SiC ink reaches 1.78x10^7 cps at a shear rate of 0.1 $(1/s)$, which is near the upper limit for screen-printable inks. However, the viscosity of the 50 wt.% ink increases to 4.75x10^7 cps, rendering it unsuitable for screen printing applications.

We next investigated the electronic properties of SiC sensor films with 20, 30, 40, and 50 wt.% particle loading, cured at 300 °C for durations of 60, 120, and 180 minutes. Electrical conductivity was measured using the four-point probe method at ambient temperature and humidity for five printed samples per test condition. As shown in Figure 3.6a) and Table I-3

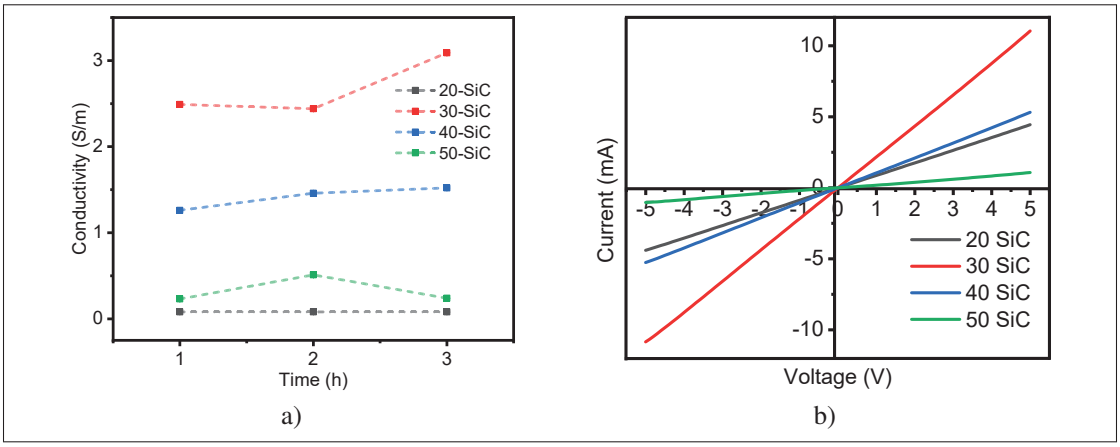

Figure 3.6 Energy dispersive X-ray (EDX) analysis micrographs display the distribution of (a) Si, (b) C, and (c) O species within the printed SiC film, confirming the material's composition and the presence of native surface oxidation on the SiC nanoparticles

(Supplementary Information), SiC inks with 30 wt.% and 40 wt.% particle loading cured for 180 minutes exhibited the highest electrical conductivities, reaching values of $3.09 \pm 3x10^{-4}$ and $1.52 \pm 1x10^{-2}$ S/m, respectively. Figure 3.6b) presents the current-voltage (I-V) characteristics of the printed humidity sensing films. The observed linear ohmic behavior between -5V and +5V indicates that the device functions as a resistor, where the current is directly proportional to the applied voltage (Dubourg, Katona, Rodović, Savić, Kitic, Niarchos, Jancović & Crnojević-Bengin, 2017).

Baseline resistance values for all printed inks were recorded under ambient conditions of temperature and humidity, with the data provided in Table I-4 (Supplementary Information). Films loaded with 20 wt.% particles exhibited minimal changes in baseline resistance across all three curing cycles. In contrast, the 50 wt.% loaded samples displayed the highest baseline resistance, with notable inconsistencies likely due to poor printability due to its high viscosity as previously discussed. For the 30 wt.% loaded samples, a 47.5% reduction in baseline resistance was observed between 60 and 180 minutes of curing, from $582 \pm 8\ \Omega$ to $306 \pm 30\ \Omega$. Similarly, the 40 wt.% samples exhibited a 33.5% reduction from $1078 \pm 19\ \Omega$ to $717 \pm 19\ \Omega$. These reductions in baseline resistance can be attributed to film densification with increasing curing time (Kim, Lee, Kim & Hur, 2020; Koshi, Nomura & Yoshida, 2020; Rao,

Mukherjee & Reddy, 2017). These results indicate that films cured at 300 °C for 180 minutes offer optimal performance for humidity sensors. It is noteworthy that the 30 wt.% samples exhibited lower overall baseline resistance compared to the 40 wt.% loadings.

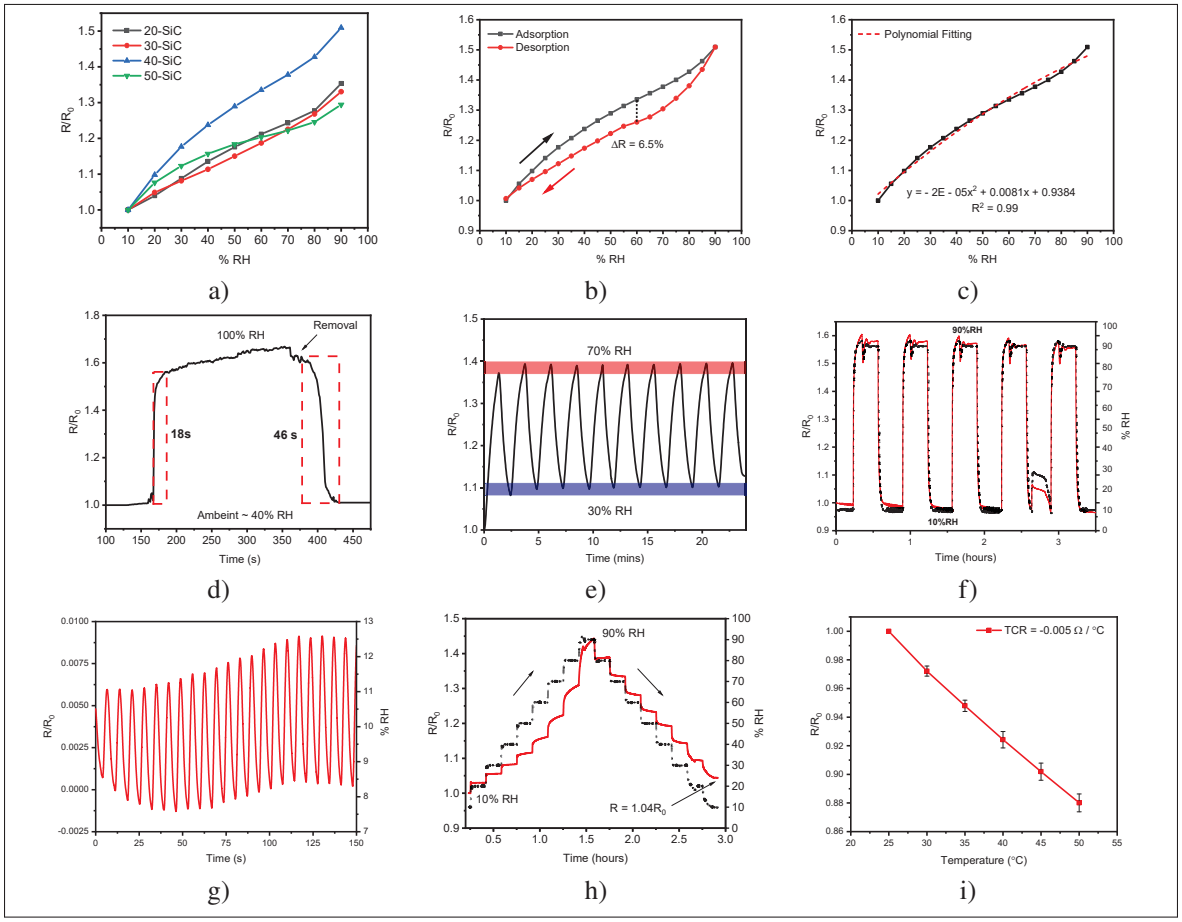

Figure 3.7 Characteristics of the printed SiC humidity sensors include: (a) response of 20, 30, 40, and 50 wt.% SiC humidity sensors cured at 300 °C for 180 minutes. Performance of the 40 wt.% SiC sensors: (b) adsorption/desorption plot showing a hysteresis of 6.5% at 60% RH, (c) response curve with polynomial fitting, (d) plot determining adsorption/desorption time constants via a drop test, (e) high-speed cycling of the SiC humidity sensor between 30-70% RH, (f) long-term cycling between 10-90% RH over a 3.5-hour period, (g) detection of minute variations in %RH using the 40 wt.% printed SiC humidity sensor, (h) long-term cycling between 10-90% RH in 10% RH increments, and (i) temperature coefficient of resistance measured at different temperatures

Figure 3.7a) demonstrates the humidity sensing performance of printed sensors with varying SiC loadings after curing for 180 minutes. Each concentration was tested with three samples, each cycled five times between 10-90% RH at a constant temperature of 25 °C. As expected, all devices showed increased electrical resistance with rising relative humidity (%RH), a behavior attributed to the swelling mechanism (Duan *et al.*, 2021b), which will be further elaborated in the subsequent section. Table 3.2 provides the evolution of the electrical response (R/R_0) for the humidity sensors across different loading concentrations and curing times. The humidity sensor response was calculated using Equation 3.1 (Joshi, Kim, Kim, Song, Park, Kim & Shin, 2020):

$$\%(R/R_0) = \frac{R_{90} - R_{10}}{R_{10}} x100\% \tag{3.1}$$

Table 3.2 Humidity sensor response (% change in resistance R/R_0) over different SiC loadings and cure temperatures.

Time (h)	**20-SiC**	**30-SiC**	**40-SiC**	**50-SiC**
	R/R$_0$			
1	31.65 ± 1.43	18.48 ± 1.60	28.75 ± 1.80	41.70 ± 3.88
2	31.85 ± 2.89	22 ± 1.68	37.65 ± 4	35.50 ± 3.15
3	29.31 ± 3.16	28.75 ± 3	**45.20 ± 5.71**	30.72 ± 4.73

Where R represents the electrical resistance at 10% and 90% RH. Notably, the 40 wt.% loaded SiC ink cured for 180 minutes demonstrated a response of 45.2 ± 5.71% (R/R_0), which was calculated using Eq. 3.1 over the tested humidity range. Conversely, the 20 wt.% loaded sensor exhibited consistent response across all curing times, suggesting that the particle densification process was complete after 60 minutes of curing. The 50 wt.% loading, however, resulted in a decrease in response, likely due to film cracking and disruption of conductive pathways. These findings are consistent with the observed changes in electrical conductivity and baseline resistance. The 30 wt.% and 40 wt.% loaded films showed enhanced response and sensitivity with longer curing times, corresponding with their electrical properties.

Device sensitivity and hysteresis are calculated as per equations 3.2 and 3.3 respectively.

$$S = \frac{R_{90} - R_{10}}{\Delta RH} \tag{3.2}$$

$$H = \frac{\Delta H_{max}}{S} \tag{3.3}$$

The sensitivity of the 40 wt.% SiC sensor was determined to be 5.34 ± 0.6 Ω/%RH, with a maximum hysteresis of 6.5% RH at 60% RH. Further characterization of the 40 wt.% SiC ink is shown in Figure 3.7b), which illustrates the adsorption and desorption behavior between 10-90% RH. The sensor followed a second-order polynomial fit governed by Equation 4.1, with an R^2 coefficient of 0.99, as depicted in Figure 3.7c).

$$y = -0.5X^2 + 0.0081X + 0.9384 \tag{3.4}$$

The adsorption and desorption time constants (response and recovery times) are crucial in assessing how quickly a sensor can detect changes in relative humidity. The testing procedure, detailed in the supporting information, is summarized in Figure I-3. Upon water drop deposition, Figure 3.7d) shows a rapid increase in device response until saturation, followed by a sharp drop in response after water removal, eventually returning to the baseline state. Since this test was conducted under ambient conditions, the %RH ranged between 40% (ambient humidity) and 100% (water saturation). The measured adsorption and desorption times were 18 s and 46 s, respectively. These time constants are consistent with other recently reported printed humidity sensors (Duan *et al.*, 2021b; Li *et al.*, 2014; Wang *et al.*, 2012b).

We evaluated the reproducibility of the humidity sensor responses through rapid cycling at the maximum permissible speed of the test chamber, within a limited testing range of 30-70% RH, as shown in Figure 3.7e). The sensors exhibit minimal variability, with only a slight drift in baseline resistance during the initial cycles. This drift can be tentatively attributed to the relaxation of the porous SiC particle network as the RH changes. Long-term reliability was also assessed by cycling the sensors over extended periods. Initially, the sensors were cycled five

times between 10-90% RH over 3.5 hours, as presented in Figure 3.7f). The sensors responded consistently to the RH variations, indicating excellent long-term cycling stability. Moreover, the sensors demonstrated the ability to detect small variations in RH (≤4%), occurring as the test chamber stabilized at each point. Remarkably, response changes as small as 0.003% (R/R_0) were successfully recorded, as illustrated in Figure 3.7g). In a separate experiment (Figure 3.7h)), the sensors were subjected to incremental changes in humidity from 10-90% RH, with 10% RH steps and a stabilization period of 15 minutes between each step. The sensors maintained stable performance with only a slight baseline resistance drift (4%) after the cycling was completed. The temperature dependence of the sensor, measured between 25 °C and 50 °C at a constant 40% RH, is depicted in Figure 3.7i). The three devices tested exhibited a small negative temperature coefficient of resistance (NTCR) of $-0.005\,\Omega\,°C^{-1}$, which is likely due to increased charge carrier hopping between neighboring SiC nanoparticles as the temperature rises (Schubert, Münch, Schuurman, Poulain, Kita & Moos, 2019). Notably, the SiC humidity sensors display a positive resistance change with increasing RH and a negative resistance change with rising temperature. However, the small NTCR suggests that temperature has a limited impact on overall sensor performance.

For a comparative analysis, the characteristics of recently reported (1) printed resistive humidity sensors and (2) SiC-based humidity sensors are summarized in Table 3.3. It is worth noting that no prior studies on fully screen-printed SiC humidity sensors were found. Our sensors present an optimal balance between performance, material cost, fabrication cost, and architectural simplicity. Although some solid-state devices offer comparable or superior performance and response times (Arman Kuzubasoglu, 2022), their high material costs and fabrication complexities limit their suitability for large-scale applications (Phung, Gafurov, Kim, Kim, Kim & Lee, 2021). Table 3.3 also highlights SiC humidity sensors fabricated through more intricate processes such as chemical vapor deposition or SiC nanowire networks. These nanowire-based sensors offer higher aspect ratios and an increased number of contact points compared to nanoparticle-based devices, potentially leading to higher responses, while a well-dispersed porous SiC network enables faster adsorption and desorption times. However, the fabrication techniques used for these sensors

significantly increase processing costs. In contrast, our screen-printed SiC nanoparticle-based devices provide sufficient performance for many applications, while being produced at a much lower cost using manufacturing-grade equipment.

Table 3.3 Comparison of sensing performance of recently reported humidity senors

Material	**Fabrication**	**Device Type**	**Testing Range (%RH)**	**Response (R/R_0)**	**Adsorption/ desportion time**	**Ref**
Printed resistive humiditiy sensors						
CNF/CB/TX-100	screen printing	resistive	30-90	120%	10s / 6s	Tachibana *et al.* (2022)
daily carbon ink	paint brush	resistive	0-95	178.7%	56s / 14s	Duan *et al.* (2021b)
Graphene	CVD	resistive	10-90	1.2%	0.6 / 0.4	Smith, Elgammal, Niklaus, Delin, Fischer, Vaziri, Forsberg, Råsander, Hugosson, Bergqvist, Schröder, Kataria, Östling & Lemme (2015)
MWCNT/polyimide	in-situ polymerization	resistive	20-90	12.8%	5s / 600s	Tang, Chan & Zhang (2011)
RGO/PDDA	layered self-assembly	resistive	11-97	37.4%	108s / 94s	Zhang, Tong & Xia (2014a)
PEG / gold nano particles	inkjet printing	resistive	1.8-95	10^4	1.2s / 3s	Su, Chiu, Chen, Yesilmen, Schulz, Ketelsen, Vossmeyer & Liao (2019)
PHEMA	gravure printing	resistive	30-80	172%	-	Reddy, Narakathu, Atashbar, Rebros, Rebrosova & Joyce (2011a)
MWCNT w/ integrated printed heater	screen printing	resistive	10-90	55%	4.6 min / 30.9 min	Zhang, Maddipatla, Bose, Hajian, Narakathu, Williams, Mitchell & Atashbar (2020b)
Graphene / methyl red	inkjet printing	resistive	5-95	96.36	0.251s / 0.35s	Ali, Hassan, Hassan, Bae & Lee (2016)
polyDADMAC	direct write printing	resistive	10-90	> 99%	7s / 213s	Yan, Huang, Sang, Liang, Wan, Shao & Gu (2021)
Reported SiC humidity sensors						
SiC 2D nanosheets	spin coating	resistive	11-95	-	3s / 3s	Sun *et al.* (2018c)
SiC on $p-Si$ wafer	PECVD	capacitive	10-90	200%	3 min / 4 min	Connolly, Pham, Groeneweg, Sarro & French (2004b)
SiC nanopaper	SiC nanowire compression	resistive	30-65	90%	41s / 124s	Li *et al.* (2014)
SiC nanowires on nanoporous Si pillar array	CVD + etching	capacitive	11-95	960%	105s / 85s	Wang *et al.* (2012b)
SiC nano particle ink	**screen printing**	**resistive**	**10-90**	**45.2%**	**18s / 46s**	**This work**

3.3.2 Humidity Sensing Mechanism

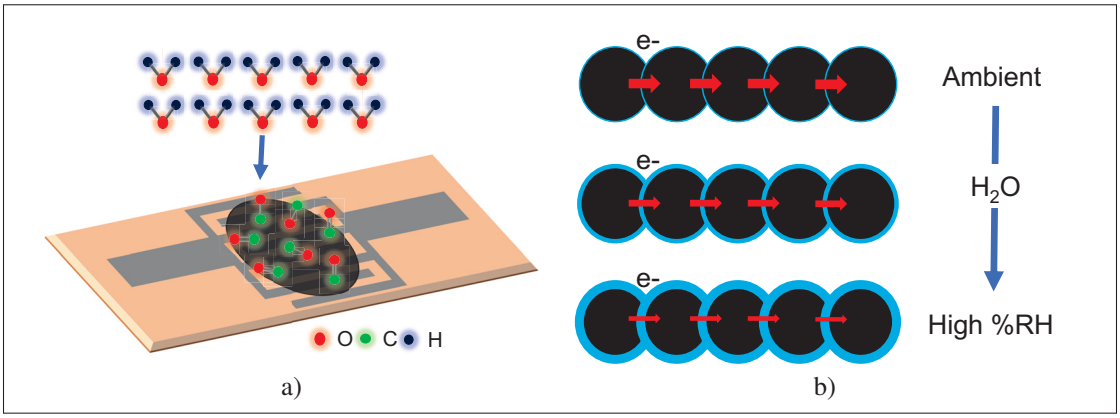

Figure 3.8 Representation of the humidity sensing mechanism: (a) schematic illustrating the adsorption of water molecules onto the SiC humidity sensor film, and (b) the reduction in charge carrier mobility with increasing %RH

The responsivity of resistance-type humidity sensors is primarily driven by the adsorption and desorption of water molecules by the sensing material (Duan, Jiang, Yan, Wang, Yuan, Zhao, Sun, Xie, Du & Tai, 2019). A negative resistance change with increasing RH can generally be attributed to the presence of hydrophilic functional groups, such as $-\mathrm{OH}$, $\mathrm{C}=\mathrm{O}$, and $\mathrm{C}-\mathrm{O}$, which promote water molecule attachment to the sensing film surface (Sun *et al.*, 2018c). This leads to ionization and the production of hydronium ions (H_3O^+) (Jang & Han, 2017), facilitating proton movement and thereby reducing resistance through proton hopping in the Grotthuss chain reaction (Li, Zhang, Yang, Wu, Wu, Jiang, Zhou & Liu, 2022). Conversely, positive resistance change in humidity-sensitive materials typically results from swelling of the sensing film as it absorbs water molecules (Dai, Feng, Li, Zhang & Li, 2018; Jiang, Fei, Jiang, Wang & Zhang, 2014; Jung, Park, Park & Kim, 2006; Liu, Miao, Liu, Lin, Zhang, Song, Huang & Lin, 2015; Yoo, Lim, Min, Lee, Lee & Park, 2010b). In our case, the printed SiC humidity sensing films exhibit a positive resistance change with increasing RH. This can be further elucidated through XPS and FTIR measurements, as shown in Figure 3.5a). XPS analysis of the SiC thermistor films reveals that only 1.6% of atomic oxygen is bonded to carbon, forming $\mathrm{C}-\mathrm{O}$ and $\mathrm{O}-\mathrm{C}=\mathrm{O}$ hydrophilic groups. The results also confirm the formation of a silicon oxide shell around the

SiC particles, with 8.1% and 11.8% atomic oxygen bonded to silicon atoms forming $Si-CO$ and $Si-O_2$ species, respectively. Silicon dioxide (SiO_2) is known for its strong hydrophilic properties (Xu & Zhang, 2021) due to the presence of hydroxyl ($-OH$) groups on its surface, which is why it is often used to enhance humidity sensing performance (Duan, Zhao, Li, Wang, Jiang, Zhang, Liu & Tai, 2020; Gomez, Morgan, Hayes-Gill, Correia & Korposh, 2018; Jung *et al.*, 2006; Viegas, Goicoechea, Corres, Santos, Ferreira, Araújo & Matias, 2009). However, FTIR measurements (Figure 3.5b)) confirm that all $-OH$ groups are removed from the sensing film after curing at 300 °C.

Figure 3.8 presents a schematic illustration of the adsorption mechanism of water molecules onto printed SiC films. Under dry conditions, the electrical resistance of SiC remains minimal, as electron transport is facilitated by tunneling between the nanoparticles (Sachin, Pandey & Jaiswal, 2022). The porous nature of the SiC nanoparticle film offers a high surface-to-volume ratio, allowing significant adsorption of water molecules via capillary condensation (Park, Seo, Park, Hwang, Lee, Jung & Yoo, 2022). As the relative humidity (%RH) increases, water molecules infiltrate the film's pores, eventually reaching equilibrium. The accumulation of adsorbed water leads to the formation of a water film around the SiC nanoparticles, thereby impeding the electron tunneling process (Duan *et al.*, 2021b). Consequently, the device exhibits higher electrical resistance at elevated %RH levels. It is important to note that deionized (DI) water, with its low electrical conductivity (approximately 1–5 μS/m) (Aldosky & Shamdeen, 2010), was employed in these experiments. While a small fraction of water molecules may dissociate to form hydronium ions, potentially enhancing electron conduction, this contribution is expected to be negligible and unlikely to significantly impact the sensing mechanism.

3.3.3 Device Integration

Due to their remarkable sensitivity and rapid response, the printed SiC humidity sensors demonstrate potential for a broad spectrum of applications. Prior research has shown that tracking variations in relative humidity (%RH) during breathing cycles can provide access to critical respiratory parameters, aiding in preventative healthcare for patients (Vaussenat,

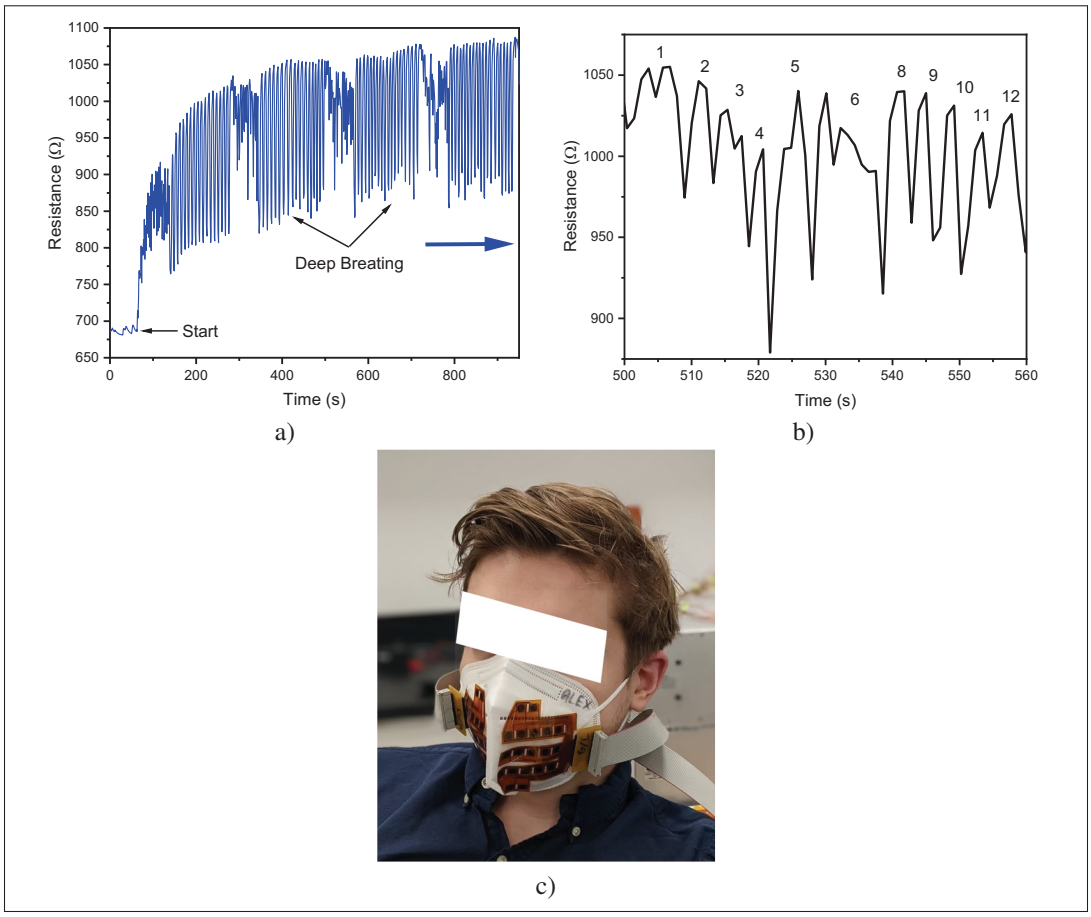

Figure 3.9 Demonstration of the application of printed SiC humidity sensors for preventative healthcare: (a) sensor response during human breathing with SiC humidity sensors attached to the exterior of a KN95 mask, (b) determination of human respiration rate based on the sensor response, and (c) photograph of the breath monitoring setup used for the measurements

Bhattacharya, Payette, Benavides-Guerrero, Perrotton, Gerlein & Cloutier, 2023). In this study, we selected a KN95 mask for integrating flexible printed SiC sensors to monitor breath, as illustrated in Figure 3.9. The sensor arrays were fabricated using an optimized 40%-loaded SiC ink formulation, cured at 300 °C for 180 minutes. These arrays were affixed to the exterior surface of the mask, as depicted in Figure 3.9c).

A simple experiment was conducted wherein a subject breathed normally for 60 seconds, followed by 10 deep respirations. Resistance values were recorded at one-second intervals, as

shown in Figure 3.9a). Owing to the rapid adsorption and desorption response of the printed sensors, distinct variations in sensor output were observed between normal and deep breathing cycles. The data acquired from such trials hold the potential for extracting physiological parameters related to respiratory rate, monitoring of chronic obstructive pulmonary diseases (COPD), asthma, and sleep apnea (Bhattacharjee, Nemade & Bandyopadhyay, 2017; Duan, Jiang & Tai, 2021a; Kano, Jarulertwathana, Mohd-Noor, Hyun, Asahara & Mekaru, 2022; Vaussenat *et al.*, 2023). For instance, Figure 3.9b) displays the change in %RH over a 60-second period, corresponding to 12 response cycles, which aligns with a normal and healthy respiration rate (Russo, Santarelli & O'Rourke, 2017). Additionally, a baseline shift in sensor resistance was noted throughout the test duration. Since the sensors were placed on the exterior of the mask, this baseline shift may be indicative of humidity saturation or potential clogging of the KN95 mask.

These humidity sensor arrays can also be employed to assess humidity distribution across a surface, as demonstrated in Figure 3.10. Figure 3.10a) illustrates a matrix of 18 sensors, with a hand placed over the sensors both with and without a glove. A rise in resistance is observed when the bare hand approaches the sensors, attributed to the moisture from the skin. In contrast, no change in sensor response occurs when the hand with a glove is placed near the sensor array. Figures 3.10b) and c) capture the transient resistance behavior in proximity to the bare hand and the recovery when exposed to hot air after the hand is removed. This highlights the potential for mapping humidity changes across large areas, which is valuable for applications such as leak and flood detection (Arshad, Ogie, Barthelemy, Pradhan, Verstaevel & Perez, 2019).

This study demonstrates that the printed SiC humidity sensors exhibit high sensitivity and reproducibility. Furthermore, the chemical inertness and biocompatibility of both Kapton and SiC (Altenberend, Molina-Lopez, Oprea, Briand, Bârsan, De Rooij & Weimar, 2013; Constantin, Aflori, Damian & Rusu, 2019b; Qu, Hu, Liu, Li & Ding, 2017; Santavirta, Takagi, Nordsletten, Anttila, Lappalainen & Konttinen, 1998) suggest these sensors could be effectively utilized in moisture detection within critical environments such as medical facilities, refineries, and greenhouses. Notably, the relatively low cost of silver ink, the Kapton substrate, and

SiC powder makes these sensors ideal candidates for low-cost, high-volume applications (Arman Kuzubasoglu, 2022).

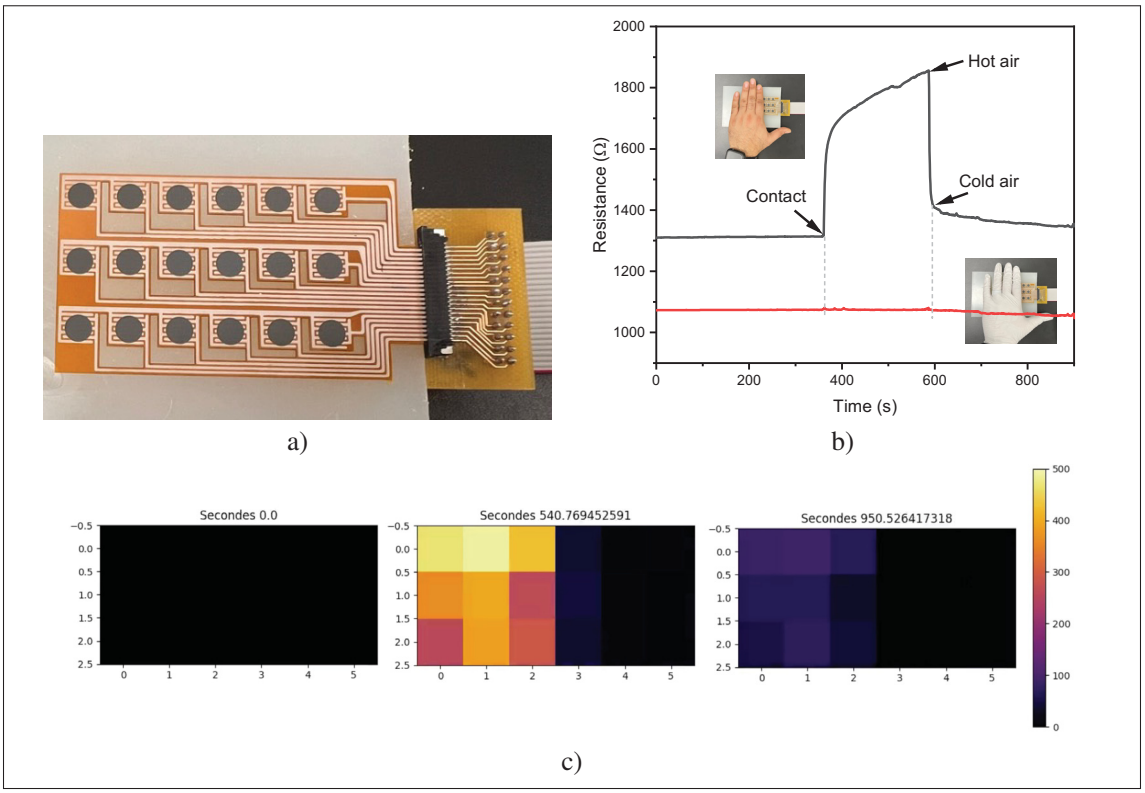

Figure 3.10 Demonstration of the application of printed SiC humidity sensors towards large area humidity detection: (a) sminiaturized implementation of a 6x3 array of SiC humidity sensors, (b) demonstration of the change in response of the printed SiC humidity sensor array with contact from human hand with and without a glove (barrier), (c) illustrating depicting the change in response

3.4 Conclusion

This study presents a high-performance humidity sensor based on a screen-printable SiC nanoparticle ink formulation. The simplicity of the device architecture, use of commercially available low-cost materials, and biocompatibility make these sensors applicable across a broad range of fields. Various SiC loadings and curing temperatures were evaluated, with the optimal performance observed at a 40 wt.% SiC particle loading and curing at 300 °C for 180 minutes. Under these conditions, the sensor achieved a response of 45.2 ± 5.7 % (R/R_0) between 10%

RH and 90% RH, with fast adsorption and desorption times of 18 seconds and 46 seconds, respectively.

These humidity sensors exhibit an increase in electrical resistance with rising %RH, primarily due to physical swelling, as the absence of hydrophilic $-OH$ groups limits water absorption. The sensor's response follows a second-order polynomial fit to %RH changes, with a high correlation coefficient (R^2 = 0.99). Additionally, the sensor demonstrated excellent thermal stability, exhibiting a low temperature coefficient of resistance (TCR) of -0.005 $\Omega/°C$. After prolonged exposure at various humidity levels, the baseline resistance showed minimal drift, with only a 4% change over three hours.

As a proof-of-concept, we demonstrated the potential application of these printed humidity sensors for monitoring human respiration within a KN95 mask. Moreover, the sensors were implemented in a matrix configuration to detect skin contact. Due to their high performance, fast response times, and stability, these sensors hold promise for critical applications in environments such as chemical storage, food production, agriculture, and flood detection.

Acknowledgments

The authors would like to thank Paul Fourmont for his mentorship towards the experimental plan. Mohammad Sadaati for perfoming the SEM and EDX analysis and Josianne Lefebvre for performing the XPS analysis. S.G.C would like to thank the NSERC-Discovery program and the Canada Research Chair program for the financial support for this project.

CHAPTER 4

ALL SCREEN PRINTED AND FLEXIBLE SILICON CARBIDE NTC THERMISTORS FOR TEMPERATURE SENSING APPLICATIONS

Wadhwa Arjun[1], Benavides-Guerrero Jaime[2], Gratuze Mathieu[1], Bolduc Martin[2], Cloutier G. Sylvain[1]

[1] Département de Génie Électrique, École de Technologie Supérieure,
1100 Rue Notre-Dame Ouest, Montréal, Québec, H3C 1K3, Canada
[2] Département de génie mécanique, Université du Québec à Trois-Rivières,
Trois-Rivi‘eres, QC G8Z 4M3, Canada

Article published in
MDPI Materials
Special issue: Latest Technologies in the Additive Manufacturing of Flexible and Printable Electronics
May 22, 2024.
https://www.mdpi.com/1996-1944/17/11/2489

Abstract

In this study, Silicon Carbide (SiC) nano-particle based serigraphic printing inks were formulated to fabricate highly sensitive and wide temperature range printed thermistors. Inter-digitated electrodes (IDE's) were screen printed onto Kapton® substrate using commercially avaiable silver ink. Thermistor inks with different weight ratios of SiC nano-particles were printed atop the IDE structures to form fully printed thermistors. The thermistors were tested over a wide temperature range form 25°C to 170°C, exhibiting excellent repeatability and stability over 15 hours of continuous operation. Optimal device performance was achieved with 30 wt.% SiC-polyimide ink. We report highly sensitive devices with a TCR of -0.556 %/°C, a thermal coefficient of 502 K (β-index) and an activation energy of 0.08 eV. Further, the thermistor demonstrates an accuracy of ±1.35°C which is well within the range offered by commercially available high sensitivity thermistors. SiC thermistors exhibit a small 6.5% drift due to changes in relative humidity between 10-90 %RH and a 4.2 % drift in baseline resistance after 100 cycles of aggressive bend testing at a 40°angle. The use of commercially available low cost

materials, simplicity of design and fabrication techniques coupled with the chemical inertness of the Kapton® substrate and SiC nanoparticles paves the way to use all-printed SiC thermistors towards a wide range of applications where temperature monitoring is vital for optimal system performance.

Keywords

Temperature Sensing, Negative Temperature Coefficient (NTC), Printed Electronics, Printed Temperature Sensors, Thermistors, Silicon Carbide, Wide Band-gap Semiconductor, Screen Printing, Silver ink.

4.1 Introduction

Temperature sensing is crucial in key industries such as automotive (Gierth, Rebenklau, Augsburg, Bachmann & Niedermeyer, 2018), health (Ali *et al.*, 2019; Ma & Soin, 2022), aerospace (Fapanni, Sardini, Borghetti, Serpelloni & Bellotti, 2023), agriculture (Rayhana, Xiao & Liu, 2021) and consumer electronics (Kuzubasoglu & Bahadir, 2020). Measuring temperature is a key variable in controlling and monitoring the intended function of a system (Khan, Ali, Khan & Bermak, 2021) and to optimize process yields (Liu, Tian, Zhang, Zhang, Liu, Zhao, Shi, Lin & Jiang, 2021). The three predominant types of printed temperature sensors are: 1. resistance temperature detectors (RTD's) (Turkani, Narakathu, Maddipatla, Altay, Fleming, Bazuin & Atashbar, 2018b), 2. thermocouples (Knoll, Offenzeller, Mayrhofer, Jakoby & Hilber, 2018b) and 3. thermistors (Katerinopoulou, Zalar, Sweelssen, Kiriakidis, Rentrop, Groen, Gelinck, van den Brand & Smits, 2019a). Choosing the correct type of temperature sensor is dependant on the sensitivity, accuracy and temperature range required for the intended applications. Thermocouples are widely used in several industries due to their small form factor, low cost and wide temperature range. Depending on the materials of construction, some thermocouple can be used in ultra high temperature conditions up to 2300 °C (Elliott, Large, Pearce & Machin, 2014). However, when compared to thermistors; thermocouples have a lower accuracy and sensitivity as their change in response is generally only a few milli-volts (Feteira, 2009). For lower temperature ranges, thermistors

and RTD's are used where RTD's typically exhibit lower sensitivity and have a slower response time as compared to thermistors (Feteira, 2009). Thermistors on the other hand, provide high sensitivity ranging between 2 to -6%/°C (Fourmont, Bai, Fortier & Cloutier, 2022a) which makes them highly desirable for sensing across a wide variety of applications (Aleksić & Nikolić, 2017). Additionally, thermistors exhibit a non-linear negative temperature coefficient (NTC) as electrical resistance decreases with increase in temperature (Turkani *et al.*, 2018a). The thermal index β of a thermistor is an indicator or its sensitivity. Devices with high β values (3000 - 5000K) are typically used for high temperature sensing applications while those with low β values (14 - 170K) are used for applications such as integrated circuit temperature compensation and random access storage memories etc (Fourmont *et al.*, 2022a; Yan, Wang & Lee, 2015)

Several fabrication techniques such as microfabricaion (Inomata, Inaoka, Okabe, Funatsu & Ono, 2020), tape casting (Chatterjee, Sengupta & Maiti, 1999) etc. have been employed in the fabrication of thermistors. With advances in the field of printed electronics over the past two decades, it has become increasingly possible to fabricate low cost, flexible temperature sensors (Barmpakos & Kaltsas, 2021). Literature suggests a significant increase in academic articles toward printed thermistors utilizing a variety of materials, substrates and printing methods for a different applications. Printing techniques such as screen (Turkani *et al.*, 2018a), inkjet (Huang *et al.*, 2013) and aerosol jet (Wang, Hong, Li & Young, 2017) printing have been successfully employed to fabricate all printed thermistors. Polymeric sensing materials such poly(3,4-ethylenedioxythiophene)-poly(styrenesulfonate) (PEDOT:PSS) (Khalaf, Ramírez, Mohamed & Issa, 2022) and Polydimethylsiloxane (PDMS) (Zhang, Chen, Bin, Zheng, San & Hofmann, 2018) have been widely printed to fabricate low-cost thermistors along with carbon derivaties such as CNT's (Turkani *et al.*, 2018a), graphene oxide (Romero, Rivadeneyra, Toral, Castillo, García-Ruiz, Morales & Rodriguez, 2018) and reduced graphene oxide (Li, Cui, Li, Liu, Li, Jian, Li, Yang & Ren, 2023b). Semi-metallic graphene is an unique material that has been widely employed as printed thermistors (Yan *et al.*, 2015) and RTD's (Kabiri Ameri, Ho, Jang, Tao, Wang, Wang, Schnyer, Akinwande & Lu, 2017). The above mentioned sensing materials are generally restricted to relatively low temperature sensing ranges generally below

100 °C due to thermal degradation. The use of ceramics combined with higher temperature sustaining substrates such as Kapton® promises a significant increase in the temperature sensing range of the printed device.

Various ceramic materials have been employed towards fabrication of wide range temperature sensors, some having a sensing range as high as 1500 °C (Ji, Tan, Lu, Zhang, Zhang & Xiong, 2019; Reimann, Töpfer, Barth, Bartsch & Müller, 2013b; Tan, Luo, Xiong, Kang, Ji, Zhang, Yang, Wang, Xue, Liu et al., 2014; Tan, Wei, Chen, Luo, Wu, Li & Xiong, 2015) using complex low and high temperature co-firing techniques (LTCC and HTCC). Transient metal oxides such as $\mathrm{Ni_xMn_{2-x}O_4}$ (Uppuluri & Szwagierczak, 2022), $\mathrm{MnNiCuO}$ (Le & Ju, 2021), and $\mathrm{BiFeO_3}$ (Fourmont *et al.*, 2022a) have been used to fabricate NTC thermistor. The fabrication of ceramic sensing devices usual employs ultra high sintering temperatures and inert environments which increases overall fabrication cost and complexity (Reimann, Töpfer, Barth, Bartsch & Muller, 2013a). Wide band gap semiconducting materials such as ZnO (II-VI), GaN (III-V) and SiC (IV-IV) exhibit excellent electrical and mechanical properties along with chemical inertness, and optical transparency which make them ideal candidates for flexible electronics devices (Nguyen, Nguyen, Nguyen, Yadav, Dinh, Masud, Singha, Do, Barton, Ta et al., 2021b). Out of these, Silicon Carbide (SiC) has been gaining significant interest in recent years towards fabricating bio-sensing devices (Oliveros *et al.*, 2013) owing to its bio compatibility (Coletti, Jaroszeski, Pallaoro, Hoff, Iannotta & Saddow, 2007; Kotzar, Freas, Abel, Fleischman, Roy, Zorman, Moran & Melzak, 2002; Zorman, 2009). Silicon Carbide comprises of covalent bonded Si and C atoms with very short bond lengths of 1.89 Å(Yang, Zhao, Fan, Deng, Lv, Lin & Li, 2014) which attribute to their mechanical and chemical stability with an electronic band-gap ranging between 2.4 to 3.2 eV depending on the polytype (Oliveros *et al.*, 2013). Silicon Carbide exists in several polytypes out of which cubic 3C-SiC (β-SiC), 4H-SiC and 6H-SiC (α-SiC) are most commonly grown and used for sensing applications. However, β-SiC is widely available in high purity and relatively low cost nano particle form. Silicon Carbide has been widely used to fabricate NTC thermistors that are predominately used in ultra high temperature and harsh environments. These thermistors are generally fabricated via processes such as chemical vapour

depositon (CVD) (de Vasconcelos, Khan, Zhang, Uchida & Katsube, 2000; Phan, Nguyen, Dinh, Qamar, Iacopi, Lu, Dao, Rais-Zadeh & Nguyen, 2019a), epitaxial SiC crystal growth (Dakshinamurthy, Quick & Kar, 2007), sputter coated electrodes on SiC single crystal wafers (Boltovets, Kholevchuk, Konakova, Kudryk, Lytvyn, Milenin, Mitin & Mitin, 2006) and transfer based (Phan *et al.*, 2019b) techniques.

SiC has been sparsely used in the field of printed electronics. Researchers have demonstrated direct ink writing of SiC in borosiloxane-colloidal dispersion for Microwave optics (Larson, Choi, Gallardo, Henderson, Niemack, Rajagopalan & Shepherd, 2016), inkjet printable SiC ink (Mott & Evans, 2001) and vat polymerization based electrically conductive SiC features (Guo, An, Khuje, Chivate, Li, Wu, Hu, Armstrong, Ren & Zhou, 2022). SiC nano particles have been employed towards applications such as electrochemical (Hallaj, Soltani, Mafakheri & Ghadermazi, 2021; Roushani, Nezhadali, Jalilian & Azadbakht, 2017), gas (Chen, Zhang, Wang & Li, 2014) and humidity (Ahmed, Abduljalil & Hashim, 2019a) sensing applications. There has been very limited work done towards printed SiC nanoparticles towards temperature sensing applications. In 2022, Aljasar et al (Aljasar *et al.*, 2022). demonstrated laser sintered SiC nano particle temperature sensors via drop casting up operational to 86 °C.

In this study, we focus on fabrication of low-cost and flexible screen printed SiC thermistors for a wide temperature range between 25 °C to +170 °C. For this purpose SiC nanoparticles are impregnated into a polymeric matrix of 4,4'-oxydianiline (polyimide) resin via simple dispersion techniques. Initially, we study the characteristics of the commercially sourced SiC nanoparticles to assess their crystalline and composition. Next we measure electronic properties of the printed SiC sensing films and determine the optimal loading fraction of particles in the ink. The fully fabricated devices are then tested for temperature sensing performance, durability and long term stability. The dependency of the SiC thermistors on relative humidity and mechanical deformation (bend testing) will also be investigated. Lastly, we calculate key thermistor performance matrices such as its temperature coefficient of resistance (TCR), thermal coefficient (β-index) and its activation energy (eV).

4.2 Experimental Section

4.2.1 Materials

Cubic Silicon Carbide (3C-SiC, beta, 99+ %, <80 nm, cubic) nanoparticles were acquired from US Research Nanomaterials, Inc (US2022). Poly(pyromellitic dianhydride- co-4,4-oxydianiline) amic acid resin was procured from Millipore Sigma (Product: 575771). 0.005-inch thick FPC Kapton® was sourced from American Durafilm. 0.002-inch thick, adhesive backed Kapton® was procured from Mcmaster-Carr (Product: 2271K72). Henkel supplied Loctite® EDAG 725A silver screen printing paste. No modifications were made to any of the materials upon receipt.

4.2.2 Ink Formulation

The screen-printable thermistor ink was formulated by incorporating varying quantities of SiC nanoparticles into the poly(pyromellitic dianhydride-co-4,4-oxydianiline) amic acid solution, ranging from 30 - 40 wt.% in 5 wt.% increments. To achieve homogeneous dispersion, a two-step dispersion process was employed. The SiC nanopowder was initially weighed and added in approximately four portions to the resin. Following each addition, the ink was mixed using a planetary mixer (Thinky ARE-310) for three cycles of one minute each, with one minute degassing intervals at 2,000 rpm. This meticulous process ensured thorough blending of the nanopowder and resin, resulting in a stable dispersion with a shelf life exceeding 6 months.

4.2.3 Device Design and Fabrication

The presented sensor structure includes two main functional layers: 1. the printed silver inter-digitated electrodes and 2. printed SiC active sensing layer. Three devices were printed for each test point to ensure repeatability. Initially, the Kapton® substrate was prepared by cleaning with 99.9% pure acetone (Millipore Sigma 270725). Silver paste was printed on to the Kapton® substrate using a KEKO P250 automatic screen printer with a 325 mesh, 0.001-inch emulsion thickness screen in an interdigitated electrodes (IDEs) format. The IDEs had a trace width and

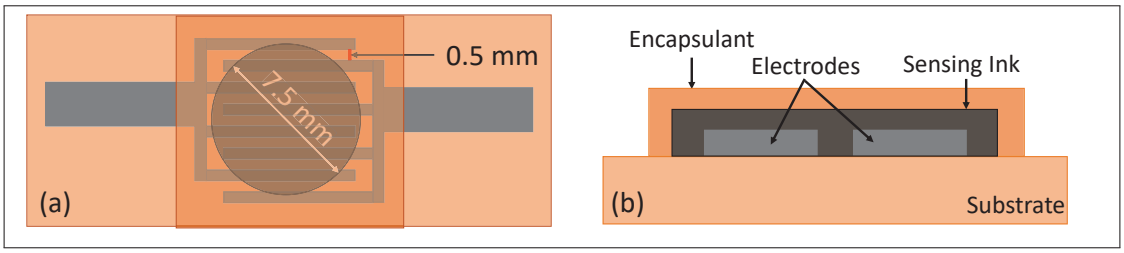

Figure 4.1 SiC thermistor schematic a) top view b) side view

spacing of 0.5 mm, as depicted in figure 4.1. The silver ink was cured in air at 300 °C for 60 minutes in a Mancorp (MC301N) reflow oven. Thermistor inks were then applied to the cured IDEs in 7.5 mm diameter circles and cured in the reflow oven for 60 minutes at 200 °C to achieve complete polymerization of the resin. Under these conditions, a polycondensation reaction occurs between a diamine and a dianhydride, resulting in the formation of polyimide (Fourmont *et al.*, 2022a). Lastly, a 0.002-inch thick adhesive backed polyimide film was applied atop two of the printed sensors to inhibit the influence of atmospheric humidity. Figures 4.2 a)-c) illustrate the fabrication process of the SiC thermistors. As high resolution optical microscpe image of the printed SiC thermsitor can be seen in Figure 4.2 d).

4.2.4 Characterization Methods

X-ray diffraction patterns were obtained using the XRD-$X'Pert^3$ system with a cobalt source and Raman micro-spectra of the SiC nano power were obtained using the and WITec alpha300A raman microspectoscopy systems with a 532 nm green laser. Ultraviolet-visible (UV-Vis) absorption spectra of the SiC nano powder was obtained from via the Perkin Elmer, Lambda 750 system. Micrographs of the printed films is obtained using a Hitachi SU8230 scanning electron microscope (SEM) equipped with a Bruker, QUANTAX FlatQUAD EDX detector for precise elemental mapping. Transmission electron microscopy on the nano particles is performed via the Jeol, JEM-F200 multi-purpose electron microscope. A Keyence VHX7000 optical microscope was used to obtain high resolution images of the sensor. Ossilla T2001A3 four-point-probe was utilized to measure the conductivity of the printed SiC films. The printed thermistors were tested in a controlled temperature and humidity 6-channel micro probe station from Nextron®

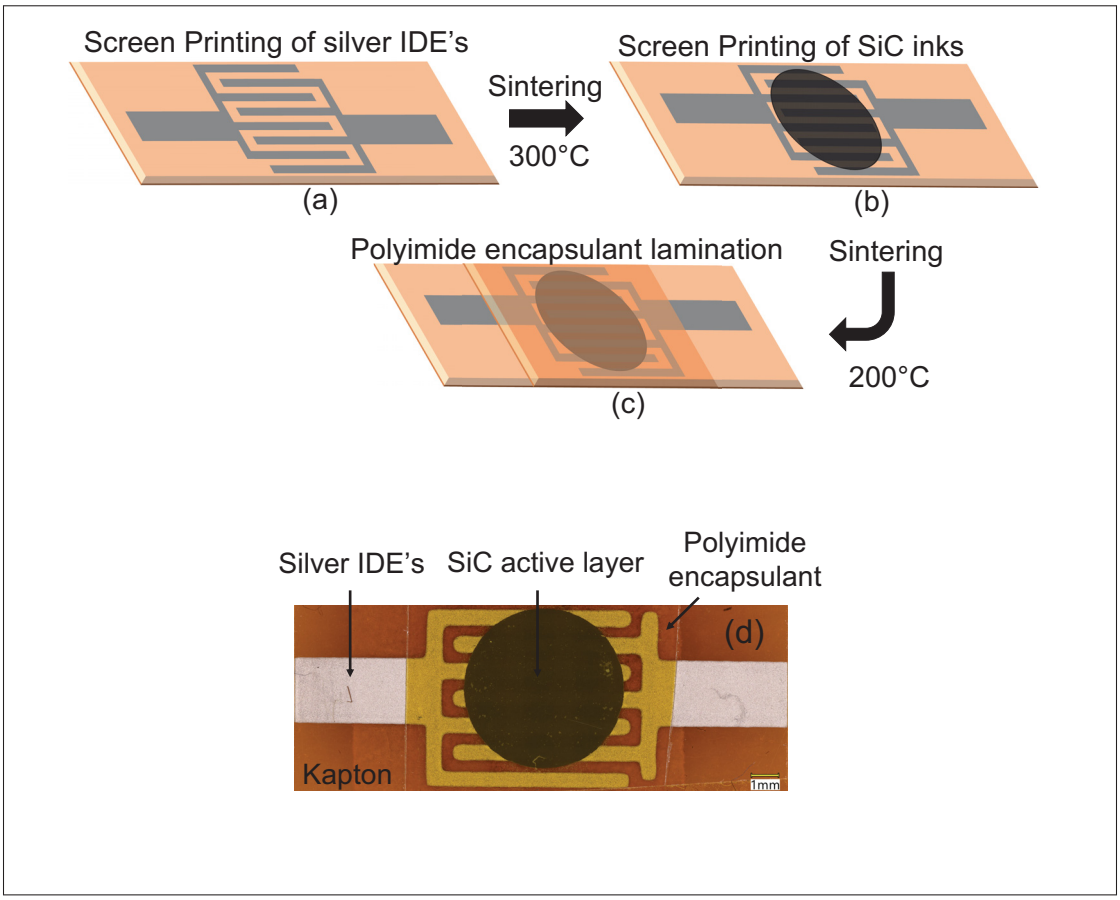

Figure 4.2 (a)- c) SiC thermistor fabrication process d) High resolution optical microscopy image of printed SiC thersmitor

(MPS-PT6C) and the two-wire resistance readout was recorded using a 40-channel digital multi-meter from Keithley (DMM 2790-L). Temperature was varied between 25 °C and 170 °C owning to the maximum temperature limit of the Nextron® at a constant rate of 10 °C/minute and a constant humidity at 40% RH. A custom Matlab script was written to process the raw data obtained from both the humidity test chamber and digital multi-meter. Figure 4.3 illustrates the experimetal setup used. Current - voltage characteristics of the thermistors was obtained using the Keithley DAQ6510 digital multi meter and the Keithley 2400 source-measure unit. Mechanical bend testing was performed using a custom setup consisting of a liner stage attached to a ball screw stepper motor. The stage was controlled via a Arduino Uno and a custom script to control travel distance, speed and number of cycles.

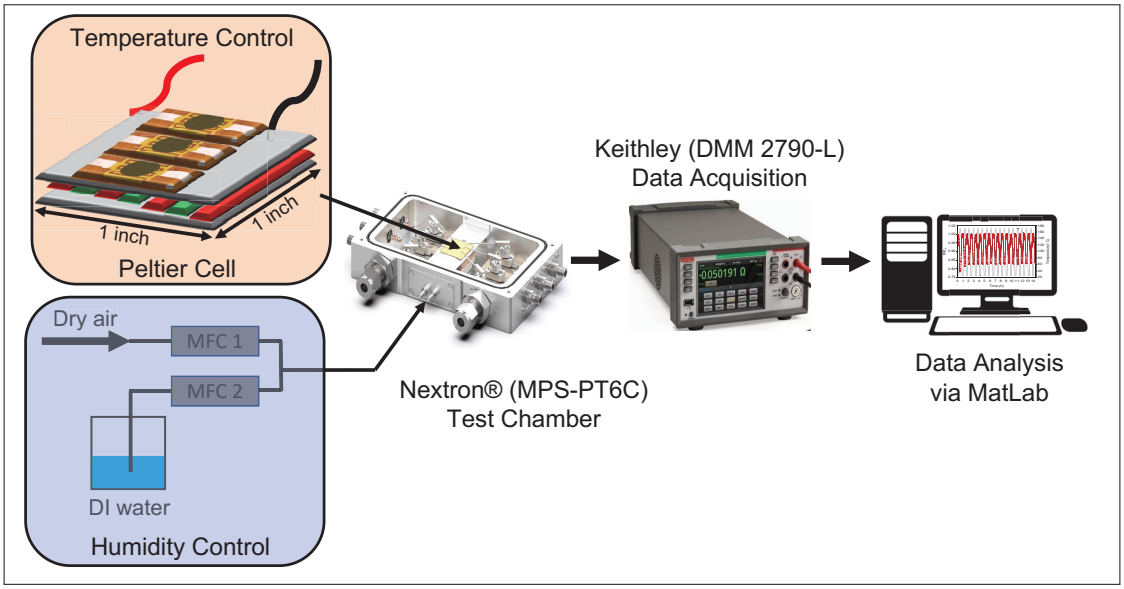

Figure 4.3 SiC thermistor test setup

4.3 Results and Discussion

4.3.1 Material Characterization

The X-ray diffraction (XRD) patterns of the commercially purchased SiC particles validate their cubic crystalline nature, exhibiting well-defined and sharp diffraction peaks, as depicted in Figure 4.4 a). The peaks observed at $2\Theta = 39.6°$, 42°, and 71.2° correspond to the 002, 200, and 311 crystalline planes of the $3C - SiC$ cubic crystal structure, consistent with the (International Centre for Diffraction Data) ICDD card: 04-002-9070 (Henager, Alvine, Roosendaal, Shin, Nguyen, Borlaug, Jiang & Arreguin, 2015; Sun, Xie, Yu, Li & Xu, 2017). Additionally, the presence of $2H - SiC$ peaks at $2\Theta = 45°(015)$ and $49°(016)$, as per the ICDD card: 04-008-2392 (Iwanowski, Fronc, Paszkowicz & Heinonen, 1999), may potentially be attributed to a blending of the two phases formed during the nanoparticle fabrication process (Shekhawat, Sudhahar, Döll, Grieseler & Pezoldt, 2023). The spectral results suggest an approximate 9:1 ratio between the two phases, respectively.

The Raman spectra of the $3C-SiC$ powder (Figure 4.4 b)) confirm its cubic crystal structure. Noteworthy peaks appear at wave numbers 785, 897, 1346, 1588, 2684, and 2916 cm^{-1}. Specifically, the peaks at 785 and 897 cm^{-1} correspond to the transverse and longitudinal optical modes of $3C-SiC$, as documented in reference (Lebedev, Oganesyan, Kozlovski, Eliseyev & Bulat, 2019b; Nakashima & Harima, 1997). The 1346 cm^{-1} peak represents the D band of carbon, peak 1588 cm^{-1} corresponds to the G band, associated with the A_{1g} vibrational mode of carbon. The peak at 2684 cm^{-1} signify the second orders of the D band, referred to as the 2D band, while the 2916 cm^{-1} peak represents the D+G band, as detailed in references (Dragomir, Valant, Fanetti & Mozharivskyj, 2016a; Zhu, Guo, Lin, Hao, Shang, Jia, Chen, Jin, Wang & Chen, 2012a).

Ultraviolet visible near infrared (UV-vis-NIR) absorption spectroscopy is performed on the $3C-SiC$ powder (Figure 4.4 c)) which indicates that the absorption edge is close to 400 nm. The electronic band gap (E_g) of the nano powder is calculated by liner fitting of the Tauc plot as seen in the inset graph. It suggests the band gap of the $3C-SiC$ nano powder is 2.75 eV which is consistent with previous reports (Batha & Carroll, 1964b; Peng, Hu, Gerlich, Zou, Liu & Zhou, 2015; Shuaib, Yogesh & Sastikumar, 2022).

4.3.2 Morphology

The morphology of the $3C-SiC$ particles is investigated via scanning electron microscopy (SEM) micrograph presented in Figure 4.4 d). We observe a densely packed film of particles with minimal porosity. Image processing software ImageJ was used to estimate the film porosity to be approximately 9.74%. Elemental mapping of the particles (Figure 4.5) reveals a uniform distribution of silicon and carbon elements along with the presence of elemental oxygen which could be attributed to the native oxide shell around the SiC particles. Table II-1 in the supplemental information section provides the mass fractions of each element observed.

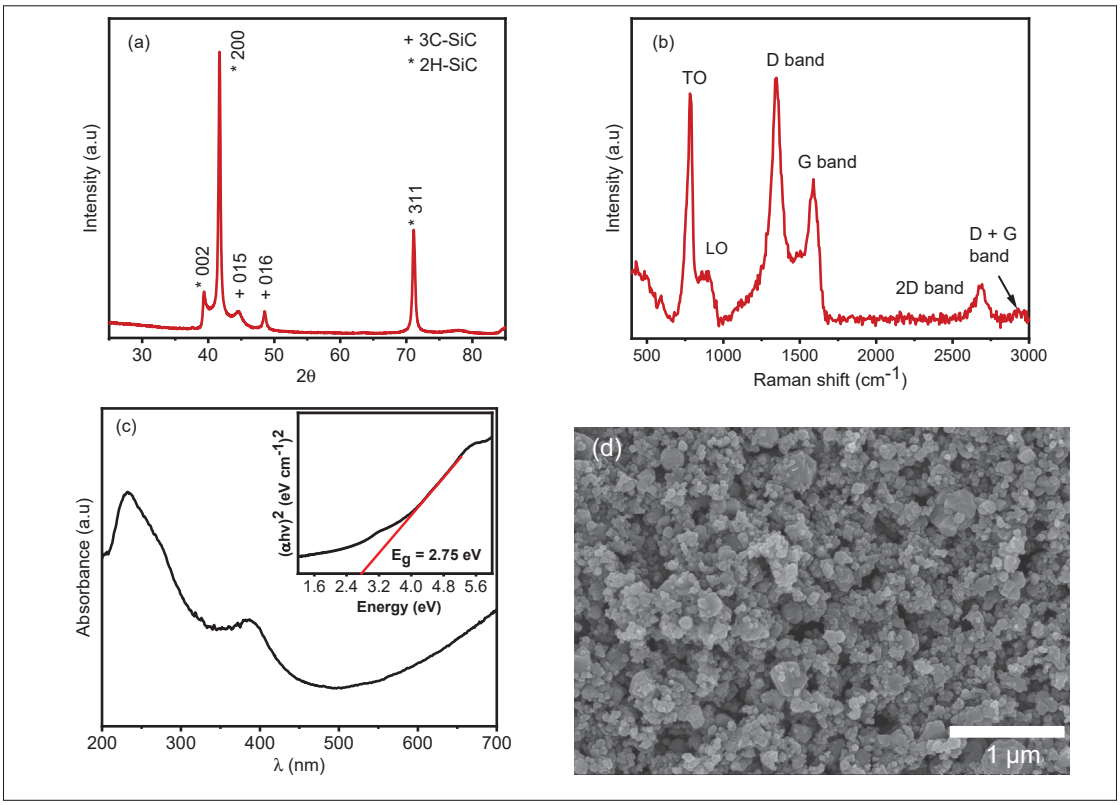

Figure 4.4 Characterization of commercially sourced $3C-SiC$ particles a) XRD spectra, b) Raman spectra c) UV-VIS spectra with Tauc plot as inset to determine electronic band gap, d) SEM micrograph

Transmission electron microscopy micrographs are shown in Figure 4.6 a)-b). The SiC particles have an average particle size of 70μm analysed using ImageJ. We confirm the presence of an approx. 2 nm thick oxide shell (SiO_x) around the SiC particles as indicated in Figure 4.6 b) (Chandrasekar & Srinivasan, 2016). The SAED pattern observed in Figure 4.6 c) allows us to calculate the inter planner atomic distance to be 0.25 nm which is assigned to the (111) cubic atomic plain (Wang, Zhang, Zhang, Han, Bi, Wang, Song & Zhang, 2018a).

4.3.3 Printed SiC Thermistor Characterization

Once the $3C-SiC$ particles have been thoroughly characterized, the screen printable thermistor ink is fabricated as described in the section 4.2.2 and printed directly atop the prepared Kapton® substrate to determine their electrical properties. Figure 4.7 a) shows the current voltage

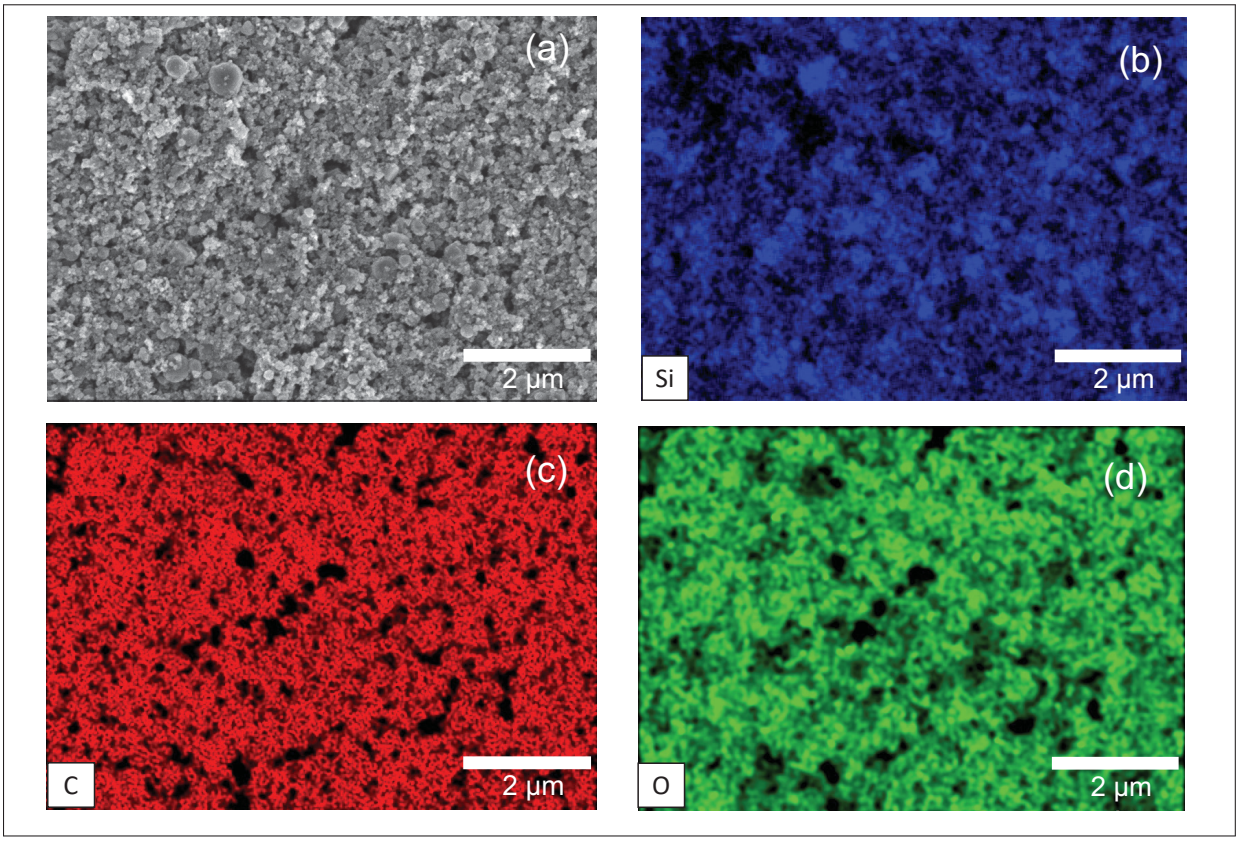

Figure 4.5 EDX imaging of a) SiC particles representing b) Si c) C and d) O species

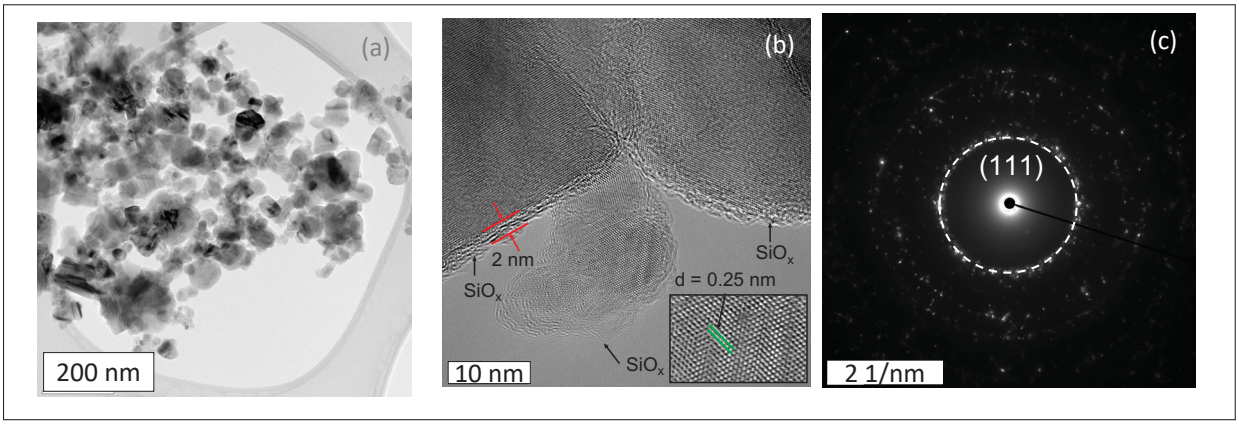

Figure 4.6 a), b) TEM micrographs and c) SAED pattern of SiC particles

characteristics of the thermistor at 25 °C. We observe a linear ohmic behavior between -5 V to 5 V indicating that the device functions as a resistor where the current is directly proportional

to the applied voltage. Further, we observed a negligible contact resistance of 0.0028 Ω at the $Ag - SiC$ interface which was determined as shown in Figure II-2 in the supplemental section.

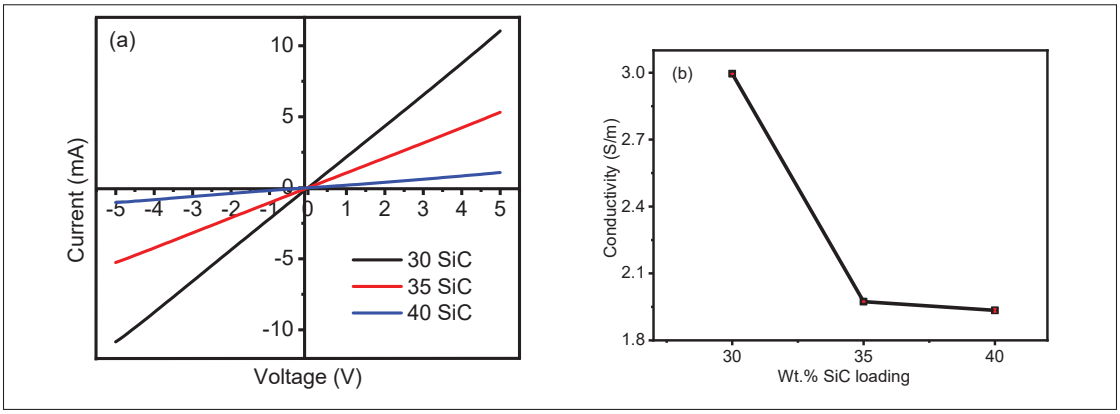

Figure 4.7 a) Current-voltage characteristics and b) electrical conductivity of 30 wt.%, 35 wt.%, 40 wt.% SiC thermistor inks

Next, we measured the electrical conductivity of the three inks via four point probe. As seen in Figure 4.7 b), the 30 wt.% loaded SiC thermistor ink formulated exhibits a maximum electrical conductivity of 2.99 ± 0.007 S m^{-1}. We observe that electrical conductivity decreases by more than 50% between the 30 wt.% and 35 wt.% loaded samples and further reduces as the loading is increased to 40 wt.%. This reduction could be attributed to the onset and growth of micro-cracks on the surface of the SiC film during the annealing process (Somalu, Yufit & Brandon, 2013). This phenomena was further investigated by acquiring SEM micrographs of films printed with the three SiC loaded inks at two different magnifications. The 30 wt.% SiC film has a dense, self leveled and uniform distribution of particles with no cracks on the surface of the film (Figure 4.8 a),b)). As the SiC loading is increased to 35.%, we observe the formation of surface imperfections and agglomerates as seen in Figure 4.8 c) and the onset of micro cracks in the films which are observed at high magnifications (Figure 4.8 d)). Lastly, the cracks are significantly more pronounced in the 40 wt.% loaded SiC film (Figures 4.8 e),f)). To further optimize the wt.% loading fraction, we studied the evolution of micro-cracks on the surface of 31, 32, 33 and 34 wt.% loaded SiC films as seem in Figure II-1 in the supplemental section. Indeed, we see a progressive increase in the quantity and size of cracks as the loading fraction is

increased. Hence, the decrease in electrical conductivity with increase in wt.% SiC loading can directly be attributed to film cracking due to the loss of conductive pathways (Kaiser, Cordill, Kirchlechner & Menzel, 2021; Kim, Haas, Friederich, Lee, Nam, Binder, Bauer, Choi, Joo, Gruber et al., 2014a).

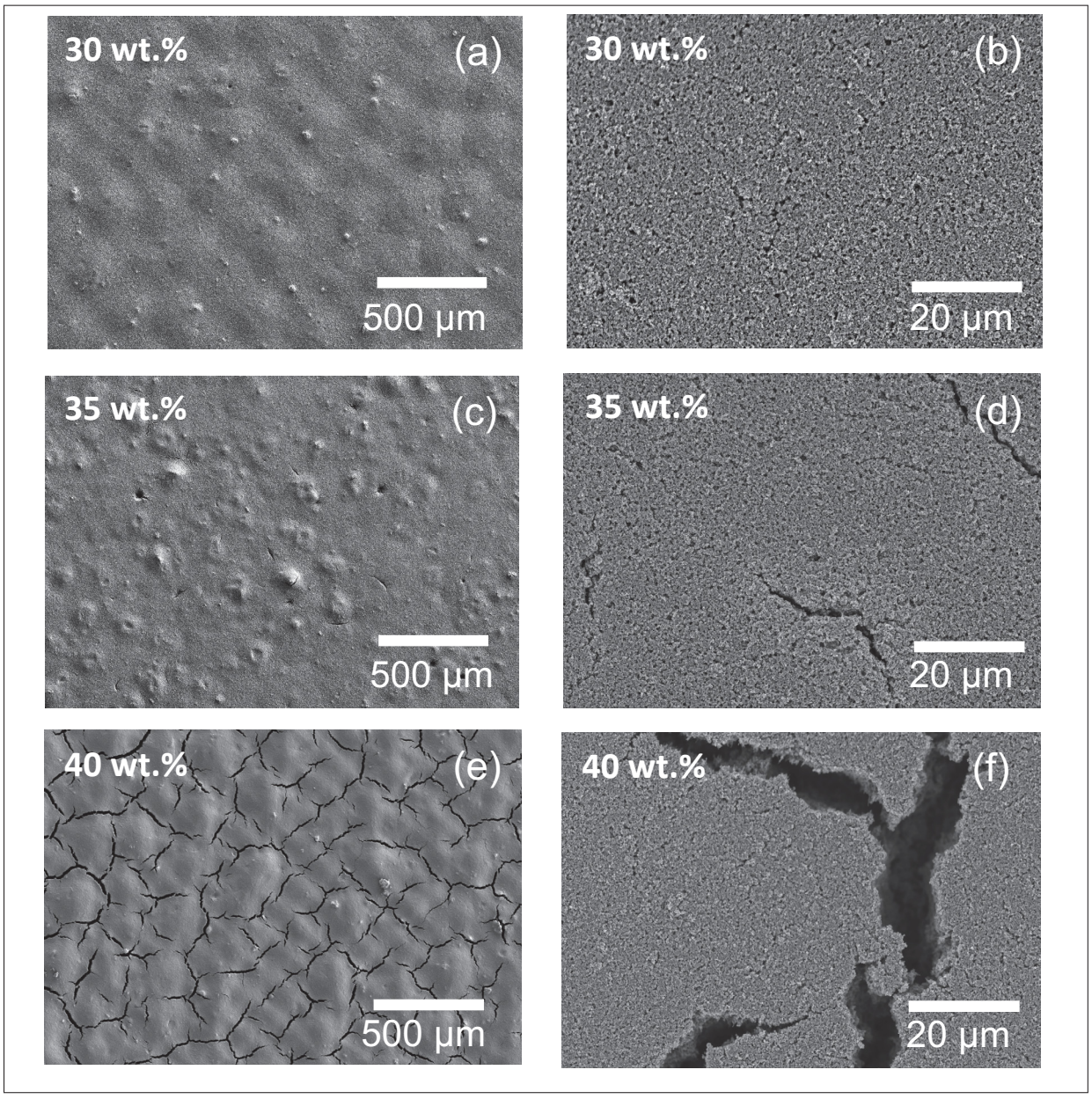

Figure 4.8 SEM micrographs of a) and b) 30 wt.% c) and d) 35 wt.% e) and f) 40 wt.% SiC thermistor inks

The silver IDE's are screen printed onto the polyimide substrate as previously and the SiC inks were then screen printed atop the silver IDE's to fabricate the thermistors as described in section 4.2.3 and Figure 4.2. Although the Kapton® substrate is rated to handle 350 °C and up to 400 °C for intermittent exposure (Diaham, 2021) the performance of the printed SiC thermistor is restricted to 170 °C due to the Nextron micro-probe stations' maximum temperature limit. Thermistors of each ink formulation were thermally cycled between 25 °C and 170 °C five times and the electrical resistance was recorded. Figure 4.9 a) shows the change in electrical resistance of all three inks with increase in temperature over five test cycles. Amongst the three ink formulations, the 30 wt.% loaded SiC thermistor showed the highest change in resistance of 41.1% going from 1267 Ω at 25 °C 988 Ω at 170 °C. The 35 wt.% and 40 wt.% SiC show a considerably low change of 20.4% and 14.7% which is less than half as compared to the 30 wt.% ink. Interestingly, the response of the three inks is identical to its change in electrical conductivity as previously discussed in Figure 4.7 b). This further validated that the increase in SiC loading significantly contributes to the degradation in the thermisors performance due to film cracking. The best performing thermistor (30 wt.% SiC) follows a second order polynomial fitting governed by Equation 4.1 with a R^2 confidence of 0.96.

$$y = -0.5X^2 + 0.0064X + 1.0714 \tag{4.1}$$

Similar to conventional SiC thermistors reported in literature (de Vasconcelos *et al.*, 2000), our screen printed SiC thermistors show a reduction in electrical resistance with increase in temperature, exhibiting a negative temperature coefficient of resistance (NTC). Figure II-3 in the supplemental section shows the response of the three individual 30 wt.% thermistors cycled 5 times each. We observed excellent repeatability across different sensors and multiple cycles.

A high performance thermistor must be stable, reliable and durable to be successfully deployed in challenging application environments (Feteira, 2009). To this effect, we subject the 30 wt.% SiC thermistor to various endurance tests. In figure 4.9 b), change in resistance of the thermsistor is recorded over 15 hours while being cycled between 25 °C and 170 °C. The device experiences minor variability during the first two thermal cycles which could be attributed to the relaxation

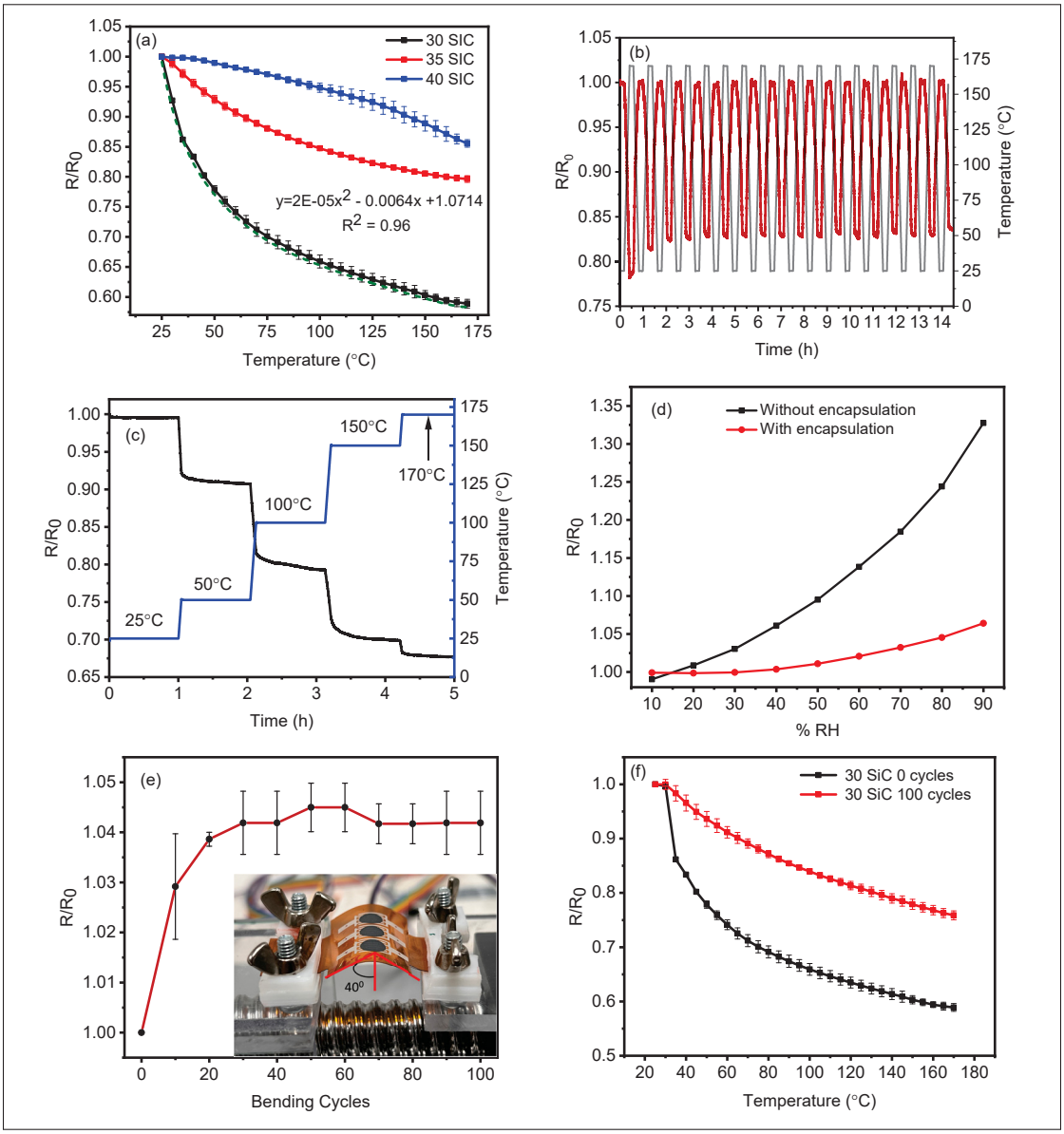

Figure 4.9 a) Electrical resistance versus temperature of 30 wt.%, 35 wt.%, 40 wt.% SiC thermistors b) long term cycling c) thermal stability d) humidity stability e) change in baseline resistance after bend testing and f) electrical resistance versus temperature plot after bend testing of 30 wt.% SiC thermistor

of the SiC film and any instabilities in the temperature test chamber at the onset of the test. Beyond this, the device is extremely stable with a minor drift in baseline resistance which was corrected via background subtraction. In order to test device stability, the 30 wt.% SiC thermistor is maintained at 25 °C, 50 °C, 100 °C, 150 °C and 170 °C for 1hr each. We observe

constant resistance at each fixed temperature suggesting device stability over a prolonged time duration (Figure 4.9 c).

The influence of humidity has a significant impact on the performance of a thermistor (Yuan, Cui, Li & Ma, 2015). Researches have shown that SiC exhibits good humidity response which is well suited to make humidity sensors (Connolly *et al.*, 2004a; Sun *et al.*, 2018b). To mitigate this effect, we have incorporated a polyimide film encapsulation layer. To ensure its effectiveness, we measure the electrical resistance of the 30 wt% SiC thermistor while varying the relative humidity between 10 %RH and 90 %RH at 25 °C. The change in resistance of two identical devices; one with and one without the polyimide film encapsulation are compared as seen in Figure 4.9 d). The device without encapsulation experiences a 32.6% change in resistance at a constant temperature indicating that the SiC film is highly sensitive to changes in relative humidity. In contrast, the device with encapsulation sees a much smaller drift of 6.5% in baseline resistance under the same conditions of %RH. The laminated polyimide encapsulant provides a high degree of protection against %RH, however this could be further improved by incorporating a fully printed insulating layer in future studies.

Mechanical flexibility of the 30 wt.% SiC thermistors was tested at an aggressive angle of 40° as seen in the inset of Figure 4.9 e). We observed a small drift in baseline resistance of 4.2 % over 100 test cycles (Figure 4.9 e)). Interestingly, majority of the change in resistance is observed during the first 20 cycles indicating deformation in the SiC sensing film at the onset of the test. Post bending, the device was cycled five times between 25 °C and 170 °C and compared to a pristine 30 wt.% device (Figure 4.9 f)). We notice a reduction in device response from 41.1% to 26.2%. This drop in performance is tentatively attributed to surface crack formation in the SiC film leading to loss of conductive pathways for effective change transfer with change in temperature.

4.3.4 Thermistor Performance

To further characterize the 30 wt.% SiC thermistor we calculate its performance parameters such as thermal index β, activation energy E_g and temperature coefficient of resistance (TCR). The electrical resistance dependence on temperature is given by the expression $R = R_o exp(\beta/T)$ where R_o is the resistance at infinite temperature and T is the absolute temperature. Thus, the thermal index can be calculated using the following (Sarrión & Morales, 1995).

$$\beta = \frac{lnR_1 - lnR_2}{(1/T_1) - (1/T_2)} \tag{4.2}$$

Here, T_1 = 248K, T_2 = 438K and R_1 and R_2 are the resistance values in Ω at the respective temperatures. The activation energy is calculated from the expression $E_g = 2k\beta$ where k is the Boltzmann constant and the TCR is calculated by the expression (Fourmont *et al.*, 2022a).

$$TCR = -\frac{\beta}{T^2} \tag{4.3}$$

Using Equations 4.2 and 4.3 , the characteristics of the printed thermistors are calculated as presented in Table 4.1. For the 30 wt.% SiC thermistor, the thermal index observed is 502 ± 11 K, the TCR value of -0.556 ± 0.012 %/°C with an activation energy of 0.08 ± 0.001 eV.

Table 4.1 Electrical performance of various printed SiC thermistor inks

Ink Name	3C-SiC wt%	PI resin wt%	TCR (%/°C)	Activation energy (eV)	Thermal index (K)
30 − SiC	**30**	**70**	**-0.556 ± 0.012**	**0.08 ± 0.001**	**502 ± 11**
35 − SiC	35	65	-0.227 ± 0.008	0.035 ± 0.001	205 ± 7.4
40 − SiC	40	60	-0.157 ± 0.0068	0.025 ± 0.001	142 ± 6

Accuracy of the printed 30 wt.% SiC thermistor was determined using the Steinhart's equation (Equation 4.4) (Steinhart & Hart, 1968; Turkani *et al.*, 2018a).

$$\frac{1}{T} = A + BlnR + C(lnR)^3 \tag{4.4}$$

Where T is the temperature in Kelvin, R is the resistance in Ω at temperature T. A,B and C are the Steinhart coefficients which are material specific and are used to calibrate the SiC thermistors accuracy. To this effect, experimentally measured resistance values at three temperatures of 25 °C (T_1 = 298 K), 100 °C (T_2 = 373 K) and 170 °C (T_3 = 443 K) are used in Equation 4.5.

$$\begin{bmatrix} 1 & ln(R_1) & ln^3(R_1) \\ 1 & ln(R_2) & ln^3(R_2) \\ 1 & ln(R_3) & ln^3(R_3) \end{bmatrix} \begin{bmatrix} A \\ B \\ C \end{bmatrix} = \begin{bmatrix} \frac{1}{T_1} \\ \frac{1}{T_2} \\ \frac{1}{T_3} \end{bmatrix} \tag{4.5}$$

For the 30 wt,% SiC thermistor, the Steinhart's coefficients are A = -8.12 x 10^{-2}, B = 1.59 x 10^{-2} and C = -8.12 x 10^{-5} with an accuracy of ±1.35 °C over the entire tested temperature range (25 °C to 170 °C) (Figure 4.10). The accuracy of the fully printed SiC thermsitors is comparable to conventional SiC and commercially available highly accurate thermistors ranging between ±0.05 °C to ±1.5 °C (Ome, 2020; The, 2020; Wasa, Tohda, Kasahara & Hayakawa, 1979).

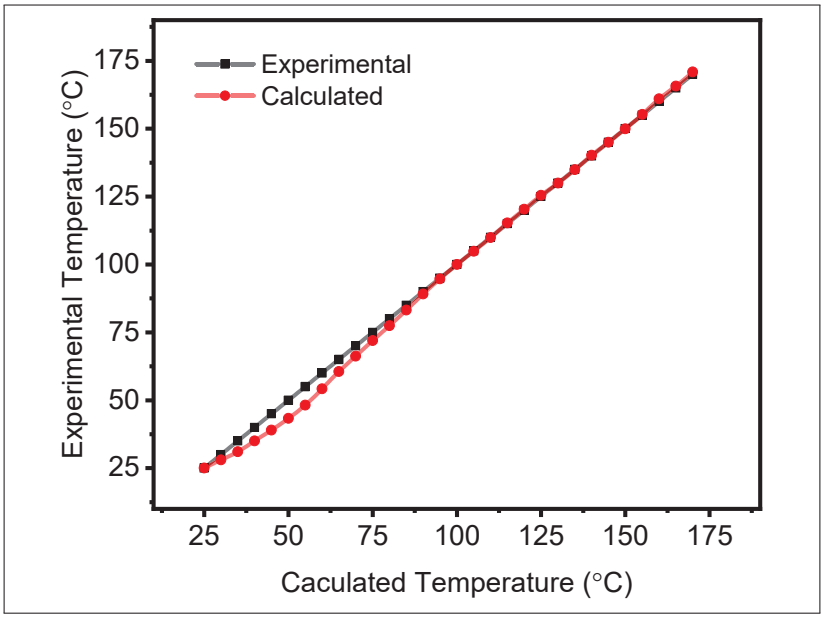

Figure 4.10 Accuracy of printed 30 wt.% SiC thermistor calculated via the Steinhart's equation

Researchers have developed several SiC based thermistors in recent years that have superior performance as compared to our all printed SiC nanoparticles based thermistors (highlighted in Table 4.2). However these thermistors are fabricated via complex and expensive processes such as chemical vapor deposition, vacuum vapor deposition and sputtering. The over all cost of fabrication and materials used limit the use of such thermistors only to highly specialised applications. On the contrary, the SiC thermistors developed in this study employs screen printing which is an inexpensive and scalable technology. Additionally, the use of commercially sourced SiC particles, polyimide rein and Kapton® substrate makes these devices relatively extremely low cost to fabricate. When compared to other printed thermistors recently reported in literature (Table 4.2), the 30 % SiC thermistors exhibit a comparable TCR coefficient over such a wide operational temperature range. Both SiC particles and Kapton® are chemically inert (Abro, Dablé, Cortés-Salazar, Amstutz & Girault, 2016), bio-compatible (Constantin, Aflori, Damian & Rusu, 2019a) and resistant to ultra high temperatures (Huseynov & Naghiyev, 2022). These properties combined with the simplicity and flexibility of our SiC thermistors allow them to accurately detect temperature variations in critical applications such as medicine, agriculture, aerospace and chemical production.

Table 4.2 State of the art of SiC based and printed thermistors

Sensing Material	**Electrodes**	**Fabrication Method**	**Temperature range**	**TCR**	**Reference**
Silicon Carbide based thermistors					
On SiC undoped wafer	Al, Au, Pt-Pd alloy	CVD	25 °C - 400 °C	-7.9%/K	(de Vasconcelos *et al.*, 2000)
Anodic bonding SiC on glass	Ni/Al	CVD	300K - 600K	-1.3%/K at 300K - 0.3%/K at 600K	(Phan *et al.*, 2019b)
n-type single crystal 21R-SiC wafer	Au- TiBx - Ni	magnetron sputtering	77K - 450K	10^5 times change in resistance	(Boltovets *et al.*, 2006)
Doped unicrystalline SiC wafer	W (Tungsten)	welding	−100 °C - 300 °C	1.9%/C	(Batha & Carroll, 1964a)
Polycrystalline CVD-SiC wafer	Pt-Pd alloy	Vacuum vapor deposition	25 °C - 365 °C	-5.5%/C	(de Vasconcelos, Zhang, Uchida & Katsube, 1998)
Printed Thermistors					
Carbon nanotubes	Ag	Screen printing	−40 °C - 100 °C	-0.4%/C	(Turkani *et al.*, 2018a)
PDMS + graphene	Copper wire	3D printing	25 °C - 70 °C	0.008%/C	(Wang, Gao, Zhang, Zheng, Xu, Xu, Shang, Jiang, Zhang & Liu, 2018b)
Graphene oxide	Ag	Inkjet printing	25 °C - 85 °C	-1.19%/C	(Kong, Le, Li, Zunino & Lee, 2012)
$BiFeO_3$ + 3.5 wt% graphene	Ag	Screen printing	25 °C - 170 °C	-0.961%/C	(Fourmont *et al.*, 2022a)
V_2O_5	Pt	Screen printing	200K - 400K	-3.7 to -1.7%/K	(Umadevi, Nagendra & Thutupalli, 1993)
3CSiC	Ag	Screen printing	25 °C - 170 °C	-0.556%/C	**This work**

4.4 Conclusions

In this study, we showcase a high performance, fully printed and flexible silicon carbide based thermistor for wide temperature range applications. Low cost serigraphic screen printing was used to fabricate sensors onto silver printed IDE's on flexible Kapton® substrate.

- SiC thermistors were cycled over a wide temperature sensing range between 25 °C and 170 °C. Three inks with different SiC ink loading's were tested and optimal device performance was achieved at 30 wt.% loading.
- At higher loading of 40 wt.%, we observed a reduction in device performance which was attributed to this onset and propagation of cracks with in the printed film leading to loss of conductive pathways.
- The 30 wt.% device exhibits a TCR of -0.556 %/°C along with a thermal index of 502K (β-index) and an activation energy of 0.08 eV. Device exhibit excellent repeatability and reliability after cycling over extended periods of time up to 15 hours.
- Printed thermistors shows a small variation in baseline resistance of 6.5% while tested over a wide relative humidity range (10 - 90 %RH).
- Aggressive bend testing was performed to test the thermisotrs flexibility. We observed a small 4.2% drift in baseline resistance of the device after 100 bend cycles at a 40°.
- Lastly, the 30 wt.% printed thermistors exhibit an accuracy of ±1.35 °C which is at par with commercially available high accuracy thermistors.

This study demonstrates that flexible, all screen printed SiC thermistors have an immense potential in the field of flexible and printed electronics. These low cost, flexible and mass producible thermistors can help improve critical user-device interactions in urgent application such as healthcare, agriculture and food monitoring.

Acknowledgments

The authors would like to thank Paul Fourmont for his contribution towards designing the experimental plan, Mohammad Saddati for performing the XRD analysis and SEM micrographs, Alexandre Perrotton for helping with the sensor data acquisition, Luis Felipe Gerlin for assisting with data plotting, Krunal Shah for assisting with device printing and Ahmed Moulay Slimani for assiting with current-voltage measurments. Sylvain G. Cloutier S.G.C. acknowledges the NSERC-Discovery program, the Canadian Department of National Defence (DND), and the Canada Research Chair program for their financial support. We would like to acknowledge the financial support of Natural Sciences and Engineering Research Council of Canada (NSERC) Collaborative Research and Development Grant CRDPJ 514369-17 and Discovery Grant RGPIN-2022-05125, MEDTEQ+ Grant 7-23 Contactless ECG V2, Signum Preemptive Healthcare Inc., Spera Medical Inc., as well as the École de Technologie Supérieure's Programme Impulsion.

CHAPTER 5

GRAIN STRUCTURE ENGINEERING IN SCREEN-PRINTED SILVER FLAKE-BASED INKS FOR HIGH-TEMPERATURE PRINTED ELECTRONICS APPLICATIONS

Wadhwa Arjun[1], Saadati Mohammad[1], Jaime Benavides-Guerrero[1], Bolduc Martin[2], Cloutier G. Sylvain[1]

[1] Département de Génie Électrique, École de Technologie Supérieure, 1100 Rue Notre-Dame Ouest, Montréal, Québec, H3C 1K3, Canada
[2] Département de génie mécanique, Université du Québec à Trois-Rivières, Trois-Rivi‘eres, QC G8Z 4M3, Canada

Article published in
MDPI Materials
Section: Electronic Materials
October 11 2024.
https://doi.org/10.3390/ma17204966

Abstract

We extensively studied serigraphic screen-printed commercial silver flake inks loaded with silicon inclusions in order to achieve pinning at the grain boundaries. Based on grain size measurements using electron backscattered diffraction (EBSD), commercial silver ink with silicon microparticle content of 5 wt.% shows a significant grain growth retardation compared to the pristine silver ink, which stabilizes electrical conductivity up to 700 °C via Zener pinning mechanism. The modified silicon-loaded silver ink experiences a two times increase in grain size when heated up to 700 °C, compared to a seven times increase for the pristine silver ink. In turn, this enables operation temperatures significantly higher than the conventional operational window of microparticle-based silver inks, which are usually limited to 400 °C. Using isothermal exposures of 10 minutes up to 4 hours this phenomenon is observed at temperatures ranging from 250 °C to 900 °C. The electrical conductivity stability, grain size evolution and oxide contents were studied up to 4 hours. The activation energy of silver ink with silicon inclusions is 54% lower than for the pristine silver ink due to pining effect, which retards grain growth via

the Zener mechanism. Most importantly, the electrical resistivity becomes stable up to 700 °C, which is more than twice the operation limit for off-the-shelf screen-printable silver flake inks. Hence, we demonstrate that adding controlled amounts of silicon particles to silver inks towards grain structure engineering can open new vistas of possibilities for screen-printed metallic inks.

5.1 Introduction

In recent years, the field of all-printed flexible hybrid electronics (FHE's) have rapidly advanced towards creating functional, flexible and low cost devices for a variety of applications. Generally, FHE devices are limited in operational temperature by the thermal limits of the conductor (melting point) or polymeric substrate (glass transition temperature). In the context of high temperature applications, FHE technologies have immense potential towards delivering robust high temperature sensors and power electronics (Li, Khuje, Chivate, Huang, Hu, An, Shao, Wang, Chang & Ren, 2020a). Key industrial sectors such as aerospace, oil and gas and chemical processing pose the opportunity to greatly benefit from the development of lost cost strain, temperature and pressure sensors to monitor critical systems and processes (Alhendi, Alshatnawi, Abbara, Sivasubramony, Khinda, Umar, Borgesen, Poliks, Shaddock, Hoel, Stoffel & Lam, 2022). Conventional conductive inks and substrates are unable perform at conditions of elevated temperature generally exceeding 300 °C to 350 °C (Lim, Cha & Gong, 2013). A robust and stable high temperature FHE device can be achieved by optimizing its three main building blocks: conductive ink, substrate and the passivisation over coat material (Sheng, Khuje, Yu, Petit, Parker, Zhuang, Kester & Ren, 2021). A successful high temperature conductive ink should be able to maintain its high electrical conductivity, undergo minimal oxidation and remain stable over extended periods of time during its service life. Traditionally, high cost and harder to process precious metal inks such as nickel, gold, platinum and palladium have been employed to make high temperature sensors and devices (Arsenov, Vlasov, Efimov, Minkov & Ivanov, 2019; Arsenov, Efimov & Ivanov, 2021; Rebenklau, Gierth, Paproth, Irrgang, Lippmann, Wodtke, Niedermeyer, Augsburg & Bechtold, 2015; Reynolds & Norton, 1986; Zhu).

Hence, there is an urgent need for low-cost and readily available inks that cater to high temperature applications. To address this, significant effort has been invested into improving traditional conductive inks via two distinct strangers; additives and alloying (Chen, Brown, Levendorf, Cai, Ju, Edgeworth, Li, Magnuson, Velamakanni, Piner, Kang, Park & Ruoff, 2011; Cruz, Ye, Kim, Reyes, Yang, Flowers & Wiley, 2018a; Ionkin, Fish, Li, Lewittes, Soper, Pepin & Carroll, 2011; Li *et al.*, 2020a; Li, Scheers, An, Chivate, Khuje, Xu, Hu, Huang, Chang, Olenick, Olenick, Choi, Zhou & Ren, 2020b; Liu, Wang, Ge, Wang, Lu, Zhao, Tang, Soomro, Hong, Yang, Xu, Li, Chen, Cai & Kang, 2020; Sheng *et al.*, 2021; Yim, Kockerbeck, Jo & Park, 2017). Passivating additives such as graphene have been used to minimize the oxidaiton of copper based conductive inks (Li *et al.*, 2020a). Similarly, $\mathrm{Ci-Ni}$, $\mathrm{Ag-Cu}$, $\mathrm{Cu-BN}$ and $\mathrm{Ag-Zn}$ alloys have also been successfully investigated towards high temperature printed device applications (Ionkin *et al.*, 2011; Li *et al.*, 2020b; Sheng *et al.*, 2021).

Silver inks remain the most widely used due to their high electrical conductivity, stability and low oxidation potential (Lee, Hsu & Tuan, 2016). It is estimated that silver inks held a market share of over 21% in 2023 (noa, 2023). Relatively low-costs and moderate sintering conditions make silver the material of choice for devices fabricated on low-temperature flexible polymeric substrates such as PET, PEN, polycarbonate, and Kapton® (Ibrahim, Akindoyo & Mariatti, 2022; Mo, Guo, Yang, Zhang, Fang, Xin, Chen, Hu, Han & Li, 2019b). A large variety of silver inks are commercially available depending on the intended printing method. Silver nanoparticle based inks are used for direct-write printing such as inkjet, aerosol jet and micro-dispensing techniques (Rajan, Roppolo, Chiappone, Bocchini, Perrone & Chiolerio, 2016), while silver micropartile inks are used for contact printing processes such as screen printing (Cano-Raya, Denchev, Cruz & Viana, 2019b).

The sintering process and mechanism of the silver particle based inks have been detailed in literature by several researchers (Chen & Suganuma, 2019; Mo *et al.*, 2019b; Oliber, Cugno, Moreno, Esquivel, Haberkorn & Fiscina, 2003; Peng *et al.*, 2015; Volkman, Yin, Bakhishev, Puntambekar, Subramanian & Toney, 2011; Wiklund, Karakoç, Palko, Yiğitler, Ruttik, Jäntti & Paltakari, 2021; Yan, 2021). The sintering process can be broken down

into two stages, densification and graing growth. Optimal sintering temperature is when maximum densification is achieved while retaining minimum grain size. This balance is challenging to achieve since denisification leads to grain growth as both processes have the same driving force and mass transport mechanism. Additionally, grain growth is required to reduce interfacial energy which eliminates pores and increases densification. Nano sized partiles tend to sinter at lower temperatures as compared to micron sized particles (Fang, 2010). Typically, silver nanoparticle inks achieve complete sinteirng at 300 °C (0.3 T_m) (Long, Du, Hu & Li, 2018). Although microparticle screen printable inks are designed for low temperature substrates they tend to achieve complete sintering at 400 °C (0.42 T_m) (Roberson, Wicker, Murr, Church & MacDonald, 2011) . Here, T_m is the is the melting temperature of bulk silver, which is 961 °C (Choo & Kim, 2017). Beyond 0.42 T_m, significant grain growth is expected, which in turn alters the electrical properties and stability of the devices (Roberson *et al.*, 2011). Thus, the operational window generally acknowledged for screen-printed silver devices is up to 400 °C. Although this satisfies most applications, high temperature FHE applications demand operation in temperatures exceeding 500 °C (Alhendi *et al.*, 2022).

Grain growth is a well-known physical mechanism where the average grain size of a poly crystalline material increases when external energy is applied (Thompson & Carel, 1996b). Grain boundaries are complex structures at crystalline domain interfaces typically 1-2 unit cells in width with higher Gibbs free energy than the bulk crystalline material. When external energy is applied to the poly crystalline material, grain boundaries move due to diffusion of atoms from convex grains into concave grains resulting in the grain boundary moving to the center of the concave grain. This is termed as grain coarsening leading to the reduction in grain boundaries and hence reducing the free energy of the poly crystalline material (Akbarpour, Farvizi & Kim, 2017; Frazier, Hu, Overman, Lavender & Joshi, 2018).

Electrical conductivity is largely dependant on grain size due to presense of trapping sites at the grain boundaries which influence electron mobility (Lee, Kim, Ahn, Ha & Kim, 2015). Electrical conductivity (σ) of nanoparticle-based inks is inversely proportional to the grain size (Chen & Suganuma, 2019; Volkman *et al.*, 2011) where as σ of microparticle-based silver

inks is expected to increase with higher grain sizes up-to 850 °C (Fang, 2010; Roberson *et al.*, 2011). However, mechanical properties such as hardness and Young's modulus tend to reduce with increase in grain size (Frazier *et al.*, 2018; Kim, Lee & Kim, 2014b; Peng *et al.*, 2015; Thompson & Carel, 1996b). Here, it is imperative to find a optimal grain size to achieve desired mechanical and electrical properties of the printed film depending on the application at hand.

Building on the pioneering work initiated by Zener-Smith, it was shown that the inclusion of controlled amounts of secondary phase particles helps in achieving grain growth control (Shahandeh & Militzer, 2013). This phenomenon is called grain boundary pinning or Zener pinning, where dispersion of secondary phase particles creates a pinning pressure that obstructs grain boundary movement to limit grain growth. Very limited work has been done to exploit such grain boundary control strategies using inclusions to engineer printable materials. Copper nanoparticles were previously alloyed with with gold (Lohmiller, Woo & Spolenak, 2010), graphene (Yu, Khuje, Sheng, Kilczewski, Parker & Ren, 2022) and silicon carbide (Akbarpour *et al.*, 2017) to achieve grain growth retardation, allowing for superior mechanical properties of the alloy for flexible printed device applications. Yttrium stabilized zirconia was also added to silver ink, retarding grain growth up-to 740 °C (Fratello, Nino, Wadhwa & Kent).

This study focuses on the process of grain growth and grain pinning of already sintered samples prepared as if they were to be used under ambient applications. Limited work is found on the electrical stability of printed silver inks at higher temperatures. It is reported that a significant increase in the grain size occurs for aerosol jet-printed silver ink at 500 °C, along with improved oxidation resistance and electrical stability at elevated temperatures (Rahman, McCloy, Ramana & Panat, 2016). Stability over long exposure time duration's is a critical parameter for the longevity and performance of high temperature devices. This works seeks to provide a thorough understanding of the impact of refractory inclusions and how they can be used to control and improve the properties of commercial silver inks for operation at higher temperatures. Intrinsic silicon particles are used due to their low electronic band-gap at room temperature of 1.12 eV and high electron mobility of $1350\,\mathrm{cm^2(V\,s)^{-1}}$ (SALEMI, 2017). This

allows for a smaller reduction in electrical conductivity of the modified ink as compared to more stable metal-oxide and carbides-based ceramics (SALEMI, 2017).

5.2 Materials and Methods

5.2.1 Materials

Widely-used commercial screen-printable silver flake-based ink Metalon® HPS-FG32 was purchased from Novacentrix Inc. Austin, TX, USA. The ink is 75 wt.% loaded with 1.5 μm silver flakes dispersed in a, w Butyl Carbitol-based solvent system. Silicon powder > 99% with particles 1-5 µm in diameter was purchased from US Research Nanomaterials Inc., Houston, TX, USA (Product: US1127). In order to study the evolution of grain size at high temperatures, Alumina substrates were employed due to their excellent high temperature stability. 0.2 inch thick Aluimina sheets were purchased from Mcmaster Carr Elmhurst, IL, USA (Product: 8462K26) and cut into 1 inch square coupons using a wet time cutting saw. No modifications were made to any of the materials upon receipt.

5.2.2 Ink Formulation

Modified ($\mathrm{Ag} - \mathrm{Si}$) ink was formulated by incorporating 3, 5, 7 and 10 wt.% loading of Si microparticles in the pristine Ag ink. To achieve homogeneous dispersion, a two step process is employed. The Si microparticles were weighed and added in approximately two portions. Each portion was added to the pristine Ag ink followed by through mixing using a Thinky ARE-310, Laguna Hills, CA, USA planetary mixer for three cycles of one minute at 2,000 rpm followed by one minute of rest intervals to allow ink degassing. This mixing procedure ensured a stable dispersion of the ink formulations with a shelf life of over six months.

5.2.3 Sample Fabrication

Cut alumina substrates were prepared by cleaning with 9.99% pure acetone (Millipore Sigma 270725). A simple 17 mm × 12 mm rectangular feature is fabricated into a 325-mesh stainless steel mesh screen as depicted in Figure 5.1(a); providing a 25.4 µm wet film thickness after manual screen-printing (one pass)as seen in Figure 5.1 a). Three samples per test temperature were fabricated for each of the modified $(Ag - Si)$ formulations to ensure repeatability and reliability of the collected data. As recommended by the silver ink manufacturer, the samples are sintered in a Mancorp, Montgomery County, PA, USA (MC301N) reflow oven at 250 °C for 60 minutes in air to remove all organic components of the ink and initiate densification.

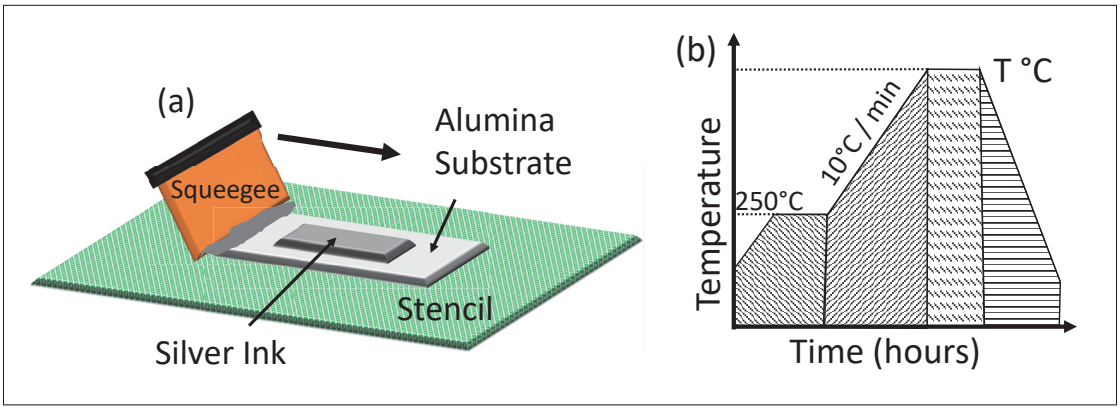

Figure 5.1 (a) Schematic of screen printing process to fabricate ink samples on alumina substrate (b) Thermal cycling ramp profile

5.2.4 Testing and Characterization

We studied the evolution of grain structure and electrical conductivity of the pristine Ag and $(Ag - Si)$ inks with incremental temperatures and exposure times. The samples were exposed to temperatures in incremental steps of 100 °C with a ramp of 10 °C min^{-1} between 400 °C and 900 °C for 10 mins, 1,2,3,4 hour of isothermal exposure times. The samples were then allowed to cool down naturally to room temperature. The thermal treatment was limited to 900 °C) to stay below the melting point of silver (961 °C) (Shyjumon, Gopinadhan, Ivanova, Quaas, Wulff, Helm & Hippler, 2006). The entire thermal process is depicted in the Figure 5.1b).

Raman micro-spectra of the modified ($Ag - Si$) inks was obtained using the WITec alpha300A (Ulm, Germany) raman microspectoscopy system with a 532 nm green laser. Particle size distribution of Si particles was determined using a Zetasizer Lab system (Malvern Panalytical Ltd, Malvern, UK). Micrographs of the printed films were obtained using a Hitachi SU8230 (Tokyo, Japan) scanning electron microscope (SEM) equipped with a Bruker (Billerica, MA, USA), QUANTAX FlatQUAD EDX detector for precise elemental mapping. The SEM is also equipped with a Bruker e-Flash HR+ detector to acquire Electron back-scattering diffraction (EBSD) micrograhs. Ossila T2001A3 (Sheffield, UK) four-point-probe was utilized to measure the electrical conductivity of the printed silver films. X-ray photoelectron spectroscopy (XPS) was performed using Thermo Fisher, VG ES- 245 CALAB 250Xi equipped with a cobalt source. Thermal galvanometric analysis TGA was performed using a Perkin Elmer's STA8000 system Waltham, MA, USA.

5.3 Results and Discussion

5.3.1 Material Characterization

The Raman spectra of the modified ($Ag - 5wt.\%Si$) is presented in Figure 5.2 a). The band at 233 cm^{-1} is attributed to the $Ag - O$ stretching mode (Wiley, Sun & Xia, 2007). The vibrational peaks at 517 cm^{-1} and 666 cm^{-1} are due to the stretching vibrations of $C - N - C$ and $C - S - C$, respectively (Arvizo, Bhattacharyya, Kudgus, Giri, Bhattacharya & Mukherjee, 2012). The bands at 1353 cm^{-1}, 1594 cm^{-1} are associated with the symmetric and anti-symmetric $C = O$ stretching vibrations of the carboxylic group (Chen, Qiao, Qiu & Chen, 2009). The peaks at 980 cm^{-1} and 517 cm^{-1} are from the silicon particles which is slight shifted as compared to crystalline silicon with a peak at 520 cm^{-1} (Kobayashi, Chewchinda, Ohtani, Odawara & Wada, 2013; Lee & Chang, 2018). We further analysed the particle size distribution of the as received Si particles. Figure 5.2 b) suggests a size range between 800 nm to 1.4 µm with an average particle size of 1.04 µm.

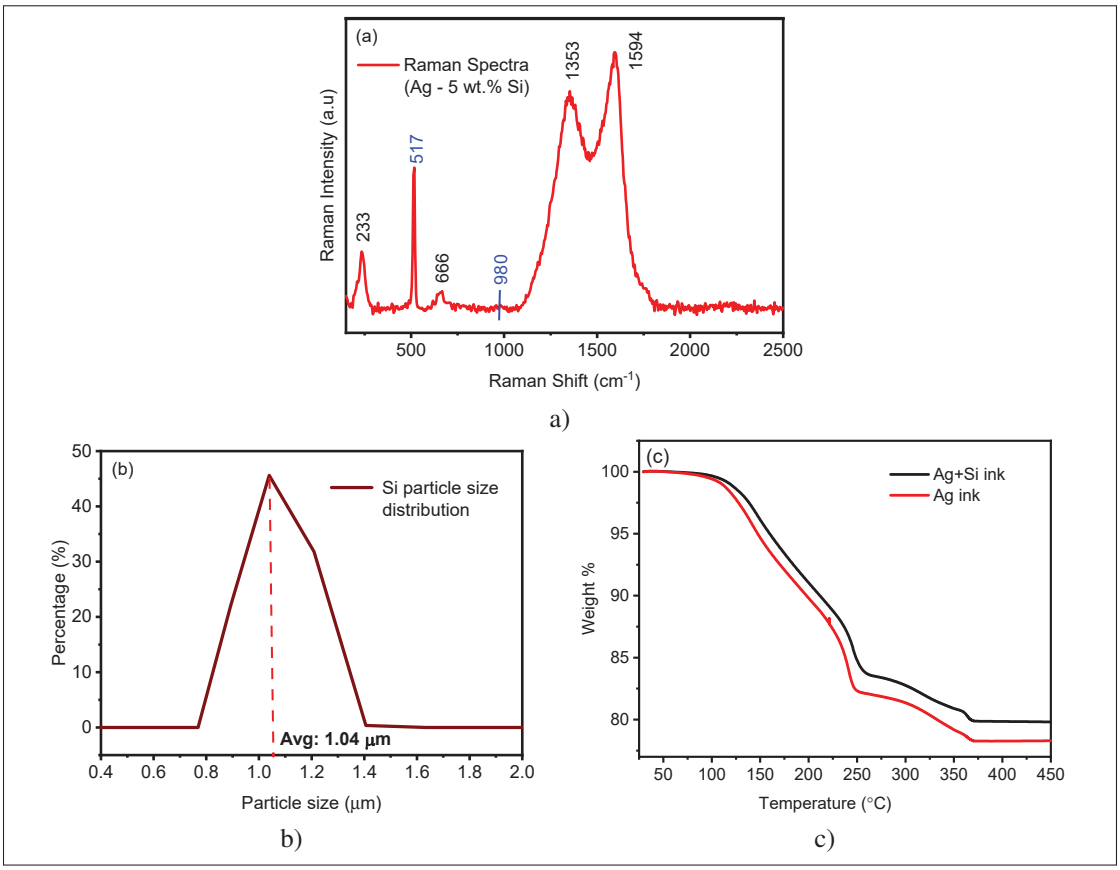

Figure 5.2 (a) Raman spectra of pristine and modified ($Ag - Si$) ink (b) particle size distribution of Si nano particles as purchased

Thermal galvanometric analysis (TGA) (Figure 5.2 c)) of both inks shows a significant drop in wt.% starting at around 120 °C until 250 °C, suggesting complete solvent burn off consistent with the boiling point Butyl Carbitol at 231 °C. A further drop in wt.% between 250 °C and 366 °C can be speculated to originate from the removal of other organics in the ink matrix such as proprietary surfactants and dispersants used by the ink manufacturer (Figure 5.2 c)). It is worth noting that the weight fraction of the modified ($Ag - Si$) ink is slightly higher than the silver ink, most likely due to the mass contribution of the silicon particles in the modified ink. The weight % of both inks remains stable beyond 400 °C, suggesting a complete sintering of the silver flakes beyond this point (Agarwala, Goh, Dinh Le, An, Peh, Yeong & Kim, 2019). After initial sintering of the pristine Ag ink, at 250 °C (for 1 hour), the silver flakes show signs of necking while maintaining their shape and structural integrity indicating onset of densification

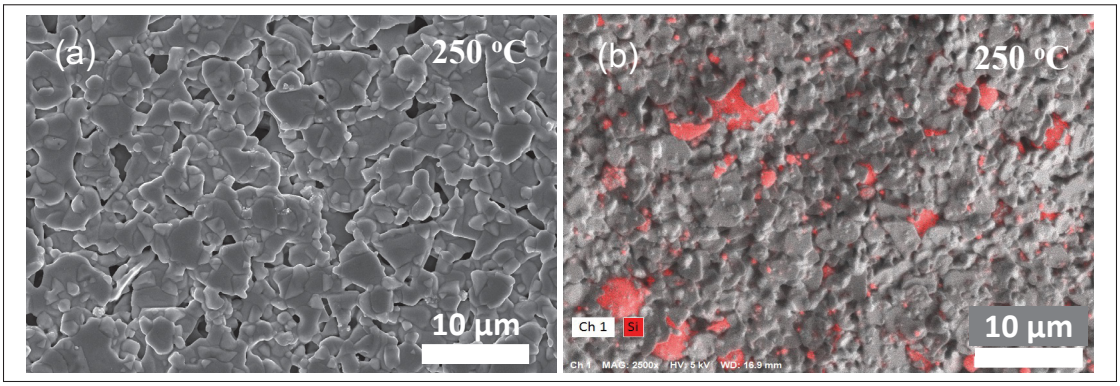

Figure 5.3 SEM micrographs of (a) pristine Agink and (b) modified $(\mathrm{Ag}-\mathrm{Si})$ silver ink sintered at 250 °C. (c) EDX map of $(\mathrm{Ag}-\mathrm{Si})$ ink sintered at 250 °C with Si particles highlighted in red

(Figure 5.3 a)). As seen in the EDX micrograph of the modified $(\mathrm{Ag}-\mathrm{Si})$ ink (Figure 5.3 b)), silicon particles (highlighted with red arrows) are uniformly dispersed across the printed and sintered film.

5.3.2 Evolution of Electrical Conductivity

Over the entire temperature range we observed the impact of grain growth and grain pinning on the electrical conductivity of both inks which was studied. To study this effect, electrical conductivity was measured via four point probe for three samples processed at each incremental treatment temperature. Each samples was probed 3 times with a samples set of 100 data points per test. In total, 900 data points of electrical conductivity were collected per samples point. The evolution of electrical conductivity of the pristine Ag ink (1 hour isothermal time per treatment temperature) is presented in Figure 5.4 a). Conductivity data for all test cases has been summarized in Table III-1 in the supplemental section.

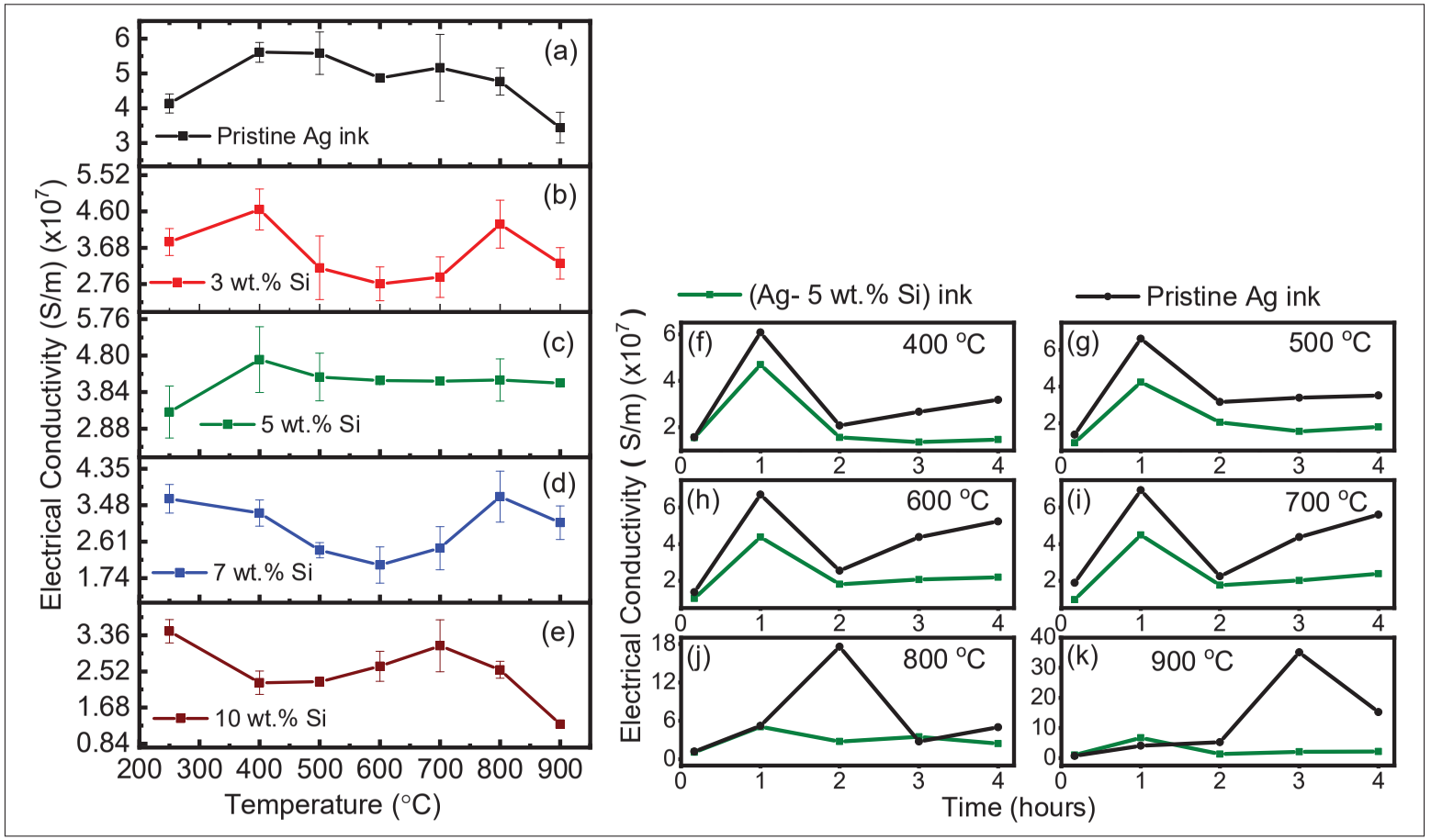

Figure 5.4 Electrical conductivity of (a) pristine Ag and modified (Ag − Si) inks with (b) 3 wt.%, (c) 5 wt.%, (d) 7 wt.%, (e) 10 wt.% silver inks treated at incremental temperatures for 1 hour isothermal exposure, electrical conductivity of pristine Ag and modified (Ag − 5wt.%Si) inks thermally treated at (f) 500 °C, (g) 500 °C, (h) 600 °C, (i) 700 °C, (j) 800 °C, (k) 900 °C over 10 mins, 1, 2, 3, 4 hours isothermal exposure

After initial sintering at the manufacturers recommended conditions, the pristine Ag ink achieves an electrical conductivity of 4.14 (± 0.27) x10^7 S/m which is appromitaley one third compared to the conductive of bulk silver of 6.2 x10^7 S/m (Jewell, Hamblyn, Claypole & Gethin, 2015). The conductivity further increases up to 500 °C with a maximum value of 5.6 (± 0.28) x10^7 S/m as grain growth continues leading to the reduction of the mean free path and micro pores leading to densely packed film. Beyond 500 °C, we observe a fall in electrical conductivity owing to the formation of pores due to continued densification of the films micro structure. Figures 5.4 b)-e) show the evolution of electrical conductivity of the modified ($\mathrm{Ag-Si}$) inks with 3, 5, 7, 10 wt.% loading of Si particles treated at incremental temperatures for 1 hour isothermal exposure. Here we note that the conductivity of all the modified ($\mathrm{Ag-Si}$) inks at 250 °C is lower compared to the pristine Ag. This reduction can be attributed to the presence of insulating Si particles in the inks. Amoung these, the 3 and 7 wt.% Si loaded inks show a initial increase in conductivity up to 400 °C indicating complete sintering followed by a reduction in conductivity due to increased grain growth. Beyond 700 °C these inks follow behave erratically.

The 10 wt.% Si loaded ink follows a different behavior, where the conductivity reduces up to 500 °C and then tends to increase gradually until 700 °C followed by a sudden drop in conductivity. The 5 wt.% Si loaded ink by far was the most stable formulation. After complete densification is achieved at 400 °C, the electrical conductivity remains extremely stable up to 900 °C. This formulation has the potential to provide the optimal balance between densification and grain growth allowing stable electrical performance at ultra high temperatures while maintaining a relatively low average grain size in the printed film micro structure allowing for optimal mechanical properties towards the desired applications. Here on, we further examine the properties of the modified ($\mathrm{Ag-5wt.\%Si}$) ink as compared to the pristine Ag ink.

A robust and stable device needs to maintain its properties over long duration of time especially in extreme environments where factors such as oxidation can play a detrimental role. To examine the electrical stability of the modified ($\mathrm{Ag-5wt.\%Si}$) ink, we tested freshly prepared samples at each temperature up to 4 hours of isothermal exposure. Figures 5.4 f)-k) compare the electrical conductivity of the pristine and 5 wt.% Si modified ink. Error bars are omitted for the simplicity

of graphical representation, however conductivity data with standard deviations are presented in Table III-2 in the supplemental section.

For the modified ($\mathrm{Ag} - 5\mathrm{wt.\%Si}$) ink up to 400 °C, the electrical conductivity peaks at 1 hour isothermal exposure which confirms the efficacy of the manufacturers recommended sintering conditions. Previous reports on micro-particle based silver inks have also described a rise in electrical resistivity between 350 °C – 450 °C, after complete sintering has taken place (Kim, Koo, Baeg, Noh, Yang, Jung, Ju & You, 2012). Beyond 1 hour, the conductivity of both inks remain stable and follow a similar trend up to 500 °C. Beyond 500 °C, the pristineAg ink shows significant variability in its conductivity at longer exposure times, suggesting the transition to near bulk-like silver due to rapid grain growth, followed by oxidation and melting of the silver ink as the temperature approaches 900 °C. These observations reinforced the practical notion that silver inks have an operational ceiling of approximately 400 °C for the pristine silver ink. In contrast, the modified ($\mathrm{Ag} - 5\mathrm{wt.\%Si}$) inks maintains stable electrical conductivity over all the tested temperatures and prolonged exposure times. Although the conductivity of the modified ink is slightly lower, it has the potential to maintain a significantly stable grain size at the same test conditions which will be explored in the next sections.

5.3.3 Evolution of Grain Size

After the thermal annealing tests, the morphology of the pristine Ag and modified ($\mathrm{Ag} - 5\mathrm{wt.\%Si}$) inks are studied via scanning electron microscopy (SEM) and Electron Backscatter Diffraction (EBSD) analysis. Figures 5.5 and Table III-3 (supplemental section) illustrate the evolution of grain size for both the pristine and modified ink over the tested temperature range for each isothermal exposure time. It is to be noted that the grain size information for each samples was acquired via EBSD measurements. For nanoparticle based inks, simpler are fast methods such as X-ray Diffraction (XRD) analysis which is limited to measuring up to 200 nm grains (Kang, Ryu, Kim & Hahn, 2011). In our case, the use of low cost micron size flake based ink requires the use of EBSD analysis which requires intense sample preparation via ion milling, leading to long and expensive experiments.

We observe a stark difference between the grain size achieved for both inks for each isothermal exposure time over the entire thermal range. Interestingly, the pristine Ag ink sees a 7 times increase in grain size while the modified ($\mathrm{Ag} - 5\mathrm{wt.\%Si}$) ink sees a much lower 2.8 times increase in overall grain size between 250 °C and 900 °C for up to 4 hours of isothermal treatment.

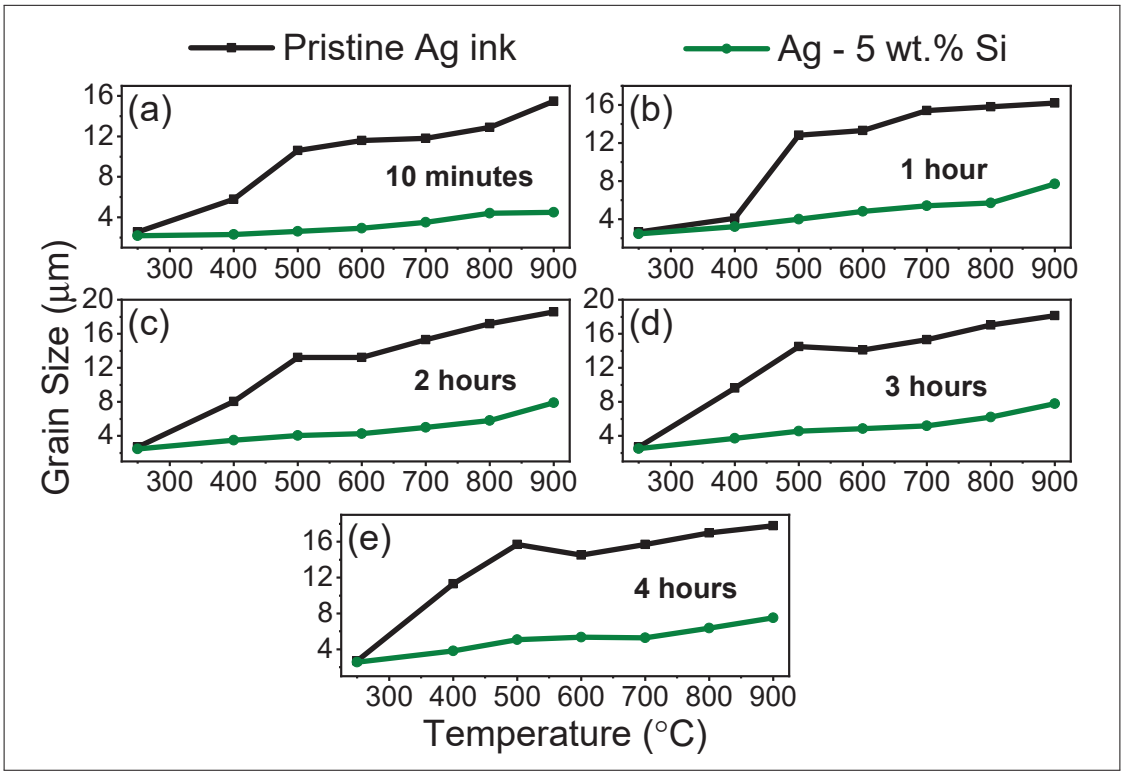

Figure 5.5 Accuracy of printed 30 wt.% SiC thermistor calculated via the Steinhart's equation

The inhibition of grain growth is largely attributed to the presence of silicon particles in the ink which facilitate Zener pinning. To further examine this phenomina, we acquired SEM and EBSD micrographs of samples treated at each temperature interval. For the pristine Ag ink, Figure 5.6 illustrate micro-structural changes with increasing temperatures, while Figure 5.7 illustrates the evolution of grain size for the same samples obtained via EBSD. The SEM micrographs indicate the formation of pores in the sample treated at 400 °C as densification accelerates leading to increased grain size. At higher temperatures, smaller grains dissolve into larger grains forming leading to a reduction in mean free path which in turn leads to an

increase in electron mobility and electrical conductivity. However, pore size also increases at the same time which is detrimental to the mechanical performance of the printed film (Aqida, Ghazali & Hashim, 2004). EBSD micrographs confirm a significant increase in grain size which can be attributed to aggravated growth and Ostwald ripening (Baker, Saha & Shu, 2013; Kim *et al.*, 2012). Grain growth by a factor of approximately seven is observed in the pristine silver ink at 900 °C. In Figure 5.6 f), the pristine silver ink shows the transformation of micron-sized silver particles to a porous bulk-like solid film due to grain growth reaching an approximate grain size of 18.2 μm after only 10-minute isothermal exposure. This is consistent with results seen in previous literature reports (Zheng, Chen, Zou & Zhang, 2022).

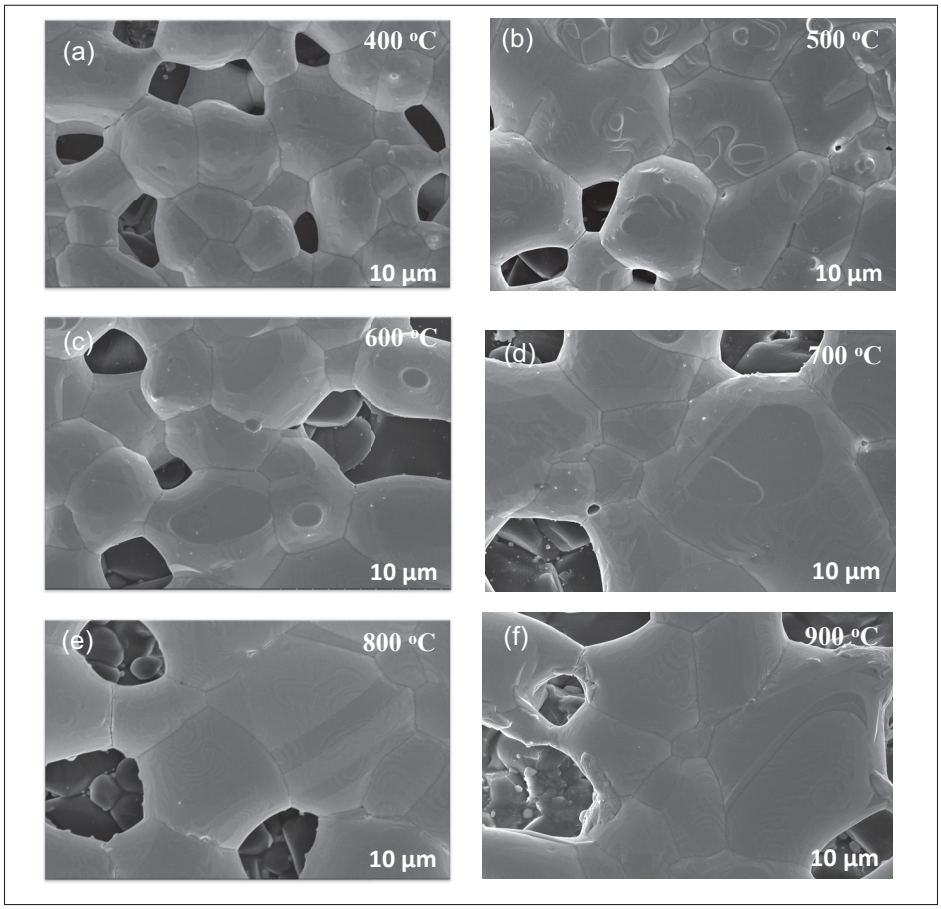

Figure 5.6 SEM micrographs of pristine Ag ink thermally treated at (a) 400 °C, (b) 500 °C, (c) 600 °C, (d) 700 °C, (e) 800 °C and (f) 900 °C for 1 hour

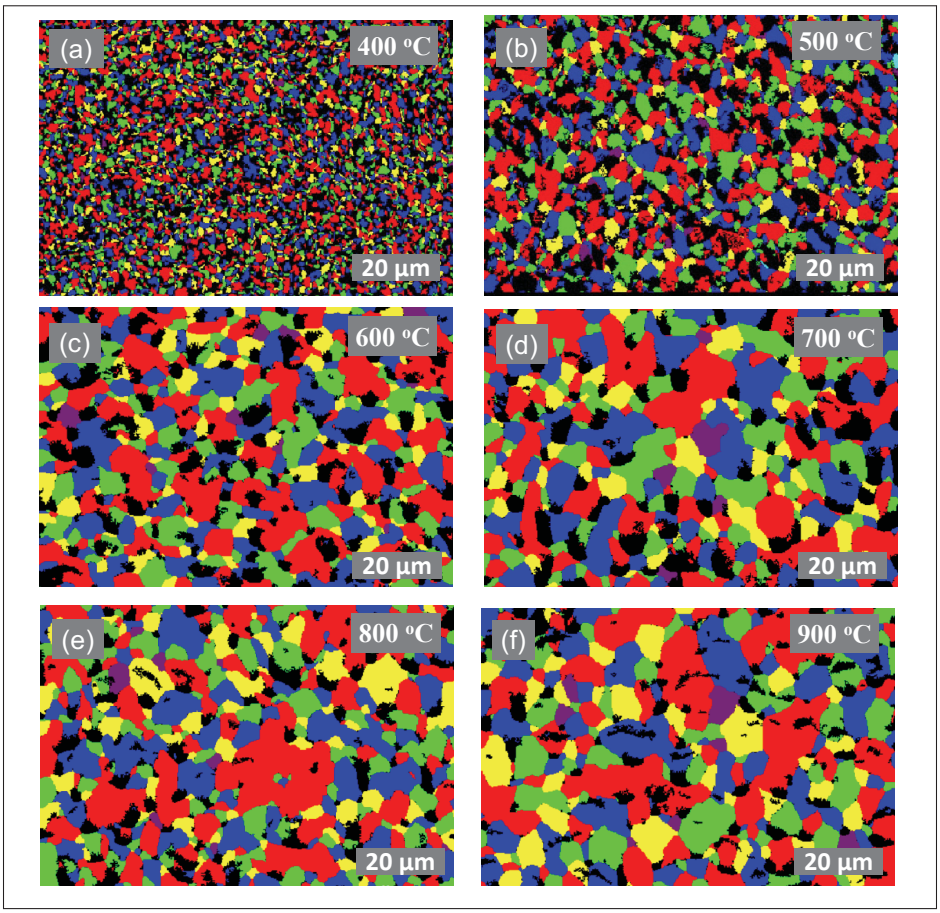

Figure 5.7 EBSD micrographs of pristine Ag ink thermally treated at (a) 400 °C, (b) 500 °C, (c) 600 °C, (d) 700 °C, (e) 800 °C and (f) 900 °C for 1 hour

Figures 5.8 and 5.9 exemplify the pinning nature of the silicon particles. Owing to the large particle size distribution in the purchased Si particles, we can segregate their impact into two main categories. First, we observe large Si particles (> 1μm) uniformly placed between segments of fused silver particles (highlighted with red arrows in Figure 5.8). These behave like pillars, physically preventing segments of silver particles from fusing to together to form bulk like material. Secondly, as the Ag grains grow, they encounter the smaller Si particles (400nm - 1μm) which exerts a drag force on the grain boundary, thus impeding its movement. The drag force exerted by the Si particles on the grain boundaries is called the pinning force which stabilizes the grain boundaries and prevent their migration. In comparison to the pristine Ag ink,

the modified ($Ag - 5wt.\%Si$) ink exhibits an average grain size of only 4.5 μm when treated at 900 °C for only 10 minutes of isothermal exposure which is less than one quarter of grain size observed at the same conditions for the pristine Ag ink.

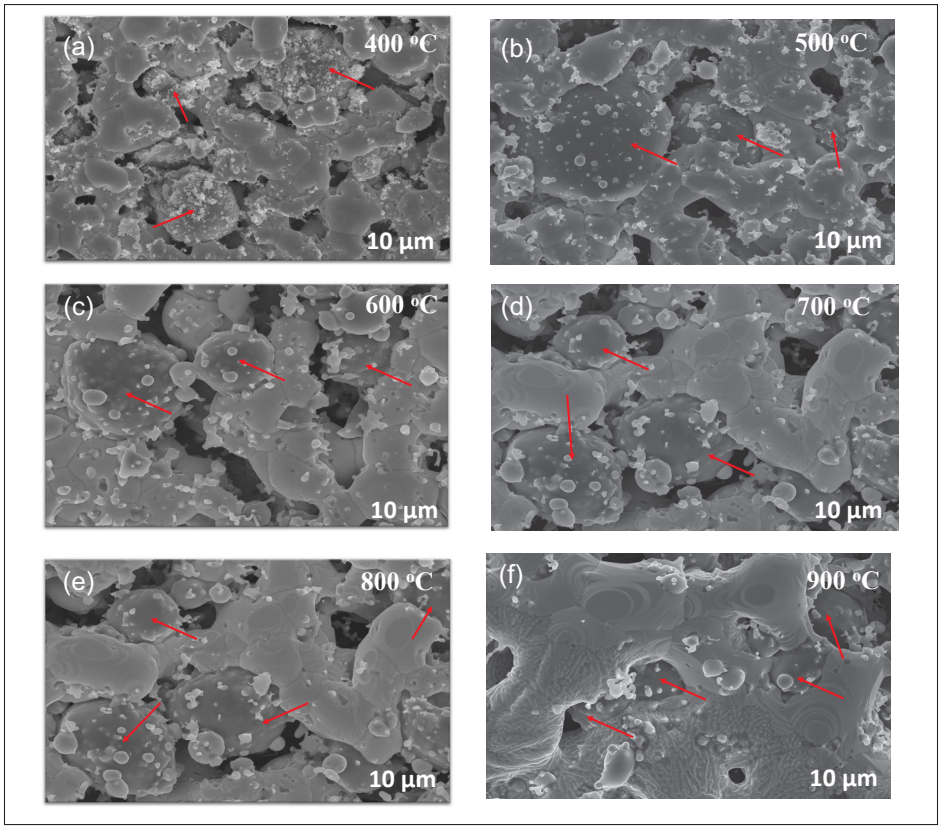

Figure 5.8 SEM micrographs of 5 wt.% modified ($Ag - 5wt.\%Si$) ink thermally treated at (a) 400 °C, (b) 500 °C, (c) 600 °C, (d) 700 °C, (e) 800 °C and (f) 900 °C for 1 hour

We further confirm the effect and large and small Si particles towards grain pinning for the modified ($Ag - 5wt.\%Si$) ink as seen ink Figure 5.10. Figure 5.10 a) shows the presence of pillar like Si particles evenly distributed with in the silver matrix retarding densification, where as Figure 5.10 b) shows the presence of smaller Si particles migrate to the grain boundary interfaces leading to Zener pinning. Figures 5.10 c) and d) present the Energy Dispersive X-ray Spectroscopy (EDX) micrographs confirming the presence of Si particles as described (highlighted in red).

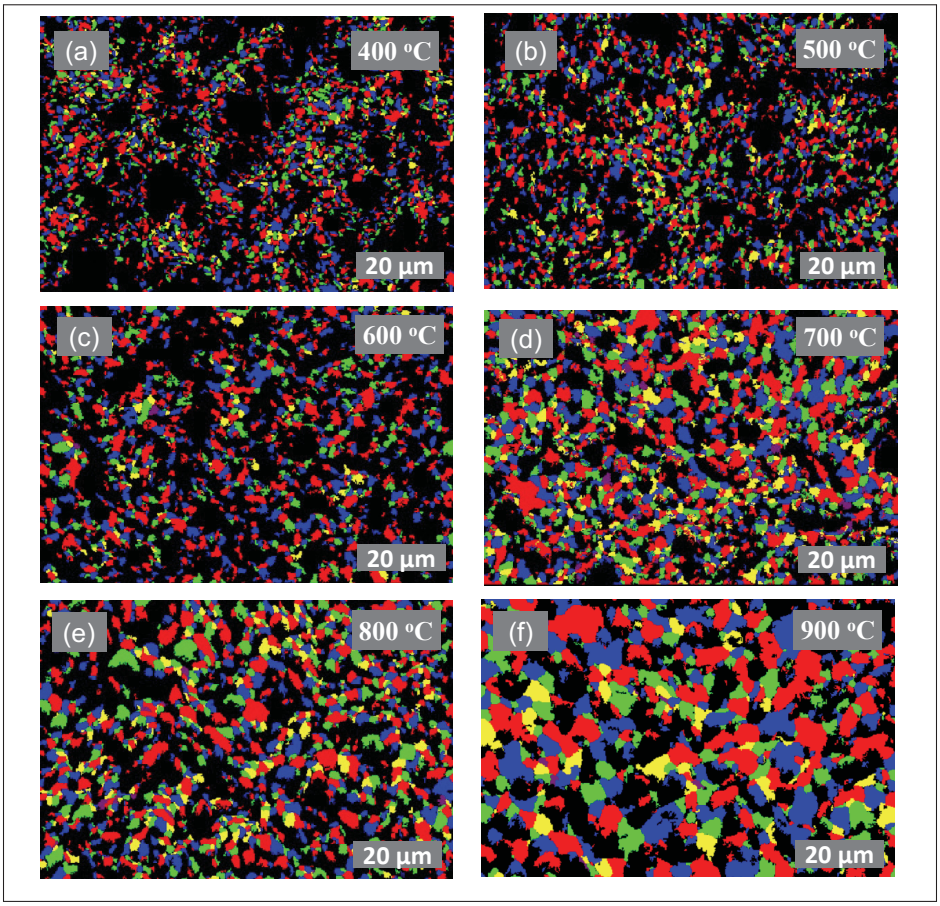

Figure 5.9 EBSD micrographs of 5 wt.% modified $(Ag - 5wt.\%Si)$ ink thermally treated at (a) 400 °C, (b) 500 °C, (c) 600 °C, (d) 700 °C, (e) 800 °C and (f) 900 °C for 1 hour

5.3.4 Oxidation States

The ratio of the atomic wt.% of oxygen contributing to the silver and silicon oxide species are determined as seen in Figure 5.11 and summarized in Tables III-4 and III-5 in the supplemental section. For prolonged exposure times of 3 and 4 hours we observe an approximate 58% increase in the AgO (silver peroxide) species for the pristine Ag ink when heated from 400 °C – 700 °C due to gradual oxidation of the silver particles (Figure 5.11 a) and b)) (Chaparro & Goudeli, 2023). This is consistent with reports of an operational ceiling of 400 °C for the pristine ink, beyond which the prints tend to oxidize (Kim, Kim & Jung, 2016). On the other hand, the concentrations of both AgO and Ag_2O species in the modified $(Ag - 5Wt.\%Si)$ ink are significantly lower

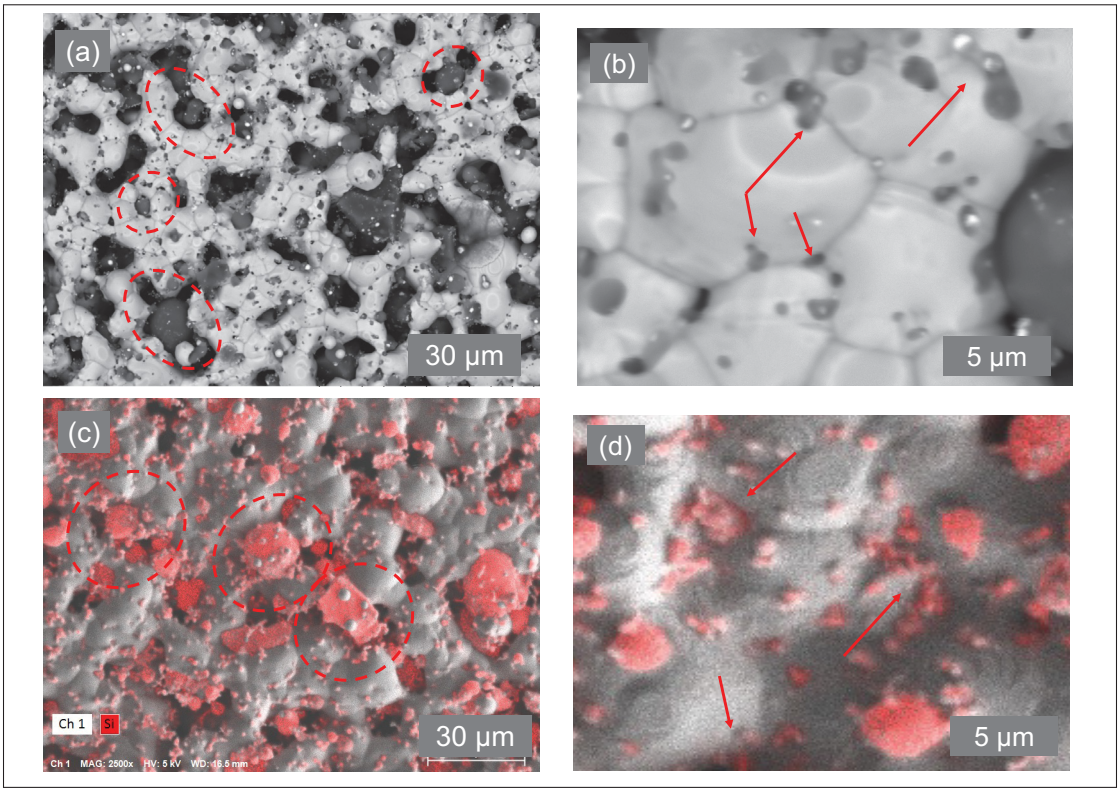

Figure 5.10 SEM and EDX micrographs exhibiting the effect of (a) and (c) large Si particles and (b) and (d) smaller Si particles on the printed films morphology respectively

when treated at the same temperatures and isothermal times and tend to decrease with increased temperatures. In addition, Figure 5.11 c) shows an increase in the amount of oxygen bonding to silicon, suggesting oxide formation becoming more pronounced beyond 400 °C (Na, Lim, Huh, Park, Lee & Lee, 2009; Okada & Iijima, 1991). X-ray photoelectron spectroscopy (XPS) spectra of the AgO and SiO_x species for temperatures ranging from 400 °C - 700 °C for 3 and 4 hours of isothermal exposures are presented in Figures III-1 in the supplemental section. Generally, silver oxide species begin to thermally decompose around 400 °C during which silver and oxygen are generated as per Equation 5.1 (L'vov, 1999):

$$2Ag_2O(s) \rightarrow 4Ag(s) + O_2(g) \tag{5.1}$$

This reaction involves the temporal formation of O before the formation of stable O_2 which results in increased oxygen presence. The Gibbs free energy change for oxide formation of Si is more negatively charged as compared to Ag, hence Si particles undergo preferential oxidation during this thermal cycling of the modified ($\mathrm{Ag} - 5\mathrm{wt.\%Si}$) ink (Matsuda, Inami, Motoyama, Sano & Hirose, 2018). This reaction is depicted in Equation 5.2.

$$2Ag_2O(s) + Si \rightarrow 4Ag(s) + SiO_2(s) \tag{5.2}$$

This process can be visualized as a scavenger effect, where the thermal energy from the furnace first decomposes the silver oxide species creating free oxygen which preferentially oxidises silicon particles, therefore maintaining the integrity of the silver. We establish that the improved stability of the modified ink is dominated by two mechanisms:

- The physical grain-pinning effect due to the silicon inclusions ions present along silver grain boundaries and preventing silver domains from recombining (Zener pinning).
- The scavenger effect of the silicon particles to preferentially oxidize as opposed to silver particles, hence redirecting the incoming thermal energy towards silicon-oxygen bonds formation.

5.3.5 Grain Growth Kinetics

Grain growth kinetics is a well establish science pioneered in the 1950's (J.E & D, 1952). Kinetics can be expressed as the n-power law shown in Equation 5.3 (Dannenberg, Stach, Groza & Dresser, 2000; Rollett, Gottstein, Shvindlerman & Molodov, 2004; Schlenker, Valero, Schock & Werner, 2004; Thompson, 2011; Wang, Zhao, Cui, Sun & Yu, 2021). Here, D_t represents the average grain size at temperature T (in °C) and D_0 represents the initial grain size. In our case, we conasider D_0 as the grain size at the manufacturers prescribed sintering temperature of the silver flake ink (250 °C). The term 't' is the exposure time in seconds and 'n' is the kinetic growth rate exponent. 'k' is the temperature and activation energy dependant

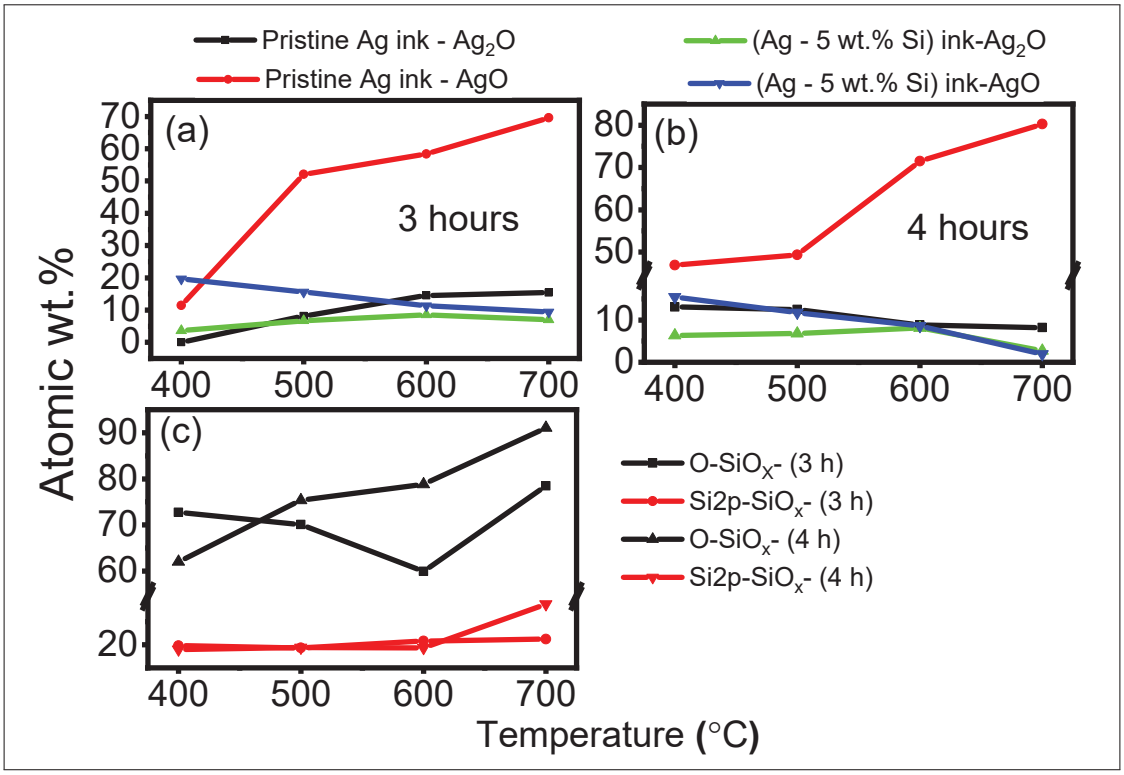

Figure 5.11 XPS analysis of the silver ink samples after annealing (a) % Oxygen concentration in silver oxide species for the pristine silver ink samples after a 3-hour isothermal annealing (b) % Oxygen concentration in silver oxide species for the pristine silver ink samples after a 4-hour isothermal annealing (c) % Oxygen in silicon oxide and total silicon oxide in the modified (Ag+Si) ink samples for 3 hour and 4 hour isothermal annealing

proportionately constant which can be calculated using Equation 5.4 (Gwalani, Salloom, Alam, Valentin, Zhou, Thompson, Srinivasan & Banerjee, 2019; Mičian, Frátrik, Moravec & Švec, 2022; Moravec, 2015), where k_0 is the pre-activation constant, 'Q' is the activation energy in kJ. mol^{-1} and 'R' is the universal gas constant.

$$D_t^n - D_0^n = kt \tag{5.3}$$

$$k = k_0 exp^{((-Q)/(RT))} \tag{5.4}$$

By adding a controlled amount of silicon particles to the silver ink (5 wt.%), a significant reduction in grain growth due to silver grain boundary pinning is observed. Thus, the grain

growth equation can be modeled using the following Equation 5.5 (Akbarpour & Hesari, 2016; Zhu, Godfrey, Hansen & Zhang, 2017):

$$\frac{D_0 - D_t}{D_{max}} + ln\left(\frac{(D_{max} - D_0)}{D_{max} - D_t}\right) = \frac{k}{D_{max}^2} \tag{5.5}$$

where the D_{max} represents the maximum grain size achieved at an exposure temperature with increase in exposure time. For the purpose of these calculations, we consider the grain size values obtained at 4 hours of isothermal exposure as the D_{max} values and grain size at 250 °C as the D_0 for each annealing cycle. The rate constant 'k' is calculated from Equation 5.5 for 1 hour of isothermal annealing and then fitted in Equation 5.5, and the kinetic growth rate exponents are also calculated by fitting the experimental data and their values are shown in Table 5.1.

Table 5.1 Calculations of n, k, activation energies (Q) and R^2 values based on experimental results after 1 hour isothermal annealing at 400 °C, 500 °C, 600 °C and 700 °C

Temperature	**Ag only ink**		**(Ag-5 wt.% Si) ink**	
	n	k	n	k
400 °C	1.58	0.010	2.41	0.012
500 °C	3.01	0.264	2.01	0.010
600 °C	3.57	0.433	2.20	0.016
700 °C	4.15	0.826	2.36	0.024
Growth rate	**Abnormal**		**Normal**	
Q (kJ mol^{-1})	80.2 ± 19.15		38.52 ± 7.345	
R^2	0.9		0.93	

Generally, n = 2 is considered normal grain growth controlled by curvature driven grain boundary migration (Hosseini, Enayati & Karimzadeh, 2014) and surface diffusion (Zheng *et al.*, 2022). When n = 3 and higher, the grain growth is considered abnormal and can attributed to a combined effect of solute precipitation, grain boundary grooving, impurity drag or volume diffusion along the grain boundaries (Hillert, 1965). By substituting the calculated values of 'k', we obtain the n values for both inks. Accordingly, the slope of the $\mathrm{Ln(k)}$ evolution as a function of the reciprocal of the isothermal temperatures ($\frac{1}{RT}$) directly provides the activation energies for each ink as shown in Figure 5.12.

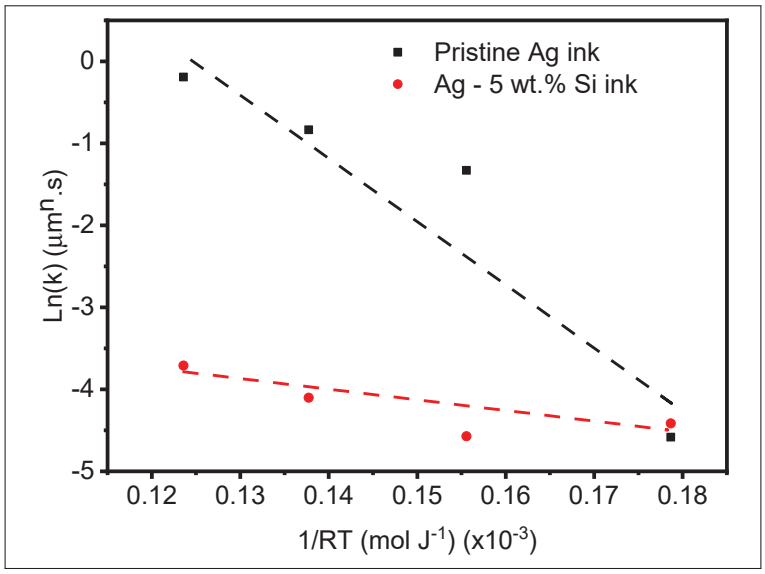

Figure 5.12 Arrhenius plot of the parameter k versus isothermal exposure temperatures

The pristine Ag ink experiences normal grain growth up-to its optimal sintering temperature of 400 °C (n=1.58), beyond which it follows an abnormal grain growth regime (n>3) between 500 °C - 800 °C which is agreeable with other studies (Koo & Yoon, 2001). The activation energy is estimated to be 80.2 ± 19.15 kJ mol^{-1} which is in line with the reported activation energy of silver thin films of between 30 - 95 kJ mol^{-1} (Dannenberg *et al.*, 2000; Zheng *et al.*, 2022). The modified ($Ag - 5wt.\%Si$) ink exhibits normal grain growth (n < 3) and essentially stagnant over the entire temperature range. This is a strong indicative of the pinning effect of the Si particles. The modified ink has achieves a lower activation energy of 38 kJ mol^{-}1, which are consistent with the impact of grain boundary pinning in micro particle systems (Akbarpour *et al.*, 2017; Dannenberg *et al.*, 2000; Wu, Zhao, Zheng & Ding, 2011).

5.4 Conclusions

The electrical stability of screen-printable silver ink for use at temperatures higher than 400 °C is poor. We have successfully demonstrated a silicon-based extrinsic grain boundary engineering

process that offers benefits in minimizing grain growth, while maintaining a high and stable electrical conductivity at significantly higher temperatures.

- Between 400 °C to 700 °C, the modified $(\mathrm{Ag-Si})$ undergoes a 2x increase in overall grain size exhibiting normal grain growth. Whereas the pristine silver ink undergoes a 7x increase in grain size and exhibits abnormal grain growth.

- The electrical conductivity of both inks reaches a maximum at 1 hour of isothermal exposure to each temperature point indicating a transition point from sintering to grain growth. Between 1 and 2 hours of exposure, the electrical conductivity reduced indicating grain growth.

- Beyond 3 hours the pristine silver ink shows an erratic rise in electrical conductivity indicating grain growth transitioning to bulk material phase. This phenomenon is significant at higher exposure temperature (800 °C - 900 °C).

- On the other hand, beyond 2 hours the electrical conductivity of the modified $(\mathrm{Ag-Si})$ ink remains stable due to the Zener pinning effect.

- XPS data confirms a stark rise in silver oxide species in the pristine silver ink with increase in exposure temperatures while the silicon particles in the modified $(\mathrm{Ag-Si})$ ink preferentially bond with the oxygen behaving like scavengers there by retarding the oxidation of the silver ink.

- The calculated activation energy for the modified $(\mathrm{Ag-Si})$ inks is between 38 – 43 kJ mol^{-1} which is significantly lower than the pristine ink.

Using this strategy, the operational window of low-cost silver micro particle ink can be enhanced up to 700 °C, with stable electrical conductivity and minute changes in its grain size. The authors intend to test the application of this modified ink as a functional material for high temperature measurement in future work.

Acknowledgments

The authors thank Francios-Xavier Fortier for assistance with electrical conductivity measurements, Luis Felipe Gerlain for assistance with data plotting and visualization and Josianne Lafebvre for performing XPS measurements. Sylvain G. Cloutier acknowledges the NSERC-Discovery and Canada Research Chair programs for their financial support.

CONCLUSION AND RECOMMENDATIONS

Summary

In accordance with the objectives set at the beaning of this doctoral thesis we first focused our efforts towards understanding silicon carbide as a functional material, its properties, fabrication techniques and applications (Chapter 1). We then dive into understanding key concepts pertaining to the thesis subject such as printing technologies and materials, fundamentals of the characterization techniques used, operating principles of printed temperature and humidity sensors and limitations of printed interconnects (Chapter 2).

We choose silicon carbide as the focus of thesis PhD project due to its excellent stability, bio compatibility and ease to fabricate commercially. Coupled with the use of low complexity, high volume fabrication techniques, silicon cardie based printed sensors are strong candidates for demanding applications. An important focus of this project was to simplify the ink and device fabrication process for potential technology transfer for industrial scale manufacturing and deployment. To this effect, commercially available silicon carbide nanoparticles and ink vehicles were used. The respected ink formulations were optimized to maximize device performance and repeatability. Additionally, screen printing which is a repeatable and low cost fabrication technique is used throughout this project. This opens up new avenues to deploy printed silicon carbide sensors into large scale environments.

In this project we present first of their kind printed humidity (Chapter 3) and temperature (Chapter 4) sensors based on screen printable silicon carbide nanoparticle inks. Two distinct ink formulations were developed for each sensor types. We thoroughly characterize the SiC nanoparticles and solvent systems used. The printed sensors were characterized and their response, sensitivity, stability and repeatability were quantified and reported. Additionally, we extensively investigate the mechanism of failure in commercial silver flake ink for screen printed

interdigitated electrode applications (Chapter 5). We determine that by adding small controlled amounts of silicon particles leads to the stabilization of the inks micro structure and its electrical conductivity. The silicon particles initiate the Zener pinning mechanism preventing silver grains from growing and also preferentially oxidize as compared to silver further stabilizing the conductivity and performance of the silver ink. I am very confident that the contributions made by this PhD thesis will greatly benefit the advancement of printed physical sensors and their applications.

Future research outlook

With the knowledge, know how and results assimilated during the course of this PhD project, we open new avenues for future research on the above mentioned topics. Silicon carbide is well known for its ability to perform under extreme temperatures, corrosive environments and its bio-compatibility. This makes it well suited for sensing in areas such as aviation and aerospace, oil and gas, nuclear, chemical production, wearable and medical devices etc. Printed temperature sensors are often limited to nominal or moderately elevated conditions of temperature where the substrate, printed interconnects (IDE's for example), external connections and read out mechanisms are the limiting factors. The SiC thermistors developed in this study can potentially be fabricated onto ceramic substrates coupled with the modified $\mathrm{Ag-Si}$ inks for interconnects for potential ultra high temperature applications up to at least 700 °C.

Similarly, our printed SiC humidity sensors can be further optimized to be robustly integrated into printed medical intervention technologies such as wearables, smart diagnostic bandages etc. Extensive research can be performed on the saturation stability of the printed sensors over long term stability and determine their life span based on response degradation. Lastly, the modified silver ink can be further improved by testing different commercially available inks with silicon as the additive or alternate ceramic additives. Our research establishes the premise and

the need for such modifications. Precious metal inks such as gold and platinum can potentially be replaced with a well characterized ceramic modified silver ink which poses huge cost savings.

Statement of original work

This doctoral thesis highlights various contributions:

- **Printed silicon carbide based humidity sensors:** We fabricated highly sensitive humidity sensors based on silicon carbide nanomaterials inks that were formulated and optimized. These inks were screen printed to form flexible humidity sensors which have an ultra fast response and show potential in applications such as medical intervention and large area humidity detection.

- **Printed silicon carbide based temperature sensors:** We report repeatable, and high sensitivity silicon carbide based temperature sensors operating over a wide temperature range of 25 °C - 170 °C. The silicon carbide nanomaterial based sensing inks is dispersed in commercially available ink vehicle making it a potential scalable technology for large volume production and deployment.

- **Modified silver inks for high temperature applications:** we investigate the impact of grain growth on the morphology and electrical conductivity of low temperature, commercial screen printable silver flake ink. We observe that grain size dramatically increases with increase in temperature and sintering time. The addition of 5 at. % of silicon particles significantly helps restrict the increase in grain size and also stabilizes the electrical conductivity of the ink up to at least 700 °C. This opens the possibility of using these low cost inks for harsh environment applications.

Academic achievements

During the course of this doctoral thesis the follow peer reviewed journal articles have been published:

1. **Wadhwa, A.**, Benavides-Guerrero, J., Gratuze, M., Bolduc, M. and Cloutier, S.G., 2024. All Screen Printed and Flexible Silicon Carbide NTC Thermistors for Temperature Sensing Applications. Materials, 17(11), p.2489.

2. **Wadhwa, A.**, Saadati, M., Guerrero, J.B., Bolduc, M. and Cloutier, S.G., 2024. Grain Structure Engineering in Screen-Printed Silver Flake-Based Inks for High-Temperature Printed Electronics Applications.Materials, 17(20), p.4966.

3. **Wadhwa, A.**, Perrotton, A, Tehreian M.H., Zirakjou, A., Benavides-Guerrero, J., Gratuze, M., Vaussenat, F., Bolduc, M., Cloutier, S.G. Flexible Screen-Printed SiC-based Humidity Sensors.
   Submitted to Nautre Communications Engineering.

4. Taherian, M.H., **Wadhwa, A.**, Fortier, F.X., Gerlein, L.F., Shah, K., Cloutier, S.G. and Bolduc, M., 2024. Reshaping surface dynamics in Kapton® substrate for advanced printed electronics: An investigation of intense pulsed light, laser and plasma treatments. MRS Advances, pp.1-8.

5. Taherian, M.H., **Wadhwa, A.**, Akbari, M., Cloutier, S.G. and Bolduc, M., 2024. Surface Energy of Polymer Substrates for Flexible Electronics: A Comparative Study of Polyimide, PET, and Ceramic coated PET. Journal of Electrical Systems, 20(10s), pp.158-164.

6. Taherian, M.H., Shah, K., Gerlein, L.F., **Wadhwa, A.**, Moulay A.S, Benavides-Guerrero, J., Cloutier, S.G., Bolduc, M. Photonic Sintering of Non-Oxide Ceramics for Printed Electronics: A Comprehensive Mini Review.
   Submitted to: Journal of Synthesis and Sintering

7. Morelli, L., **Wadhwa, A.**, Cloutier, S.G., Bolduc, M., Gagnon, G., Zednik, R.J. Printed Hybrid Capacitive Kirigami Sensor: Enhancing Flexibility and Conformability for Improved Motion Artifacts.
   Accepted by IOP: Flexible and Printed Electronics, pending publication.

8. Fortier, F.X., Benavides-Guerrero, J., **Wadhwa. A.**, Bolduc, M. and Cloutier, S.G. Two-Step Laser-Induced Graphitization of a Polyimide Sheet for Built-In Circuit Elements.
   To be submitted

9. Moulay A.S, **Wadhwa, A.**, Cloutier S.G., Izquierdo R. Controlling Optical and Electrical Properties of Perovskite Films and the Performance of Solar Cells Using Photonic Curing Process.
   To be submitted

Additionally, the main research topics were also presented at academic and industrial conferences during the course of this PhD project:

1. **Wadhwa, A.**, Banerjee, D., Benavides-Guerrero, J., Bolduc, M., Cloutier, S.G. Impact of grain boundary pinning using silicon refractory inclusions on screen printed silver flake inks for high temperature printed electronics applications.
   Presented at: Materials Research Society (MRS), Fall 2022 meeting and exhibition, Boston, MA, USA.

2. **Wadhwa, A.**, Benavides-Guerrero, J., Perrotton, A, Bolduc, M., Cloutier, S.G. All Screen-Printed; Silicon Carbide Thermistors for Wide Temperature Range Applications.
   Presented at: Large-area, Organic & Printed Electronics Convention (LOPEC), February 2023 meeting and exhibition, Munich, Germany.

3. **Wadhwa, A.**, Perrotton, A, Vaussenat, F., Benavides-Guerrero, J., Carolina, A., Machucha, F., Bolduc, M., Cloutier, S.G. Screen Printed Silicon Carbide Humidity Sensors for

Simultaneous Respiration Rate and Mask Fouling Detection.

Presented at: The FLEX conference, July 2023 meeting and exhibition, San Francisco, CA, USA.

APPENDIX I

CHAPTER 3: FLEXIBLE SCREEN-PRINTED SIC-BASED HUMIDITY SENSORS

Figure I-1 illustrated the design of the printed SiC humidity sensor. Three identical sensors were fabricated atop a 1 square inch sample of substrate. All three devices were tested under identical conditions to demonstrate device repeatability and reproducability.

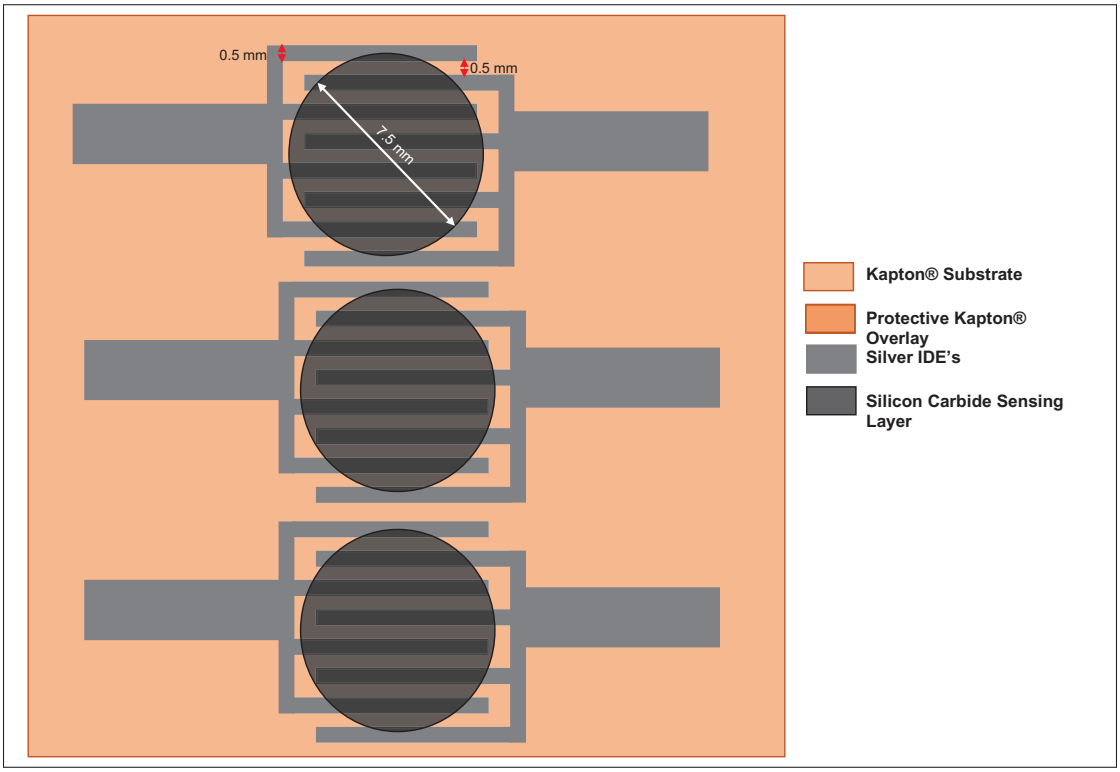

Figure A I-1 Printed device geometry

High resolution laser microscope image and height profiles of the humidity sensor are presented in Figure I-2 a). Figure I-2 b) shows a three dimensional height map of the sensor with the highest points highlighted in red and lowest points in blue. Single line profilometry was performed on the sample in both X and Y directions where Figure I-2 c) shows the variations in height of the sample along with X travel. We can clearly see the locations of the IDE traces with a maximum height of approximately 12 µm. Similarly, an approximate height of 23 µm was observed in the Y travel direction as seen in Figure I-2 d).

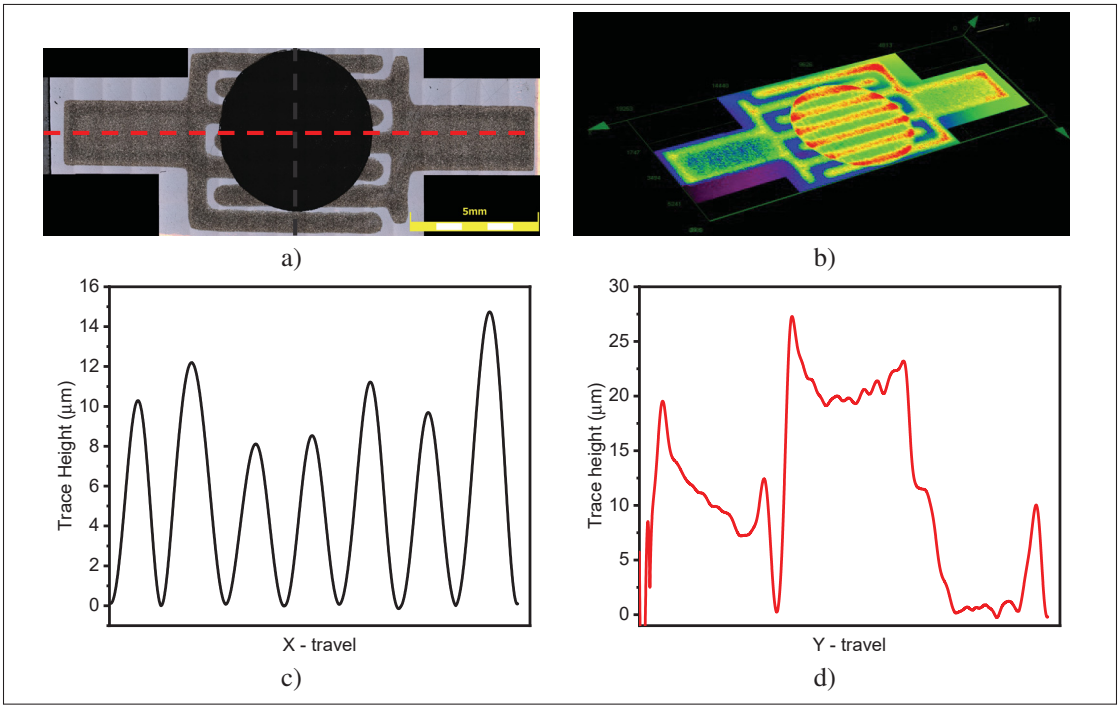

Figure A I-2 (a) High resolution optical microscopy image of printed SiC humidity sensor (b) three dimensional height profile reconstruction image of sensor, line scan profilometry of sensor in the (c) X and (d) Y directions

Figure I-3 shows the experimental setup to determine the adsorption and desorption times of the SiC humidity sensor. The sensor was positioned in the Nextron® and connected to the Keithley data recorder. Initially, device resistance was recorded under ambient conditions before a water droplet was introduced via a micro-pipette. The sensor was able to operate for over 10 minutes even when covered with a water droplet. Its resistance increased by over 46 times in just 18 seconds before saturating. The sensor was allowed to remain under saturation for over 10 minutes where we observed a small increase in the resistance of the device which was due to the continued infiltration of the water molecules with in the porous surface of the printed SiC sensing film. Once the water was removed with a blow dryer, the sensor's resistance almost returned to its initial level in 46 seconds.

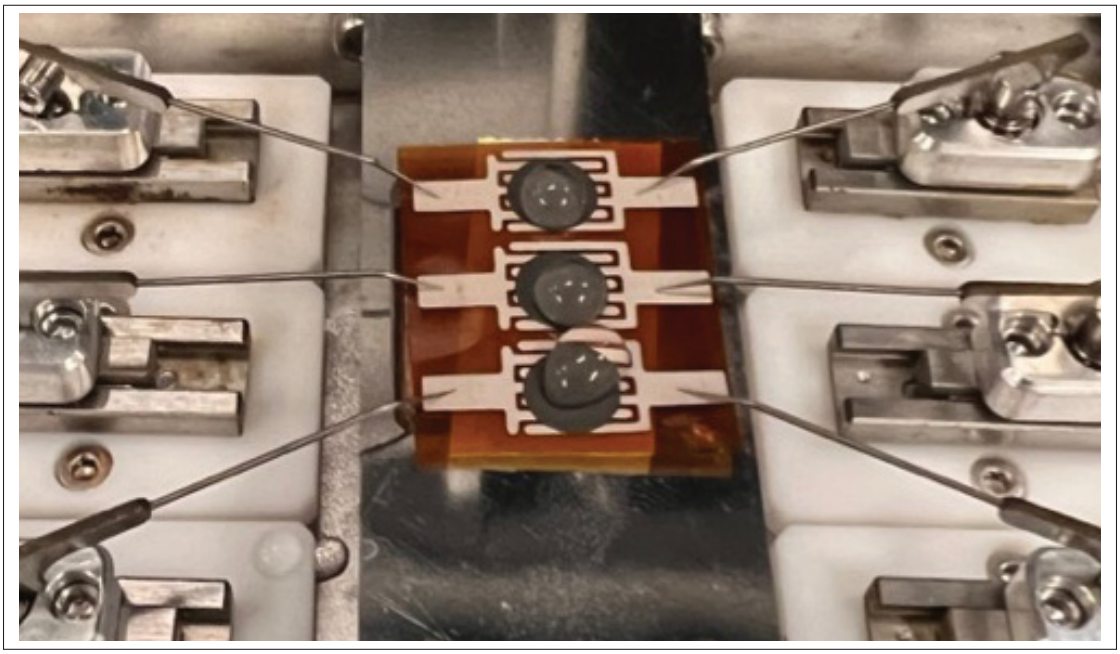

Figure A I-3 Test setup for determining adsorption / desorption times

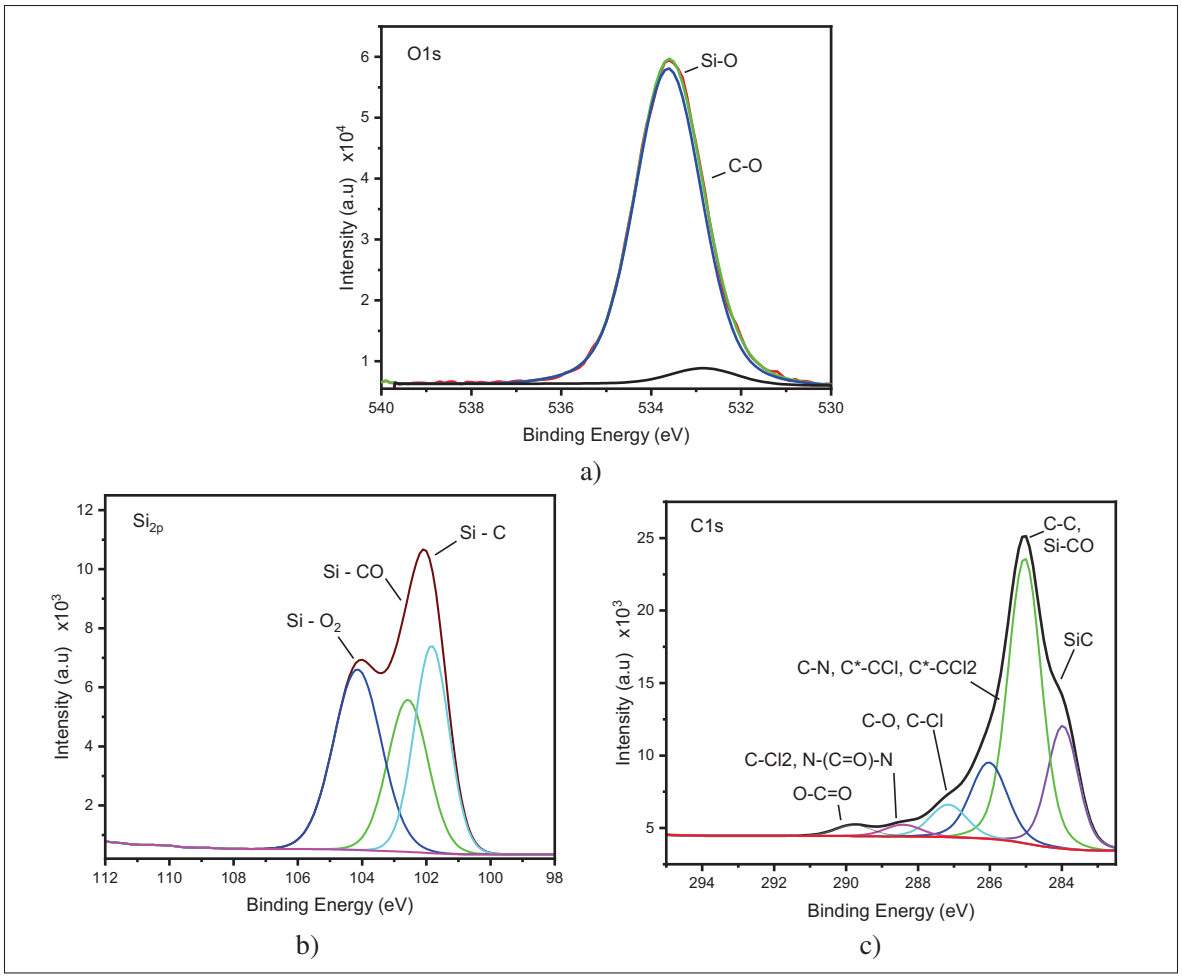

Figure A I-4 Individual element XPS spectra of SiC humidity sensor inks. (a) O1s, (b) Si2p and (c) C1s individual XPS spectra for cured ink

Figure I-5 illustrates the Ritveld refinement XRD spectra for the as received SiC nanoaparticles. Default Ritvelds refinement was performed to estimate the weight ratio of the 3C and 2H SiC polytypes detected in the nanopowder via the XRD spectra. Table I-1 highlights the fitting parameters obtained indicating a good fitting. It is worth mentioning that the quantification is complicated and sensitive to the refinement parameters due to the overlapped peaks of two phases at high intensity peaks.

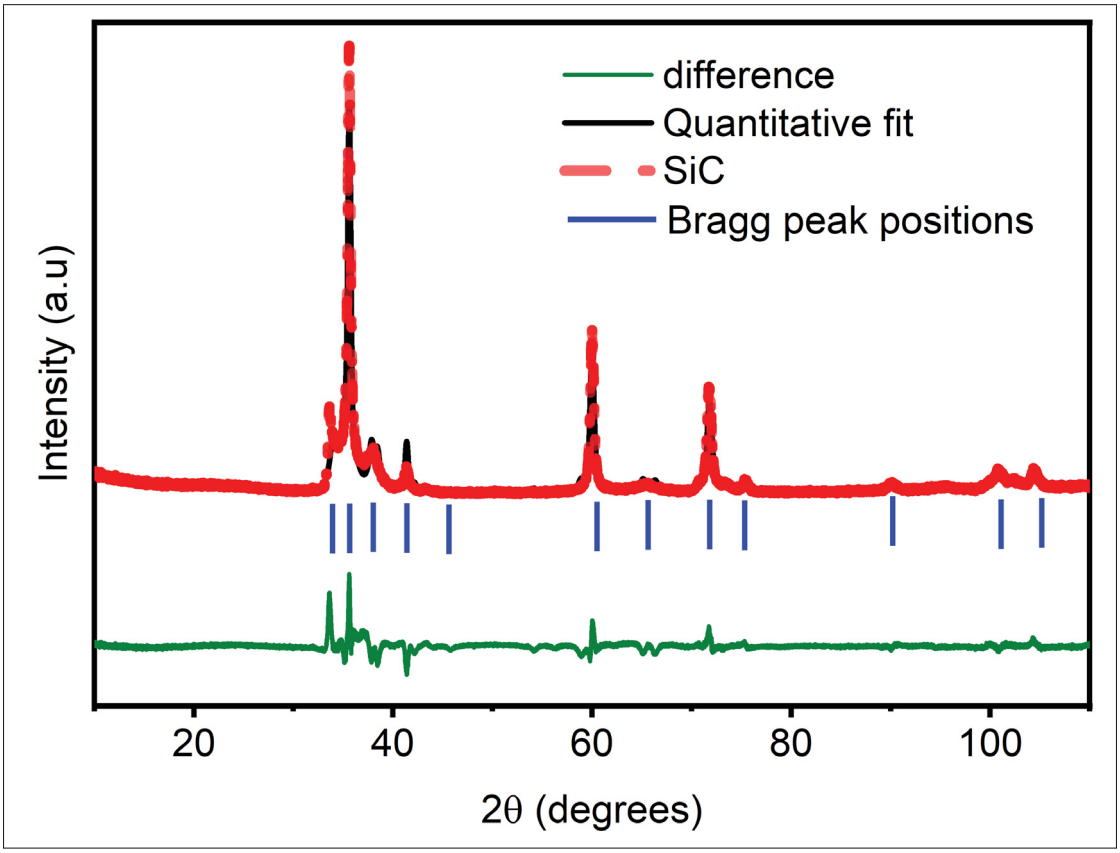

Figure A I-5 Output from default Ritveld refinement analysis of the XRD spectra of the commercial SiC nanoparticles. The red spectra represents the experimental data obtained from XRD analysis and the overlapping black spectra represents the calculated fitting. The vertical lines indicate the bragg peak positions in the XRD spectra. The difference between the experimental data and quantitative fitting is shown at the bottom highlighted in green.

Table A I-1 Ritveld refinement parameters

Parameter	Values (%)
R_p	13.25
R_{wp}	18.69
R_{Exp}	4.38
X^2	4.26

Table A I-2 XPS data for 30 wt.% SiC thermistor ink cured at 300 °C for 180 min

Name	Peak	Atomic wt.%
Si2p SiC	101.8	9.50
Si2p SiCO	102.5	8.10
Si2p SiO2	104.1	11.80
Cl2p3 C-Cl, C-Cl2	201.1	0.50
C1s SiC	283.9	8.90
C1s C-C, SiCO	285	19.50
C1s C-N, C*-CCl, C*-CCl2	286	5.20
C1s C-O, C-Cl	287.1	2.20
C1s C-Cl2, N-(C=O)-N	288.5	1.10
C1s O-C=O	290	0.60
N1s NH_3	398.9	0.70
N1s N-(C=O)-N	400	0.70
N1s N-C-O	401.1	0.50
O1s C-O	532.8	1.60
O1s Si-O	533.6	29.20
Total atomic wt.%		**100**

Table A I-3 Electrical conductivity of 20, 30, 40, 50wt.% loaded SiC humidity sensor versus 60, 120, 180 minutes cure time at 300 °C

Cure time (mins)	**Conductivity (S/m)**			
	20-SiC	30-SiC	40-SiC	50-SiC
60	$0.8 \pm 8x10^3$	$2.49 \pm 5x10^4$	$1.26 \pm 3x10^4$	$0.23 \pm 2x10^4$
120	$0.8 \pm 6x10^3$	$2.44 \pm 3x10^4$	$1.46 \pm 7x10^4$	$0.51 \pm 2x10^4$
180	$0.8 \pm 1x10^2$	$\mathbf{3.09 \pm 3x10^4}$	$1.52 \pm 1.4x10^3$	$0.24 \pm 1x10^4$

Table A I-4 Baseline resistance values of 20, 30, 40, 50wt.% loaded SiC humidity sensor versus 60, 120, 180 minutes cure time at 300 °C

Cure time (mins)	**Baseline Resistance (Ω)**			
	20-SiC	**30-SiC**	**40-SiC**	**50-SiC**
60	1556 ± 69	582 ± 8	1078 ± 6	5703 ± 686
120	1618 ± 30	426 ± 29	970 ± 66	4052 ± 195
180	1754 ± 43	306 ± 30	**717 ± 19**	6156 ± 840

APPENDIX II

CHAPTER 4: ALL SCREEN PRINTED AND FLEXIBLE SILICON CARBIDE NTC THERMISTORS FOR TEMPERATURE SENSING APPLICATIONS

Table A II-1 Atomic % of elemental C, O and Si observed in elemental micrographs as seen in Figure 4.5

Element	**Atomic %**
Carbon	36.48
Oxygen	12.42
Silicon	51.10
Total	**100.00**

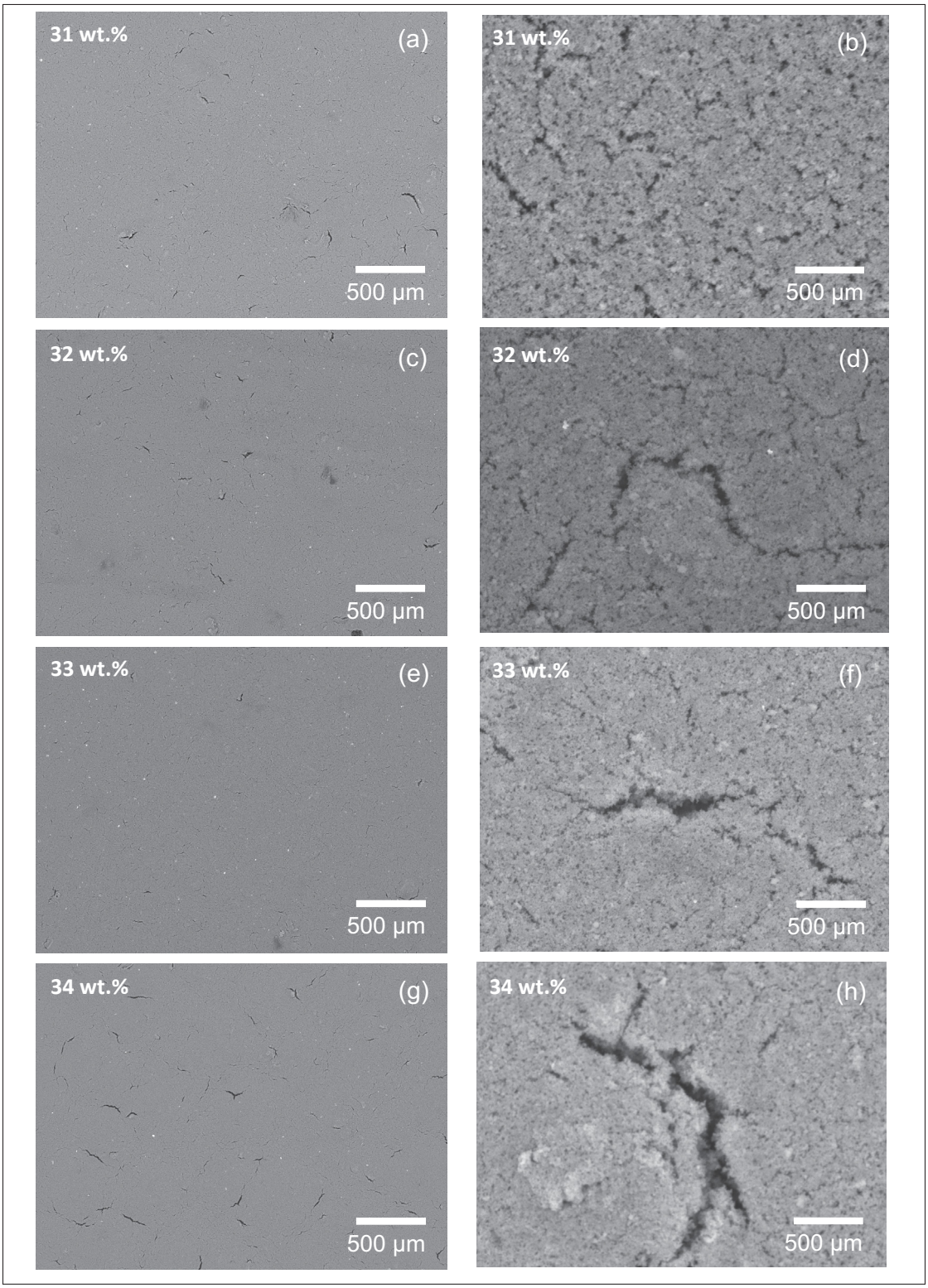

Figure A II-1 SEM micrographs of a) and b) 31 wt.%, c) and d) 32 wt.%, e) and f) 33 wt.%, g) and h) 34 wt.% SiC thermistor inks

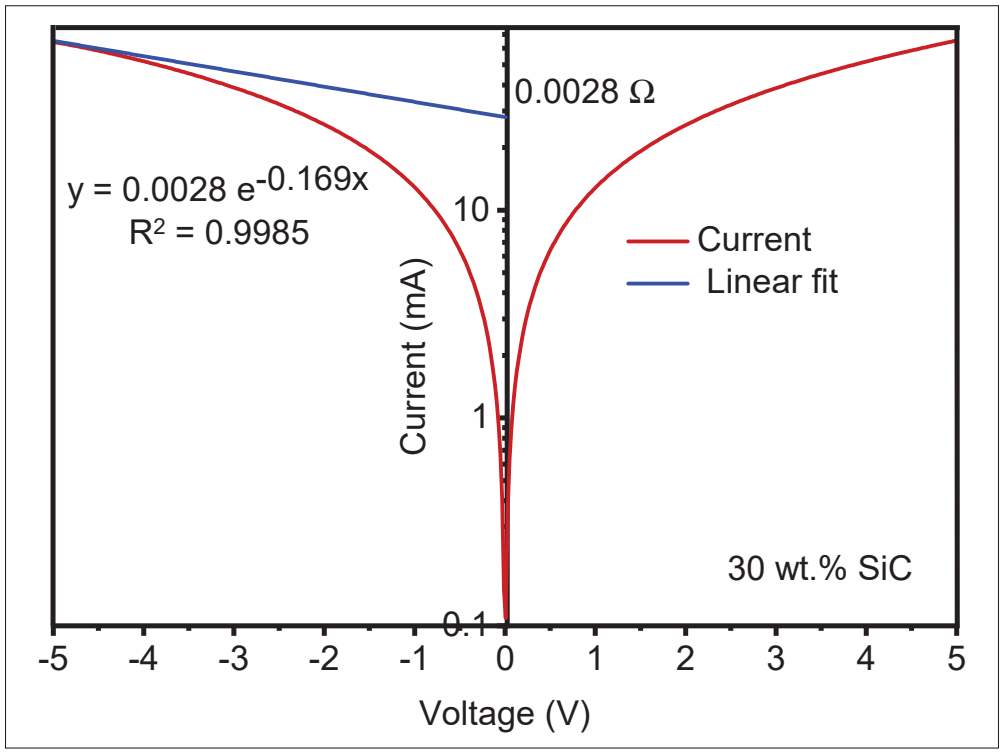

Figure A II-2 Current-voltage curve to determine contact resistance of $Ag - SiC$ interface

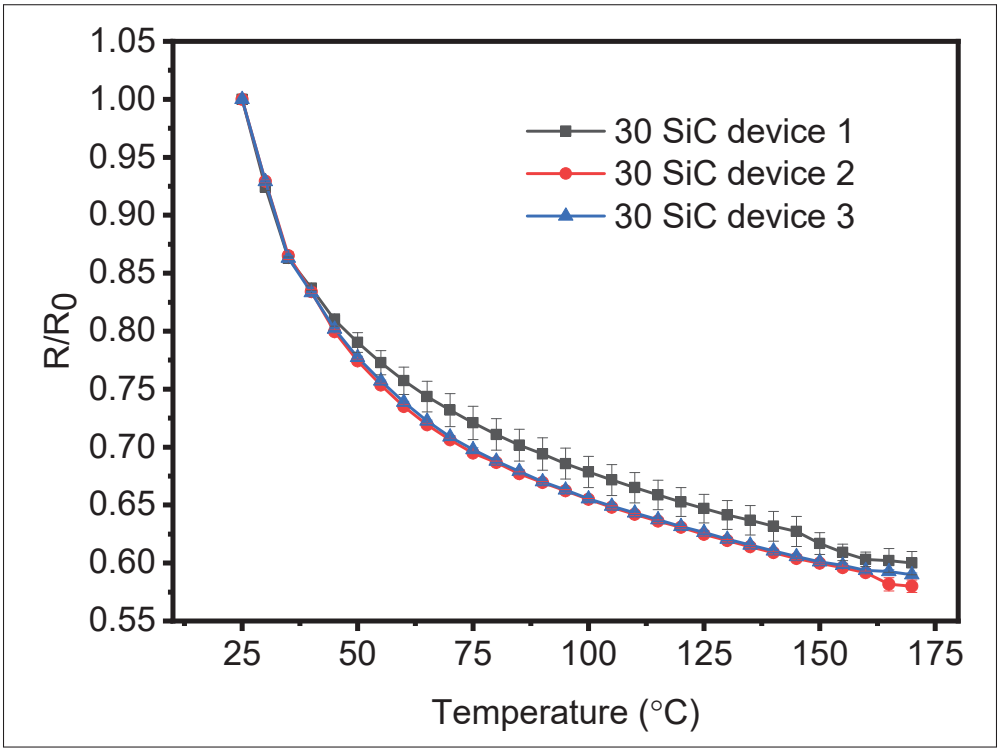

Figure A II-3 Electrical resistance versus temperature of three individual 30 wt.% SiC thermistors over 5 thermal cycles each

APPENDIX III

CHAPTER 5: GRAIN STRUCTURE ENGINEERING IN SCREEN-PRINTED SILVER FLAKE BASED INKS FOR HIGH-TEMPERATURE PRINTED ELECTRONICS APPLICATIONS

Table A III-1 Electrical conductivity data of pristine and modified $(\mathrm{Ag}-\mathrm{Si})$ inks with 3, 5, 7, 10 wt.% Si particles thermally treated for 1 hour isothermal exposure at 250 °C, 400 °C, 500 °C, 600 °C, 700 °C, 800 °C, 900 °C

Temperature	**Electrical Conductivity (S/m)** ($x10^7$)				
	Pristine Ag ink	**3 wt.% Si**	**5 wt.% Si**	**7 wt.% Si**	**10 wt.% Si**
250 °C	4.14 ± 0.27	3.83 ± 0.34	3.32 ± 0.22	3.46 ± 0.27	0.935 ± 0.34
400 °C	5.61 ± 0.27	4.65 ± 0.34	4.69 ± 0.685	3.46 ± 0.35	3.29 ± 0.34
500 °C	5.58 ± 0.28	3.17 ± 0.52	4.24 ± 0.866	1.96 ± 0.58	2.41 ± 0.31
600 °C	4.87 ± 0.61	2.76 ± 0.8	4.14 ± 0.63	2.79 ± 0.26	2.05 ± 0.18
700 °C	5.16 ± 0.41	2.93 ± 0.43	4.13 ± 0.22	3.12 ± 0.42	2.98 ± 0.43
800 °C	4.77 ± 0.96	4.28 ± 0.51	4.16 ± 0.93	2.41 ± 0.574	3.68 ± 0.51
900 °C	3.44 ± 0.4	3.28 ± 0.6	4.08 ± 0.56	1.29 ± 0.23	3.06 ± 0.6

Table A III-2 Electrical conductivity data of pristine and modified $(\mathrm{Ag}-5\mathrm{wt.\%Si})$ inks thermally treated between 250 °C and 900 °C for isothermal exposure times of 10 mins, 1, 2, 3, 4 hours

Temperature	**Electrical Conductivity (S/m)** ($x10^7$)									
	Pristine Ag Ink					**Modified (Ag - 5 wt.% Si) ink**				
	10 mins	**1 hr**	**2 hr**	**3 hr**	**4 hr**	**10 mins**	**1 hr**	**2 hr**	**3 hr**	**4 hr**
250 °C	0.6 ± 0.085	2.9 ± 0.75	1.77 ± 0.14	2.08 ± 0.46	2.33 ± 0.76	0.825 ± 0.08	3.7 ± 0.4	1.12 ± 0.67	1.15 ± 0.12	1.12 ± 0.26
400 °C	1.58 ± 0.46	6.08 ± 0.88	2.08 ± 0.14	2.66 ± 0.46	3.18 ± 0.76	1.55 ± 0.54	4.69 ± 0.37	1.56 ± 0.67	1.36 ± 0.27	1.47 ± 0.26
500 °C	1.36 ± 0.25	6.62 ± 0.64	3.15 ± 0.85	3.38 ± 0.2	3.52 ± 3.60	0.925 ± 0.16	4.24 ± 0.88	2.04 ± 0.38	1.54 ± 0.27	1.79 ± 0.21
600 °C	1.37 ± 0.3	6.70 ± 0.82	2.55 ± 0.8	4.38 ± 0.41	5.24 ± 0.93	1.03 ± 0.34	4.39 ± 0.53	1.8 ± 0.13	2.06 ± 0.63	2.19 ± 0.6
700 °C	1.88 ± 0.62	6.96 ± 0.69	2.24 ± 0.465	4.38 ± 0.651	5.61 0.38	0.965 ± 0.3	4.50 ± 0.9	1.76 ± 0.23	2.01 ± 0.43	2.37 ± 0.44
800 °C	1.17 ± 0.153	5.21 ± 0.6	1.76 ± 0.389	2.77 ± 0.451	4.99 ± 0.67	1.07 ± 0.14	5.07 ± 0.556	2.77 ± 0.485	3.49 ± 0.41	2.41 ± 0.35
900 °C	6.92 ± 0.135	4.11 ± 0.44	5.26 ± 0.5	5.15 ± 0.41	5.26 ± 0.73	9.82 ± 0.18	6.76 ± 0.63	1.31 ± 0.293	2.04 ± 0.498	2.17 ± 0.146

Table A III-3 Grain size evolution of pristine and modified ($Ag - 5wt.\%Si$) inks thermally treated between 250 °C and 900 °C for isothermal exposure times of 10 mins, 1, 2, 3, 4 hours

Temperature	**Grain Size Evolution (μm)**									
	Pristine Ag Ink					**Modified (Ag - 5 wt.% Si) ink**				
	10 mins	**1 hr**	**2 hr**	**3 hr**	**4 hr**	**10 mins**	**1 hr**	**2 hr**	**3 hr**	**4 hr**
250 °C	2.7	2.64	2.67	2.7	2.72	2.16	2.44	2.48	2.51	2.56
400 °C	4.1	4.1	8.06	9.63	11.3	2.3	3.2	3.5	3.7	3.83
500 °C	12.8	12.8	13.2	14.5	15.7	2.6	4	4.03	4.55	5.08
600 °C	13.3	13.3	13.2	14.1	14.5	2.9	4.8	4.27	4.85	5.35
700 °C	15.4	15.4	15.3	15.3	15.7	3.5	5.4	5	5.18	5.28
800 °C	15.8	15.8	17.16	17.04	16.97	4.4	5.7	5.8	6.2	6.35
900 °C	16.2	16.2	18.56	18.135	17.768	4.5	7.7	7.9	7.8	7.5

Table A III-4 Atomic wt.% of oxygen species observed via XPS analysis for samples treated for 3 hours isothermal exposure

Ag Ink					**Modified (Ag+Si) Ink**				
Species (%)	400 °C	500 °C	600 °C	700 °C	**Species (%)**	400 °C	500 °C	600 °C	700 °C
O1s O in Ag2O	0	1.4	2.8	3.3	O1s O in Ag2O	1.5	2.9	3.9	3.3
O1s O in AgO	1.2	8.9	11.2	14.9	O1s O in AgO	8.1	6.8	5.2	4.4
O1s C-O-C, C=O	6	4.7	3.8	1.9	O1s O in SiOx, C=O, C-O-C	29.9	30.5	27.5	36.8
O1s O in C-O	3.3	2.1	1.4	1.3	O1s O in C-O	1.6	3.3	9.3	2.4
					Si2p in SiOx	19.8	19.3	20.8	21.2
Total	10.5	17.1	19.2	21.4	**Total**	41.1	43.5	45.9	46.9
% AgO	11.42	52.04	58.33	69.62	% AgO	19.70	15.63	11.32	9.38
% Ag_2O	0	8.18	14.58	15.42	% Ag_2O	3.64	6.66	8.49	7.03
					% SiO_x	72.74	70.11	59.91	78.46

Table A III-5 Atomic wt.% of oxygen species observed via XPS analysis for samples treated for 4 hours isothermal exposure

Ag Ink					**Modified (Ag+Si) Ink**				
Species (%)	400 °C	500 °C	600 °C	700 °C	**Species (%)**	400 °C	500 °C	600 °C	700 °C
O1s O in Ag2O	3.4	1.8	2	2.2	O1s O in Ag2O	2.7	3	3.7	1.6
O1s O in AgO	12.2	7.1	16.3	21.6	O1s O in AgO	6.6	5.2	3.9	1.1
O1s C-O-C, C=O	9	4	3.1	2.3	O1s O in SiOx, C=O, C-O-C	26.5	33.4	35.8	52.9
O1s O in C-O	1.4	1.5	1.4	0.8	O1s O in C-O	6.9	2.7	2	2.5
					Si2p in SiOx	19	19.4	19.3	28.8
Total	26	14.4	22.8	26.9	**Total**	42.7	44.3	45.4	58.1
% AgO	46.92	49.30	71.49	80.29	% AgO	15.45	11.73	8.59	1.89
% Ag_2O	13.07	12.5	8.77	8.17	% Ag_2O	6.32	6.77	8.14	2.75
					% SiO_x	62.06	75.39	78.85	91.04

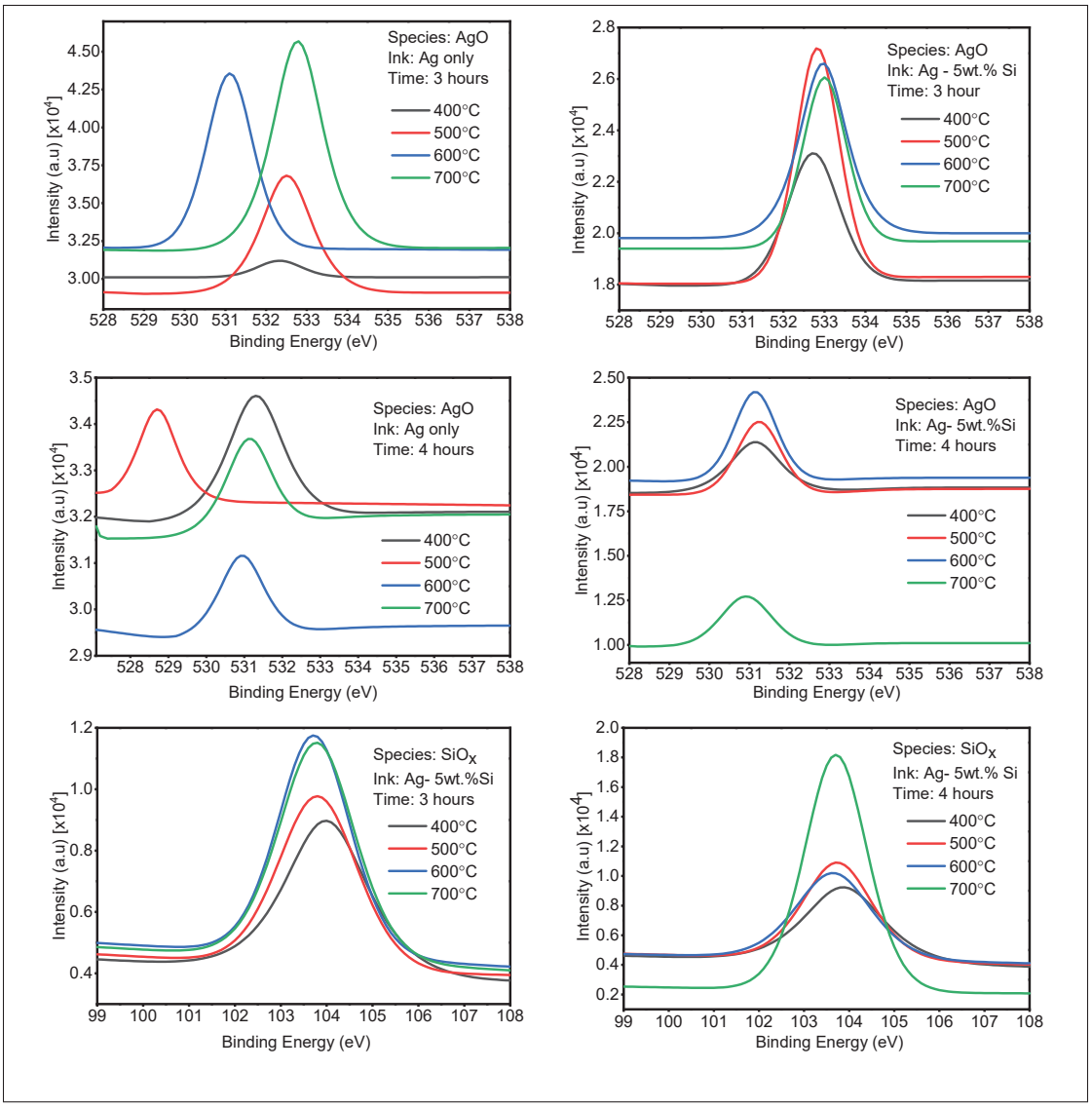

Figure A III-1 XPS spectra of AgO species observed in (a) pristine Ag ink at 3 hours, (b) modified $Ag-5wt.\%Si$ ink at 3 hours, (c) pristine Ag ink at 4 hours, (b) modified $Ag-5wt.\%Si$ ink at 4 hours isothermal exposure at 400 °C, 500 °C, 600 °C and 700 °C. XPS spectra of SiO_x species observed at (e) 3 hours and (f) 4 hours of isothermal exposure

LISTE DE RÉFÉRENCES BIBLIOGRAPHIQUES

Screen Making for Printed Electronics- Specification and Tolerancing. Consulted at https://www.ipc.org/system/files/technical_resource/E40%26S02_02%20-%20Jesse%20Greenwood%20.pdf.

ASTM F2252/F2252M-13e1 - Standard Practice for Evaluating Ink or Coating Adhesion to Flexible Packaging Materials Using Tape. Consulted at https://webstore.ansi.org/standards/astm/astmf2252f2252m13e1.

Silicon Carbide SiC Nanopowder / Nanoparticles (SiC, beta, 99+%, <80 nm, cubic). Consulted at https://www.us-nano.com/inc/sdetail/373.

(2015). An Introduction to EBSD. Consulted at https://www.azom.com/article.aspx?ArticleID=11770.

(2020). What Is A Thermistor And How Does It Work? Accessed on March 11, 2024, Consulted at https://www.omega.ca/en/resources/thermistor#:~:text=Thermistors%20are%20highly%20accurate%20(ranging,C%20and%20100%C2%B0C.

(2020). Thermistor Vs Rtd Temperature Measurement Accuracy – Application Note. Accessed on March 11, 2024, Consulted at https://www.bapihvac.com/application_note/thermistor-vs-rtd-temperature-measurement-accuracy-application-note/.

(2023). Global Conductive Ink Market By Product (Dielectric Ink and Conductive Silver Ink), By Application (Membrane Switches, Photovoltaic, Automotive, and Displays), By Region and Companies - Industry Segment Outlook, Market Assessment, Competition Scenario, Trends and Forecast 2023-2033Conductive Ink Market Size, Share | CAGR of 6.3%. *Market.us*, Report ID 67457, 374.

Abbas, K. (2020). *Handbook of Digital CMOS Technology, Circuits, and Systems*. Springer Nature.

Abderrazak, H. & Hmida, E. (2011). Silicon carbide: synthesis and properties. *Properties and applications of Silicon Carbide*, 361–388.

Abro, D. M., Dablé, P., Cortés-Salazar, F., Amstutz, V. & Girault, H. (2016). Characterization of surface state of inert particles: case of Si and SiC. *Journal of Minerals and Materials Characterization and Engineering*, 4(1), 62–72.

Acenson, E. (1893). PRODUCTION OF ARTIFICIAL CRYSTALLINE CARBON ACEOUs MATERIALs.

Acheson, E. G. (1893). PRODUCTION OF ARTIFICIAL CRYSTALLINE CARBON ACEOUs MATERIALS,. Google Patents. US Patent US492767A, Consulted at https://patents .google.com/patent/US492767A/en.

Adachi, S. (2009). *Properties of semiconductor alloys: group-IV, III-V and II-VI semiconductors*. John Wiley & Sons.

Afonso Camargo, S. E., Mohiuddeen, A. S., Fares, C., Partain, J. L., Carey IV, P. H., Ren, F., Hsu, S.-M., Clark, A. E. & Esquivel-Upshaw, J. F. (2020). Anti-bacterial properties and biocompatibility of novel SiC coating for dental ceramic. *Journal of Functional Biomaterials*, 11(2), 33.

Agarwala, S., Goh, G. L., Dinh Le, T.-S., An, J., Peh, Z. K., Yeong, W. Y. & Kim, Y.-J. (2019). Wearable Bandage-Based Strain Sensor for Home Healthcare: Combining 3D Aerosol Jet Printing and Laser Sintering. *ACS Sensors*, 4(1), 218–226. doi: 10.1021/acssensors.8b01293.

Agathopoulos, S. (2012). Combustion synthesis of ultra-fine SiC powders in low pressure N2-atmosphere. *Ceramics International*, 38(5), 4165–4171.

Ahmed, H., Abduljalil, H. M. & Hashim, A. (2019a). Structural, optical and electronic properties of novel (PVA–MgO)/SiC nanocomposites films for humidity sensors. *Transactions on Electrical and Electronic Materials*, 20(3), 218–232.

Ahmed, H., Abduljalil, H. M. & Hashim, A. (2019b). Analysis of Structural, Optical and Electronic Properties of Polymeric Nanocomposites/Silicon Carbide for Humidity Sensors. *Transactions on Electrical and Electronic Materials*, 20(3), 206–217. doi: 10.1007/s42341-019-00100-2.

Akbarpour, M. R., Farvizi, M. & Kim, H. S. (2017). Microstructural and kinetic investigation on the suppression of grain growth in nanocrystalline copper by the dispersion of silicon carbide nanoparticles. *Materials & Design*, 119, 311–318. doi: 10.1016/j.matdes.2017.01.077.

Akbarpour, M. R. & Hesari, F. A. (2016). Characterization and hardness of TiCu–Ti $_2$ Cu $_3$ intermetallic material fabricated by mechanical alloying and subsequent annealing. *Materials Research Express*, 3(4), 045004. doi: 10.1088/2053-1591/3/4/045004.

Al-Qahtani, A. M., Ali, S., Khan, A. & Bermak, A. (2023). Performance optimization of wearable printed human body temperature sensor based on silver interdigitated electrode and carbon-sensing film. *Sensors*, 23(4), 1869.

Aldosky, H. Y. Y. & Shamdeen, S. M. H. (2010). A new system for measuring electrical conductivity of water as a function of admittance. *Journal of Electrical Bioimpedance*, 2(1), 86–92. doi: 10.5617/jeb.203.

Alekseev, S., Shamatulskaya, E., Volvach, M., Gryn, S., Korytko, D., Bezverkhyy, I., Iablokov, V. & Lysenko, V. (2017). Size and surface chemistry tuning of silicon carbide nanoparticles. *Langmuir*, 33(47), 13561–13571.

Aleksić, O. S. & Nikolić, P. M. (2017). Recent advances in NTC thick film thermistor properties and applications. *Facta universitatis-series: Electronics and Energetics*, 30(3), 267–284.

Alexander Jr, F., Price, D. T. & Bhansali, S. (2010). Optimization of interdigitated electrode (IDE) arrays for impedance based evaluation of Hs 578T cancer cells. *Journal of Physics: Conference Series*, 224(1), 012134.

Alexey Kamyshny, S. M. *Nanomaterials for 2D and 3D printing*.

Alhendi, M., Alshatnawi, F., Abbara, E. M., Sivasubramony, R., Khinda, G., Umar, A. I., Borgesen, P., Poliks, M. D., Shaddock, D., Hoel, C., Stoffel, N. & Lam, T.-K. H. (2022). Printed electronics for extreme high temperature environments. *Additive Manufacturing*, 54, 102709. doi: 10.1016/j.addma.2022.102709.

Ali, S., Hassan, A., Hassan, G., Bae, J. & Lee, C. H. (2016). All-printed humidity sensor based on graphene/methyl-red composite with high sensitivity. *Carbon*, 105, 23–32. doi: 10.1016/j.carbon.2016.04.013.

Ali, S., Khan, S. & Bermak, A. (2019). Inkjet-printed human body temperature sensor for wearable electronics. *IEEE access*, 7, 163981–163987.

Aljasar, S. A., Xu, Y. & Qasaimeh, M. R. (2022). Design, Fabrication and Characterization of flexible laser reduced Silicon Carbide nanoparticle thermal heater sensor. *2022 4th International Youth Conference on Radio Electronics, Electrical and Power Engineering (REEPE)*, pp. 1–5.

Allen, M., Alastalo, A., Suhonen, M., Mattila, T., Leppäniemi, J. & Seppa, H. (2011). Contactless electrical sintering of silver nanoparticles on flexible substrates. *IEEE Transactions on Microwave Theory and Techniques*, 59(5), 1419–1429.

Allen, M. L., Aronniemi, M., Mattila, T., Alastalo, A., Ojanperä, K., Suhonen, M. & Seppä, H. (2008). Electrical sintering of nanoparticle structures. *Nanotechnology*, 19(17), 175201.

Altenberend, U., Molina-Lopez, F., Oprea, A., Briand, D., Bârsan, N., De Rooij, N. F. & Weimar, U. (2013). Towards fully printed capacitive gas sensors on flexible PET substrates based on Ag interdigitated transducers with increased stability. *Sensors and Actuators B: Chemical*, 187, 280–287. doi: 10.1016/j.snb.2012.11.025.

Amjadi, M., Kyung, K.-U., Park, I. & Sitti, M. (2016). Stretchable, skin-mountable, and wearable strain sensors and their potential applications: a review. *Advanced Functional Materials*, 26(11), 1678–1698.

An, Z., Wang, H., Zhu, C., Cao, H. & Xue, J. (2019a). Synthesis and formation mechanism of porous silicon carbide stacked by nanoparticles from precipitated silica/glucose composites. *Journal of Materials Science*, 54(4), 2787–2795.

An, Z., Xue, J., Cao, H., Zhu, C. & Wang, H. (2019b). A facile synthesis of silicon carbide nanoparticles with high specific surface area by using corn cob. *Advanced Powder Technology*, 30(1), 164–169.

Angayarkanni, S. & Philip, J. (2015). Review on thermal properties of nanofluids: Recent developments. *Advances in colloid and interface science*, 225, 146–176.

Anthony, L. J. (1855). SUBLMATON PROCESS FOR MANUEFACTURING SILICON CARBIDE CRYSTALS. Google Patents. US Patent US492767A, Consulted at https://patents.google.com/patent/US2854364A/en.

Appadurai, M. & Raj, E. F. I. (2022). Epoxy/silicon carbide (sic) nanocomposites based small scale wind turbines for urban applications. *International Journal of Energy and Environmental Engineering*, 13(1), 191–206.

Aqida, S. N., Ghazali, M. I. & Hashim, J. (2004). Effects Of Porosity On Mechanical Properties Of Metal Matrix Composite: An Overview. *Jurnal Teknologi A*, (40A), 17–32. Number: 40A Publisher: Penerbit UTM Press.

Arman Kuzubasoglu, B. (2022). Recent Studies on the Humidity Sensor: A Mini Review. *ACS Applied Electronic Materials*, 4(10), 4797–4807. doi: 10.1021/acsaelm.2c00721. Publisher: American Chemical Society.

Arrabito, G., Aleeva, Y., Pezzilli, R., Ferrara, V., Medaglia, P. G., Pignataro, B. & Prestopino, G. (2020). Printing ZnO Inks: From Principles to Devices. *Crystals*, 10(6), 449. doi: 10.3390/cryst10060449. Number: 6 Publisher: Multidisciplinary Digital Publishing Institute.

Arsenov, P. V., Vlasov, I. S., Efimov, A. A., Minkov, K. N. & Ivanov, V. V. (2019). Aerosol Jet Printing of Platinum Microheaters for the Application in Gas Sensors. *IOP Conference Series: Materials Science and Engineering*, 473, 012042. doi: 10.1088/1757-899X/473/1/012042.

Arsenov, P. V., Efimov, A. A. & Ivanov, V. V. (2021). Optimizing Aerosol Jet Printing Process of Platinum Ink for High-Resolution Conductive Microstructures on Ceramic and Polymer Substrates. *Polymers*, 13(6), 918. doi: 10.3390/polym13060918.

Arshad, B., Ogie, R., Barthelemy, J., Pradhan, B., Verstaevel, N. & Perez, P. (2019). Computer Vision and IoT-Based Sensors in Flood Monitoring and Mapping: A Systematic Review. *Sensors (Basel, Switzerland)*, 19(22), 5012. doi: 10.3390/s19225012.

Arvizo, R. R., Bhattacharyya, S., Kudgus, R. A., Giri, K., Bhattacharya, R. & Mukherjee, P. (2012). Intrinsic therapeutic applications of noble metal nanoparticles: past, present and future. *Chemical Society Reviews*, 41(7), 2943–2970. doi: 10.1039/c2cs15355f.

Awotunde, M. A., Adegbenjo, A. O., Obadele, B. A., Okoro, M., Shongwe, B. M. & Olubambi, P. A. (2019). Influence of sintering methods on the mechanical properties of aluminium nanocomposites reinforced with carbonaceous compounds: A review. *Journal of Materials Research and Technology*, 8(2), 2432–2449.

Ayalew, T. (2004). *SiC semiconductor devices technology, modeling and simulation*. (Ph.D. thesis, Technische Universität Wien).

Azevedo, R. G., Jones, D. G., Jog, A. V., Jamshidi, B., Myers, D. R., Chen, L., Fu, X.-a., Mehregany, M., Wijesundara, M. B. & Pisano, A. P. (2007). A SiC MEMS resonant strain sensor for harsh environment applications. *IEEE Sensors Journal*, 7(4), 568–576.

Bagheri, B., Shamsipur, A., Abdollahzadeh, A. & Mirsalehi, S. E. (2023). Investigation of SiC nanoparticle size and distribution effects on microstructure and mechanical properties of Al/SiC/Cu composite during the FSSW process: experimental and simulation. *Metals and Materials International*, 29(4), 1095–1112.

Baker, S. P., Saha, K. & Shu, J. B. (2013). Effect of thickness and Ti interlayers on stresses and texture transformations in thin Ag films during thermal cycling. *Applied Physics Letters*, 103(19), 191905. doi: 10.1063/1.4829364.

Baliga, B. J. (2018). *Wide Bandgap Semiconductor Power Devices: Materials, Physics, Design, and Applications*. Woodhead Publishing.

Bantz, C., Koshkina, O., Lang, T., Galla, H.-J., Kirkpatrick, C. J., Stauber, R. H. & Maskos, M. (2014). The surface properties of nanoparticles determine the agglomeration state and the size of the particles under physiological conditions. *Beilstein journal of nanotechnology*, 5(1), 1774–1786.

Barillet, S., Jugan, M.-L., Laye, M., Leconte, Y., Herlin-Boime, N., Reynaud, C. & Carrière, M. (2010a). In vitro evaluation of SiC nanoparticles impact on A549 pulmonary cells: cyto-, genotoxicity and oxidative stress. *Toxicology letters*, 198(3), 324–330.

Barillet, S., Simon-Deckers, A., Herlin-Boime, N., Mayne-L'Hermite, M., Reynaud, C., Cassio, D., Gouget, B. & Carrière, M. (2010b). Toxicological consequences of TiO 2, SiC nanoparticles and multi-walled carbon nanotubes exposure in several mammalian cell types: an in vitro study. *Journal of nanoparticle research*, 12, 61–73.

Barmpakos, D., Segkos, A., Tsamis, C. & Kaltsas, G. (2017). A disposable flexible humidity sensor directly printed on paper for medical applications. *Journal of Physics: Conference Series*, 931(1), 012003. doi: 10.1088/1742-6596/931/1/012003. Publisher: IOP Publishing.

Barmpakos, D. & Kaltsas, G. (2021). A review on humidity, temperature and strain printed sensors—Current trends and future perspectives. *Sensors*, 21(3), 739.

Batha, H. & Carroll, P. (1964a). Unicrystalline silicon carbide thermistor. *IEEE Transactions on Component Parts*, 11(2), 129–134.

Batha, H. & Carroll, P. (1964b). Unicrystalline Silicon Carbide Thermistor. *IEEE Transactions on Component Parts*, 11(2), 129–134. doi: 10.1109/TCP.1964.1135009. Conference Name: IEEE Transactions on Component Parts.

Beduk, T., Bihar, E., Surya, S. G., Castillo, A. N., Inal, S. & Salama, K. N. (2020). A paper-based inkjet-printed PEDOT: PSS/ZnO sol-gel hydrazine sensor. *Sensors and Actuators B: Chemical*, 306, 127539.

Beedasy, V. & Smith, P. J. (2020). Printed electronics as prepared by inkjet printing. *Materials*, 13(3), 704.

Beke, D., Jánosi, T. Z., Somogyi, B., Major, D. Á., Szekrényes, Z., Erostyák, J., Kamarás, K. & Gali, A. (2016). Identification of luminescence centers in molecular-sized silicon carbide nanocrystals. *The Journal of Physical Chemistry C*, 120(1), 685–691.

Beniwal, A., Ganguly, P., Aliyana, A. K., Khandelwal, G. & Dahiya, R. (2023). Screen-printed graphene-carbon ink based disposable humidity sensor with wireless communication. *Sensors and Actuators B: Chemical*, 374, 132731.

Berzelius, J. (2022). *Annalytical Physics*, 1, 169.

Bhalla, A. S., Guo, R. & Roy, R. (2000). The perovskite structure—a review of its role in ceramic science and technology. *Materials research innovations*, 4(1), 3–26.

Bhattacharjee, M., Nemade, H. B. & Bandyopadhyay, D. (2017). Nano-enabled paper humidity sensor for mobile based point-of-care lung function monitoring. *Biosensors and Bioelectronics*, 94, 544–551. doi: 10.1016/j.bios.2017.03.049.

Bhattacharya, P., Fornari, R. & Kamimura, H. (2011). *Comprehensive semiconductor science and technology*. Newnes.

Bhore, S. S. (2013). *Formulation and Evaluation of Resistive Inks for Applications in Printed Electronics*. (Master's thesis, Western Michigan University).

Bieniek, T., Janczyk, G., Sitnik, A. & Messina, A. (2019). The first and european sic eigth inches pilot line reaction project as a driver for key european sic technologies focused on power electronics development. *TechConnect Briefs*, 256–259.

Bigorra, J., Borrego, C., Fontanilles, J. & Giró, J. (2000). Innovative electrical and electronic architecture for vehicles with dual voltage power networks. In-vehicle application. *SAE transactions*, 232–239.

Bocchetta, P., Frattini, D., Ghosh, S., Mohan, A. M. V., Kumar, Y. & Kwon, Y. (2020). Soft materials for wearable/flexible electrochemical energy conversion, storage, and biosensor devices. *Materials*, 13(12), 2733.

Boltovets, N., Kholevchuk, V., Konakova, R., Kudryk, Y. Y., Lytvyn, P., Milenin, V., Mitin, V. & Mitin, E. (2006). A silicon carbide thermistor. *Semiconductor Physics Quantum Electronics & Optoelectronics*.

Borsella, E., Caneve, L., Fantoni, R., Piccirillo, S., Basili, N. & Enzo, S. (1989). Investigation of the mechanism of CO2 laser driven production of ultrafine sinterable (Si3N4 and SiC) powders. *Applied Surface Science*, 36(1-4), 213–220.

Buchanan, R. C. (2018). *Ceramic materials for electronics*. CRC press.

Burke, J. & Turnbull, D. (1952). Recrystallization and grain growth. *Progress in metal physics*, 3, 220–292.

Byrappa, K. & Ohachi, T. (2003). *Crystal growth technology*. Elsevier.

Calabrese, G., Pimpolari, L., Conti, S., Mavier, F., Majee, S., Worsley, R., Wang, Z., Pieri, F., Basso, G., Pennelli, G. et al. (2020). Inkjet-printed graphene Hall mobility measurements and low-frequency noise characterization. *Nanoscale*, 12(12), 6708–6716.

Caliendo, C., Verona, E., D'Amico, A., Furlani, A., Iucci, G. & Russo, M. V. (1993). Surface acoustic wave humidity sensor. *Sensors and Actuators B: Chemical*, 16(1), 288–292. doi: 10.1016/0925-4005(93)85197-I.

Cano-Raya, C., Denchev, Z. Z., Cruz, S. F. & Viana, J. C. (2019a). Chemistry of solid metal-based inks and pastes for printed electronics–A review. *Applied Materials Today*, 15, 416–430.

Cano-Raya, C., Denchev, Z. Z., Cruz, S. F. & Viana, J. C. (2019b). Chemistry of solid metal-based inks and pastes for printed electronics – A review. *Applied Materials Today*, 15, 416–430. doi: 10.1016/j.apmt.2019.02.012.

Carneiro, Í. & Simões, S. (2020). Recent advances in EBSD characterization of metals. *Metals*, 10(8), 1097.

Casady, J. B. & Johnson, R. W. (1996). Status of silicon carbide (SiC) as a wide-bandgap semiconductor for high-temperature applications: A review. *Solid-State Electronics*, 39(10), 1409–1422.

Casady, J. B., Dillard, W. C., Johnson, R. W. & Rao, U. (1996). A hybrid 6H-SiC temperature sensor operational from 25/spl deg/C to 500/spl deg/C. *IEEE Transactions on Components, Packaging, and Manufacturing Technology: Part A*, 19(3), 416–422.

Castelletto, S., Almutairi, A. F. M., Thalassinos, G., Lohrmann, A., Buividas, R., Lau, D., Reineck, P., Juodkazis, S., Ohshima, T., Gibson, B. et al. (2017). Fluorescent color centers in laser ablated 4H-SiC nanoparticles. *Optics letters*, 42(7), 1297–1300.

Chamberlin, R. V. (2003). Critical behavior from Landau theory in nanothermodynamic equilibrium. *Physics Letters A*, 315(3-4), 313–318.

Chandrasekar, M. & Srinivasan, N. (2016). Role of SiOx on the photoluminescence properties of β-SiC. *Ceramics International*, 42(7), 8900–8908.

Chang, J., He, J., Mao, M., Zhou, W., Lei, Q., Li, X., Li, D., Chua, C.-K. & Zhao, X. (2018). Advanced material strategies for next-generation additive manufacturing. *Materials*, 11(1), 166.

Chaparro, D. & Goudeli, E. (2023). Oxidation Rate and Crystallinity Dynamics of Silver Nanoparticles at High Temperatures. *The Journal of Physical Chemistry C*, 127(27), 13389–13397. doi: 10.1021/acs.jpcc.3c03163. Publisher: American Chemical Society.

Chatterjee, S., Sengupta, K. & Maiti, H. S. (1999). A miniature PTC thermistor based sensor element fabricated by tape casting technique. *Sensors and Actuators B: Chemical*, 60(2-3), 155–160.

Chen, C. & Suganuma, K. (2019). Microstructure and mechanical properties of sintered Ag particles with flake and spherical shape from nano to micro size. *Materials & Design*, 162, 311–321. doi: 10.1016/j.matdes.2018.11.062.

Chen, D., Qiao, X., Qiu, X. & Chen, J. (2009). Synthesis and electrical properties of uniform silver nanoparticles for electronic applications. *Journal of Materials Science*, 44(4), 1076–1081. doi: 10.1007/s10853-008-3204-y.

Chen, F., Li, G., Zhao, E. R., Li, J., Hableel, G., Lemaster, J. E., Bai, Y., Sen, G. L. & Jokerst, J. V. (2018a). Cellular toxicity of silicon carbide nanomaterials as a function of morphology. *Biomaterials*, 179, 60–70.

Chen, H., Wang, X., Xue, F., Huang, Y., Zhou, K. & Zhang, D. (2018b). 3D printing of SiC ceramic: Direct ink writing with a solution of preceramic polymers. *Journal of the European Ceramic Society*, 38(16), 5294–5300.

Chen, H., Wang, X., Xue, F., Huang, Y., Zhou, K. & Zhang, D. (2018c). 3D printing of SiC ceramic: Direct ink writing with a solution of preceramic polymers. *Journal of the European Ceramic Society*, 38(16), 5294–5300. doi: 10.1016/j.jeurceramsoc.2018.08.009.

Chen, J., Zhang, J., Wang, M. & Li, Y. (2014). High-temperature hydrogen sensor based on platinum nanoparticle-decorated SiC nanowire device. *Sensors and Actuators B: Chemical*, 201, 402–406.

Chen, Q., Chen, R., Su, J., He, Q., Tan, B., Xu, C., Huang, X., Dai, Q. & Lu, J. (2022). The mechanisms of grain growth of Mg alloys: a review. *Journal of Magnesium and Alloys*, 10(9), 2384–2397.

Chen, S., Brown, L., Levendorf, M., Cai, W., Ju, S.-Y., Edgeworth, J., Li, X., Magnuson, C. W., Velamakanni, A., Piner, R. D., Kang, J., Park, J. & Ruoff, R. S. (2011). Oxidation Resistance of Graphene-Coated Cu and Cu/Ni Alloy. *ACS Nano*, 5(2), 1321–1327. doi: 10.1021/nn103028d. Publisher: American Chemical Society.

Chen, W., Son, N., Janzen, E., Hofmann, D. & Meyer, B. (1997). Effective masses in SiC determined by cyclotron resonance experiments. *physica status solidi (a)*, 162(1), 79–93.

Chen, Z. & Brandon, N. (2016). Inkjet printing and nanoindentation of porous alumina multilayers. *Ceramics International*, 42(7), 8316–8324.

Chesnokov, V., Luchihina, V. & Prosvirin, I. (2015). Effect of the carbon nanomaterials structure on silica carbothermal reduction. *Diamond and Related Materials*, 60, 14–19.

Choo, D. C. & Kim, T. W. (2017). Degradation mechanisms of silver nanowire electrodes under ultraviolet irradiation and heat treatment. *Scientific Reports*, 7(1), 1696. doi: 10.1038/s41598-017-01843-9.

Choyke, W. (1969). Optical properties of polytypes of SiC: interband absorption, and luminescence of nitrogen-exciton complexes. In *Silicon Carbide–1968* (pp. S141–S152). Elsevier.

Choyke, W. & Devaty, R. (2004). Optical properties of SiC: 1997–2002. In *Silicon Carbide: Recent Major Advances* (pp. 413–435). Springer.

Choyke, W. & Patrick, L. (1962). Exciton Recombination Radiation and Phonon Spectrum of 6 H SiC. *Physical Review*, 127(6), 1868.

Chuasontia, I., Sirisom, W., Nakpathomkun, N., Toommee, S., Pechyen, C., Tangnorawich, B. & Parcharoen, Y. (2023). Development and characterization of nano-ink from silicon carbide/multi-walled carbon nanotubes/synthesized silver nanoparticles for non-enzymatic paraoxon residuals detection. *Micromachines*, 14(8), 1613.

Chvála, A., Marek, J., Drobnỳ, J., Stuchlíková, L., Messina, A. A., Vinciguerra, V. & Donoval, D. (2022). Characterization and evaluation of current transport properties of power SiC Schottky diode. *Materials Today: Proceedings*, 53, 285–288.

Claudel, J., Ngo, T.-T., Kourtiche, D. & Nadi, M. (2020). Interdigitated sensor optimization for blood sample analysis. *Biosensors*, 10(12), 208.

Coletti, C., Jaroszeski, M., Pallaoro, A., Hoff, A., Iannotta, S. & Saddow, S. (2007). Biocompatibility and wettability of crystalline SiC and Si surfaces. *2007 29th Annual International Conference of the IEEE Engineering in Medicine and Biology Society*, pp. 5849–5852.

Connolly, E., French, P., Pham, H. & Sarro, P. (2002). Relative humidity sensors based on porous polysilicon and porous silicon carbide. *SENSORS, 2002 IEEE*, 1, 499–502.

Connolly, E., Pham, H., Groeneweg, J., Sarro, P. & French, P. (2004a). Silicon carbide membrane relative humidity sensor with aluminium electrodes. *17th IEEE International Conference on Micro Electro Mechanical Systems. Maastricht MEMS 2004 Technical Digest*, pp. 193–196.

Connolly, E., Pham, H., Groeneweg, J., Sarro, P. & French, P. (2004b). Silicon carbide membrane relative humidity sensor with aluminium electrodes. *17th IEEE International Conference on Micro Electro Mechanical Systems. Maastricht MEMS 2004 Technical Digest*, pp. 193–196. doi: 10.1109/MEMS.2004.1290555.

Constantin, C. P., Aflori, M., Damian, R. F. & Rusu, R. D. (2019a). Biocompatibility of polyimides: A mini-review. *Materials*, 12(19), 3166.

Constantin, C. P., Aflori, M., Damian, R. F. & Rusu, R. D. (2019b). Biocompatibility of Polyimides: A Mini-Review. *Materials (Basel, Switzerland)*, 12(19), 3166. doi: 10.3390/ma12193166.

Coombs, C. F. (2001). *Printed circuits handbook*. McGraw-Hill.

Coutts, T., Young, D., Gessert, T., Ginley, D. & Hosono, H. (2011). Handbook of Transparent Conductors. Springer Boston, MA, USA:.

Craton, M. T., He, Y., Roch, A., Chahal, P. & Papapolymerou, J. (2019). Additively manufactured interdigitated capacitors using barium titanate nanocomposite inks. *2019 49th European Microwave Conference (EuMC)*, pp. 488–491.

Creighton, J. & Ho, P. (2001). Introduction to chemical vapor deposition (CVD). *ASM International*, 407.

Cruz, M. A., Ye, S., Kim, M. J., Reyes, C., Yang, F., Flowers, P. F. & Wiley, B. J. (2018a). Multigram Synthesis of Cu-Ag Core–Shell Nanowires Enables the Production of a Highly Conductive Polymer Filament for 3D Printing Electronics. *Particle & Particle Systems Characterization*, 35(5), 1700385. doi: 10.1002/ppsc.201700385. _eprint: https://onlinelibrary.wiley.com/doi/pdf/10.1002/ppsc.201700385.

Cruz, S., Azevedo, G., Cano-Raya, C., Manninen, N. & Viana, J. C. (2021). Thermoelectric response of a screen printed silver-nickel thermocouple. *Materials Science and Engineering: B*, 264, 114929.

Cruz, S. M. F., Rocha, L. A. & Viana, J. C. (2018b). Printing technologies on flexible substrates for printed electronics. In *Flexible electronics*. IntechOpen.

Cui, Z. (2016). *Printed electronics: materials, technologies and applications*. John Wiley & Sons.

Cummins, G. & Desmulliez, M. P. (2012). Inkjet printing of conductive materials: a review. *Circuit world*, 38(4), 193–213.

Dai, H., Feng, N., Li, J., Zhang, J. & Li, W. (2018). Chemiresistive humidity sensor based on chitosan/zinc oxide/single-walled carbon nanotube composite film. *Sensors and Actuators B: Chemical*, 283. doi: 10.1016/j.snb.2018.12.056.

Dai, J., Ogbeide, O., Macadam, N., Sun, Q., Yu, W., Li, Y., Su, B.-L., Hasan, T., Huang, X. & Huang, W. (2020). Printed gas sensors. *Chemical Society Reviews*, 49(6), 1756–1789.

Dakshinamurthy, S., Quick, N. & Kar, A. (2007). Temperature-dependent optical properties of silicon carbide for wireless temperature sensors. *Journal of Physics D: Applied Physics*, 40(2), 353.

Dang, W., Vinciguerra, V., Lorenzelli, L. & Dahiya, R. (2017). Printable stretchable interconnects. *Flexible and Printed Electronics*, 2(1), 013003.

Dannenberg, R., Stach, E. A., Groza, J. R. & Dresser, B. J. (2000). In-situ TEM observations of abnormal grain growth, coarsening, and substrate de-wetting in nanocrystalline Ag thin films. *Thin Solid Films*, 370(1), 54–62. doi: 10.1016/S0040-6090(99)00947-5.

Davidsen, J. E. (2011). *Formation of silicon carbide in the silicomanganese process*. (Master's thesis, Institutt for materialteknologi).

Davis, R. F., Kelner, G., Shur, M., Palmour, J. W. & Edmond, J. A. (1991). Thin film deposition and microelectronic and optoelectronic device fabrication and characterization in monocrystalline alpha and beta silicon carbide. *Proceedings of the IEEE*, 79(5), 677–701.

de Hazan, Y. & Penner, D. (2017). SiC and SiOC ceramic articles produced by stereolithography of acrylate modified polycarbosilane systems. *Journal of the European Ceramic Society*, 37(16), 5205–5212.

de Vasconcelos, E. A., Khan, S., Zhang, W., Uchida, H. & Katsube, T. (2000). Highly sensitive thermistors based on high-purity polycrystalline cubic silicon carbide. *Sensors and Actuators A: Physical*, 83(1-3), 167–171.

de Vasconcelos, E. A., Zhang, W. Y., Uchida, H. & Katsube, T. (1998). Potential of high-purity polycrystalline silicon carbide for thermistor applications. *Japanese journal of applied physics*, 37(9R), 5078.

Delfino, I., Ricciardi, V. & Lepore, M. (2021). Synchrotron FTIR microspectroscopy investigations on biochemical changes occurring in human cells exposed to proton beams. *Applied Sciences*, 12(1), 336.

Deng, D., Jin, Y., Cheng, Y., Qi, T. & Xiao, F. (2013). Copper nanoparticles: aqueous phase synthesis and conductive films fabrication at low sintering temperature. *ACS applied materials & interfaces*, 5(9), 3839–3846.

Dexter, M., Gao, Z., Bansal, S., Chang, C.-H. & Malhotra, R. (2018). Temperature, crystalline phase and influence of substrate properties in intense pulsed light sintering of copper sulfide nanoparticle thin films. *Scientific reports*, 8(1), 2201.

Diaham, S. (2021). Polyimide in electronics: Applications and processability overview. *Polyimide for Electronic and Electrical Engineering Applications*, 2020–2021.

Dimitriou, E. & Michailidis, N. (2021). Printable conductive inks used for the fabrication of electronics: an overview. *Nanotechnology*, 32(50), 502009.

Donald Lupo,Klaus Hecker, W. C. & Ranfeld, C. (2017). *OE-A Roadmap for Organic and Printed Electronics, 7th edition*. OE-A (Organic and Printed Electronics Association).

Dong, H., Liu, W., Li, Y., Chen, X. & Wang, D. (2023). Fully Printed Flexible Zinc Oxide Patch for Wearable UV Light Sensing. *Advanced Electronic Materials*, 9(12), 2300469. doi: 10.1002/aelm.202300469. _eprint: https://onlinelibrary.wiley.com/doi/pdf/10.1002/aelm.202300469.

Dorfman, K. D., Adrahtas, D. Z., Thomas, M. S. & Frisbie, C. D. (2020). Microfluidic opportunities in printed electrolyte-gated transistor biosensors. *Biomicrofluidics*, 14(1).

Dragomir, M., Valant, M., Fanetti, M. & Mozharivskyj, Y. (2016a). A facile chemical method for the synthesis of 3C–SiC nanoflakes. *RSC advances*, 6(26), 21795–21801.

Dragomir, M., Valant, M., Fanetti, M. & Mozharivskyj, Y. (2016b). A facile chemical method for the synthesis of 3C–SiC nanoflakes. *RSC Advances*, 6(26), 21795–21801. doi: 10.1039/C6RA00789A. Publisher: Royal Society of Chemistry.

Duan, Z.-H., Zhao, Q.-N., Li, C.-Z., Wang, S., Jiang, Y.-D., Zhang, Y.-J., Liu, B.-H. & Tai, H.-L. (2020). Enhanced positive humidity sensitive behavior of p-reduced graphene oxide decorated with n-WS2 nanoparticles. *Rare Metals*, 40. doi: 10.1007/s12598-020-01524-z.

Duan, Z., Jiang, Y., Yan, M., Wang, S., Yuan, Z., Zhao, Q., Sun, P., Xie, G., Du, X. & Tai, H. (2019). Facile, Flexible, Cost-Saving, and Environment-Friendly Paper-Based Humidity Sensor for Multifunctional Applications. *ACS Applied Materials & Interfaces*, 11(24), 21840–21849. doi: 10.1021/acsami.9b05709. Publisher: American Chemical Society.

Duan, Z., Jiang, Y. & Tai, H. (2021a). Recent advances in humidity sensors for human body related humidity detection. *Journal of Materials Chemistry C*, 9(42), 14963–14980. doi: 10.1039/D1TC04180K. Publisher: The Royal Society of Chemistry.

Duan, Z., Jiang, Y., Zhao, Q., Huang, Q., Wang, S., Zhang, Y., Wu, Y., Liu, B., Zhen, Y. & Tai, H. (2021b). Daily writing carbon ink: Novel application on humidity sensor with wide detection range, low detection limit and high detection resolution. *Sensors and Actuators B: Chemical*, 339, 129884. doi: 10.1016/j.snb.2021.129884.

Dubey, C. & Kumar, B. (2018). Organic Humidity Sensors with Different Materials and Its Application in Environment Monitoring. *2018 5th IEEE Uttar Pradesh Section International Conference on Electrical, Electronics and Computer Engineering (UPCON)*, pp. 1–6. doi: 10.1109/UPCON.2018.8597009.

Dubourg, G., Katona, J., Rodović, M., Savić, S., Kitic, G., Niarchos, G., Jancović, N. & Crnojević-Bengin, V. (2017). Flexible and highly sensitive humidity sensors using screen-printed TiO2 nanoparticles as sensitive layer. *Journal of Physics: Conference Series*, 939, 012008. doi: 10.1088/1742-6596/939/1/012008.

Eckstein, R. (2016). *Aerosol jet printed electronic devices and systems*. (Ph.D. thesis, Dissertation, Karlsruhe, Karlsruher Institut für Technologie (KIT), 2016).

Eickhoff, M., Möller, H., Kroetz, G., Berg, J. v. & Ziermann, R. (1999). A high temperature pressure sensor prepared by selective deposition of cubic silicon carbide on SOI substrates. *Sensors and Actuators A: Physical*, 74(1-3), 56–59.

El-Diasty, F. (2004). Simulation of CO2 laser pyrolysis during preparation of SiC nanopowders. *Optics communications*, 241(1-3), 121–135.

Elements, A. Silicon Carbide Nanoparticles. Consulted at https://www.americanelements.com/silicon-carbide-nanoparticles-409-21-2.

Elliott, C., Large, M., Pearce, J. & Machin, G. (2014). Compatibility of materials for use at high temperatures with W–Re thermocouples. *International Journal of Thermophysics*, 35, 1202–1214.

Engel, L., Benito-Altamirano, I., Tarantik, K. R., Pannek, C., Dold, M., Prades, J. D. & Wöllenstein, J. (2021). Printed sensor labels for colorimetric detection of ammonia, formaldehyde and hydrogen sulfide from the ambient air. *Sensors and Actuators B: Chemical*, 330, 129281.

Eric, F. S. & Ramsden, C. A. (2016). *Heterocyclic Chemistry in the 21st Century: A Tribute to Alan Katritzky*. Academic Press.

Eun, K., Chon, M.-W., Yoo, T.-H., Song, Y.-W. & Choa, S.-H. (2015). Electromechanical properties of printed copper ink film using a white flash light annealing process for flexible electronics. *Microelectronics Reliability*, 55(5), 838–845.

Fang, Z. Z. (2010). *Sintering of Advanced Materials*. Elsevier.

Fapanni, T., Sardini, E., Borghetti, M., Serpelloni, M. & Bellotti, S. (2023). Preliminary Results on Fully-Printed and Silver-Based Temperature Sensors for Aerospace Industry. *2023 IEEE International Workshop on Metrology for Industry 4.0 & IoT (MetroInd4. 0&IoT)*, pp. 200–204.

Farahani, H., Wagiran, R. & Hamidon, M. N. (2014a). Humidity sensors principle, mechanism, and fabrication technologies: a comprehensive review. *Sensors*, 14(5), 7881–7939.

Farahani, H., Wagiran, R. & Hamidon, M. N. (2014b). Humidity Sensors Principle, Mechanism, and Fabrication Technologies: A Comprehensive Review. *Sensors (Basel, Switzerland)*, 14(5), 7881–7939. doi: 10.3390/s140507881.

Feteira, A. (2009). Negative temperature coefficient resistance (NTCR) ceramic thermistors: an industrial perspective. *Journal of the American Ceramic Society*, 92(5), 967–983.

Fourmont, P., Bai, Y., Fortier, F.-X. & Cloutier, S. G. (2022a). Graphene-enhanced screen-printed BiFeO3-based thermistors. *ACS Applied Electronic Materials*, 4(12), 5905–5913.

Fourmont, P., Bai, Y., Fortier, F.-X. & Cloutier, S. G. (2022b). Graphene-Enhanced Screen-Printed BiFeO3-Based Thermistors. *ACS Applied Electronic Materials*, 4(12), 5905–5913. doi: 10.1021/acsaelm.2c01093. Publisher: American Chemical Society.

Fratello, V., Nino, G., Wadhwa, A. & Kent, L.

Frazier, W. E., Hu, S., Overman, N., Lavender, C. & Joshi, V. V. (2018). Short communication on Kinetics of grain growth and particle pinning in U-10 wt.% Mo. *Journal of Nuclear Materials*, 498, 254–258. doi: 10.1016/j.jnucmat.2017.10.041.

Frewin, C., Locke, C., Mariusso, L., Weeber, E. & Saddow, S. (2013). Silicon carbide neural implants: In vivo neural tissue reaction. *2013 6th International IEEE/EMBS Conference on Neural Engineering (NER)*, pp. 661–664.

Fukuda, K., Hikichi, K., Sekine, T., Takeda, Y., Minamiki, T., Kumaki, D. & Tokito, S. (2013). Strain sensitivity and durability in p-type and n-type organic thin-film transistors with printed silver electrodes. *Scientific Reports*, 3(1), 2048.

Gadzira, M., Gnesin, G., Mykhaylyk, O. & Andreyev, O. (1998). Synthesis and structural peculiarities of nonstoichiometric β-SiC. *Diamond and related materials*, 7(10), 1466–1470.

Gaffet, E. & Harmelin, M. (1990). Crystal-amorphous phase transition induced by ball-milling in silicon. *Journal of the Less Common Metals*, 157(2), 201–222.

Gao, X., Wang, R., Zhao, J., Huang, J., Gao, Y. & Liu, H. (2020). Influence of surface oxide layer of SiC powder on the rheological properties of its slurry. *International Journal of Applied Ceramic Technology*, 17(2), 484–490.

Garlapati, S. K., Divya, M., Breitung, B., Kruk, R., Hahn, H. & Dasgupta, S. (2018). Printed electronics based on inorganic semiconductors: From processes and materials to devices. *Advanced Materials*, 30(40), 1707600.

Gerlein, L. F., Benavides-Guerrero, J. A. & Cloutier, S. G. (2024). Photonic post-processing of a multi-material transparent conductive electrode architecture for optoelectronic device integration. *RSC advances*, 14(7), 4748–4758.

Gierth, P., Rebenklau, L., Augsburg, K., Bachmann, E. & Niedermeyer, L. (2018). Novel thermocouples for automotive applications. *Journal of Sensors and Sensor systems*, 7(1), 43–49.

Gilshtein, E., Bolat, S., Sevilla, G. T., Cabas-Vidani, A., Clemens, F., Graule, T., Tiwari, A. N. & Romanyuk, Y. E. (2020). Inkjet-Printed Conductive ITO Patterns for Transparent Security Systems. *Advanced Materials Technologies*, 5(9), 2000369.

Gomari, S. & Sharafi, S. (2010). Microstructural characterization of nanocrystalline chromium carbides synthesized by high energy ball milling. *Journal of Alloys and Compounds*, 490(1-2), 26–30.

Gomez, D., Morgan, S. P., Hayes-Gill, B. R., Correia, R. G. & Korposh, S. (2018). Polymeric optical fibre sensor coated by SiO2 nanoparticles for humidity sensing in the skin microenvironment. *Sensors and Actuators B: Chemical*, 254, 887–895. doi: 10.1016/j.snb.2017.07.191.

Gómez-Gómez, A., Moyano, J. J., Román-Manso, B., Belmonte, M., Miranzo, P. & Osendi, M. I. (2019). Highly-porous hierarchical SiC structures obtained by filament printing and partial sintering. *Journal of the European Ceramic Society*, 39(4), 688–695.

Gong-yi, L., Jun, M., Gang, P., Wei, C., Zeng-yong, C., Yi-he, L., Tian-jiao, H. & Xiao-dong, L. (2014). Room-Temperature Humidity-Sensing Performance of SiC Nanopaper. *American Chemical Society Applied Materials and Interfaces*.

Gordon, S. E., Dorfman, J. R., Kirk, D. & Adams, K. (2012). Advances in conductive inks across multiple applications and deposition platforms. *Proceedings of the IPC APEX EXPO*.

Granqvist, C. G. (2007). Transparent conductors as solar energy materials: A panoramic review. *Solar energy materials and solar cells*, 91(17), 1529–1598.

GreyViews. (2021). Golbal Printed Electronics Market Overview. Consulted at https://greyviews.com/reports/printed-electronics-market/62.

Grundas, S. (2011). *Advances in induction and microwave heating of mineral and organic materials*. BoD–Books on Demand.

Gryshkov, O., Klyui, N. I., Temchenko, V. P., Kyselov, V. S., Chatterjee, A., Belyaev, A. E., Lauterboeck, L., Iarmolenko, D. & Glasmacher, B. (2016). Porous biomorphic silicon carbide ceramics coated with hydroxyapatite as prospective materials for bone implants. *Materials Science and Engineering: C*, 68, 143–152.

Guichelaar, P. J. (1997). Acheson process. In *Carbide, nitride and boride materials synthesis and processing* (pp. 115–129). Springer.

Guo, P., Tian, B., Liang, J., Yang, X., Tang, G., Li, Q., Liu, Q., Zheng, K., Chen, X. & Wu, W. (2023). An All-Printed, Fast-Response Flexible Humidity Sensor Based on Hexagonal-WO3 Nanowires for Multifunctional Applications. *Advanced Materials*, 35(41), 2304420.

Guo, Z., An, L., Khuje, S., Chivate, A., Li, J., Wu, Y., Hu, Y., Armstrong, J., Ren, S. & Zhou, C. (2022). 3D-printed electrically conductive silicon carbide. *Additive Manufacturing*, 59, 103109.

Gupta, A. A., Arunachalam, S., Cloutier, S. G. & Izquierdo, R. (2018). Fully aerosol-jet printed, high-performance nanoporous ZnO ultraviolet photodetectors. *ACS Photonics*, 5(10), 3923–3929.

Gupta, A., Ghosh, T. & Jacob, C. (2007). The influence of diluent gas composition and temperature on SiC nanopowder formation by CVD. *Journal of materials science*, 42, 5142–5146.

Gwalani, B., Salloom, R., Alam, T., Valentin, S. G., Zhou, X., Thompson, G., Srinivasan, S. G. & Banerjee, R. (2019). Composition-dependent apparent activation-energy and sluggish grain-growth in high entropy alloys. *Materials Research Letters*, 7(7), 267–274. doi: 10.1080/21663831.2019.1601644.

Gómez-Gómez, A., Moyano, J. J., Román-Manso, B., Belmonte, M., Miranzo, P. & Osendi, M. I. (2019). Highly-porous hierarchical SiC structures obtained by filament printing and partial sintering. *Journal of the European Ceramic Society*, 39(4), 688–695. doi: 10.1016/j.jeurceramsoc.2018.12.034.

Haggerty, J. S. & Cannon, W. R. (1981). Sinterable powders from laser-driven reactions. In *Laser-induced chemical processes* (pp. 165–241). Springer.

Hai, Z., Su, Z., Zhu, K., Pan, Y. & Luo, S. (2024). Printed Thick Film Resistance Temperature Detector for Real-Time Tube Furnace Temperature Monitoring. *Sensors*, 24(10), 2999.

Hallaj, R., Soltani, E., Mafakheri, S. & Ghadermazi, M. (2021). A surface-modified silicon carbide nanoparticles based electrochemical sensor for free interferences determination of caffeine in tea and coffee. *Materials Science and Engineering: B*, 274, 115473.

Harris, G. L. (1995). *Properties of silicon carbide*. Iet.

Harris, K. D., Elias, A. L. & Chung, H.-J. (2016). Flexible electronics under strain: a review of mechanical characterization and durability enhancement strategies. *Journal of materials science*, 51, 2771–2805.

Hart, A. H., Owuor, P. S., Hamel, J., Bhowmik, S., Asif, S. S., Gentles, A. X., Ozden, S., Tsafack, T., Keyshar, K., Mital, R. et al. (2020). Ultra-low density three-dimensional nano-silicon carbide architecture with high temperature resistance and mechanical strength. *Carbon*, 164, 143–149.

Hazzledine, P. & Oldershaw, R. (1990). Computer simulation of Zener pinning. *Philosophical Magazine A*, 61(4), 579–589.

He, H., Chen, R., Zhang, L., Williams, T., Fang, X. & Shen, W. (2020). Fabrication of single-crystalline gold nanowires on cellulose nanofibers. *Journal of colloid and interface science*, 562, 333–341.

He, R., Ding, G., Zhang, K., Li, Y. & Fang, D. (2019). Fabrication of SiC ceramic architectures using stereolithography combined with precursor infiltration and pyrolysis. *Ceramics International*, 45(11), 14006–14014.

Henager, C. H., Alvine, K. J., Roosendaal, T. J., Shin, Y., Nguyen, B. N., Borlaug, B. A., Jiang, W. & Arreguin, S. A. (2015). Nanocrystalline SiC and Ti3SiC2 Alloys for Reactor Materials: Annual Report. doi: 10.2172/1188907.

Heydemann, V., Schulze, N., Barrett, D. & Pensl, G. (1996). Growth of 6H and 4H silicon carbide single crystals by the modified Lely process utilizing a dual-seed crystal method. *Applied physics letters*, 69(24), 3728–3730.

Higgins, G. (1974). Grain-boundary migration and grain growth. *Metal Science*, 8(1), 143–150.

Hillert, M. (1965). On the theory of normal and abnormal grain growth. *Acta Metallurgica*, 13(3), 227–238. doi: 10.1016/0001-6160(65)90200-2.

Horike, S., Fukushima, T., Saito, T., Koshiba, Y., Morimoto, M., Misaki, M. & Ishida, K. (2018). Thermodynamics and kinetics of polyoxyethylene alkyl ether evaporation from inkjet-printed carbon nanotube thin films by vacuum annealing. *Flexible and Printed Electronics*, 3(2), 025006.

Hosseini, S. N., Enayati, M. H. & Karimzadeh, F. (2014). Nanoscale Grain Growth Behaviour of CoAl Intermetallic Synthesized by Mechanical Alloying. *Bulletin of Materials Science*, 37(3), 383–387. doi: 10.1007/s12034-014-0672-3.

Hsu, C.-H., Cloutier, S. G., Palefsky, S. & Xu, J. (2010). Synthesis of Diamond Nanowires Using Atmospheric-Pressure Chemical Vapor Deposition. *Nano Letters*, 10(9), 3272–3276. doi: 10.1021/nl100616x. Publisher: American Chemical Society.

Huang, C.-C., Kao, Z.-K. & Liao, Y.-C. (2013). Flexible miniaturized nickel oxide thermistor arrays via inkjet printing technology. *ACS applied materials & interfaces*, 5(24), 12954–12959.

Huang, Z., Tang, Y., Guo, H., Feng, X., Zhang, T., Li, P., Qian, B. & Xie, Y. (2020). 3D printing of ceramics and graphene circuits-on-ceramics by thermal bubble inkjet technology and high temperature sintering. *Ceramics International*, 46(8), 10096–10104.

Huang, Z., Liang, B., Jiang, D. & Tan, S. (1996). Preparation of nanocrystal SiC powder by chemical vapour deposition. *Journal of materials science*, 31, 4327–4332.

Hung, K.-Y., Chang, Y.-T., Chien, C.-H., Ding, C.-F., Tsai, M.-C. & Young, H.-T. (2020). Investigation of ink modification for aerosol jet printing process on FR-4 substrate. *The International Journal of Advanced Manufacturing Technology*, 111, 1147–1156.

Huseynov, E. & Garibov, A. (2017). Effects of neutron flux on the temperature dependency of permittivity of 3C-SiC nanoparticles. *Silicon*, 9, 753–759.

Huseynov, E. M. (2017). Permittivity-frequency dependencies study of neutron-irradiated nanocrystalline silicon carbide (3C-SiC). *Nano*, 12(06), 1750068.

Huseynov, E. M. (2018). Neutron irradiation, amorphous transformation and agglomeration effects on the permittivity of nanocrystalline silicon carbide (3C-SiC). *Nano*, 13(03), 1830002.

Huseynov, E. M. & Naghiyev, T. G. (2021). Study of thermal parameters of nanocrystalline silicon carbide (3C-SiC) using DSC spectroscopy. *Applied Physics A*, 127(4), 267.

Huseynov, E. M. & Naghiyev, T. G. (2022). Various thermal parameters investigation of 3C-SiC nanoparticles at the different heating rates. *Applied Physics A*, 128(2), 115.

Ibrahim, N., Akindoyo, J. O. & Mariatti, M. (2022). Recent development in silver-based ink for flexible electronics. *Journal of Science: Advanced Materials and Devices*, 7(1), 100395. doi: 10.1016/j.jsamd.2021.09.002.

Iijima, M. & Kamiya, H. (2008). Surface modification of silicon carbide nanoparticles by azo radical initiators. *The Journal of Physical Chemistry C*, 112(31), 11786–11790.

Iijima, S. (1991). Helical microtubules of graphitic carbon. *nature*, 354(6348), 56–58.

Ikeda, M., Matsunami, H. & Tanaka, T. (1980). Site effect on the impurity levels in 4 H, 6 H, and 1 5 R SiC. *Physical Review B*, 22(6), 2842.

Imam, S. A., Choudhary, A. & Sachan, V. K. (2015). Design issues for wireless sensor networks and smart humidity sensors for precision agriculture: A review. *2015 International Conference on Soft Computing Techniques and Implementations (ICSCTI)*, pp. 181–187. doi: 10.1109/ICSCTI.2015.7489591.

Inomata, N., Inaoka, R., Okabe, K., Funatsu, T. & Ono, T. (2020). Short-term temperature change detections and frequency signals in single cultured cells using a microfabricated thermistor. *Sensing and Bio-Sensing Research*, 27, 100309.

Instruments, E. What is Raman Spectroscopy? Consulted at https://www.edinst.com/blog/what-is-raman-spectroscopy/.

Intratec. (2019). Silicon Carbide Prices - historic and current. Consulted at https://www.intratec.us/chemical-markets/silicon-carbide-price.

Ionkin, A. S., Fish, B. M., Li, Z. R., Lewittes, M., Soper, P. D., Pepin, J. G. & Carroll, A. F. (2011). Screen-Printable Silver Pastes with Metallic Nano-Zinc and Nano-Zinc Alloys for Crystalline Silicon Photovoltaic Cells. *ACS Applied Materials & Interfaces*, 3(2), 606–611. doi: 10.1021/am1011996. Publisher: American Chemical Society.

Islam, M. R., Afroj, S., Yin, J., Novoselov, K. S., Chen, J. & Karim, N. (2024). Advances in Printed Electronic Textiles. *Advanced Science*, 11(6), 2304140.

Ivanov, P. & Chelnokov, V. (1992). Recent developments in SiC single-crystal electronics. *Semiconductor science and technology*, 7(7), 863.

Iwanowski, R., Fronc, K., Paszkowicz, W. & Heinonen, M. (1999). XPS and XRD study of crystalline 3C-SiC grown by sublimation method. *Journal of alloys and compounds*, 286(1-2), 143–147.

Jamshidi, B., Azevedo, R. G., Wijesundara, M. B. & Pisano, A. P. (2007). Corrosion enhanced capacitive strain gauge at 370 C. *SENSORS, 2007 IEEE*, pp. 804–807.

Jang, J. H. & Han, J. I. (2017). Cylindrical relative humidity sensor based on poly-vinyl alcohol (PVA) for wearable computing devices with enhanced sensitivity. *Sensors and Actuators A: Physical*, 261, 268–273. doi: 10.1016/j.sna.2017.05.011.

J.E, B. & D, T. (1952). Recrystallization and grain growth. *Progress in Metal Physics*, Volume 3, 220–244. Consulted at https://www.sciencedirect.com/science/article/abs/pii/0502820552900099?via%3Dihub.

Jeong, H., Noh, Y. & Lee, D. (2019a). Highly stable and sensitive resistive flexible humidity sensors by means of roll-to-roll printed electrodes and flower-like TiO2 nanostructures. *Ceramics International*, 45(1), 985–992.

Jeong, H., Noh, Y. & Lee, D. (2019b). Highly stable and sensitive resistive flexible humidity sensors by means of roll-to-roll printed electrodes and flower-like TiO2 nanostructures. *Ceramics International*, 45(1), 985–992. doi: 10.1016/j.ceramint.2018.09.276.

Jewell, E., Hamblyn, S., Claypole, T. & Gethin, D. (2015). Deposition of High Conductivity Low Silver Content Materials by Screen Printing. *Coatings*, 5(2), 172–185. doi: 10.3390/coatings5020172. Number: 2 Publisher: Multidisciplinary Digital Publishing Institute.

Ji, Y., Tan, Q., Lu, X., Zhang, G., Zhang, W. & Xiong, J. (2019). Wireless passive separated LC temperature sensor based on high-temperature co-fired ceramic operating up to 1500° C. *Journal of Micromechanics and Microengineering*, 29(3), 035015.

Jiang, K., Fei, T., Jiang, F., Wang, G. & Zhang, T. (2014). A dew sensor based on modified carbon black and polyvinyl alcohol composites. *Sensors and Actuators B: Chemical*, 192, 658–663. doi: 10.1016/j.snb.2013.11.004.

Jiang, S., Gao, S., Kong, J., Jin, X., Wei, D., Li, D. & Xing, P. (2019a). Study on the synthesis of β-SiC nanoparticles from diamond-wire silicon cutting waste. *RSC advances*, 9(41), 23785–23790.

Jiang, S., Gao, S., Kong, J., Jin, X., Wei, D., Li, D. & Xing, P. (2019b). Study on the synthesis of -SiC nanoparticles from diamond-wire silicon cutting waste. *RSC Advances*, 9(41), 23785–23790. doi: 10.1039/C9RA03383A. Publisher: Royal Society of Chemistry.

Jiang, Y., Islam, M. N., He, R., Huang, X., Cao, P.-F., Advincula, R. C., Dahotre, N., Dong, P., Wu, H. F. & Choi, W. (2023). Recent advances in 3D printed sensors: materials, design, and manufacturing. *Advanced Materials Technologies*, 8(2), 2200492.

Joshi, S. R., Kim, B., Kim, S.-K., Song, W., Park, K., Kim, G.-H. & Shin, H. (2020). Low-cost and fast-response resistive humidity sensor comprising biopolymer-derived carbon thin film and carbon microelectrodes. *Journal of The Electrochemical Society*, 167(14), 147511.

Juhász, L. & Mizsei, J. (2009). Humidity sensor structures with thin film porous alumina for on-chip integration. *Thin Solid Films*, 517(22), 6198–6201.

Jung, U. H., Park, K. T., Park, E. H. & Kim, S. H. (2006). Improvement of low-humidity performance of PEMFC by addition of hydrophilic SiO2 particles to catalyst layer. *Journal of Power Sources*, 159(1), 529–532. doi: 10.1016/j.jpowsour.2005.11.050.

Kabiri Ameri, S., Ho, R., Jang, H., Tao, L., Wang, Y., Wang, L., Schnyer, D. M., Akinwande, D. & Lu, N. (2017). Graphene electronic tattoo sensors. *ACS nano*, 11(8), 7634–7641.

Kaija, K., Pekkanen, V., Mäntysalo, M., Koskinen, S., Niittynen, J., Halonen, E. & Mansikkamäki, P. (2010). Inkjetting dielectric layer for electronic applications. *Microelectronic Engineering*, 87(10), 1984–1991.

Kaiser, T., Cordill, M. J., Kirchlechner, C. & Menzel, A. (2021). Electrical and mechanical behaviour of metal thin films with deformation-induced cracks predicted by computational homogenisation. *International Journal of Fracture*, 231(2), 223–242.

Kamat, P. V. (2008). Quantum dot solar cells. Semiconductor nanocrystals as light harvesters. *The Journal of Physical Chemistry C*, 112(48), 18737–18753.

Kamyshny, A. & Magdassi, S. (2019). Conductive nanomaterials for 2D and 3D printed flexible electronics. *Chemical Society Reviews*, 48(6), 1712–1740.

Kamyshny, A., Steinke, J. & Magdassi, S. (2011). Metal-based inkjet inks for printed electronics. *The Open applied physics journal*, 4(1).

Kang, J. S., Ryu, J., Kim, H. S. & Hahn, H. T. (2011). Sintering of Inkjet-Printed Silver Nanoparticles at Room Temperature Using Intense Pulsed Light. *Journal of Electronic Materials*, 40(11), 2268–2277. doi: 10.1007/s11664-011-1711-0.

Kano, S., Jarulertwathana, N., Mohd-Noor, S., Hyun, J. K., Asahara, R. & Mekaru, H. (2022). Respiratory Monitoring by Ultrafast Humidity Sensors with Nanomaterials: A Review. *Sensors*, 22(3), 1251. doi: 10.3390/s22031251. Number: 3 Publisher: Multidisciplinary Digital Publishing Institute.

Kant, T., Shrivas, K., Kumar, A., Dewangan, K. et al. (2023). Graphene-silver nano-ink for inkjet printing of paper electrode for electrochemical sensing of 4-nitrophenol. *Materials Chemistry and Physics*, 307, 128161.

Kappe, C. O. (2004). Controlled microwave heating in modern organic synthesis. *Angewandte Chemie International Edition*, 43(46), 6250–6284.

Karim, A. B., Hassan, A., Akanda, M. & Mallik, A. (2018). Monitoring food storage humidity and temperature data using IoT. *MOJ Food Process Technol*, 6(4), 400–404.

Károlyházy, G., Beke, D., Zalka, D., Lenk, S., Krafcsik, O., Kamarás, K. & Gali, Á. (2020). Novel method for electroless etching of 6H–SiC. *Nanomaterials*, 10(3), 538.

Karthik, P., Singh, S. P. et al. (2015). Copper conductive inks: synthesis and utilization in flexible electronics. *RSC advances*, 5(79), 63985–64030.

Karunarathne, T., Wijesinghe, W., Rathuwadu, N., Karalasingam, A., Manoharan, N., Sameera, S., Sandaruwan, C., Amaratunga, G. & De Silva, S. (2020). Fabrication and characterization of partially conjugated poly (vinyl alcohol) based resistive humidity sensor. *Sensors and Actuators A: Physical*, 314, 112263.

Katerinopoulou, D., Zalar, P., Sweelssen, J., Kiriakidis, G., Rentrop, C., Groen, P., Gelinck, G. H., van den Brand, J. & Smits, E. C. (2019a). Large-area all-printed temperature sensing surfaces using novel composite thermistor materials. *Advanced Electronic Materials*, 5(2), 1800605.

Katerinopoulou, D., Zalar, P., Sweelssen, J., Kiriakidis, G., Rentrop, C., Groen, P., Gelinck, G. H., van den Brand, J. & Smits, E. C. P. (2019b). Large-Area All-Printed Temperature Sensing Surfaces Using Novel Composite Thermistor Materials. *Advanced Electronic Materials*, 5(2), 1800605. doi: 10.1002/aelm.201800605.

Kavitha, N., Balasubramanian, M. & Vashistha, Y. D. (2011). Synthesis and characterization of nano silicon carbide powder from agricultural waste. *Transactions of the Indian Ceramic Society*, 70(3), 115–118.

KAWAMURA, F., YAMANE, H., YAMADA, T., YIN, S. & SATO, T. (2007). Low Temperature Synthesis of. BETA.-SiC Powder by the Na Flux Method using Fullerene and Silicon. *Journal of the Ceramic Society of Japan*, 115(1337), 74–76.

Khalaf, A. M., Ramírez, J. L., Mohamed, S. A. & Issa, H. H. (2022). Highly sensitive interdigitated thermistor based on PEDOT: PSS for human body temperature monitoring. *Flexible and Printed Electronics*, 7(4), 045012.

Khaled, E., Hassan, H., Girgis, A. & Metelka, R. (2008). Construction of novel simple phosphate screen-printed and carbon paste ion-selective electrodes. *Talanta*, 77(2), 737–743.

Khan, S., Ali, S., Khan, A. & Bermak, A. (2021). Wearable printed temperature sensors: Short review on latest advances for biomedical applications. *IEEE reviews in biomedical engineering*.

Khan, Y., Thielens, A., Muin, S., Ting, J., Baumbauer, C. & Arias, A. C. (2020). A new frontier of printed electronics: flexible hybrid electronics. *Advanced Materials*, 32(15), 1905279.

Kim, B.-J., Haas, T., Friederich, A., Lee, J.-H., Nam, D.-H., Binder, J. R., Bauer, W., Choi, I.-S., Joo, Y.-C., Gruber, P. A. et al. (2014a). Improving mechanical fatigue resistance by optimizing the nanoporous structure of inkjet-printed Ag electrodes for flexible devices. *Nanotechnology*, 25(12), 125706.

Kim, D. U., Kim, K.-S. & Jung, S.-B. (2016). Effects of oxidation on reliability of screen-printed silver circuits for radio frequency applications. *Microelectronics Reliability*, 63, 120–124.

Kim, I. & Kim, J. (2010). The effect of reduction atmospheres on the sintering behaviors of inkjet-printed Cu interconnectors. *Journal of applied physics*, 108(10).

Kim, I., Lee, T.-M. & Kim, J. (2014b). A study on the electrical and mechanical properties of printed Ag thin films for flexible device application. *Journal of Alloys and Compounds*, 596, 158–163. doi: 10.1016/j.jallcom.2014.01.184.

Kim, K.-S. & Chung, G.-S. (2011). Characterization of porous cubic silicon carbide deposited with Pd and Pt nanoparticles as a hydrogen sensor. *Sensors and Actuators B: Chemical*, 157(2), 482–487.

Kim, M., Koo, J. B., Baeg, K.-J., Noh, Y.-Y., Yang, Y. S., Jung, S.-W., Ju, B.-K. & You, I.-K. (2012). Effect of Curing Temperature on Nano-Silver Paste Ink for Organic Thin-Film Transistors. *Journal of Nanoscience and Nanotechnology*, 12(4), 3272–3275. doi: 10.1166/jnn.2012.5639.

Kim, N. W., Lee, D.-G., Kim, K.-S. & Hur, S. (2020). Effects of Curing Temperature on Bending Durability of Inkjet-Printed Flexible Silver Electrode. *Nanomaterials*, 10(12), 2463. doi: 10.3390/nano10122463. Number: 12 Publisher: Multidisciplinary Digital Publishing Institute.

Kim, Y. D. & Hone, J. (2017). Screen printing of 2D semiconductors. *Nature*, 544(7649), 167–168.

Kimoto, T. & Cooper, J. A. (2014). *Fundamentals of silicon carbide technology: growth, characterization, devices and applications*. John Wiley & Sons.

Klosterman, D. A., Chartoff, R. P., Osborne, N. R., Graves, G. A., Lightman, A., Han, G., Bezeredi, A. & Rodrigues, S. (1999). Development of a curved layer LOM process for monolithic ceramics and ceramic matrix composites. *Rapid Prototyping Journal*, 5(2), 61–71.

Knippenberg, W. F. (1963). Growth phenomena in silicon carbide. *Philips Research Report*, 18, 161–274.

Knoll, M., Offenzeller, C., Jakoby, B. & Hilber, W. (2018a). Material screening for fully printed polymer-based thermocouples designed for use in harsh environments. *Measurement Science and Technology*, 29(10), 105104.

Knoll, M., Offenzeller, C., Mayrhofer, B., Jakoby, B. & Hilber, W. (2018b). A screen printed thermocouple-array on a flexible substrate for condition monitoring. *Proceedings*, 2(13), 803.

Ko, H., Kapadia, R., Takei, K., Takahashi, T., Zhang, X. & Javey, A. (2012a). Multi-functional, flexible electronic systems based on engineered nanostructured materials. *Nanotechnology*, 23(34), 344001.

Ko, S.-M., Koo, S.-M., Cho, W.-S., Hwnag, K.-T. & Kim, J.-H. (2012b). Synthesis of SiC nano-powder from organic precursors using RF inductively coupled thermal plasma. *Ceramics international*, 38(3), 1959–1963.

Kobayashi, H., Chewchinda, P., Ohtani, H., Odawara, O. & Wada, H. (2013). Effects of Laser Energy Density on Silicon Nanoparticles Produced Using Laser Ablation in Liquid. *Journal of Physics: Conference Series*, 441(1), 012035. doi: 10.1088/1742-6596/441/1/012035.

Koc, R., Glatzmaier, G. & Sibold, J. (2001). β-SiC production by reacting silica gel with hydrocarbon gas. *Journal of materials science*, 36, 995–999.

Kohler, C., Nikfalazar, M., Friederich, A., Wiens, A., Sazegar, M., Jakoby, R. & Binder, J. R. (2015). Fully screen-printed tunable microwave components based on optimized barium strontium titanate thick films. *International Journal of Applied Ceramic Technology*, 12, E96–E105.

Komazaki, Y. & Uemura, S. (2019). Stretchable, printable, and tunable PDMS-CaCl2 microcomposite for capacitive humidity sensors on textiles. *Sensors and Actuators B: Chemical*, 297, 126711. doi: 10.1016/j.snb.2019.126711.

Kong, D., Le, L. T., Li, Y., Zunino, J. L. & Lee, W. (2012). Temperature-dependent electrical properties of graphene inkjet-printed on flexible materials. *Langmuir*, 28(37), 13467–13472.

Koo, J. B. & Yoon, D. Y. (2001). The dependence of normal and abnormal grain growth in silver on annealing temperature and atmosphere. *Metallurgical and Materials Transactions A*, 32(3), 469–475. doi: 10.1007/s11661-001-0063-4.

Koshi, T., Nomura, K.-i. & Yoshida, M. (2020). Resistance Reduction of Conductive Patterns Printed on Textile by Curing Shrinkage of Passivation Layers. *Micromachines*, 11(6), 539. doi: 10.3390/mi11060539.

Kotzar, G., Freas, M., Abel, P., Fleischman, A., Roy, S., Zorman, C., Moran, J. M. & Melzak, J. (2002). Evaluation of MEMS materials of construction for implantable medical devices. *Biomaterials*, 23(13), 2737–2750.

Koyanagi, T., Terrani, K., Harrison, S., Liu, J. & Katoh, Y. (2021). Additive manufacturing of silicon carbide for nuclear applications. *Journal of Nuclear Materials*, 543, 152577.

Krebs, F. C., Jørgensen, M., Norrman, K., Hagemann, O., Alstrup, J., Nielsen, T. D., Fyenbo, J., Larsen, K. & Kristensen, J. (2009). A complete process for production of flexible large area polymer solar cells entirely using screen printing—first public demonstration. *Solar Energy Materials and Solar Cells*, 93(4), 422–441.

Kueseng, K. & Jacob, K. (2006). Natural rubber nanocomposites with SiC nanoparticles and carbon nanotubes. *European Polymer Journal*, 42(1), 220–227.

Kumar, A., Kumar, A. & Chandra, R. (2018). Fabrication of porous silicon filled Pd/SiC nanocauliflower thin films for high performance H2 gas sensor. *Sensors and Actuators B: Chemical*, 264, 10–19.

Kuzubasoglu, B. A. & Bahadir, S. K. (2020). Flexible temperature sensors: A review. *Sensors and Actuators A: Physical*, 315, 112282.

Lambrecht, W. R., Limpijumnong, S., Rashkeev, S. & Segall, B. (1997). Electronic band structure of SiC polytypes: a discussion of theory and experiment. *physica status solidi (b)*, 202(1), 5–33.

Langenderfer, M. J., Fahrenholtz, W. G., Chertopalov, S., Zhou, Y., Mochalin, V. N. & Johnson, C. E. (2020). Detonation synthesis of silicon carbide nanoparticles. *Ceramics International*, 46(5), 6951–6954.

Larpkiattaworn, S., Ngernchuklin, P., Khongwong, W., Pankurddee, N. & Wada, S. (2006). The influence of reaction parameters on the free Si and C contents in the synthesis of nano-sized SiC. *Ceramics International*, 32(8), 899–904.

Larson, C. M., Choi, J. J., Gallardo, P. A., Henderson, S. W., Niemack, M. D., Rajagopalan, G. & Shepherd, R. F. (2016). Direct ink writing of silicon carbide for microwave optics. *Advanced Engineering Materials*, 18(1), 39–45.

Lasi, H., Fettke, P., Kemper, H.-G., Feld, T. & Hoffmann, M. (2014). Industry 4.0. *Business & information systems engineering*, 6, 239–242.

Le, D. T. & Ju, H. (2021). Solution synthesis of cubic spinel Mn–Ni–Cu–O thermistor powder. *Materials*, 14(6), 1389.

Lebedev, A. A., Oganesyan, G. A., Kozlovski, V. V., Eliseyev, I. A. & Bulat, P. V. (2019a). Radiation Defects in Heterostructures 3C-SiC/4H-SiC. *Crystals*, 9(2), 115. doi: 10.3390/cryst9020115. Number: 2 Publisher: Multidisciplinary Digital Publishing Institute.

Lebedev, A., Oganesyan, G., Kozlovski, V., Eliseyev, I. & Bulat, P. (2019b). Radiation defects in heterostructures 3C-SiC/4H-SiC. *Crystals*, 9(2), 115.

Lee, D.-H., Choi, J., Chae, H., Chung, C.-H. & Cho, S. (2009). Screen-printed white OLED based on polystyrene as a host polymer. *Current Applied Physics*, 9(1), 161–164.

Lee, D.-S., Han, S.-D., Huh, J.-S. & Lee, D.-D. (1999). Nitrogen oxides-sensing characteristics of WO3-based nanocrystalline thick film gas sensor. *Sensors and Actuators B: Chemical*, 60(1), 57–63.

Lee, J. H., Kim, Y. H., Ahn, S. J., Ha, T. H. & Kim, H. S. (2015). Grain-size effect on the electrical properties of nanocrystalline indium tin oxide thin films. *Materials Science and Engineering: B*, 199, 37–41. doi: 10.1016/j.mseb.2015.04.011.

Lee, S.-K., Hsu, H.-C. & Tuan, W.-H. (2016). Oxidation Behavior of Copper at a Temperature below 300 °C and the Methodology for Passivation. *Materials Research*, 19(1), 51–56. doi: 10.1590/1980-5373-MR-2015-0139.

Lee, W.-J. & Chang, Y.-H. (2018). Growth without Postannealing of Monoclinic VO2 Thin Film by Atomic Layer Deposition Using VCl4 as Precursor. *Coatings*, 8(12), 431. doi: 10.3390/coatings8120431. Number: 12 Publisher: Multidisciplinary Digital Publishing Institute.

Lee, Y. J., Lee, C. & Lee, H. M. (2018). Synthesis of oxide-free aluminum nanoparticles for application to conductive film. *Nanotechnology*, 29(5), 055602.

Lely, J. A. (1955). Representation of single crystals of silicon carbide and control of the type and amount of incorporated impurities. *Ber. German Keram. Ges*, 32, 229–231.

Lerner, R., Eisenbrandt, S., Bonafede, S., Meitl, M. A., Fecioru, A., Trindade, A. J., Reiner, R., Waltreit, P. & Bower, C. A. (2016). Heterogeneous Integration of Microscale Gallium Nitride Transistors by Micro-Transfer-Printing. *2016 IEEE 66th Electronic Components and Technology Conference (ECTC)*, pp. 1186–1189. doi: 10.1109/ECTC.2016.373.

Li, C., Cai, Y., Hu, J., Liu, J., Dai, H., Xu, Q., Zhang, C., Zhang, X., Liu, K., Kosinova, M. L. et al. (2023a). SiC/Graphene Film by Laser CVD as an Implantable Sensor Material for Dopamine Detection. *ACS Applied Materials & Interfaces*, 15(22), 27399–27410.

Li, G.-y., Ma, J., Peng, G., Chen, W., Chu, Z.-y., Li, Y.-h., Hu, T.-j. & Li, X.-d. (2014). Room-Temperature Humidity-Sensing Performance of SiC Nanopaper. *ACS Applied Materials & Interfaces*, 6(24), 22673–22679. doi: 10.1021/am5067496. Publisher: American Chemical Society.

Li, H. & Lim, S. (2022). Screen printing of surface-modified barium titanate/polyvinylidene fluoride nanocomposites for high-performance flexible piezoelectric nanogenerators. *Nanomaterials*, 12(17), 2910.

Li, H., Liu, J., Sheng, T., Li, J., Zhang, D. & Jiang, Y. (2024). All-SiC fiber-optic sensor for pressure and temperature dual-mode sensing in harsh environments. *Sensors and Actuators A: Physical*, 373, 115388.

Li, J., Tian, J. & Dong, L. (2000). Synthesis of SiC precursors by a two-step sol–gel process and their conversion to SiC powders. *Journal of the European Ceramic Society*, 20(11), 1853–1857.

Li, W., Li, W., Wang, M., Liu, G. & Chen, M. (2016). Direct writing of stable Cu–Ag-based conductive patterns for flexible electronics. *Rsc Advances*, 6(13), 10670–10676.

Li, X., Lou, C., Li, W., Wang, L., Gao, F., Shao, G., Chen, S. & Yang, W. (2021). High-performance field emitters based on SiC nanowires with designed electron emission sites. *ACS Applied Materials & Interfaces*, 13(2), 3062–3069.

Li, X., Cui, T., Li, X., Liu, H., Li, D., Jian, J., Li, Z., Yang, Y. & Ren, T. (2023b). Wearable Temperature Sensors Based on Reduced Graphene Oxide Films. *Materials*, 16(17), 5952.

Li, Z., Khuje, S., Chivate, A., Huang, Y., Hu, Y., An, L., Shao, Z., Wang, J., Chang, S. & Ren, S. (2020a). Printable Copper Sensor Electronics for High Temperature. *ACS Applied Electronic Materials*, 2(7), 1867–1873. doi: 10.1021/acsaelm.0c00358. Publisher: American Chemical Society.

Li, Z., Scheers, S., An, L., Chivate, A., Khuje, S., Xu, K., Hu, Y., Huang, Y., Chang, S., Olenick, K., Olenick, J., Choi, J. H., Zhou, C. & Ren, S. (2020b). All-Printed Conformal High-Temperature Electronics on Flexible Ceramics. *ACS Applied Electronic Materials*, 2(2), 556–562. doi: 10.1021/acsaelm.9b00798. Publisher: American Chemical Society.

Li, Z., Zhang, M., Yang, L., Wu, R., Wu, Z., Jiang, Y., Zhou, L. & Liu, Y. (2022). The Effect of Surface Hydroxyls on the Humidity-Sensitive Properties of LiCl-Doped ZnSn(OH)6 Sphere-Based Sensors. *Nanomaterials*, 12(3), 467. doi: 10.3390/nano12030467.

Lim, D.-I., Cha, J.-R. & Gong, M.-S. (2013). Preparation of flexible resistive micro-humidity sensors and their humidity-sensing properties. *Sensors and Actuators B: Chemical*, 183, 574–582. doi: 10.1016/j.snb.2013.04.031.

Lim, H. S., Kim, S. J., Jang, H. W. & Lim, J. A. (2017). Intense pulsed light for split-second structural development of nanomaterials. *Journal of Materials Chemistry C*, 5(29), 7142–7160.

Lin, H., Gerbec, J. A., Sushchikh, M. & McFarland, E. W. (2008). Synthesis of amorphous silicon carbide nanoparticles in a low temperature low pressure plasma reactor. *Nanotechnology*, 19(32), 325601.

Liu, G., Wang, J., Ge, Y., Wang, Y., Lu, S., Zhao, Y., Tang, Y., Soomro, A. M., Hong, Q., Yang, X., Xu, F., Li, S., Chen, L.-J., Cai, D. & Kang, J. (2020). Cu Nanowires Passivated with Hexagonal Boron Nitride: An Ultrastable, Selectively Transparent Conductor. *ACS Nano*, 14(6), 6761–6773. doi: 10.1021/acsnano.0c00109. Publisher: American Chemical Society.

Liu, H., Miao, Y., Liu, B., Lin, W., Zhang, H., Song, B., Huang, M. & Lin, L. (2015). Relative Humidity Sensor Based on S-Taper Fiber Coated With SiO2 Nanoparticles. *IEEE Sensors Journal*, 15(6), 3424–3428. doi: 10.1109/JSEN.2015.2389519. Conference Name: IEEE Sensors Journal.

Liu, K., Wu, T., Bourell, D. L., Tan, Y., Wang, J., He, M., Sun, H., Shi, Y. & Chen, J. (2018a). Laser additive manufacturing and homogeneous densification of complicated shape SiC ceramic parts. *Ceramics International*, 44(17), 21067–21075.

Liu, R., Liu, M. & Chang, J. (2017). Large-scale synthesis of monodisperse SiC nanoparticles with adjustable size, stoichiometric ratio and properties by fluidized bed chemical vapor deposition. *Journal of Nanoparticle Research*, 19, 1–13.

Liu, Y., Ren, W., Shi, P., Liu, D., Zhang, Y., Liu, M., Ye, Z.-G., Jing, W., Tian, B. & Jiang, Z. (2018b). A highly thermostable In2O3/ITO thin film thermocouple prepared via screen printing for high temperature measurements. *Sensors*, 18(4), 958.

Liu, Z., Tian, B., Zhang, B., Zhang, Z., Liu, J., Zhao, L., Shi, P., Lin, Q. & Jiang, Z. (2021). High-Performance Temperature Sensor by Employing Screen Printing Technology. *Micromachines*, 12(8), 924.

Lodhe, M., Selvam, A., Udayakumar, A. & Balasubramanian, M. (2016). Effect of polycarbosilane addition to a mixture of rice husk and coconut shell on SiC whisker growth. *Ceramics International*, 42(2), 2393–2401.

Loganathan, S. & Sankaran, S. (2017). Surface chemical studies on silicon carbide suspensions in the presence of poly (ethylene glycol) and chitosan. *Sci Publ Gr*, 2(1), 6–20.

Lohmiller, J., Woo, N. C. & Spolenak, R. (2010). Microstructure–property relationship in highly ductile Au–Cu thin films for flexible electronics. *Materials Science and Engineering: A*, 527(29), 7731–7740. doi: 10.1016/j.msea.2010.08.043.

Long, X., Du, C., Hu, B. & Li, M. (2018). Comparison of sintered silver micro and nano particles: from microstructure to property. *2018 20th International Conference on Electronic Materials and Packaging (EMAP)*, pp. 1–4. doi: 10.1109/EMAP.2018.8660953.

Louat, N. (1974). On the theory of normal grain growth. *Acta metallurgica*, 22(6), 721–724.

Lozano, O., Laloy, J., Alpan, L., Mejia, J., Rolin, S., Toussaint, O., Dogné, J.-M., Lucas, S. & Masereel, B. (2012). Effects of SiC nanoparticles orally administered in a rat model: biodistribution, toxicity and elemental composition changes in feces and organs. *Toxicology and applied pharmacology*, 264(2), 232–245.

Lu, R., Hao, W., Kong, L., Zhao, K., Bai, H., Lei, L. & Liu, Z. (2023). Self-reducing copper paste with high conductivity and oxidation resistance for flexible substrate by intensive pulsed light sintering. *Journal of Materials Science: Materials in Electronics*, 34(6), 510.

Lu, Y., Xu, K., Yang, M.-Q., Tang, S.-Y., Yang, T.-Y., Fujita, Y., Honda, S., Arie, T., Akita, S. & Chueh, Y.-L. (2021). Highly stable Pd/HNb 3 O 8-based flexible humidity sensor for perdurable wireless wearable applications. *Nanoscale Horizons*, 6(3), 260–270. Consulted at https://pubs.rsc.org/en/content/articlehtml/2021/nh/d0nh00594k. Publisher: Royal Society of Chemistry.

Luo, G., Zhang, Z., Hu, J., Zhang, J., Sun, Y., Shen, Q. & Zhang, L. (2020). Study on Rheological Behavior of Micro/Nano-Silicon Carbide Particles in Ethanol by Selecting Efficient Dispersants. *Materials*, 13, 1496. doi: 10.3390/ma13071496.

Lupo, D., Clemens, W., Breitung, S. & Hecker, K. (2013). OE-A roadmap for organic and printed electronics. *Applications of Organic and Printed Electronics: A Technology-Enabled Revolution*, 1–26.

L'vov, B. V. (1999). Kinetics and mechanism of thermal decomposition of silver oxide. *Thermochimica Acta*, 333(1), 13–19. doi: 10.1016/S0040-6031(99)00085-4.

Ma, L.-Y. & Soin, N. (2022). Recent progress in printed physical sensing electronics for wearable health-monitoring devices: A review. *IEEE Sensors Journal*, 22(5), 3844–3859.

Magdassi, S., Azoubel, S., Layani, M., Grouchko, M. & Kamyshny, A. (2012). Nanomaterials for Printed Electronics. *NIP & Digital Fabrication Conference*, 28, 561–563.

Mahović Poljaček, S., Tomašegović, T., Strižić Jakovljević, M. & Donevski, D. (2023). Surface Modification and Properties of Thin Ink Films with Added TiO2 and ZnO Nanoparticles Applied on Paperboard Substrates. *Materials*, 16(2), 478.

Majid, M., Habib, S., Javed, A. R., Rizwan, M., Srivastava, G., Gadekallu, T. R. & Lin, J. C.-W. (2022). Applications of wireless sensor networks and internet of things frameworks in the industry revolution 4.0: A systematic literature review. *Sensors*, 22(6), 2087.

Manikandan, S. & Jancirani, J. (2014). A Study of preparation and characterization of Nano-sized SiC powder using High energy ball milling. *Applied Mechanics and Materials*, 592, 13–17.

Manjunath, G., Pujari, S., Patil, D. & Mandal, S. (2020). A scalable screen-printed high performance ZnO-UV and Gas Sensor: Effect of solution combustion. *Materials Science in Semiconductor Processing*, 107, 104828.

Männl, U., Van Den Berg, C., Magunje, B., Härting, M., Britton, D., Jones, S., Van Staden, M. & Scriba, M. (2014). Nanoparticle composites for printed electronics. *Nanotechnology*, 25(9), 094004.

Maraveas, C. & Bartzanas, T. (2021). Application of Internet of Things (IoT) for optimized greenhouse environments. *AgriEngineering*, 3(4), 954–970.

Marshall, R. C., Faust, J. W. & Ryan, C. E. (1974). *Silicon carbide–1973: proceedings*. University of South Carolina Press.

Martins, P., Pereira, N., Lima, A., Garcia, A., Mendes-Filipe, C., Policia, R., Correia, V. & Lanceros-Mendez, S. (2023). Advances in printing and electronics: From engagement to commitment. *Advanced Functional Materials*, 33(16), 2213744.

Maskey, B. B., Shrestha, K., Sun, J., Park, H., Park, J., Parajuli, S., Shrestha, S., Jung, Y., Ramasundaram, S., Koirala, G. R. et al. (2020). Proving the robustness of a PEDOT: PSS-based thermistor via functionalized graphene oxide–poly (vinylidene fluoride) composite encapsulation for food logistics. *RSC advances*, 10(21), 12407–12414.

Matei, A., Constantinescu, C., Mitu, B., Filipescu, M., Ion, V., Ionita, I., Brajnicov, S., Alloncle, A.-P., Delaporte, P., Emandi, A. et al. (2015). Laser printing of azo-derivative thin films for non-linear optical applications. *Applied Surface Science*, 336, 200–205.

Matovic, B., Saponjic, A., Devecerski, A. & Miljkovic, M. (2007). Fabrication of SiC by carbothermal-reduction reactions of diatomaceous earth. *Journal of materials science*, 42, 5448–5451.

Matsuda, T., Inami, K., Motoyama, K., Sano, T. & Hirose, A. (2018). Silver oxide decomposition mediated direct bonding of silicon-based materials. *Scientific Reports*, 8(1), 10472. doi: 10.1038/s41598-018-28788-x. Publisher: Nature Publishing Group.

Medina-Santiago, A., Azucena, A. D. P., Gómez-Zea, J. M., Jesús-Magaña, J. A., de la Luz Valdez-Ramos, M., Sosa-Silva, E. & Falcon-Perez, F. (2019). Adaptive model IoT for monitoring in data centers. *IEEE Access*, 8, 5622–5634.

Mekuria, T. D., Zhang, C. & Fouad, D. E. (2019). The effect of thermally developed SiC@ SiO2 core-shell structured nanoparticles on the mechanical, thermal and UV-shielding properties of polyimide composites. *Composites Part B: Engineering*, 173, 106917.

Middelburg, L., van Driel, W. & Zhang, G. (2020). From Si towards SiC technology for harsh environment sensing. *Sensor Systems Simulations: From Concept to Solution*, 1–15.

Miller, D. R., Akbar, S. A. & Morris, P. A. (2014). Nanoscale metal oxide-based heterojunctions for gas sensing: A review. *Sensors and Actuators B: Chemical*, 204, 250–272.

Mitchell, T. E., Lagerlöf, K. & Heuer, A. (1985). Dislocations in ceramics. *Materials science and technology*, 1(11), 944–949.

Mičian, M., Frátrik, M., Moravec, J. & Švec, M. (2022). Determination of Grain Growth Kinetics of S960MC Steel. *Materials*, 15(23), 8539. doi: 10.3390/ma15238539. Number: 23 Publisher: Multidisciplinary Digital Publishing Institute.

Mo, L., Guo, Z., Yang, L., Zhang, Q., Fang, Y., Xin, Z., Chen, Z., Hu, K., Han, L. & Li, L. (2019a). Silver nanoparticles based ink with moderate sintering in flexible and printed electronics. *International journal of molecular sciences*, 20(9), 2124.

Mo, L., Guo, Z., Yang, L., Zhang, Q., Fang, Y., Xin, Z., Chen, Z., Hu, K., Han, L. & Li, L. (2019b). Silver Nanoparticles Based Ink with Moderate Sintering in Flexible and Printed Electronics. *International Journal of Molecular Sciences*, 20(9), 2124. doi: 10.3390/ijms20092124.

Mognetti, B., Barberis, A., Marino, S., Di Carlo, F., Lysenko, V., Marty, O. & Géloën, A. (2010). Preferential killing of cancer cells using silicon carbide quantum dots. *Journal of Nanoscience and Nanotechnology*, 10(12), 7971–7975.

Moissan, H. (1905). Étude du Siliciure de carbone de la météorite de cañon Diablo. *Comptes rendus Acad. sci*, 140, 405–506.

Monne, M. A., Lan, X. & Chen, M. Y. (2018). Material selection and fabrication processes for flexible conformal antennas. *International Journal of Antennas and Propagation*, 2018(1), 9815631.

Montes-García, V. & Samorì, P. Humidity Sensing with Supramolecular Nanostructures. *Advanced Materials*, n/a(n/a), 2208766. doi: 10.1002/adma.202208766. _eprint: https://onlinelibrary.wiley.com/doi/pdf/10.1002/adma.202208766.

Moravec, J. (2015). DETERMINATION OF THE GRAIN GROWTH KINETICS AS A BASE PARAMETER FOR NUMERICAL SIMULATION DEMAND. | MM Science Journal | EBSCOhost. ISSN: 1803-1269 Pages: 649, doi: 10.17973/MMSJ.2015_10_201523.

Morelli, D., Heremans, J., Beetz, C., Woo, W., Harris, G. & Taylor, C. (1994). Carrier concentration dependence of the thermal conductivity of silicon carbide. *Institute of Physics Conference Series*, 137, 313–316.

Morelli, L., Gagnon, G. & Zednik, R. J. (2023). Flexible capacitive kirigami electrode: Experimental investigation and analytical model. *IEEE Journal on Flexible Electronics*.

Morkoc, b. H., Strite, S., Gao, G., Lin, M., Sverdlov, B. & Burns, M. (1994). Large-band-gap SiC, III-V nitride, and II-VI ZnSe-based semiconductor device technologies. *Journal of Applied physics*, 76(3), 1363–1398.

Mott, M. & Evans, J. R. G. (2004). Solid Freeforming of Silicon Carbide by Inkjet Printing Using a Polymeric Precursor. *Journal of the American Ceramic Society*, 84(2), 307–13. doi: 10.1111/j.1151-2916.2001.tb00655.x.

Mott, M. & Evans, J. R. (2001). Solid freeforming of silicon carbide by inkjet printing using a polymeric precursor. *Journal of the American Ceramic Society*, 84(2), 307–13.

Mousa, H. & Teker, K. (2021). High-transconductance silicon carbide nanowire-based field-effect transistor (SiC-NWFET) for high-temperature applications. *Microelectronics International*, 38(2), 78–83.

Mukasyan, A. S., Lin, Y.-C., Rogachev, A. S. & Moskovskikh, D. O. (2013). Direct combustion synthesis of silicon carbide nanopowder from the elements. *Journal of the American ceramic society*, 96(1), 111–117.

Muzha, A., Fuchs, F., Tarakina, N. V., Simin, D., Trupke, M., Soltamov, V., Mokhov, E., Baranov, P., Dyakonov, V., Krueger, A. et al. (2014). Room-temperature near-infrared silicon carbide nanocrystalline emitters based on optically aligned spin defects. *Applied Physics Letters*, 105(24).

Müller, G., Krötz, G. & Niemann, E. (1994). SiC for sensors and high-temperature electronics. *Sensors and Actuators A: Physical*, 43(1), 259–268. doi: 10.1016/0924-4247(93)00684-V.

Na, W. K., Lim, H. M., Huh, S. H., Park, S. E., Lee, Y.-S. & Lee, S. H. (2009). Effect of the average particle size and the surface oxidation layer of silicon on the colloidal silica particle through direct oxidation. *Materials Science and Engineering: B*, 163(2), 82–87. doi: 10.1016/j.mseb.2009.05.011.

Nagai, T. & Itoh, M. (1990). SiC thin-film thermistors. *IEEE transactions on industry applications*, 26(6), 1139–1143.

Najafi, A., Golestani-Fard, F., Rezaie, H. & Ehsani, N. (2011). A study on sol–gel synthesis and characterization of SiC nano powder. *Journal of sol-gel science and technology*, 59, 205–214.

Najafkhani, F., Kheiri, S., Pourbahari, B. & Mirzadeh, H. (2021). Recent advances in the kinetics of normal/abnormal grain growth: a review. *Archives of Civil and Mechanical Engineering*, 21, 1–20.

Nakashima, S.-i. & Harima, H. (1997). Raman investigation of SiC polytypes. *physica status solidi (a)*, 162(1), 39–64.

Narakathu, B., Eshkeiti, A., Reddy, A., Rebros, M., Rebrosova, E., Joyce, M., Bazuin, B. & Atashbar, M. (2012). A novel fully printed and flexible capacitive pressure sensor. *SENSORS, 2012 IEEE*, pp. 1–4.

Ned, A. A., Okojie, R. S. & Kurtz, A. D. (1998). 6H-SiC pressure sensor operation at 600/spl deg/C. *1998 Fourth International High Temperature Electronics Conference. HITEC (Cat. No. 98EX145)*, pp. 257–260.

Ned, A. A., Kurtz, A. D., Masheeb, F. & Beheim, G. (2001). Leadless SiC pressure sensors for high temperature applications. *47th International Instrumentation Symposium, Denver, CO*.

Nersisyan, H., Lee, Y., Lee, J. & Jeong, S. (2020). Combustion Synthesis of C and SiC Nanoparticles from Na 2 CO 3–Si Mixtures: Characterization and Electrochemical Performance. *International Journal of Self-Propagating High-Temperature Synthesis*, 29, 65–76.

Neudeck, P. G., Okojie, R. S. & Chen, L.-Y. (2002). High-temperature electronics-a role for wide bandgap semiconductors? *Proceedings of the IEEE*, 90(6), 1065–1076.

Nguyen, N.-K., Nguyen, T., Nguyen, T.-K., Yadav, S., Dinh, T., Masud, M. K., Singha, P., Do, T. N., Barton, M. J., Ta, H. T., Kashaninejad, N., Ooi, C. H., Nguyen, N.-T. & Phan, H.-P. (2021a). Wide-Band-Gap Semiconductors for Biointegrated Electronics: Recent Advances and Future Directions. *ACS Applied Electronic Materials*, 3(5), 1959–1981. doi: 10.1021/acsaelm.0c01122. Publisher: American Chemical Society.

Nguyen, N.-K., Nguyen, T., Nguyen, T.-K., Yadav, S., Dinh, T., Masud, M. K., Singha, P., Do, T. N., Barton, M. J., Ta, H. T. et al. (2021b). Wide-band-gap semiconductors for biointegrated electronics: recent advances and future directions. *ACS Applied Electronic Materials*, 3(5), 1959–1981.

Nguyen, T. K., Aberoumand, S. & Dao, D. V. (2021c). Advances in Si and SiC materials for high-performance supercapacitors toward integrated energy storage systems. *Small*, 17(49), 2101775.

Niittynen, J., Abbel, R., Mäntysalo, M., Perelaer, J., Schubert, U. S. & Lupo, D. (2014). Alternative sintering methods compared to conventional thermal sintering for inkjet printed silver nanoparticle ink. *Thin Solid Films*, 556, 452–459.

Nikitin, D., Sivkov, A., Rahmatullin, I. & Ivashutenko, A. (2017). Synthesis of silicon carbide nanopowders in free flowing plasma jet with different energy levels. *Journal of Physics: Conference Series*, 830(1), 012120.

Nikkam, N., Saleemi, M., Haghighi, E. B., Ghanbarpour, M., Khodabandeh, R., Muhammed, M., Palm, B. & Toprak, M. S. (2014). Fabrication, characterization and thermophysical property evaluation of SiC nanofluids for heat transfer applications. *Nano-Micro Letters*, 6, 178–189.

Nowak, M., Mistewicz, K., Nowrot, A., Szperlich, P., Jesionek, M. & Starczewska, A. (2014). Transient characteristics and negative photoconductivity of SbSI humidity sensor. *Sensors and Actuators A: Physical*, 210, 32–40.

Nozik, A. J., Beard, M. C., Luther, J. M., Law, M., Ellingson, R. J. & Johnson, J. C. (2010). Semiconductor quantum dots and quantum dot arrays and applications of multiple exciton generation to third-generation photovoltaic solar cells. *Chemical reviews*, 110(11), 6873–6890.

O'Connor, J. R. & Smiltens, J. (1960). Silicon carbide(A high temperature semiconductor).

Ohsaki, S., Cho, D., Sano, H., Uchiyama, Y. & Kobayashi, K. (1998). Synthesis of β-SiC by the reaction of gaseous SiO with activated carbon. *Key Engineering Materials*, 159, 89–94.

Okada, R. & Iijima, S. (1991). Oxidation property of silicon small particles. *Applied Physics Letters*, 58(15), 1662–1663. doi: 10.1063/1.105129. Publisher: American Institute of Physics.

Oliber, E. A., Cugno, C., Moreno, M., Esquivel, M., Haberkorn, N. & Fiscina, J. E. (2003). Sintering of porous silver compacts at controlled heating rates in oxygen or argon. 8.

Oliveros, A., Guiseppi-Elie, A. & Saddow, S. E. (2013). Silicon carbide: a versatile material for biosensor applications. *Biomedical microdevices*, 15, 353–368.

Ouyang, J., Cormier, D., Williams, S. A. & Borkholder, D. A. (2016). Photonic sintering of aerosol jet printed lead zirconate titanate (PZT) thick films. *Journal of the American Ceramic Society*, 99(8), 2569–2577.

Park, J. W., Kang, B. H. & Kim, H. J. (2020a). A review of low-temperature solution-processed metal oxide thin-film transistors for flexible electronics. *Advanced Functional Materials*, 30(20), 1904632.

Park, J., Lee, Y., Hwang, Y. & Cho, S. (2020b). Interdigitated and wave-shaped electrode-based capacitance sensor for monitoring antibiotic effects. *Sensors*, 20(18), 5237.

Park, J. H., Jeong, S., Lee, E. J., Lee, S. S., Seok, J. Y., Yang, M., Choi, Y. & Kang, B. (2016). Transversally extended laser plasmonic welding for oxidation-free copper fabrication toward high-fidelity optoelectronics. *Chemistry of Materials*, 28(12), 4151–4159.

Park, K.-B., Kieferndorf, F., Burkart, R. M. & Agostini, B. (2020c). Optimization of 1-mw solar inverter with 1.7-kv sic mosfet module. *2020 IEEE Workshop on Wide Bandgap Power Devices and Applications in Asia (WiPDA Asia)*, pp. 1–4.

Park, S., Seo, J., Park, J., Hwang, I., Lee, H.-S., Jung, H. & Yoo, B. (2022). Capacitive humidity sensing properties of freestanding bendable porous SiO2/Si thin films. *Scientific Reports*, 12(1), 11689. doi: 10.1038/s41598-022-15955-4. Number: 1 Publisher: Nature Publishing Group.

Park, S., Lee, D.-H., Ryoo, H.-I., Lim, T.-W., Yang, D.-Y. & Kim, D.-P. (2009). Fabrication of three-dimensional SiC ceramic microstructures with near-zero shrinkage via dual crosslinking induced stereolithography. *Chemical communications*, (32), 4880–4882.

Peng, P., Hu, A., Gerlich, A. P., Zou, G., Liu, L. & Zhou, Y. N. (2015). Joining of Silver Nanomaterials at Low Temperatures: Processes, Properties, and Applications. *ACS Applied Materials & Interfaces*, 7(23), 12597–12618. doi: 10.1021/acsami.5b02134.

Perelaer, J., Schubert, U. S. & Jena, F. (2010). Inkjet printing and alternative sintering of narrow conductive tracks on flexible substrates for plastic electronic applications. *Radio frequency identification fundamentals and applications, design methods and solutions*, 265–286.

Perelaer, J., Abbel, R., Wünscher, S., Jani, R., van Lammeren, T. & Schubert, U. S. (2012). Roll-to-roll compatible sintering of inkjet printed features by photonic and microwave exposure: from non-conductive ink to 40% bulk silver conductivity in less than 15 seconds. *Advanced materials*, 24(19), 2620.

Persson, C. & Lindefelt, U. (1997). Relativistic band structure calculation of cubic and hexagonal SiC polytypes. *Journal of Applied Physics*, 82(11), 5496–5508.

Phan, H.-P., Dinh, T., Kozeki, T., Nguyen, T.-K., Qamar, A., Namazu, T., Nguyen, N.-T. & Dao, D. V. (2016a). Nano strain-amplifier: Making ultra-sensitive piezoresistance in nanowires possible without the need of quantum and surface charge effects. *Applied Physics Letters*, 109(12).

Phan, H.-P., Dinh, T., Kozeki, T., Qamar, A., Namazu, T., Dimitrijev, S., Nguyen, N.-T. & Dao, D. V. (2016b). Piezoresistive effect in p-type 3C-SiC at high temperatures characterized using Joule heating. *Scientific reports*, 6, 28499. doi: 10.1038/srep28499.

Phan, H.-P., Dowling, K. M., Nguyen, T. K., Dinh, T., Senesky, D. G., Namazu, T., Dao, D. V. & Nguyen, N.-T. (2018). Highly sensitive pressure sensors employing 3C-SiC nanowires fabricated on a free standing structure. *Materials & Design*, 156, 16–21.

Phan, H.-P., Nguyen, T.-K., Dinh, T., Qamar, A., Iacopi, A., Lu, J., Dao, D. V., Rais-Zadeh, M. & Nguyen, N.-T. (2019a). Wireless battery-free SiC sensors operating in harsh environments using resonant inductive coupling. *IEEE Electron Device Letters*, 40(4), 609–612.

Phan, H.-P., Zhong, Y., Nguyen, T.-K., Park, Y., Dinh, T., Song, E., Vadivelu, R. K., Masud, M. K., Li, J., Shiddiky, M. J. et al. (2019b). Long-lived, transferred crystalline silicon carbide nanomembranes for implantable flexible electronics. *ACS nano*, 13(10), 11572–11581.

Phan, H.-P., Dinh, T., Nguyen, T.-K., Qamar, A., Nguyen, T., Han, J., Dao, D. V., Nguyen, N.-T. et al. (2020). High temperature silicon-carbide-based flexible electronics for monitoring hazardous environments. *Journal of hazardous materials*, 394, 122486.

Photonics, W. How Does a Raman Spectrometer Work? Consulted at https://wasatchphotonics .com/technologies/how-raman-spectrometer-works/.

Phung, T. H., Gafurov, A. N., Kim, I., Kim, S. Y., Kim, K. M. & Lee, T.-M. (2021). IoT device fabrication using roll-to-roll printing process. *Scientific Reports*, 11(1), 19982. doi: 10.1038/s41598-021-99436-0. Number: 1 Publisher: Nature Publishing Group.

Polozov, I., Razumov, N., Masaylo, D., Silin, A., Lebedeva, Y. & Popovich, A. (2020). Fabrication of silicon carbide fiber-reinforced silicon carbide matrix composites using binder jetting additive manufacturing from irregularly-shaped and spherical powders. *Materials*, 13(7), 1766.

Ponraj, J. S., Dhanabalan, S. C., Attolini, G. & Salviati, G. (2016). SiC nanostructures toward biomedical applications and its future challenges. *Critical Reviews in Solid State and Materials Sciences*, 41(5), 430–446.

Pourchez, J., Forest, V., Boumahdi, N., Boudard, D., Tomatis, M., Fubini, B., Herlin-Boime, N., Leconte, Y., Guilhot, B., Cottier, M. et al. (2012). In vitro cellular responses to silicon carbide nanoparticles: impact of physico-chemical features on pro-inflammatory and pro-oxidative effects. *Journal of Nanoparticle Research*, 14, 1–12.

Precedence. (2023). Silicon Carbide Market (By Product: Black Silicon Carbide, Green Silicon Carbide; By Application: Steel, Automotive, Aerospace, Military & Defense, Electrical & Electronics, Healthcare, Others) - Global Industry Analysis, Size, Share, Growth, Trends, Regional Outlook, and Forecast 2024-2033. Consulted at https://www.precedenceresearch.com/silicon-carbide-market#:~:text=By%20product%2C%20the%20black%20SiC,the%20market%20share%20in%202023.

Puttananjegowda, K., Takshi, A. & Thomas, S. (2022). A silicon carbide electrochemical sensor for glucose detection. In *Silicon Carbide Technology for Advanced Human Healthcare Applications* (pp. 217–241). Elsevier.

Qu, C., Hu, J., Liu, X., Li, Z. & Ding, Y. (2017). Morphology and Mechanical Properties of Polyimide Films: The Effects of UV Irradiation on Microscale Surface. *Materials*, 10(11), 1329. doi: 10.3390/ma10111329.

Rade, K., Martinčič, A., Novak, S. & Kobe, S. (2013). Feasibility study of SiC-ceramics as a potential material for bone implants. *Journal of Materials Science*, 48, 5295–5301.

Rahman, M. T., McCloy, J., Ramana, C. V. & Panat, R. (2016). Structure, electrical characteristics, and high-temperature stability of aerosol jet printed silver nanoparticle films. *Journal of Applied Physics*, 120(7), 075305. doi: 10.1063/1.4960779.

Rajagopal, R. R., Rajarao, R. & Sahajwalla, V. (2017). Synthesis of glass fiber-nano silicon carbide composite by using waste printed circuit boards and compact discs as resources. *Composites Communications*, 5, 19–22.

Rajan, K., Roppolo, I., Chiappone, A., Bocchini, S., Perrone, D. & Chiolerio, A. (2016). Silver nanoparticle ink technology: state of the art. *Nanotechnology, Science and Applications*, 9, 1–13. doi: 10.2147/NSA.S68080. Publisher: Dove Medical Press _eprint: https://www.tandfonline.com/doi/pdf/10.2147/NSA.S68080.

Rajarao, R. & Sahajwalla, V. (2016). A cleaner, sustainable approach for synthesising high purity silicon carbide and silicon nitride nanopowders using macadamia shell waste. *Journal of Cleaner Production*, 133, 1277–1282.

Raju, M., Sen, S., Sarkar, D. & Jacob, C. (2021). Synthesis of 3C-silicon carbide 1D structures by carbothermal reduction process. *Journal of Alloys and Compounds*, 857, 158243.

Rao, B. G., Mukherjee, D. & Reddy, B. M. (2017). CHAPTER 1: NOVEL APPROACHES FOR PREPARATION OF NANOPARTICLES. In *Nanostructures in Therapeutic Medicine Series. Nanostructures for Novel Therapy Synthesis, Characterization and Applications* (vol. 1, pp. 875). Bucharest, Romania: Elsevier.

Rao, J. B., Catherin, G., Murthy, I. N., Rao, D. V. & Raju, B. N. (2011). Production of nano structured silicon carbide by high energy ball milling. *International Journal of Engineering, Science and Technology*, 3(4).

Rao, S., Pangallo, G., Pezzimenti, F. & Della Corte, F. G. (2015). High-performance temperature sensor based on 4H-SiC Schottky diodes. *IEEE Electron Device Letters*, 36(7), 720–722.

Rayhana, R., Xiao, G. G. & Liu, Z. (2021). Printed sensor technologies for monitoring applications in smart farming: A review. *IEEE Transactions on Instrumentation and Measurement*, 70, 1–19.

Rebenklau, L., Gierth, P., Paproth, A., Irrgang, K., Lippmann, L., Wodtke, A., Niedermeyer, L., Augsburg, K. & Bechtold, F. (2015). Temperature sensors based on thermoelectric effect. 5.

Reddy, A. S. G., Narakathu, B. B., Atashbar, M. Z., Rebros, M., Rebrosova, E. & Joyce, M. K. (2011a). Fully Printed Flexible Humidity Sensor. *Procedia Engineering*, 25, 120–123. doi: 10.1016/j.proeng.2011.12.030.

Reddy, A., Narakathu, B., Atashbar, M., Rebros, M., Rebrosova, E., Bazuin, B., Joyce, M., Fleming, P. & Pekarovicova, A. (2011b). Printed capacitive based humidity sensors on flexible substrates. *Sensor Letters*, 9(2), 869–871.

Reimann, T., Töpfer, J., Barth, S., Bartsch, H. & Muller, J. (2013a). Low-Temperature Sintered NTC Thermistor Ceramics for Thick-Film Temperature Sensors. *International Journal of Applied Ceramic Technology*, 10, 428-434. Consulted at https://api.semanticscholar.org/CorpusID:137222247.

Reimann, T., Töpfer, J., Barth, S., Bartsch, H. & Müller, J. (2013b). Low-Temperature Sintered NTC Thermistor Ceramics for Thick-Film Temperature Sensors. *International Journal of Applied Ceramic Technology*, 10(3), 428–434.

Reynolds, Q. & Norton, M. (1986). Thick Film Platinum Temperature Sensors. *Microelectronics International*, 3(1), 33–35. doi: 10.1108/eb044212.

Rieu, M., Camara, M., Tournier, G., Viricelle, J.-P., Pijolat, C., de Rooij, N. F. & Briand, D. (2016). Fully inkjet printed SnO2 gas sensor on plastic substrate. *Sensors and Actuators B: Chemical*, 236, 1091–1097.

Rim, Y. S., Bae, S.-H., Chen, H., De Marco, N. & Yang, Y. (2016). Recent progress in materials and devices toward printable and flexible sensors. *Advanced Materials*, 28(22), 4415–4440.

Rivadeneyra, A., Fernández-Salmerón, J., Banqueri, J., López-Villanueva, J. A., Capitan-Vallvey, L. F. & Palma, A. J. (2014). A novel electrode structure compared with interdigitated electrodes as capacitive sensor. *Sensors and Actuators B: Chemical*, 204, 552–560.

Roberson, D. A., Wicker, R. B., Murr, L. E., Church, K. & MacDonald, E. (2011). Microstructural and Process Characterization of Conductive Traces Printed from Ag Particulate Inks. *Materials*, 4(6), 963–979. doi: 10.3390/ma4060963.

Roberson, D. A., Wicker, R. & MacDonald, E. (2012). Ohmic curing of printed silver conductive traces. *Journal of electronic materials*, 41, 2553–2566.

Roccaforte, F., Fiorenza, P., Greco, G., Nigro, R. L., Giannazzo, F., Iucolano, F. & Saggio, M. (2018). Emerging trends in wide band gap semiconductors (SiC and GaN) technology for power devices. *Microelectronic Engineering*, 187, 66–77.

Rollett, A. D., Gottstein, G., Shvindlerman, L. S. & Molodov, D. A. (2004). Grain boundary mobility – a brief review. *Zeitschrift für Metallkunde*, 95(4), 226–229. doi: 10.3139/146.017938.

Romero, F. J., Rivadeneyra, A., Toral, V., Castillo, E., García-Ruiz, F., Morales, D. P. & Rodriguez, N. (2018). Design guidelines of laser reduced graphene oxide conformal thermistor for IoT applications. *Sensors and Actuators A: Physical*, 274, 148–154.

Rong, M. Z., Zhang, M. Q., Shi, G., Ji, Q. L., Wetzel, B. & Friedrich, K. (2003). Graft polymerization onto inorganic nanoparticles and its effect on tribological performance improvement of polymer composites. *Tribology International*, 36(9), 697–707.

Round, H. J. (1991). A note on carborundum. In *Semiconductor devices: pioneering papers* (pp. 879–879). World Scientific.

Roushani, M., Nezhadali, A., Jalilian, Z. & Azadbakht, A. (2017). Development of novel electrochemical sensor on the base of molecular imprinted polymer decorated on SiC nanoparticles modified glassy carbon electrode for selective determination of loratadine. *Materials Science and Engineering: C*, 71, 1106–1114.

Roveti, D. K. (2001). Choosing a humidity sensor: A review of three technologies this discussion of the operating principles of capacitive, resisitive, and thermal conductivity humidity sensors also addresses their advantages, disadvantages, and applications. *Sensors-the Journal of Applied Sensing Technology*, 18(7), 54–58.

Russo, M. A., Santarelli, D. M. & O'Rourke, D. (2017). The physiological effects of slow breathing in the healthy human. *Breathe*, 13(4), 298–309. doi: 10.1183/20734735.009817. Publisher: European Respiratory Society Section: Reviews.

Sachin, Pandey, B. K. & Jaiswal, R. L. (2022). Electrical conductivity of semiconducting nanoparticles. *Physica B: Condensed Matter*, 646, 414279. doi: 10.1016/j.physb.2022.414279.

Saddow, S. E. (2011). *Silicon carbide biotechnology: a biocompatible semiconductor for advanced biomedical devices and applications*. Elsevier.

Saddow, S. E. (2022). Silicon carbide technology for advanced human healthcare applications. *Micromachines*, 13(3), 346.

Saha, J., Kumar, N. & Panda, S. K. (2022). A futuristic silicon-carbide (SiC) based electric-vehicle fast charging/discharging (FC/dC) station. *IEEE Journal of Emerging and Selected Topics in Power Electronics*.

Saidina, D., Eawwiboonthanakit, N., Mariatti, M., Fontana, S. & Hérold, C. (2019). Recent development of graphene-based ink and other conductive material-based inks for flexible electronics. *Journal of Electronic Materials*, 48, 3428–3450.

Saini, I., Sharma, A., Rozra, J., Dhiman, R., Aggarwal, S. & Sharma, P. K. (2015). Modification of structural, thermal, and electrical properties of PVA by addition of silicon carbide nanocrystals. *Journal of Applied Polymer Science*, 132(34).

Saini, I., Sharma, A., Dhiman, R., Chandak, N., Aggarwal, S. & Sharma, P. K. (2017). Functionalized SiC nanocrystals for tuning of optical, thermal, mechanical and electrical properties of polyvinyl alcohol. *Thin Solid Films*, 628, 176–183.

SALEMI, A. (2017). *Silicon Carbide Technology for High- and Ultra-High-Voltage Bipolar Junction Transistors and PiN Diodes*. (Doctoral Thesis in Information and Communication Technology, KTH Royal Institute of Technology, Stockholm, Sweden). Consulted at http://www.diva-portal.org/smash/get/diva2:1054818/FULLTEXT01.pdf.

Sánchez-Bajo, F. & Cumbrera, F. (1997). The use of the pseudo-Voigt function in the variance method of X-ray line-broadening analysis. *Journal of Applied Crystallography*, 30(4), 427–430.

Santavirta, S., Takagi, M., Nordsletten, L., Anttila, A., Lappalainen, R. & Konttinen, Y. T. (1998). Biocompatibility of silicon carbide in colony formation test in vitro. A promising new ceramic THR implant coating material. *Archives of Orthopaedic and Trauma Surgery*, 118(1-2), 89–91. doi: 10.1007/s004020050319.

Saroia, J., Wang, Y., Wei, Q., Lei, M., Li, X., Guo, Y. & Zhang, K. (2020). A review on 3D printed matrix polymer composites: its potential and future challenges. *The international journal of advanced manufacturing technology*, 106, 1695–1721.

Sarrión, M. L. M. & Morales, M. (1995). Preparation and characterization of NTC thermistors: nickel manganites doped with lithium. *Journal of the American Ceramic Society*, 78(4), 915–921.

Schadt, M., Pensl, G., Devaty, R., Choyke, W., Stein, R. & Stephani, D. (1994). Anisotropy of the electron Hall mobility in 4H, 6H, and 15R silicon carbide. *Applied physics letters*, 65(24), 3120–3122.

Schaffer, W. J., Negley, G., Irvine, K. & Palmour, J. (1994). Conductivity anisotropy in epitaxial 6H and 4H SiC. *MRS Online Proceedings Library (OPL)*, 339, 595.

Schlenker, T., Valero, M., Schock, H. & Werner, J. (2004). Grain growth studies of thin Cu(In, Ga)Se2 films. *Journal of Crystal Growth*, 264(1-3), 178–183. doi: 10.1016/j.jcrysgro.2004.01.020.

Schubert, M., Münch, C., Schuurman, S., Poulain, V., Kita, J. & Moos, R. (2019). Novel Method for NTC Thermistor Production by Aerosol Co-Deposition and Combined Sintering. *Sensors (Basel, Switzerland)*, 19(7), 1632. doi: 10.3390/s19071632.

See, A., Hassan, J., Hashim, M., Wahab, Z. A., Halim, D. N. F. A., Abdullah, M. S. & Azis, R. S. (2016). Dielectric behavior of β-SiC nanopowders in air between 30 and 400° C. *Journal of Materials Science: Materials in Electronics*, 27, 6623–6629.

Seeberg, T. M., Røyset, A., Jahren, S. & Strisland, F. (2011). Printed organic conductive polymers thermocouples in textile and smart clothing applications. *2011 annual international conference of the IEEE Engineering in Medicine and Biology Society*, pp. 3278–3281.

Sellin, P. & Vaitkus, J. (2006). New materials for radiation hard semiconductor dectectors. *Nuclear Instruments and Methods in Physics Research Section A: Accelerators, Spectrometers, Detectors and Associated Equipment*, 557(2), 479–489.

Semmelroth, K., Krieger, M., Pensl, G., Nagasawa, H., Püsche, R., Hundhausen, M., Ley, L., Nerding, M. & Strunk, H. P. (2004). Growth of 3C-SiC bulk material by the modified Lely method. *Materials Science Forum*, 457, 151–156.

Senesky, D. G., Jamshidi, B., Cheng, K. B. & Pisano, A. P. (2009). Harsh environment silicon carbide sensors for health and performance monitoring of aerospace systems: A review. *IEEE Sensors Journal*, 9(11), 1472–1478.

Seo, J., Sankarasubramanian, S. & Lee, B. (2018). Templated, carbothermal reduction synthesis of mesoporous silicon carbide from carbon nanotube–mesoporous silica core–shell composite. *Bulletin of Materials Science*, 41, 1–6.

Serway, R. A., Jewett, J. W. & Peroomian, V. (2000). *Physics for scientists and engineers*. Saunders college publishing Philadelphia.

Shahandeh, S. & Militzer, M. (2013). Grain boundary curvature and grain growth kinetics with particle pinning. *Philosophical Magazine*, 93(24), 3231–3247. doi: 10.1080/14786435.2013.805277.

Shcherban, N. D., Filonenko, S. M., Yaremov, P. S., Sergiienko, S. A., Ilyin, V. G. & Murzin, D. Y. (2017). Carbothermal synthesis of porous silicon carbide using mesoporous silicas. *Journal of Materials Science*, 52, 3917–3926.

Shekhawat, D., Sudhahar, D., Döll, J., Grieseler, R. & Pezoldt, J. (2023). Phase formation of cubic silicon carbide from reactive silicon–carbon multilayers. *MRS Advances*, 1–5.

Shen, A., Kim, S. B., Bailey, C., Ma, A. W. & Dardona, S. (2018). Direct write fabrication of platinum-based thick-film resistive temperature detectors. *IEEE Sensors Journal*, 18(22), 9105–9111.

Shen, T., Koch, C., McCormick, T., Nemanich, R., Huang, J. & Huang, J. (1995). The structure and property characteristics of amorphous/nanocrystalline silicon produced by ball milling. *Journal of materials research*, 10(1), 139–148.

Shen, W., Zhang, X., Huang, Q., Xu, Q. & Song, W. (2014). Preparation of solid silver nanoparticles for inkjet printed flexible electronics with high conductivity. *Nanoscale*, 6(3), 1622–1628.

Sheng, A., Khuje, S., Yu, J., Petit, D., Parker, T., Zhuang, C.-G., Kester, L. & Ren, S. (2021). Ultrahigh Temperature Copper-Ceramic Flexible Hybrid Electronics. *Nano Letters*, 21(21), 9279–9284. doi: 10.1021/acs.nanolett.1c02942. Publisher: American Chemical Society.

Sherif El-Eskandarany, M., Sumiyama, K. & Suzuki, K. (1995). Mechanical solid state reaction for synthesis of β–SiC powders. *Journal of Materials Research*, 10, 659–667.

Shi, H., Liu, C., Xu, J., Song, H., Lu, B., Jiang, F., Zhou, W., Zhang, G. & Jiang, Q. (2013). Facile fabrication of PEDOT: PSS/polythiophenes bilayered nanofilms on pure organic electrodes and their thermoelectric performance. *ACS applied materials & interfaces*, 5(24), 12811–12819.

Shimizu, Y., Arai, H. & Seiyama, T. (1985). Theoretical studies on the impedance-humidity characteristics of ceramic humidity sensors. *Sensors and Actuators*, 7(1), 11–22.

Shin, K.-Y., Park, N. S., Hwang, J. Y., Kang, K. & Lee, S.-H. (2018). Sintering process of inkjet-printed silver patterns using a heated inert gas. *Microelectronic Engineering*, 193, 91–97.

Shor, J. S., Goldstein, D. & Kurtz, A. D. (1993). Characterization of n-type beta-SiC as a piezoresistor. *IEEE transactions on electron devices*, 40(6), 1093–1099.

Shou, W., Mahajan, B. K., Ludwig, B., Yu, X., Staggs, J., Huang, X. & Pan, H. (2017). Nanoparticles: Low-Cost Manufacturing of Bioresorbable Conductors by Evaporation–Condensation-Mediated Laser Printing and Sintering of Zn Nanoparticles (Adv. Mater. 26/2017). *Advanced Materials*, 29(26).

Shuaib, E. P., Yogesh, G. K. & Sastikumar, D. (2022). Amorphous and photoluminescent crystalline silicon carbide nanoparticles synthesized by laser ablation in liquids. *Materials Today: Proceedings*, 50, 2745–2750. doi: 10.1016/j.matpr.2020.08.453.

Shyjumon, I., Gopinadhan, M., Ivanova, O., Quaas, M., Wulff, H., Helm, C. A. & Hippler, R. (2006). Structural deformation, melting point and lattice parameter studies of size selected silver clusters. *The European Physical Journal D - Atomic, Molecular, Optical and Plasma Physics*, 37(3), 409–415. doi: 10.1140/epjd/e2005-00319-x.

Singh, M., Haverinen, H. M., Dhagat, P. & Jabbour, G. E. (2010). Inkjet printing—process and its applications. *Advanced materials*, 22(6), 673–685.

Singh, S., Bhaskar, R., Narayanan, K. B., Kumar, A. & Debnath, K. (2024). Development of silicon carbide (SiC)-based composites as microwave-absorbing materials (MAMs): a review. *Journal of the European Ceramic Society*.

Sivkov, A., Nikitin, D., Pak, A. Y. & Rakhmatullin, I. (2013). Production of ultradispersed crystalline silicon carbide by plasmodynamic synthesis. *Journal of Superhard Materials*, 35, 137–142.

Sivkov, A., Nikitin, D., Pak, A. Y. & Rakhmatullin, I. (2015). Influence of plasmodynamic synthesis energy in Si-C system on the product phase composition and dispersion. *Nanotechnologies in Russia*, 10(1), 34–41.

Slack, G. A. (1964). Thermal conductivity of pure and impure silicon, silicon carbide, and diamond. *Journal of Applied physics*, 35(12), 3460–3466.

Smith, A. D., Elgammal, K., Niklaus, F., Delin, A., Fischer, A. C., Vaziri, S., Forsberg, F., Råsander, M., Hugosson, H., Bergqvist, L., Schröder, S., Kataria, S., Östling, M. & Lemme, M. C. (2015). Resistive graphene humidity sensors with rapid and direct electrical readout. *Nanoscale*, 7(45), 19099–19109. doi: 10.1039/C5NR06038A. Publisher: The Royal Society of Chemistry.

Smith, E. H. (2013). *Mechanical engineer's reference book*. Butterworth-Heinemann.

Soga, T., Jimbo, Y., Suzuki, K. & Citterio, D. (2013). Inkjet-Printed Paper-Based Colorimetric Sensor Array for the Discrimination of Volatile Primary Amines. *Analytical Chemistry*, 85(19), 8973–8978. doi: 10.1021/ac402070z. Publisher: American Chemical Society.

Somalu, M., Yufit, V. & Brandon, N. (2013). The effect of solids loading on the screen-printing and properties of nickel/scandia-stabilized-zirconia anodes for solid oxide fuel cells. *International journal of hydrogen energy*, 38(22), 9500–9510.

Son, N., Persson, C., Lindefelt, U., Chen, W., Meyer, B., Hofmann, D. & Janzén, E. (2004). Cyclotron resonance studies of effective masses and band structure in SiC. *Silicon Carbide: Recent Major Advances*, 437–460.

Steinhart, J. S. & Hart, S. R. (1968). Calibration curves for thermistors. *Deep sea research and oceanographic abstracts*, 15(4), 497–503.

Su, C.-H., Chiu, H.-L., Chen, Y.-C., Yesilmen, M., Schulz, F., Ketelsen, B., Vossmeyer, T. & Liao, Y.-C. (2019). Highly Responsive PEG/Gold Nanoparticle Thin-Film Humidity Sensor via Inkjet Printing Technology. *Langmuir: the ACS journal of surfaces and colloids*, 35(9), 3256–3264. doi: 10.1021/acs.langmuir.8b03433.

Su, P.-G. & Tsai, W.-Y. (2004). Humidity sensing and electrical properties of a composite material of nano-sized SiO2 and poly (2-acrylamido-2-methylpropane sulfonate). *Sensors and Actuators B: Chemical*, 100(3), 417–422.

Suganuma, K. (2014). *Introduction to printed electronics*. Springer Science & Business Media.

Sun, B., Xie, R., Yu, C., Li, C. & Xu, H. (2017). Structural characterization of SiC nanoparticles. *Journal of Semiconductors*, 38(10), 103002.

Sun, J., Wang, W. & Yue, Q. (2016). Review on microwave-matter interaction fundamentals and efficient microwave-associated heating strategies. *Materials*, 9(4), 231.

Sun, K., Wang, T., Gong, W., Lu, W., He, X., Eddings, E. G. & Fan, M. (2022). Synthesis and potential applications of silicon carbide nanomaterials/nanocomposites. *Ceramics International*, 48(22), 32571–32587.

Sun, L., Han, C., Wu, N., Wang, B. & Wang, Y. (2018a). High temperature gas sensing performances of silicon carbide nanosheets with an n–p conductivity transition. *RSC Advances*, 8(25), 13697–13707. doi: 10.1039/C8RA02164C. Publisher: Royal Society of Chemistry.

Sun, L., Wang, B. & Wang, Y. (2018b). A novel silicon carbide nanosheet for high-performance humidity sensor. *Advanced Materials Interfaces*, 5(6), 1701300.

Sun, L., Wang, B. & Wang, Y. (2018c). A Novel Silicon Carbide Nanosheet for High-Performance Humidity Sensor. *Advanced Materials Interfaces*, 5(6), 1701300. doi: 10.1002/admi.201701300. _eprint: https://onlinelibrary.wiley.com/doi/pdf/10.1002/admi.201701300.

Sun, L., Wang, B. & Wang, Y. (2019). A Schottky-junction-based platinum nanoclusters@ silicon carbide nanosheet as long-term stable hydrogen sensors. *Applied Surface Science*, 473, 641–648.

Sun, L., Wang, B. & Wang, Y. (2020). High-temperature gas sensor based on novel Pt single atoms@ SnO2 nanorods@ SiC nanosheets multi-heterojunctions. *ACS applied materials & interfaces*, 12(19), 21808–21817.

Suttrop, W., Pensl, G., Choyke, W., Stein, R. & Leibenzeder, S. (1992). Hall effect and infrared absorption measurements on nitrogen donors in 6H-silicon carbide. *Journal of applied physics*, 72(8), 3708–3713.

Suzuki, T., Yonenaga, I. & Kirchner, H. (1995). Yield strength of diamond. *Physical review letters*, 75(19), 3470.

Svensson, I., Artursson, E., Leanderson, P., Berglind, R. & Lindgren, F. (1997). Toxicity in vitro of some silicon carbides and silicon nitrides: whiskers and powders. *American journal of industrial medicine*, 31(3), 335–343.

Syed, N., Zavabeti, A., Ou, J. Z., Mohiuddin, M., Pillai, N., Carey, B. J., Zhang, B. Y., Datta, R. S., Jannat, A., Haque, F., Messalea, K. A., Xu, C., Russo, S. P., McConville, C. F., Daeneke, T. & Kalantar-Zadeh, K. (2018). Printing two-dimensional gallium phosphate out of liquid metal. *Nature Communications*, 9(1), 3618. doi: 10.1038/s41467-018-06124-1. Number: 1 Publisher: Nature Publishing Group.

Sze, S. & Ng, K. (2007). Physics of semiconductor devices 3rd edn john wiley & sons. *Inc., New Jersey*, 293.

Tachibana, S., Wang, Y.-F., Sekine, T., Takeda, Y., Hong, J., Yoshida, A., Abe, M., Miura, R., Watanabe, Y., Kumaki, D. & Tokito, S. (2022). A Printed Flexible Humidity Sensor with High Sensitivity and Fast Response Using a Cellulose Nanofiber/Carbon Black Composite. *ACS Applied Materials & Interfaces*, 14(4), 5721–5728. doi: 10.1021/acsami.1c20918.

Taguchi, T., Yamamoto, S., Kodama, K. & Asaoka, H. (2015). Synthesis of heterostructured SiC and C–SiC nanotubes by ion irradiation-induced changes in crystallinity. *Carbon*, 95, 279–285.

Taguchi, T., Yamamoto, S. & Ohba, H. (2021). Synthesis and formation mechanism of novel double-thick-walled silicon carbide nanotubes from multiwalled carbon nanotubes. *Applied Surface Science*, 551, 149421.

Tairov, Y. M. & Tsvetkov, V. (1978). Investigation of growth processes of ingots of silicon carbide single crystals. *Journal of crystal growth*, 43(2), 209–212.

Taka, Y. (2016). Chemistry in Pictures: SiC crystal, brah! Consulted at https://cen.acs.org/articles/96/web/2018/01/Chemistry-Pictures-SiC-crystal-brah.html.

Tan, H. W., Choong, Y. Y. C., Kuo, C. N., Low, H. Y. & Chua, C. K. (2022). 3D printed electronics: Processes, materials and future trends. *Progress in Materials Science*, 127, 100945.

Tan, Q., Luo, T., Xiong, J., Kang, H., Ji, X., Zhang, Y., Yang, M., Wang, X., Xue, C., Liu, J. et al. (2014). A harsh environment-oriented wireless passive temperature sensor realized by LTCC technology. *Sensors*, 14(3), 4154–4166.

Tan, Q., Wei, T., Chen, X., Luo, T., Wu, G., Li, C. & Xiong, J. (2015). Antenna-resonator integrated wireless passive temperature sensor based on low-temperature co-fired ceramic for harsh environment. *Sensors and Actuators A: Physical*, 236, 299–308.

Tang, Q.-Y., Chan, Y. C. & Zhang, K. (2011). Fast response resistive humidity sensitivity of polyimide/multiwall carbon nanotube composite films. *Sensors and Actuators B: Chemical*, 152(1), 99–106. doi: 10.1016/j.snb.2010.09.016.

Tendero, C., Tixier, C., Tristant, P., Desmaison, J. & Leprince, P. (2006). Atmospheric pressure plasmas: A review. *Spectrochimica Acta Part B: Atomic Spectroscopy*, 61(1), 2–30.

Terrani, K. A., Lach, T., Wang, H., Coq, A. L., Linton, K., Petrie, C., Koyanagi, T. & Byun, T. S. (2021). Irradiation stability and thermomechanical properties of 3D-printed SiC. *Journal of Nuclear Materials*, 551, 152980. doi: 10.1016/j.jnucmat.2021.152980.

Terrani, K., Jolly, B. & Trammell, M. (2020). 3D printing of high-purity silicon carbide. *Journal of the American Ceramic Society*, 103(3), 1575–1581.

Thompson, C. (2011). Grain Growth in Polycrystalline Thin Films. *MRS Proceedings*, 343. doi: 10.1557/PROC-343-3.

Thompson, C. V. & Carel, R. (1996a). Stress and grain growth in thin films. *Journal of the Mechanics and Physics of Solids*, 44(5), 657–673.

Thompson, C. V. & Carel, R. (1996b). Stress and grain growth in thin films. *Journal of the Mechanics and Physics of Solids*, 44(5), 657–673. doi: 10.1016/0022-5096(96)00022-1.

Timofeeva, E. V., Smith, D. S., Yu, W., France, D. M., Singh, D. & Routbort, J. L. (2010). Particle size and interfacial effects on thermo-physical and heat transfer characteristics of water-based α-SiC nanofluids. *Nanotechnology*, 21(21), 215703.

Tong, C. (2022). *Advanced Materials for Printed Flexible Electronics*. Springer.

Tu, T. & Jiang, G. (2018). SiC reticulated porous ceramics by 3D printing, gelcasting and liquid drying. *Ceramics International*, 44(3), 3400–3405.

Turkani, V. S., Maddipatla, D., Narakathu, B. B., Bazuin, B. J. & Atashbar, M. Z. (2018a). A carbon nanotube based NTC thermistor using additive print manufacturing processes. *Sensors and Actuators A: Physical*, 279, 1–9.

Turkani, V. S., Narakathu, B. B., Maddipatla, D., Altay, B. N., Fleming, P. D., Bazuin, B. J. & Atashbar, M. Z. (2018b). Nickel based printed resistance temperature detector on flexible polyimide substrate. *2018 IEEE SENSORS*, pp. 1–4.

Turkani, V. S., Maddipatla, D., Narakathu, B. B., Altay, B. N., Fleming, P. D., Bazuin, B. J. & Atashbar, M. Z. (2019). Nickel based RTD fabricated via additive screen printing process for flexible electronics. *Ieee Access*, 7, 37518–37527.

Umadevi, P., Nagendra, C. & Thutupalli, G. (1993). Structural, electrical and infrared optical properties of vanadium pentoxide (V2O5) thick-film thermistors. *Sensors and Actuators A: Physical*, 39(1), 59–69.

Uppuluri, K. & Szwagierczak, D. (2022). Fabrication and characterization of screen printed NiMn2O4 spinel based thermistors. *Sensor Review*, 42(2), 177–186.

Vacca, A., Mascia, M., Rizzardini, S., Corgiolu, S., Palmas, S., Demelas, M., Bonfiglio, A. & Ricci, P. C. (2015). Preparation and characterisation of transparent and flexible PEDOT: PSS/PANI electrodes by ink-jet printing and electropolymerisation. *RSC advances*, 5(97), 79600–79606.

Van Haeringen, W., Bobbert, P. & Backes, W. (1997). On the band gap variation in SiC polytypes. *physica status solidi (b)*, 202(1), 63–79.

Varghese, J. & Sebastian, M. (2017). Dielectric Inks. *Microwave Materials and Applications 2V Set*, 457–480.

Vaseem, M., Lee, S.-K., Kim, J.-G. & Hahn, Y.-B. (2016). Silver-ethanolamine-formate complex based transparent and stable ink: Electrical assessment with microwave plasma vs thermal sintering. *Chemical Engineering Journal*, 306, 796–805.

Vaughan, G. L., Jordan, J. & Karr, S. (1991). The toxicity, in vitro, of silicon carbide whiskers. *Environmental research*, 56(1), 57–67.

Vaussenat, F., Bhattacharya, A., Payette, J., Benavides-Guerrero, J. A., Perrotton, A., Gerlein, L. F. & Cloutier, S. G. (2023). Continuous Critical Respiratory Parameter Measurements Using a Single Low-Cost Relative Humidity Sensor: Evaluation Study. *JMIR Biomedical Engineering*, 8(1), e47146. doi: 10.2196/47146.

Verma, A. & Stellacci, F. (2010). Effect of surface properties on nanoparticle–cell interactions. *small*, 6(1), 12–21.

Viegas, D., Goicoechea, J., Corres, J. M., Santos, J. L., Ferreira, L. A., Araújo, F. M. & Matias, I. R. (2009). A fibre optic humidity sensor based on a long-period fibre grating coated with a thin film of SiO2 nanospheres. *Measurement Science and Technology*, 20(3), 034002. doi: 10.1088/0957-0233/20/3/034002.

Vinoth, E. & Gopalakrishnan, N. (2020). Fabrication of interdigitated electrode (IDE) based ZnO sensors for room temperature ammonia detection. *Journal of Alloys and Compounds*, 824, 153900.

Virtanen, J., Ukkonen, L., Bjorninen, T., Elsherbeni, A. Z. & Sydänheimo, L. (2011). Inkjet-printed humidity sensor for passive UHF RFID systems. *IEEE Transactions on Instrumentation and Measurement*, 60(8), 2768–2777.

Volkman, S. K., Yin, S., Bakhishev, T., Puntambekar, K., Subramanian, V. & Toney, M. F. (2011). Mechanistic Studies on Sintering of Silver Nanoparticles. *Chemistry of Materials*, 23(20), 4634–4640. doi: 10.1021/cm202561u.

Volm, D., Meyer, B., Hofmann, D., Chen, W., Son, N., Persson, C., Lindefelt, U., Kordina, O., Sörman, E., Konstantinov, A. et al. (1996). Determination of the electron effective-mass tensor in 4H SiC. *Physical Review B*, 53(23), 15409.

Voorhees, P. W. (1985). The theory of Ostwald ripening. *Journal of Statistical Physics*, 38, 231–252.

Vu, T. T. N., Teyssedre, G., Le Roy, S. & Laurent, C. (2017). Maxwell–Wagner effect in multi-layered dielectrics: interfacial charge measurement and modelling. *Technologies*, 5(2), 27.

Wadhwa, A. (2015). Run-time ink stability in pneumatic aerosol jet printing using a split stream solvent add back system.

Wadhwa, A., Guerrero, J. B., Gratuze, M., Bolduc, M. & Cloutier, S. G. (2024). All Screen Printed and Flexible Silicon Carbide NTC Thermistors for Temperature Sensing Applications.

Wan, Y. (2024). Wide bandgap (WBG) semiconductors in power electronics: the future of electric vehicles.

Wang, B., Wang, Y., Lei, Y., Xie, S., Wu, N., Gou, Y., Han, C., Shi, Q. & Fang, D. (2016). Vertical SnO 2 nanosheet@ SiC nanofibers with hierarchical architecture for high-performance gas sensors. *Journal of Materials Chemistry C*, 4(2), 295–304.

Wang, C., Hong, G.-Y., Li, K.-M. & Young, H.-T. (2017). A miniaturized nickel oxide thermistor via aerosol jet technology. *Sensors*, 17(11), 2602.

Wang, H. Y., Wang, Y. Q., Hu, Q. F. & Li, X. J. (2012a). Capacitive humidity sensing properties of SiC nanowires grown on silicon nanoporous pillar array. *Sensors and Actuators B: Chemical*, 166, 451–456.

Wang, H. Y., Wang, Y. Q., Hu, Q. F. & Li, X. J. (2012b). Capacitive humidity sensing properties of SiC nanowires grown on silicon nanoporous pillar array. *Sensors and Actuators B: Chemical*, 166-167, 451–456. doi: 10.1016/j.snb.2012.02.087.

Wang, J. & Jiang, X. (2020). Review and analysis of SiC MOSFETs' ruggedness and reliability. *IET Power Electronics*, 13(3), 445–455.

Wang, J., Zhang, Y., Zhang, H., Han, L., Bi, Y., Wang, H., Song, S. & Zhang, S. (2018a). Low-temperature catalytic synthesis of SiC nanopowder from liquid phenolic resin and diatomite. *Advances in Applied Ceramics*, 117(3), 147–154.

Wang, Q., Li, Y., Jin, S. & Sang, S. (2015a). Catalyst-free hybridization of silicon carbide whiskers and expanded graphite by vapor deposition method. *Ceramics International*, 41(10), 14359–14366.

Wang, W., Song, Q., Zhang, S., Li, Y., Ahmad, M. & Gong, Y. (2020a). The loss analysis and efficiency optimization of power inverter based on SiC mosfet s under the high-switching frequency. *IEEE Transactions on Industry Applications*, 57(2), 1521–1534.

Wang, X., Zhao, J., Cui, E., Sun, Z. & Yu, H. (2021). Grain growth kinetics and grain refinement mechanism in Al2O3/WC/TiC/graphene ceramic composite. *Journal of the European Ceramic Society*, 41(2), 1391–1398. doi: 10.1016/j.jeurceramsoc.2020.10.019.

Wang, Y.-F., Sekine, T., Takeda, Y., Yokosawa, K., Matsui, H., Kumaki, D., Shiba, T., Nishikawa, T. & Tokito, S. (2020b). Fully Printed PEDOT:PSS-based Temperature Sensor with High Humidity Stability for Wireless Healthcare Monitoring. *Scientific Reports*, 10(1), 2467. doi: 10.1038/s41598-020-59432-2. Number: 1 Publisher: Nature Publishing Group.

Wang, Y., Dong, S., Li, X., Hong, C. & Zhang, X. (2022). Synthesis, properties, and multifarious applications of SiC nanoparticles: A review. *Ceramics International*, 48(7), 8882–8913.

Wang, Y., Hou, X., Xu, W. & Tian, M. (2015b). Effects of reaction temperature on the synthesis of high purity silicon carbide powder. *Materials Research Innovations*, 19(sup5), S5–1338.

Wang, Z., Gao, W., Zhang, Q., Zheng, K., Xu, J., Xu, W., Shang, E., Jiang, J., Zhang, J. & Liu, Y. (2018b). 3D-printed graphene/polydimethylsiloxane composites for stretchable and strain-insensitive temperature sensors. *ACS applied materials & interfaces*, 11(1), 1344–1352.

Wasa, K., Tohda, T., Kasahara, Y. & Hayakawa, S. (1979). Highly-reliable temperature sensor using rf-sputtered SiC thin film. *Review of Scientific Instruments*, 50(9), 1084–1088.

Weisensel, L., Travitzky, N., Sieber, H. & Greil, P. (2004). Laminated object manufacturing (LOM) of SiSiC composites. *Advanced Engineering Materials*, 6(11), 899–903.

Wellmann, P., Müller, R., Queren, D., Sakwe, S. & Pons, M. (2006). Vapor growth of SiC bulk crystals and its challenge of doping. *Surface and Coatings Technology*, 201(7), 4026–4031.

Wen, N., Zhang, L., Jiang, D., Wu, Z., Li, B., Sun, C. & Guo, Z. (2020). Emerging flexible sensors based on nanomaterials: recent status and applications. *Journal of Materials Chemistry A*, 8(48), 25499–25527. doi: 10.1039/D0TA09556G. Publisher: The Royal Society of Chemistry.

Werner, C., Godlinski, D., Zöllmer, V. & Busse, M. (2013). Morphological influences on the electrical sintering process of Aerosol Jet and Ink Jet printed silver microstructures. *Journal of Materials Science: Materials in Electronics*, 24, 4367–4377.

Wiklund, J., Karakoç, A., Palko, T., Yiğitler, H., Ruttik, K., Jäntti, R. & Paltakari, J. (2021). A Review on Printed Electronics: Fabrication Methods, Inks, Substrates, Applications and Environmental Impacts. *Journal of Manufacturing and Materials Processing*, 5(3), 89. doi: 10.3390/jmmp5030089. Number: 3 Publisher: Multidisciplinary Digital Publishing Institute.

Wiley, B., Sun, Y. & Xia, Y. (2007). Synthesis of Silver Nanostructures with Controlled Shapes and Properties. *Accounts of Chemical Research*, 40(10), 1067–1076. doi: 10.1021/ar7000974. Publisher: American Chemical Society.

Wu, C., Fang, X., Guo, X., Zhao, L., Tian, B. & Jiang, Z. (2020). Optimal design of SiC piezoresistive pressure sensor considering material anisotropy. *Review of Scientific Instruments*, 91(1).

Wu, L., Zhang, L., Sun, M., Liu, R., Yu, L. & Lv, Y. (2017). Metal-free cataluminescence gas sensor for hydrogen sulfide based on its catalytic oxidation on silicon carbide nanocages. *Analytical chemistry*, 89(24), 13666–13672.

Wu, M., Gong, Z., Kuehne, A., Kanibolotsky, A., Chen, Y., Perepichka, I., Mackintosh, A., Gu, E., Skabara, P. J., Pethrick, R. et al. (2009). Hybrid GaN/organic microstructured light-emitting devices via ink-jet printing. *Optics Express*, 17(19), 16436–16443.

Wu, R., Zhou, K., Yue, C. Y., Wei, J. & Pan, Y. (2015). Recent progress in synthesis, properties and potential applications of SiC nanomaterials. *Progress in Materials Science*, 72, 1–60.

Wu, S. P., Zhao, Q. Y., Zheng, L. Q. & Ding, X. H. (2011). Behaviors of ZnO-doped silver thick film and silver grain growth mechanism. *Solid State Sciences*, 13(3), 548–552. doi: 10.1016/j.solidstatesciences.2010.12.024.

Wu, X., Fan, J., Qiu, T., Yang, X., Siu, G. & Chu, P. K. (2005). Experimental evidence for the quantum confinement effect in 3 C-SiC nanocrystallites. *Physical review letters*, 94(2), 026102.

Wünscher, S., Abbel, R., Perelaer, J. & Schubert, U. S. (2014). Progress of alternative sintering approaches of inkjet-printed metal inks and their application for manufacturing of flexible electronic devices. *Journal of Materials Chemistry C*, 2(48), 10232–10261.

Xia, Y., Zhang, H. & Ouyang, J. (2010). Highly conductive PEDOT: PSS films prepared through a treatment with zwitterions and their application in polymer photovoltaic cells. *Journal of Materials Chemistry*, 20(43), 9740–9747.

Xu, B. & Zhang, Q. (2021). Preparation and Properties of Hydrophobically Modified Nano-SiO2 with Hexadecyltrimethoxysilane. *ACS Omega*, 6(14), 9764–9770. doi: 10.1021/acsomega.1c00381. Publisher: American Chemical Society.

Xu, M., Girish, Y. R., Rakesh, K. P., Wu, P., Manukumar, H. M., Byrappa, S. M., Byrappa, K. et al. (2021). Recent advances and challenges in silicon carbide (SiC) ceramic nanoarchitectures and their applications. *Materials Today Communications*, 28, 102533.

Xu, Q., Zhao, J., Pecunia, V., Xu, W., Zhou, C., Dou, J., Gu, W., Lin, J., Mo, L., Zhao, Y. et al. (2017). Selective conversion from p-type to n-type of printed bottom-gate carbon nanotube thin-film transistors and application in complementary metal–oxide–semiconductor inverters. *ACS applied materials & interfaces*, 9(14), 12750–12758.

Yamada, O., Miyamoto, Y. & Koizumi, M. (1986). Self-propagating high-temperature synthesis of the SiC. *Journal of materials research*, 1(2), 275–279.

Yamada, T., Araki, F., Ishihara, J. & Miyajima, K. (2019). Fabrication of silicon carbide nanoparticles using picosecond pulsed laser ablation in acetone with characterizations from TEM and XRD. *AIP Advances*, 9(10).

Yamamoto, J. K., Lanagan, M. T., Bhalla, A. S., Newnham, R. E. & Cross, L. E. (1989). Dielectric properties of microporous glass in the microwave region. *Journal of the American Ceramic Society*, 72(6), 916–921.

Yamashita, S., Sakai, H. & Murata, H. (2019). Application of Gold Powder Made from Gold Leaf for Conductive Inks. *IEICE Transactions on Electronics*, 102(2), 176–179.

Yan, C., Wang, J. & Lee, P. S. (2015). Stretchable graphene thermistor with tunable thermal index. *ACS nano*, 9(2), 2130–2137.

Yan, F.-J., Huang, W.-Q., Sang, X.-H., Liang, J.-G., Wan, X., Shao, F. & Gu, X.-F. (2021). Direct ink write printing of resistive-type humidity sensors. *Flexible and Printed Electronics*, 6(4), 045007. doi: 10.1088/2058-8585/ac310b. Publisher: IOP Publishing.

Yan, J. (2021). A Review of Sintering-Bonding Technology Using Ag Nanoparticles for Electronic Packaging. *Nanomaterials*, 11(4), 927. doi: 10.3390/nano11040927.

Yang, C. C. & Mai, Y.-W. (2014). Thermodynamics at the nanoscale: A new approach to the investigation of unique physicochemical properties of nanomaterials. *Materials Science and Engineering: R: Reports*, 79, 1–40.

Yang, K., Li, J., Qi, L., Zhang, H., Zhang, D. & Yan, H. (2011). Combustion synthesis of SiC nanosized powders at low nitrogen pressure. *Powder metallurgy*, 54(4), 529–532.

Yang, L., Zhao, H., Fan, S., Deng, S., Lv, Q., Lin, J. & Li, C.-P. (2014). Label-free electrochemical immunosensor based on gold–silicon carbide nanocomposites for sensitive detection of human chorionic gonadotrophin. *Biosensors and Bioelectronics*, 57, 199–206.

Yang, S., Cai, W., Zeng, H. & Xu, X. (2009a). Ultra-fine β-SiC quantum dots fabricated by laser ablation in reactive liquid at room temperature and their violet emission. *Journal of Materials Chemistry*, 19(38), 7119–7123.

Yang, W. & Wang, C. (2016). Graphene and the related conductive inks for flexible electronics. *Journal of materials chemistry C*, 4(30), 7193–7207.

Yang, Y., Lin, Z.-M. & Li, J.-T. (2009b). Synthesis of SiC by silicon and carbon combustion in air. *Journal of the European Ceramic Society*, 29(1), 175–180.

Yang, Z.-G. & Shaw, L. (1996). Synthesis of nanocrystalline SiC at ambient temperature through high energy reaction milling. *Nanostructured Materials*, 7(8), 873–886.

Yang, Z. (2016). *Flexible substrate technology for millimeter wave applications*. (Ph.D. thesis, INSA de Toulouse).

Yermekova, Z., Mansurov, Z. & Mukasyan, A. (2010). Influence of precursor morphology on the microstructure of silicon carbide nanopowder produced by combustion syntheses. *Ceramics International*, 36(8), 2297–2305.

Yim, C., Kockerbeck, Z. A., Jo, S. B. & Park, S. S. (2017). Hybrid Copper-Silver-Graphene Nanoplatelet Conductive Inks on PDMS for Oxidation Resistance Under Intensive Pulsed Light. *ACS applied materials & interfaces*, 9(42), 37160–37165. doi: 10.1021/acsami.7b10748.

Yoo, K.-P., Lim, L.-T., Min, N.-K., Lee, M. J., Lee, C. J. & Park, C.-W. (2010a). Novel resistive-type humidity sensor based on multiwall carbon nanotube/polyimide composite films. *Sensors and Actuators B: Chemical*, 145(1), 120–125.

Yoo, K.-P., Lim, L.-T., Min, N.-K., Lee, M. J., Lee, C. J. & Park, C.-W. (2010b). Novel resistive-type humidity sensor based on multiwall carbon nanotube/polyimide composite films. *Sensors and Actuators B: Chemical*, 145(1), 120–125. doi: 10.1016/j.snb.2009.11.041.

Yu, H., Zhu, J., Yang, L., Dai, B., Baraban, L., Cuniberti, G. & Han, J. (2015). Superhydrophobic carbon nanotube/silicon carbide nanowire nanocomposites. *Materials & Design*, 87, 198–204.

Yu, J., Khuje, S., Sheng, A., Kilczewski, S., Parker, T. & Ren, S. (2022). High-Temperature Copper–Graphene Conductors via Aerosol Jetting. *Advanced Engineering Materials*, 24(9), 2200284. doi: 10.1002/adem.202200284. _eprint: https://onlinelibrary.wiley.com/doi/pdf/10.1002/adem.202200284.

Yu, X., Terakawa, S., Hayashi, S., Asaka, T., Itoigawa, F., Ono, S. & Takayanagi, J. (2017). Carbonization of silicon nanoparticles via ablation induced by femtosecond laser pulses in hexane. *Arabian Journal for Science and Engineering*, 42, 4221–4226.

Yuan, W., Cui, X., Li, Y. & Ma, C. (2015). Effects of relative humidity on thermistor mount measurements. *2015 40th International Conference on Infrared, Millimeter, and Terahertz waves (IRMMW-THz)*, pp. 1–2.

Yuan, Y., Liu, C., Li, H., Li, Y., Cao, X., Su, J., Cheng, L., Yuan, L., Zhang, X. & Li, J. (2017). Annealing effect in a nitrogen atmosphere on structural and optical properties of In 2 Te 5 thin films. *Optical Materials Express*, 7(11), 4147–4155.

Zakharko, Y., Rioux, D., Patskovsky, S., Lysenko, V., Marty, O., Bluet, J.-M. & Meunier, M. (2011). Direct synthesis of luminescent SiC quantum dots in water by laser ablation. *physica status solidi (RRL)–Rapid Research Letters*, 5(8), 292–294.

Zavanelli, N. & Yeo, W.-H. (2021). Advances in screen printing of conductive nanomaterials for stretchable electronics. *ACS omega*, 6(14), 9344–9351.

Zeng, F.-W., Liu, X.-X., Diamond, D. & Lau, K. T. (2010). Humidity sensors based on polyaniline nanofibres. *Sensors and Actuators B: Chemical*, 143(2), 530–534.

Zhang, C., Zhang, Y., Cao, K., Guo, Z., Han, Y., Hu, W., Wu, Y., She, Y. & He, Y. (2021). Ultrasensitive and reversible room-temperature resistive humidity sensor based on layered two-dimensional titanium carbide. *Ceramics International*, 47(5), 6463–6469.

Zhang, D., Tong, J. & Xia, B. (2014a). Humidity-sensing properties of chemical reduced graphene oxide/polymer nanocomposite film sensor based on layer-by-layer nano self-assembly. *Sensors and Actuators B: Chemical*, 197, 66–72. doi: 10.1016/j.snb.2014.02.078.

Zhang, J., Li, W., Jia, Q., Lin, L., Huang, J. & Zhang, S. (2015). Molten salt assisted synthesis of 3C–SiC nanowire and its photoluminescence properties. *Ceramics International*, 41(10), 12614–12620.

Zhang, N., Li, J., Wang, L., Long, H., Wang, X. & Kan, H. (2010). Influence of lanthanum on synthesis of SiC nanopowder. *Powder metallurgy*, 53(1), 82–85.

Zhang, N., Lin, C.-M., Senesky, D. G. & Pisano, A. P. (2014b). Temperature sensor based on 4H-silicon carbide pn diode operational from 20 C to 600 C. *Applied Physics Letters*, 104(7).

Zhang, S., Chen, C., Bin, W., Zheng, X., San, H. & Hofmann, W. (2018). Dual-axis thermal convective inclinometer based on CNT/PDMS composite. *Journal of Materials Science: Materials in Electronics*, 29, 18997–19004.

Zhang, S., Tu, R. & Goto, T. (2012). High-speed epitaxial growth of β-SiC film on Si (111) single crystal by laser chemical vapor deposition. *Journal of the American Ceramic Society*, 95(9), 2782–2784.

Zhang, X., Turkani, V. S., Hajian, S., Bose, A. K., Maddipatla, D., Hanson, A. J., Narakathu, B. B. & Atashbar, M. Z. (2019). Novel Printed Carbon Nanotubes Based Resistive Humidity Sensors. *2019 IEEE International Conference on Flexible and Printable Sensors and Systems (FLEPS)*, 1–3. doi: 10.1109/FLEPS.2019.8792298. Conference Name: 2019 IEEE International Conference on Flexible and Printable Sensors and Systems (FLEPS) ISBN: 9781538693049 Place: Glasgow, United Kingdom Publisher: IEEE.

Zhang, X., Maddipatla, D., Bose, A. K., Hajian, S., Narakathu, B. B., Williams, J. D., Mitchell, M. F. & Atashbar, M. Z. (2020a). Printed carbon nanotubes-based flexible resistive humidity sensor. *IEEE Sensors Journal*, 20(21), 12592–12601.

Zhang, X., Maddipatla, D., Bose, A. K., Hajian, S., Narakathu, B. B., Williams, J. D., Mitchell, M. F. & Atashbar, M. Z. (2020b). Printed Carbon Nanotubes-Based Flexible Resistive Humidity Sensor. *IEEE Sensors Journal*, 20(21), 12592–12601. doi: 10.1109/JSEN.2020.3002951. Conference Name: IEEE Sensors Journal.

Zhang, Y., Sheng, L., Fang, Y., An, K., Yu, L., Liu, Y. & Zhao, X. (2017). Synthesis of 3C-SiC nanowires from a graphene/Si configuration obtained by arc discharge method. *Chemical Physics Letters*, 678, 17–22.

Zheng, L.-Q., Chen, Z.-H., Zou, J.-P. & Zhang, Z.-J. (2022). Grain Growth and Microstructure of Silver Film Doped Finite Glass on Ferrite Substrates at High Annealing Temperature. *Russian Journal of Physical Chemistry A*, 96(7), 1519–1524. doi: 10.1134/S0036024422070184.

Zhong, Y., Shaw, L. L., Manjarres, M. & Zawrah, M. F. (2010). Synthesis of silicon carbide nanopowder using silica fume. *Journal of the American Ceramic Society*, 93(10), 3159–3167.

Zhou, N., Zhang, L., Wang, W., Zhang, X., Zhang, K., Chen, M., Huang, Y., He, R. & Fang, D. (2023). Stereolithographically 3D Printed SiC Metastructure for Ultrabroadband and High Temperature Microwave Absorption. *Advanced Materials Technologies*, 8(4), 2201222. doi: 10.1002/admt.202201222. _eprint: https://onlinelibrary.wiley.com/doi/pdf/10.1002/admt.202201222.

Zhou, W., Liu, X. & Zhang, Y. (2006). Simple approach to β-SiC nanowires: synthesis, optical, and electrical properties. *Applied Physics Letters*, 89(22).

Zhou, Y., Han, S.-T. & Roy, V. (2014). Nanocomposite dielectric materials for organic flexible electronics. In *Nanocrystalline Materials* (pp. 195–220). Elsevier.

Zhu, J., Liu, Z., Wu, X., Xu, L., Zhang, W. & Chu, P. K. (2007). Luminescent small-diameter 3C-SiC nanocrystals fabricated via a simple chemical etching method. *Nanotechnology*, 18(36), 365603.

Zhu, K. N., Godfrey, A., Hansen, N. & Zhang, X. D. (2017). Microstructure and mechanical strength of near- and sub-micrometre grain size copper prepared by spark plasma sintering. *Materials & Design*, 117, 95–103. doi: 10.1016/j.matdes.2016.12.042.

Zhu, K., Guo, L., Lin, J., Hao, W., Shang, J., Jia, Y., Chen, L., Jin, S., Wang, W. & Chen, X. (2012a). Graphene covered SiC powder as advanced photocatalytic material. *Applied Physics Letters*, 100(2).

Zhu, K., Guo, L., Lin, J., Hao, W., Shang, J., Jia, Y., Chen, L., Jin, S., Wang, W. & Chen, X. (2012b). Graphene covered SiC powder as advanced photocatalytic material. *Applied Physics Letters*, 100(2), 023113. doi: 10.1063/1.3676042.

Zhu, Q., Dong, X., Hu, J., Yang, J., Zhang, X., Ding, Y. & Dong, S. (2020). High strength aligned SiC nanowire reinforced SiC porous ceramics fabricated by 3D printing and chemical vapor infiltration. *Ceramics International*, 46(5), 6978–6983.

Zhu, Y.

Zikulnig, J., Chang, S., Bito, J., Rauter, L., Roshanghias, A., Carrara, S. & Kosel, J. (2023). Printed electronics technologies for additive manufacturing of hybrid electronic sensor systems. *Advanced Sensor Research*, 2(7), 2200073.

Zocca, A., Lima, P., Diener, S., Katsikis, N. & Günster, J. (2019). Additive manufacturing of SiSiC by layerwise slurry deposition and binder jetting (LSD-print). *Journal of the European Ceramic Society*, 39(13), 3527–3533.

Zorman, C. A. (2009). Silicon carbide as a material for biomedical microsystems. *2009 Symposium on Design, Test, Integration & Packaging of MEMS/MOEMS*, pp. 1–7.

Zorman, C. A. & Parro, R. J. (2008). Micro-and nanomechanical structures for silicon carbide MEMS and NEMS. *physica status solidi (b)*, 245(7), 1404–1424.

Zuo, J., Tavakoli, S., Mathavakrishnan, D., Ma, T., Lim, M., Rotondo, B., Pauzauskie, P., Pavinatto, F. & MacKenzie, D. (2020). Additive manufacturing of a flexible carbon monoxide sensor based on a SnO2-graphene nanoink. *Chemosensors*, 8(2), 36.